DEVELOPMENT OF ZEOLITE/BIO-MAGNETITE NANOCOMPOSITES FOR ELIMINATION OF PHARMACEUTICAL POLLUTANTS IN AQUEOUS SOLUTION: EXPERIMENTAL AND COMPUTATIONAL STUDIES

BY

KAMGANG DJIOKO Fredy Harcel (B.Sc., M.Sc., UYI)

ACEFUELS/20/Ph.D./14000104

A THESIS SUBMITTED TO THE POSTGRADUATE SCHOOL, FEDERAL UNIVERSITY OF TECHNOLOGY, OWERRI

IN PARTIAL FULFILMENT OF THE REQUIREMENTS FOR THE AWARD OF THE DEGREE OF DOCTOR OF PHILOSOPHY (Ph.D.) IN NANOTECHNOLOGY

OCTOBER, 2024

CERTIFICATION

This is to certify that this work "Development of zeolite/bio-magnetite nanocomposites for elimination of pharmaceutical pollutants in aqueous solution: experimental and computational studies" was carried out by Kamgang Djioko Fredy Harcel, Reg. number (ACE-FUELS/20/Ph.D./14000104) in partial fulfillment of the requirements for the award of the degree of Doctor of Philosophy in Nanotechnology in the African Center of Excellence in Future Energy and Electrochemical Systems (ACE-FUELS), Federal University of Technology, Owerri.

Prof. (Mrs.) Chinyere A. Madu
(Supervisor)

06/01/2025
Date

Prof. Georges K. Youbi
(Co-Supervisor)

06/01/2025
Date

Dr. Simeon C. Nwanonenyi
(Co-Supervisor)

06/01/2025
Date

Prof. (Mrs) Chinyere A. Madu
(Programme Coordinator)

06/02/2025
Date

Prof. Emeka E. Oguzie
(Center Leader, ACE-FUELS)

06/02/25
Date

Prof. (Mrs.) Justina N. Nwosu
(Dean, Postgraduate School)

Date

Prof. Agbaje Lateef
(External examiner)

22/IV/2024
Date

DEDICATION

This dissertation is dedicated to my parents, Mr. DJIOKO Michel and Mrs. MEGANTCHOU Pauline Pulchérie

ACKNOWLEDGEMENTS

This work was carried out at the Physical Chemistry Laboratory for the Environment and Materials at the University of Yaoundé 1 (Cameroon) and at the laboratory of the African Centre of Excellence on Future Energy and Electrochemical Systems at the Federal University of Technology, Owerri (Nigeria).

These few lines will allow me to thank those responsible and the people who contributed directly or indirectly to the completion of this work both at the scientific level and at the personal level, and without their help, this work would never have been possible.

I would like to express my deepest gratitude to Prof. Chinyere Ada Madu, Professor Geoges Kamgang Youbi and Dr. Nwanonenyi Simeon Chukwudozie for the honour of supervising this work and for their availability, passion, patience and all the attention they gave me throughout the completion of this work. I would like to express my deepest gratitude to them for the completion of this work.

I would also like to thank Prof. Emeka Emmanuel Oguzie Head of ACE-FUELS Center for the warm welcome he gave me in his research center, his availability also for his encouragement and motivation.

The efforts of the postgraduate school cannot be overemphasized due its immense support in going through the study, especially the Dean, Prof. (Mrs.) Justine N. Nwosu, the Associate Dean, the Assistant Registrar, the Deputy Bursar, the Schedule Officers and all other members of staff in the school just to mention a few.

I would like to express my gratitude to the members of the jury who kindly devoted part of their time to my thesis. I would also like to thank Professor Agbaje Lateef of the Ladoke Akintola University of Technology, Ogbomoso, for agreeing to examine this thesis.

My sincere gratitude goes to Prof S.O. Onyekuru, who is the Research Coordinator of ACE-FUELS, FUTO, for his relentless efforts and guidance in ensuring that proper procedure was followed for the speedy conclusion of this work.

A special thank you to Mr. Fotsop Cyrille Ghislain who made a decisive contribution to the advancement of this work.

All my thanks then go to the teachers of the African Center of Excellence on Future Energy and Electrochemical Systems of the Federal University and Technology of Owerri

(ACEFUELS FUTO) and the Faculty of Science of the University of Yaoundé I for their contributions to my academic training.

Furthermore, our thanks are due to World Bank for financing this work through the ACE Impact project in partnership with the African Center of Excellence on Future Energy and Electrochemical Systems of the Federal University of Technology of Owerri (ACEFUELS FUTO).

I would also like to thank the research team of the laboratory of physical chemistry of the environment and materials of the University of Yaoundé 1 (Cameroon) as well as that of the laboratory of the African Center of Excellence on Future Energy and Electrochemical Systems of the Federal University and Technology of Owerri (Nigeria) for their frank collaboration and their contribution to the realization of this thesis.

A warm thank you to my friends Talla Kamte Jean Vincent, Agoumtie Tatong Olivier Lebon, Meguiguem Romual, Mbekou Calvine Melva, Ngeuna Tiomo Lucresse Kora, Tsopben Merveille Jodelle and Djoumessi Arielle Belone who had confidence in me and who, through their presence, their support and their motivation, helped me overcome some difficult moments.

A special thank you to my family, my brothers and sisters for their financial and moral support, their prayers and their encouragement.

TABLE OF CONTENTS

LIST OF TABLES

LIST OF FIGURES

LIST OF ABBREVIATIONS

CIP:	Ciprofloxacin
PC:	Pharmaceutical Contaminant
QM:	Quantum mechanics
MC:	Monte Carlo
DFT:	Density Functional Theory
MD:	Molecular Dynamics
TP:	*Terbernaemontana Penduliflora*
ZSM-5:	Zeolite Socony Mobil-5
EC:	Emerging Contaminants
WTP:	Wastewater Treatment Plants
DNA:	Deoxyribonucleic Acid
RNA:	Ribonucleic Acid
HPLC:	High-Performance Liquid Chromatography
LC:	Liquid Chromatography
GC:	Gas Chromatography
MS:	Mass Spectrometry
FT-NIR:	Fourier Transform Near-Infrared
FT-IR:	Fourier Transform Infrared
AOPs:	Advanced Oxidation Processes
BET:	Brunauer, Emmet and Teller
NaCl:	Sodium Chloride
HCl:	Hydrochloric acid
IONPs :	Iron Oxide Nanoparticles
IZA-SC :	International Zeolite Association Structure Commission
LTA:	Lynde Type A
μ:	Chemical Potential
χ:	Electronegativity

η:	Hardness
S:	Softness
ω:	Electrophilicity
ΔEgap:	Gap energy
ε:	Nucleophile
ω-:	Electron donating power
ω+:	Electroacceptance power
ΔN:	Transported electrons
$f_k^{\pm}$:	Indices of Fukui
I:	Ionization energy
A:	Electron affinity
HSAB:	Hard Acids and Soft Bases
XRD:	X-ray diffraction
TGA:	Thermogravimetric Analysis
SEM:	Scanning Electron Microscopy
EDS:	Energy Dispersive Spectroscopy
ΔG° :	Giggs free enthalpy variation
ΔH° :	Enthalpy Variation
ΔS° :	Entropy Variation
DOS:	Density of states
PBE:	Perdew-Burke-Ernzerhof
GGA:	Generalized Gradient Approximation
Eads:	Adsorption Energy
RDF:	Radial Distribution Function
JCPDS:	Joint Committee on Powder Diffraction Standards
BJH:	Barrett–Joyner–Halenda
LUMO:	Lowest Unoccupied Molecular Orbital
HOMO:	Highest Occupied Molecular Orbital
MAS-NMR:	Magic-angle rotation and nuclear magnetic resonance

ABSTRACT

Discharges of pharmaceutical micropollutants (antibiotics) are steadily increasing. These toxic, persistent pollutants are generally responsible for a number of adverse health effects. The main objective of this work was to synthesize biomagnetite/zeolite nanocomposites for the effective removal of ciprofloxacin in aqueous solution. Biomagnetite nanoparticles were synthesized by the co-precipitation method, zeolite 4A and nanocomposites by the hydrothermal method and characterized by FT-IR, XRD, XRF, MAS-NMR, TGA/DTG, SEM/EDS, BET and pHpzc analysis. Batch adsorption experiments were conducted to evaluate the adsorption capacity of zeolite 4A and nanocomposites, and then study the effect of loading of magnetite nanoparticles in nanocomposites for the removal of ciprofloxacin as pollutant model in aqueous solution. Thus, the zeolites 4A were synthesized from raw kaolin by the hydrothermal method, While, the bio-magnetite nanoparticles were synthesized by co-precipitation method using *Tabernaemontana penduliflora* as stabilizing and reducing agents and the nanocomposites by coating method. It was noted that the synthesized nanocomposites had a paramagnetic mesoporous crystalline structure with a cubic morphology coated with magnetite nanoparticles and a high specific surface area (53.258 m^2/g) compared to that of zeolites 4A (34.232m^2/g and 38.443 m^2/g). The adsorption of ciprofloxacin on different materials, revealed the maximum adsorption for zeolites 4A was also obtained at pH 8, a contact time 80 minutes, an initial concentration of the CIP 60 ppm and a dose of zeolite 4A of 20 mg at 25°C. The removal efficiency was 91.75% and 90.74% with a maximum adsorption capacity (q_{max}) 87.72 mg/g and 95.24 mg/g obtained from the Langmuir model for zeolite 4A derived from Kaolin picked up in the locality of Bong and Famgamg, respectively. For the MZ-6 nanocomposite, the maximum adsorption for zeolite 4A was obtained at pH 8, a contact time 60 minutes, an initial CIP concentration 90 ppm and an MZ-6 dose of 10 mg at 25°C. The removal efficiency was 98.78% with a maximum adsorption capacity (q_{max}) 175.44 mg/g. Isotherm studies suggested that the Langmuir isotherm was the most suitable. Which indicates that the adsorption process of CIP was monolayer adsorption on a homogeneous surface. The DFT results revealed that in the aqueous phase, the CIP molecule is stable, reactive in the form of zweitterion (CIP±) and that the oxygen, nitrogen atoms and the aromatic ring were responsible for this reactivity. The Monte Carlo simulation results showed that the adsorption of CIP molecules on the surface of zeolite 4A and MZ composite were favorable and spontaneous and the predominant interaction was chemisorption. In addition, CIP molecules showed high affinities with the surface of the MZ composite. The regeneration study showed that the synthesized adsorbents were chemically stable and recyclable. We can therefore affirm that abundant natural resources such as kaolin and certain plants can contribute to the preparation of low-cost but highly effective materials for combating water pollution.

Key words**:** *Ciprofloxacin, zeolite 4A, magnetite nanoparticles, adsorption, nanocomposite.*

CHAPTER ONE
INTRODUCTION

1.1 Background information

Every year, water consumption is increasing due to population growth, urbanization, industrial development, as well as changes in agricultural methods and land use (Norfazilah Wan Ismail & Umairah Mokhtar, 2021). One of the most serious problems facing living beings today is the lack of fresh water. Ensuring sustainable water and wastewater management is essential to ensure the healthy functioning of the community and the environment in general. However, the current situation has revealed the presence of various categories of pharmaceutical contaminants in fresh water (Norfazilah Wan Ismail & Umairah Mokhtar, 2021). Currently, pharmaceuticals are widely present in waters, soils and sediments, which can be detrimental to both the aquatic environment and human health (Saied et al., 2022). Pharmaceuticals are essential to saving many lives, but they are also a major source of complex environmental pollutants. According to recent research, levels of pharmaceutical pollutants exceeding 0.1 μ g /L in source water and 0.05 μ g /L in treated water are observed (Vinayagam et al., 2022). Among the pharmaceutical contaminants identified are antibiotics. These products are attracting increasing attention and raising environmental concerns around the world. According to certain ecotoxicological research, even at a low concentration of a few ng/L, they could have carcinogenic, mutagenic or harmful consequences on the endocrine system (Li et al., 2020). In feces and urine, approximately 60 to 90% of antibiotics are excreted in the form of the prototype or its metabolites (Wei et al., 2023), and eventually spread into the environment through the hospital wastewater, aquaculture wastewater and private wastewater. Due to their low concentrations in the environment, antibiotics are considered emerging pollutants, ranging from 100 ng /L to 10 μ g /L in wastewater and from 100 ng /L to 500 ng /L in industrial and hospital wastewater (Harcel et al., 2024).

Fluoroquinolones are the most commonly used antibiotics in human and veterinary medicine (Cheikh et al., 2023). However, due to their intensive use, antibiotics are frequently found in the final effluent of wastewater treatment plants (WTPs) (Kovalakova et al., 2020). Ciprofloxacin (CIP; $C_{17}H_{18}O_3N_3F$) is a widely used second generation zwitterionic antibiotic that is active on a wide range of Gram-positive and Gram-negative bacteria (Cheikh et al., 2023). CIP is frequently found in contaminated groundwater and wastewater due to its use in the

treatment of many human and animal diseases (Atugoda et al., 2021). Due to the development of resistant strains via chromosomal alterations and chronic allergic reactions, the transfer of CIP antibiotic into natural aquatic habitats poses a significant risk to human health and ecological systems (Wei et al., 2023). CIP has been identified as a new genotoxic product and mutagenic micropollutant from a toxicological point of view (Chohan et al., 2019). CIP exhibits low biodegradability in ecosystems due to its antibacterial properties, resulting in a higher tendency to survive and accumulate in the environment (Atugoda et al., 2021). Effluents containing the antibiotic CIP must be sufficiently purified before being discharged into water bodies. Therefore, the removal of IPC from water has become an increasingly crucial and relevant task.

Different conventional methods are developed to remove CIP in contaminated water, such as adsorption (Jara-cobos et al., 2023; Khan et al., 2020), photocatalytic degradation (Rajiv et al., 2021), ozonation (Nemati et al.,2019), electroflocculation (Chang et al., 2020), electrocoagulation (Zaied et al., 2020) as well as biological treatment methods (Norfazilah Wan Ismail & Umairah Mokhtar, 2021 ; Oktem et al., 2008). Among these methods, adsorption is the most efficient in removing organic substances present in wastewater even at very low concentrations (Chang et al., 2020; Oliveira et al., 2024). Due to its ease of use, simplicity, flexibility, ease of installation, availability of different varieties of adsorbents, low energy consumption and reusability of adsorbents (Belachew, 2022; Carolina et al., 2020), this method is the most promising. It allows soluble substances to be collected in a solution towards a suitable solid interface called an adsorbent.

The characteristics and performance of the adsorbent material play a crucial role in the effectiveness of pollutant removal (Neolaka et al., 2022). According to a literature review, quality adsorbent materials are solid materials that have a large surface area and a large pore volume, with a high affinity for pollutants. It is also necessary for these materials to exhibit exceptional psychochemical stability (Khashei Siuki et al., 2021). Nowadays, the progress of low-cost adsorbents is attracting more and more attention, especially for eradicating pharmaceutical contaminants (PCs) from the aquatic environment (Saied et al., 2022). In general, affordable inorganic adsorbents are superior to organic materials in their mechanical strength, temperature resistance and chemical stability. Adsorbents such as biochar (Shang et al. 2016), chitosan (Dumitru et al. 2024), diatomaceous earth (García-Alonso et al. 2019), pillared clay (Jara-cobos

et al. 2023), and activated carbon (Avcı et al. 2019) have been used to remove CIP in aqueous solution, but the cost of production is high, limiting their use.

In recent years, zeolite mineral has been increasingly used as an inexpensive adsorbent based on inorganic materials to remove PCs (Neolaka et al., 2022). Zeolite is characterized by its porous hydration aluminosilicate structure and its three-dimensional structure composed of AlO_4 and SiO_4 (Zavareh et al., 2018). Due to their hierarchical structure, high ion exchange capacity, environmental compatibility, remarkable physicochemical stability, excellent thermal performance and affordable cost, zeolite 4A obtained from kaolin has attracted great interest. Typically, zeolite 4A is produced using sodium silicate and aluminate hydrogel which is actually very expensive. To reduce production costs, kaolin is generally used as a precursor in the manufacture of zeolites due to its high concentration of silica and alumina. The peculiarity of their porous structure and thermal stability compared to other types of zeolites make them ideal for various practical applications, such as gas and vapor separation, membrane reactors, and chemically selective adsorption (De-Magalhães et al., 2022). Zeolite 4A is a negatively charged chemical compound, which allows it to combine with compensating cations through ion exchange.

Generally, complete separation of zeolite in solution is difficult during the adsorption process, resulting in the production of a secondary pollutant. If zeolite 4A were designed to become a magnetic material, it would be possible to avoid this problem by easily separating it from the solution using an external magnetic field. It is possible to combine iron oxide (Fe_3O_4) with zeolite 4A to create a magnetic adsorbent material. The stability of the Fe_3O_4 is excellent, its specific surface area is high, its co-efficiency is high, its toxicity is low and it is biocompatible (Altaf et al., 2021), its magnetic reactivity is excellent, its dispersibility is high and its surface modification is easy (Parajuli et al., 2020). Due to its super paramagnetic properties, iron oxide nanocomposites have been shown to be extremely effective in a number of environmental remediation effects (Neolaka et al., 2022). Currently, the biosynthesis of magnetite nanoparticles using biological materials and organisms such as algae, bacteria, yeast, fungi and plants is very attractive, economical and increases the number of active sites on the surface of the adsorbent (Seabra et al., 2013). Magnetite nanoparticles are stabilized through the use of powerful biomolecule stabilizing agents, whether produced naturally or found in biological resources (Izadiyan et al., 2020).

Adsorption is a surface phenomenon that can lead to chemical or physical interactions between the adsorbent and the adsorbate. However, it is difficult to identify the atoms, and sometimes even the types of bonds and the mechanism involved in the experimental process. Computer simulation is used in various scientific fields, especially in the field of adsorption, as an innovative technique. Computer simulation provides a precise understanding of the macroscopic behavior of materials by examining these materials microscopically (Acar, 2022). Computer simulations rely on techniques such as quantum mechanics (QM), Monte Carlo (MC), density functional theory (DFT), and molecular dynamics (MD). The effectiveness of molecular modeling and other computer simulation methods has been proven in analyzing the characteristics and interactions between different chemical structures, as well as in providing reliable data for all biological, chemical and physical characterizations (Sedik et al., 2022). Based on the experimental results, molecular simulation provides an effective method to analyze and understand the adsorption process. Currently, many researchers have used MC and DFT methods to analyze the adsorption behaviors of gases (Lucresse et al., 2023), dyes (Khnifira, Hamidi, & Sadiq, 2022), and inhibitors. corrosion (Nwanonenyi, Obasi, Obidiegwu, & Chukwujike, 2020) on the surface of an adsorbent.

1.2 Problem statement

Pharmaceutical contaminants such as antibiotics in wastewater are not readily biodegradable and therefore attract microorganisms. The lack or insufficiency of treatment methods results in their accumulation in the water cycle, which generates biological water pollution that therefore constitutes a permanent threat to human and animal health.

1.3 Objectives

The main objective of this study is to develop zeolite 4A/bio-magnetite nanocomposites capable of eliminating ciprofloxacin in aqueous solution with high efficiency.

The specifics objectives of this study are to:

1. Synthesize and characterize zeolite 4A based on crude kaolin, bio-magnetite based on the extract of *Terbernaemontana penduliflora* leaf and bio-magnetite@zeolite 4A nanocomposites;
2. Assess the adsorption removal of ciprofloxacin in aqueous solution;

3. Study the effect of bio-magnetite loading within the zeolite 4A framework on the adsorption process of ciprofloxacin and the recovery of zeolite 4A after adsorption;
4. Study the reactivity, stability of ciprofloxacin in aqueous solution and interactions, as well as the adsorption mechanism of ciprofloxacin on the surface of the synthesized adsorbents using DFT and MC simulations.

1.4 Research questions

1. Can raw kaolin from the locality of Fotouni, West Cameroon be a good precursor of alumina and silica for the synthesis of zeolite 4A?
2. Can zeolite 4A synthesized by hydrothermal method through local material exhibits excellent physicochemical stability, good thermal performance, adsorption capacity and PC removal efficiency?
3. Extracts from the leaf of *Terbernaemontana penduliflora* (TP) containing phytochemical compounds be capable of stabilizing and modifying the surface of magnetite nanoparticles?
4. Can the transformation of zeolite 4A into a magnetic material facilitate its recovery in solution after adsorption process and improve its PC removal capacity?
5. Can DFT and MC simulations make it possible to predict the reactivity, the stability as well as the types and nature of the interactions involved during the adsorption process?

1.5 Justification of the study

The production of zeolite 4A from chemical reagents such as silica and alumina are an expensive process due to production and purchasing costs. This is the reason why, in recent decades, many researchers have been interested in finding alternative sources of silica and alumina, coming from less expensive and abundant sources (Belachew, 2021). Several materials, including those that are perceived as waste, have already been successfully exploited in this direction (Nayak et al., 2023). In order to serve as a precursor, the material must be accessible, easy to find, produced in large quantities and rich in silica and alumina, with a low concentration of impurities (Wang, Sun, Zhang, & Cao, 2019a). Therefore, in this study, we used raw kaolin for the production of zeolite 4A. Kaolin is a clay material rich in silica and alumina and which is abundant in nature, very accessible and inexpensive and its composition depends on the collection area.

Raw kaolin recovered from two sites in the locality of Fotouni was used as a source of silica and alumina during the synthesis of zeolite 4A. Unlike other zeolites, zeolite 4A is known to have a large specific surface area, high ion exchange capacity, exceptional hydration/rehydration and adsorption power, making it a quality molecular sieve. superior (Wang, Sun, Zhang, & Cao, 2019b). For example, ZSM-5 zeolite cannot adsorb molecules with a size larger than 0.62 nm (De Magalhães et al., 2022). Thus, the pore configuration plays a crucial role in the adsorption capacity and intracrystalline diffusion of molecular compounds. The proportion of silicates and aluminates (Si/Al) indicates the hydrophilic or hydrophobic nature of the zeolites. With a value greater than 8, it is theoretically hydrophobic (Bessa et al., 2017). The Si/Al ratio of zeolite 4A is approximately 1, therefore it is very hydrophilic and therefore favorable for adsorption.

Generally, it is difficult to completely recover zeolite 4A in solution after adsorption, resulting in the formation of secondary pollutant. This problem could be avoided if zeolite 4 A were intended to become a magnetic material, by easily separating it from the solution by an external magnetic field. Magnetite is a super-paramagnetic material, it was synthesized using plant extracts as a stabilizing and reducing agent, in order to reduce the use of commercialized chemicals compounds. The magnetite nanoparticles thus synthesized were incorporated into the zeolite framework to form the nanocomposites in order to contribute to environmental remediation at a reasonable cost.

Computer simulations are a very valuable technique that allows us to better understand the behavior at the microscale of pollutants in aqueous solution and their interactions with the adsorbent surface during the adsorption process.

1.6 Scope of the study

The interest of this work is to provide a better solution in the development of efficient and lower cost adsorbent materials in the application of wastewater treatment. The use of raw kaolin for the production of zeolite 4A is interesting because of their contribution to reducing the costs of eliminating pollutants. While promoting the latter and thus contributing to the protection of the environment. It also provides ideal technology in the valorization of local materials which can be marketed.

1.7 Research impacts

1.7.1 Project beneficiaries

1. Local community: Local areas or materials collected can boost the economy, improve living conditions and create jobs.

2. Wastewater treatment industries: Businesses will benefit from the supply of new, more environmentally refined, more reliable, recyclable wastewater treatment materials at affordable prices.

3. Investors and developers: Companies will be able to invest in the industrial production of bio-magnetite@zeolite 4A nanocomposites and the manufacturing of new adsorption water treatment devices.

4. Environmental Conservation: Wastewater treatment will increase the availability of fresh water resources for the nourishment of flora and fauna.

5. Technological innovation: Research and development of green adsorbent materials can lead to technological advancements and innovations in the wastewater treatment sector.

1.7.2 Project activities

1. Optimize the production of zeolite adsorbents from raw kaolin

2. Examine the different ways the zeolite and pollutant interact

3. Synthesize biomagnetite nanoparticles from plant extracts

4. Transform the zeolite into a magnetic nanocomposite to increase its adsorption capacity and facilitate its recovery and after adsorption process

5. Eliminate pharmaceutical pollutants present in wastewater

1.7.3 Expected results

1. *Terbernaemontana penduliflora* leaf extracts effectively prevented the formation of aggregates around magnetite nanoparticles and enhanced the nanoparticle surface with multiple spaces and pores, providing numerous active sites to promote interaction with contaminants.

2. The synthesized bio-magnetite@zeolite 4A nanocomposites demonstrated exceptional stability, high specific surface area, exceptional magnetic reactivity and above all, high affinity with contaminants.

3. The synergistic effect of these two materials made it possible to increase the capacity for eliminating pollutants in aqueous solution under optimal conditions such as adsorbent dose, contact time, system pH and initial contaminant concentration.

CHAPTER TWO

LITERATURE REVIEW

1.8 General information on pharmaceutical pollutants

Micropollutants, also called “Emerging Contaminants”, are pollutants present at low concentrations in the environment. Most micropollutants belong to the group of substances of synthetic origin characterized by significant toxicological effects, even at very low concentrations (Pico et al., 2019).

The term “emerging contaminants” refers to a heterogeneous set of several environments of molecules and metabolites whose presence in the environment had not been previously detected (Zaied et al., 2020). Studies of monitoring of these contaminants are relatively recent, even though these substances have been present in the environment for a long time. Emerging contaminants (ECs) are man-made or natural chemicals and microorganisms that have not actually been monitored in the environment. These substances are currently not covered by water quality regulations, have not been previously studied, and are considered potential threats to the ecosystem and to human health and safety (Zaied et al., 2020). ECs include:

i. Polycyclic aromatic hydrocarbons
ii. Pesticides
iii. Metals
iv. Personal hygiene and cosmetic products
v. Disinfection by-products
vi. Medication

1.8.1 Sources of pharmaceutical contaminants in the environment

Pharmaceutical compounds can enter environmental matrices in different ways (see Figure 2.1) (González-González et al., 2022; Samal, Mahapatra, & Hibzur Ali, 2022). These substances can come from occasional sources such as wastewater treatment plant waste, wastewater from the pharmaceutical industry or even landfill leachate. There are different sources of contamination, such as runoff, soil leaching or leachate infiltration. However, wastewater treatment plants (WTPs) are perceived as the main source of environmental pollution

by medicinal substances, because they are not intended to treat this type of pollutant (Vinayagam et al., 2022). The levels measured in WTP effluents generally vary from a few nb/l to a few µ g/l.

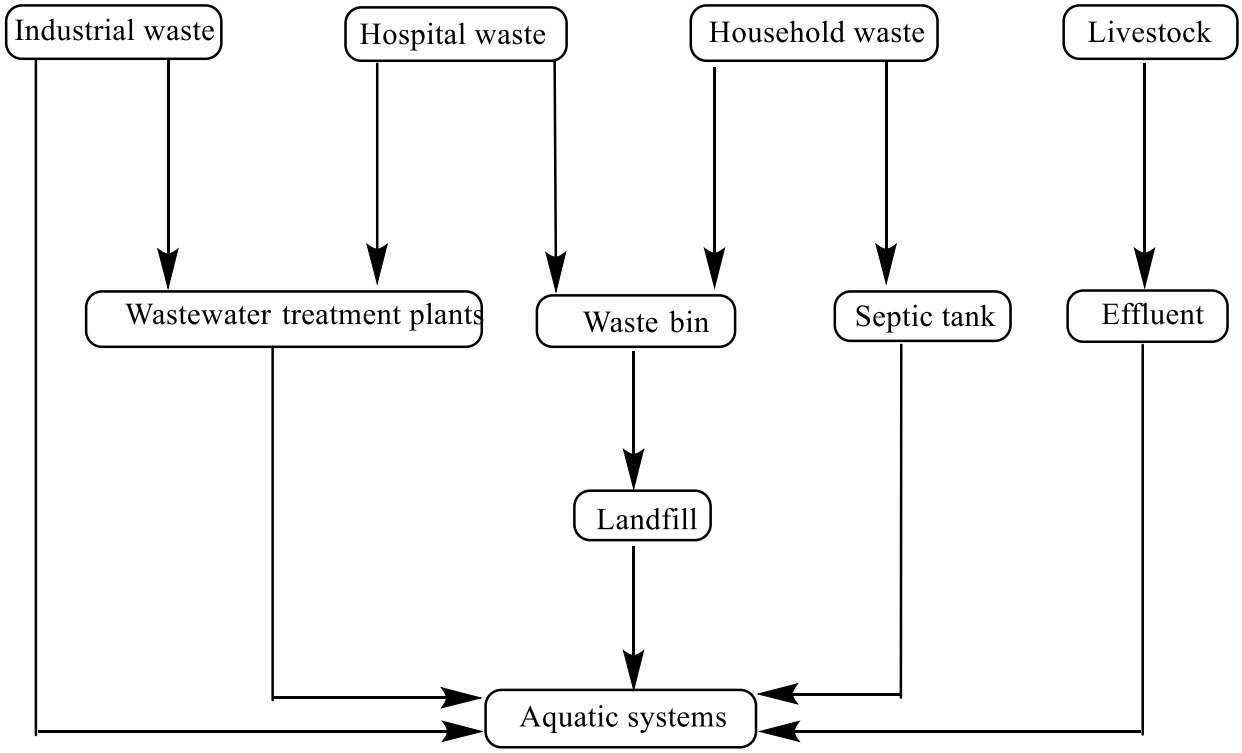

Figure.2.1. Pathways of PCs in aquatic systems (Natarajan et al., 2022).

1.8.2 Toxic effects of pharmaceutical contaminants on the environment and humans

Numerous studies have been carried out on the effects of drug residues on humans, and aquatic fauna and flora. It has been shown that even at low concentrations, drug residues would have consequences on the functioning of ecosystems, in particular on the behavior of aquatic organisms (Wei et al., 2023). Acute toxicity effect assessments are the most common toxicity studies. It is possible to study the latter *in vivo*, in animals after being exposed to high doses, or *in vitro,* using tests on cells (Samal et al., 2022). Regarding the consequences for humans, endocrine disruptors such as bisphenol A and 17 β-estradiol are suspected to contribute to the development of breast cancer and prostate cancer (Damgaard et al., 2015). However, with regard to prolonged exposure, it seems that certain molecules are active at concentrations ranging from micrograms to ten micrograms per liter, such as carbamazepine on crustaceans, antibiotics on cyanobacteria or fluoxetine on poisons (Serna-Galvis, Berrio-Perlaza, & Torres-Palma, 2017).

According to Desbiolles et al. (2018), hormones are active at much lower concentrations, close to nanogram per liter. On the other hand, 10 million vultures in Asia were killed by diclofenac in the 2000s (Kümmerer, 2010). There is now a large body of data confirming the harmful effects of drug residues on the environment, and they are widely disseminated.

In general, the physicochemical properties of PCs and their natural attenuation determine their alteration. Table 2.1 presents the physicochemical characteristics of PCs prevalent in wastewater (Martín-Pozo et al., 2019). Some drugs have similar effects on humans and other animals (Klosterhaus, Grace, Hamilton, & Yee, 2013). Pharmaceuticals are designed to interact with certain receptors in humans and animals. Therefore, these chemicals may interact with similar receptors found in other ecological species. Certain pharmaceutical substances such as ciprofloxacin, fluoxetine, diclofenac, ibuprofen and carbamazepine are known to be carcinogenic to environmental organisms in varying amounts. Diclofenac, for example, causes severe kidney failure in humans (Patel et al., 2018). Pharmaceuticals can also be consumed by humans through the consumption of plants, vegetables, fruits, seafoods and meat.

Table 2.1: Physicochemical characteristic of PCs common in wastewater.

Name of the pharmaceutical	Molecular mass (g/mol)	Chemical formulation	Solubility in water (g/L)	pKa	Kd	Log Kow
Antibiotics						
Amoxicillin	365.4	$C_{16}H_{19}N_3O_5S$	Insoluble	3.2;11.17	3.82	0.87
Nalidixic acid	232.235	$C_{12}H_{12}N_2O_3$	Almost impossible	8.6	/	1.41
Ciprofloxacin	331.334	$C_{17}H_{18}FN_3O_3$	1.35	6.1;8.74	3.4	0.28
Tylosin	916.1	$C_{46}H_{77}NO_{17}$	50	/	1.5-2.0	/
Norfloxcin	355.78	$C_{16}H_{18}FN_3O_3$	0.28	6.37;8.75	2.9	0.46
NSAIDS						
Diclofenac	318.1	$C_{14}H_{10}Cl_2NN_aO_2$	0.00482	4.15	0.2	4.51
Ibuprofen	206.29	$C_{13}H_{18}O_2$	Insoluble	4.91	3.7×10^{-7}	3.97
Naproxen	230.26	$C_{14}H_{14}O_3$	0.0299	4.15	/	3.18
Flurbiprofen	244.261	$C_{15}H_{13}FO_2$	Insoluble	/	/	/
Ketoprofen	254.281	$C_{16}H_{14}O_3$	0.005	4.45	1.5	3.12
Fibrates						
Clofibric acid	214,645	$C_{10}H_{11}ClO_3$	0.583	3.2	31,622	2.9
Gemfibrilbrozil	250.33	$C_{15}H_{22}O_3$	Insoluble	4.5	/	4.77
Anticonvulsants						
Carbamazepine	236.33	$C_{15}H_{12}N_2O$	Insoluble	13.9	1.02	2.45
Analgesics						
Acetaminophen	151,169	$C_8H_9NO_2$	14	9.38	0.2	0.46
Hormones						
Estrogen	272.38	$C_{18}H_{24}O_2$	Insoluble	/	288,403	3.67

1.8.3 Effects of antibiotics in the aquatic environment

An antibiotic is defined as a natural or synthetic chemical substance used in human and veterinary medicine to treat bacterial infections (Asghar et al., 2019). Antibiotics have the ability to destroy or stop the proliferation of bacteria by acting in different ways, such as inhibiting the production of the bacterial wall, attacking the cytoplasmic membrane which must normally remain intact to ensure the survival of bacteria, inhibition of protein production or even inhibition of the production of nucleic acids DNA and RNA, which are essential components for the cell (Yang, Zhong, Li, Du, & Li, 2022). On the other hand, as mentioned earlier, excessive use of these medicinal substances leads to water pollution. The levels observed in natural environments differ depending on consumption practices, environmental conditions and wastewater treatment methods used in each country (Antonelli, Malpass, Da Silva, & Vieira, 2020).

Pharmaceutical products present in the environment can cause harmful consequences on fauna and flora, as well as health repercussions for humans (Wu et al., 2019). It is clear that antibiotics are prevalent in nature and polluting our water resources, leading to negative consequences for health and the environment. These risks must be taken into account today by decision-makers and encourage them to implement resolution and prevention strategies.

1.8.4 Diagnostic techniques for detection of pharmaceutical contaminants in wastewater

Chromatography and spectroscopy techniques can be used for EC acquisition methods such as PCs. The most common analytical methods for identifying and detecting various compounds in any type of sample are chromatography. Some of these ways are briefly described here

2.2.4.1. Liquid chromatography (LC)

High-performance liquid chromatography (HPLC) or LC is a good analytical method used to analyze large numbers of relatively polar and unstable ECs in different samples. These LC techniques provide an effective standing phase by reducing particle size, resulting in better fixation and shorter duration. As a result, ultra-high performance liquid chromatography (UHPLC) is generally preferred over conventional LC (Hernández, Ibáñez, Bade, Bijlsma, & Sancho, 2014). UHPLC uses particles smaller than 1.7 µ m and almost always proceeds in a reversible phase mode (Pico et al., 2019). Methanol or acetonitrile as organic solvents

(sometimes also acidified with formic acid or acetic acid) are usually used as mobile phases for the reverse phase of the separation of acidified waters by ECs (with small quantities formic acid or acetic acid). Diaz-Cruz et al (2009) found that among all LC methods, the most widely used stationary phase for analyzing pharmaceutical contaminants is a shrink phase with C18-bonded octadecyl or octadecyl-bonded silica packing bound at C8 (Díaz-Cruz et al., 2009).

2.2.4.2. Gas chromatography

One of the analytical techniques that can be used to classify, analyze and identify chemical compounds in any gazeous sample is gas chromatography (GC). The most common method, which combines GC with mass spectrometry (MS), can provide accurate results. However, GC is more effective than LC in detecting finer impurities, such as medications and personal care products (Martín-Pozo et al., 2019). The GC pathway requires the incorporation of an alternative product to improve the chromatographic behavior of the analysts due to the high polarity and low flexibility of the analysts, such as hydroxyl, amines and amides (Samal et al., 2022).

2.2.4.3. Fourier transform near-infrared spectroscopy

Methods such as Fourier transform near-infrared spectroscopy (FT-NIR) have recently been developed to overcome traditional obstacles. In their work, Quintalas et al (2019), developed a combination of FT-NIR and chemometrics to identify pharmaceutical compounds such as ibuprofen, ciprofloxacin, carbamazepine, estradiol, ethinyl estradiol and sulfamethoxazole in contaminated water (Quintelas, Mesquita, Ferreira, & Amaral, 2019). To identify interaction samples and define datasets, the chemometric method was used using the Kolmogorov-Smirnov test, boxplot identification and key component analysis. Next, a small-scale inverse analysis was performed to determine the best-estimate model for pharmaceutical drug measurement.

2.2.5 Physico-chemical treatment methods of PC

1.8.4.1 ***Coagulation-flocculation***

Generally, the coagulation-flocculation method is used to eliminate colloidal pollutants present in water. This method can be used during the pretreatment phase of hospital and industrial effluents, as well as in the primary and/or tertiary phase of urban wastewater (Zaied et al., 2020).

This is a method that involves the incorporation of inorganic coagulants that neutralize the surface charge of suspended particles and promote their sedimentation. A chemical reagent added afterwards makes it possible to improve sedimentation (decantation) and create larger flocs which will be more easily removed from the suspension by filtration (González-González et al., 2022). Filtration systems can be influenced by membrane functional groups and hydrophobic and ionic interactions. However, this method presents two main disadvantages: on the one hand, the creation of large quantities of sludge contaminated by the pollutants retained, which are themselves hazardous waste to be managed and could be assimilated to secondary pollution. On the other hand, the low rate of elimination of pharmaceutical products, which does not exceed 10% in certain situations (González-González et al., 2022).

1.8.4.2 *Oxidation*

Chemical oxidation involves the use of an oxidizing agent to directly attack compounds in the presence of water. This process offers the advantage of not displacing the pollution but of eliminating it effectively; it frequently makes it possible to obtain more easily biodegradable molecules, or even to completely mineralize fauna (Moussa, Narcisse, & Meite, 2018). Ozone is the main oxidizing agent used to treat EC, because it has high oxidizing power at ambient temperature and pressure. It can be produced on site from air or pure oxygen and dissolves in the aqueous phase. In the aqueous phase, ozone acts in two different ways:

i. Directly through of the ozone molecule;
ii. Indirectly, through hydroxyl radicals obtained from the self-decomposition of ozone in solution;
iii. Under normal conditions, direct action is only really effective on electrophilic compounds, while indirect action is not selective, but is low by the limited production of radicals and their very short lifespan.

Lately, new technologies called advanced oxidation processes (AOPs) have been developed to generate a larger quantity of radicals and take advantage of their high oxidizing power and non-selectivity (Ebrahiminezhad, Zare-hoseinabadi, Berenjian, & Ghasemi, 2017).

These methods involve the use of different agents (oxidants, radiation, metal oxides, etc.) in a homogeneous or heterogeneous manner. Even if these methods are extremely efficient, they are

more complex to implement on a large scale, and there are still few applications that have gone beyond the laboratory or pilot installation stage.

2.2.5.3 Reverse osmosis

The reverse osmosis method is commonly used to purify water in the pharmaceutical field. Its operating mechanism relies on the passage of water through a semi-permeable membrane which eliminates impurities such as bacteria, viruses and dissolved solids. Setting up and maintaining reverse osmosis systems is relatively simple, as they can remove up to 99% of impurities from water (Río-gamero, Alonso, Kori, & Meli, 2018).

2.2.5.4 Adsorption

Adsorption refers to the formation of a layer of material from a gas or liquid phase on the surface of an adsorbent, which can result in physical and/or chemical adsorption. For several years, the process of eliminating PCs by adsorption has continued to attract the scientific community. Adsorption, in general, is a simple, inexpensive and above all effective design process even at very low concentrations (less than 1 ng/L) and it makes it possible to retain soluble substances in a solution towards a suitable solid interface (Stan et al., 2017; Wakejo, Meshasha, Kang, & Chebude, 2022). As a result, several types of adsorbent materials have already been used for the elimination of PCs in solution which can be classified into three large classes: alumino-silicates (zeolite and clay) (Ashiq et al., 2019; Atugoda et al., 2021; Wu et al., 2019), carbon materials (activated carbons, graphene and biochar) (Siipola, Pflugmacher, Romar, Wendling, & Koukkari, 2020; Wakejo et al., 2022) and finally bio-adsorbents or natural adsorbent (chitosan and lignocellulosic residues) (Anchique et al., 2021; Dumitru, Neagu, Miron, In, & Dur, 2024). However, it is difficult to separate them from water after adsorption (Lingamdinne, Koduru, & Karri, 2019).

2.3 General information on the adsorption phenomenon

Adsorption is a surface phenomenon by which molecules, ions or atoms of a fluid (adsorbate) attach to the surface of a solid (adsorbent) according to various more or less intense processes (Banu et al., 2021). The sites where molecules attach are called active sites. The adsorption process occurs until an equilibrium state is obtained to which a well-defined concentration of the solute corresponds.

It is one of the most widely used methods for removing pollutants in aqueous solution. The adsorption of a solute by a solid is based on forces acting between the adsorbent (solid) and the solute (adsorbate). Depending on the binding energies involved, these forces can be classified according to their intensities among Van Der Waals, coulomb and LEWIS acid-base interactions (Chang et al., 2020; Siipola et al., 2020). Thus, we distinguish two types of adsorptions, namely: physical adsorption (physisorption) and chemical adsorption (chemisorption).

2.3.1. Adsorption types

2.3.1.1. Physical adsorption

In physical adsorption (physisorption), the fixation of the adsorbate molecules on the adsorbent surface is carried out either by Van der Waals forces or by forces due to electrostatic interactions for adsorbents having an ionic structure. In this case, adsorption takes place by ion exchange where an ion in solution displaces another ion of the same sign located on the surface of the solid (Asbollah, Syaadii, Sahid, & Waatriah, 2022). Physical adsorption generally occurs at low temperatures and is characterized by low adsorption energy which defined the strength of the bonds created. This energy, between 0 and 40 kJ/mole, is considered low (Vinayagam et al., 2022). These interactions are not very specific, reversible and desorption can be complete. Physical adsorption is rapid and generally limited by diffusion phenomena.

2.3.1.2. Chemical adsorption

Chemical adsorption (chemisorption) is a reaction for the formation of chemical bonds between the surface of the adsorbent and the adsorbate molecules. The binding energy is much stronger than in the case of physisorption and the process is much less reversible and sometimes irreversible. This type of adsorption involves a high transformation energy of the order of 100 kJ/mol with specific interactions (Ngeno, Shikuku, Orata, Baraza, & Kimosop, 2019). Chemisorption is complete when all the active centers present on the surface of the adsorbent have established a bond with the molecules of the adsorbate. Two types of connections may be possible: a purely ionic bond in which the atom or ion plays the role of electron donor or acceptor, i.e. a covalent bond (Pradhan, Singh, & Kumar, 2022). Table 2.2 brings together some criteria for differentiating between chemisorption and physisorption.

Table 2.2: Comparison between chemisorption and physisorption.

Settings	Physisorption	Chemisorption
Adsorption energy	<40 Kj/mol	>80 Kj/mol
System temperature	Weak	High
Nature of the connection	Van Der Waals/ electrostatics	Covalent/ionic
Regeneration of the adsorbent	Easy	Difficult or impossible
Activation energy	Not appreciated	Can be put into play
Kinetics of adsorption	Very fast, reversible	Slow, irreversible
Layers formed	Multi or monolayers	monolayers

2.3.2 Adsorption mechanism

The process by which atoms in the fluid phase adhere to atoms in the solid phase is known as adsorption. It mainly occurs in four (04) stages:

i. **Transport of solutes**: the adsorbates from the external liquid (or gas) phase migrate towards those located in the vicinity of the adsorbent surface.
ii. **Film diffusion:** Transfer of the solute through a liquid film to the surface of the adsorbent.
iii. **Interstitial diffusion:** Transfer of solute to the porous structure from the outer surface of the adsorbent to the active sites.
iv. **Adsorption:** contact between the solute and the active sites. Once adsorbed, the molecule is considered immobile. Thus involving electrostatic attraction, sometimes strong chemical bonds and allocation of electrons resulting in hydrogen bonds (Samal et al., 2022).

Adsorbent porosity, specific surface area, pore volumes and surface functional group coverage of the adsorbent significantly impact the adsorption efficiency (Norfazilah Wan Ismail & Umairah Mokhtar, 2021). Figure 2.2 illustrates the adsorption mechanism and the various interactions involved in the removal of organic pollutants.

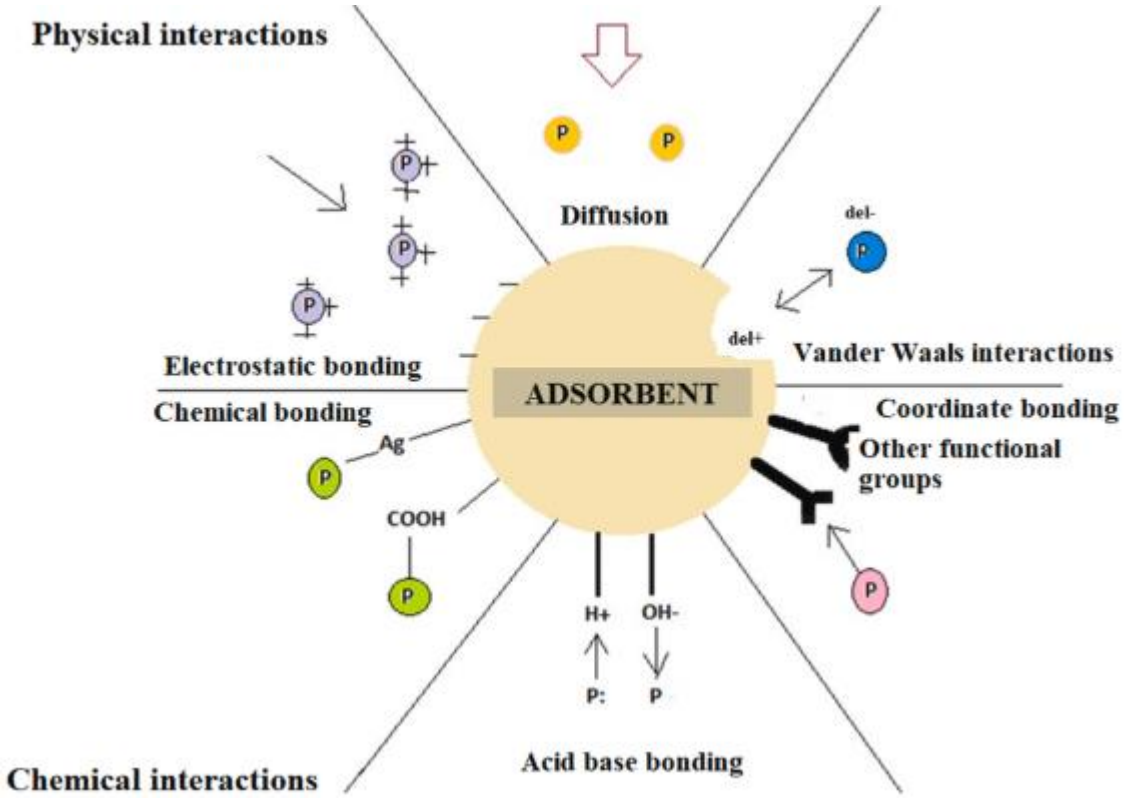

Figure 2.1: Comparison between chemisorption and physisorption.

2.3.3 Factors affecting adsorption balance

The adsorption balance between an adsorbate and an adsorbent depends on several factors, the main ones of which are described below.

2.3.3.1 *Specific surface area*

Adsorption is proportional to the specific surface area. The dependence of adsorption kinetics on the external surface dimension of the particles is fundamental for the use of an adsorbent. This external specific surface area, however, only represents a minimal portion of the total surface area available for adsorption. This total surface area can be increased by grinding the solid mass which further multiplies its total porosity (Wang et al., 2019b).

2.3.3.2 *Porosity*

Porosity is related to pore size. As a result, most adsorbents of practical importance are porous solids. The importance of this parameter is mainly relative to the geometric selectivity of the molecules to be adsorbed. Indeed, the greater or lesser diffusion in the pores will be influenced by the diameter of the pores (Siipola et al., 2020).

2.3.3.3 *Nature of the adsorbate*

The less soluble a substance is in a solvent, the better it is adsorbed. In addition, adsorption in aqueous solution increases when going through a series of homologs (organic substances that perform the same functions and have similar structures) (Panda et al., 2021).

2.3.3.4 *Polarity*

A polar solute will have more affinity for a solvent or for the more polar adsorbent. Preferential adsorption of organic compounds with limited solubility in aqueous solution (hydrocarbons, chlorinated, fluorinated, phenolic derivatives and other benzene derivatives) is important with hydrophobic adsorbents (activated carbon, porous polymer). On the other hand, it is insignificant with very hydrophilic polar adsorbents (zeolite, silica gel, alumina, etc.)

2.3.3.5 *pH of solution*

The pH has significant effects on the adsorption characteristics because it influences both the adsorbent (through his Point Zero Charge) and the adsorbate (Wei et al., 2023). Adsorption therefore depends on the net surface charge of the adsorbent. The latter is conditioned by the nature of the functional groups present on the absorbent surface and which is generally a combination of positively and negatively charged groups. Monitoring the evolution of the surface charge allows us to see that it passes through a state of neutrality of this surface charge, the pH corresponding to this state is called pH of the point of zero charge (pHpzc). Thus, when pH <pHpzc, the net surface charge is positive and negative when pH > pHpzc (Harcel et al., 2024).

2.3.3.6 *Temperature*

Adsorption is an endothermic or exothermic phenomenon depending on the adsorbent material and the nature of the adsorbed species (ions or molecules) (Mohammed, M-ridha, Abed, & Amal, 2021). Numerous adsorption enthalpy values are presented in the literature, thus attesting to the variability of thermodynamic processes.

2.3.4 Classification of adsorption isotherms

The best indicator of the textural characteristics of the adsorbent is the appearance of the adsorption isotherms. It is essential to take into account objective experimental data before seeking to obtain quantitative information. The classification of adsorption isotherms into very different types, initially described by Brunauer, Emmett and Teller and Brunauer , Deming, Deming and Taller (Mgbemere, Ekpe, Lawal, Ovri, & Chaudhary, 2019; Vinayagam et al., 2020), can be used to the analysis. We reproduce this classification in Figure 2.3

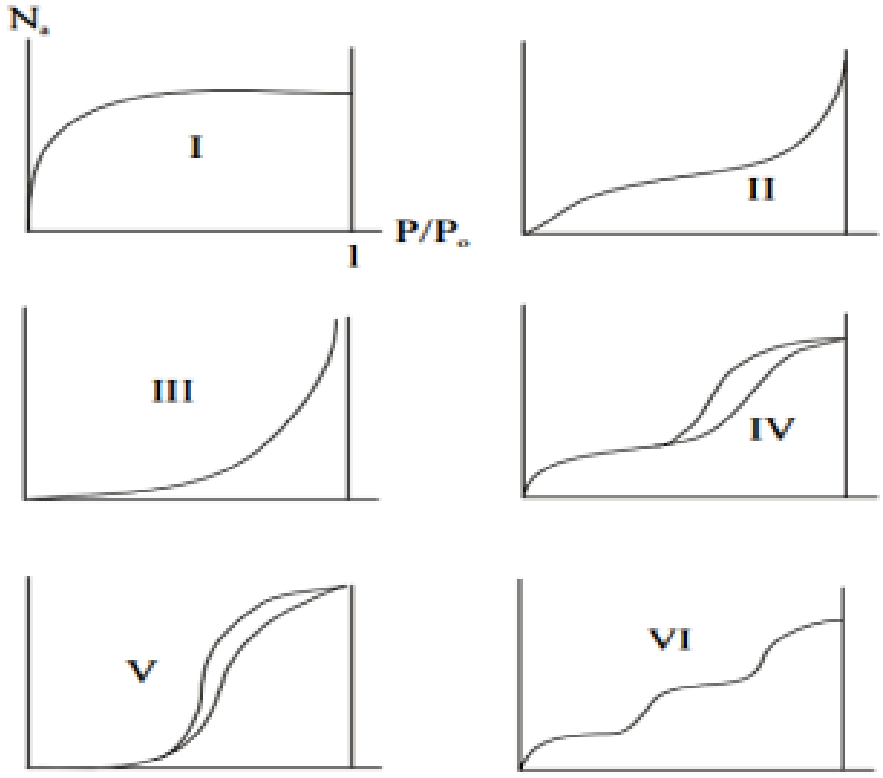

Figure 2.2: Classification of adsorption isotherms

Type I is the Langmuir type which is distinguished by the presence of a horizontal line which highlights the saturation of the adsorbent. This isotherm is obtained with adsorbents which only have micropores which fill at lower pressures as their width is smaller. The solid adsorbs a single layer of the adsorbate, resulting in this type of isotherm.

Type II is known as sigmoid. According to Brunauer, Emmet and Teller (BET), the first part of the curve corresponds to monomolecular adsorption, then a multimolecular layer of indefinite thickness is formed. The adsorbed layer gradually thickens on the surface of non-porous or microporous adsorbents, resulting in this isotherm. The type II adsorption isotherm is considered to be multimolecular adsorption.

For the type III isotherm, the curves have a concavity oriented towards the ordinate axis. The quantity of adsorbents adsorbed continues to increase. It is possible to create an infinite multimolecular layer on the surface of the adsorbent.

The adsorption isotherm of type IV is similar to that of type II. In this situation, a process of capillary condensation is observed, where the maximum level obtained for the adsorbed quantity corresponds to the full filling of all the gaps.

The type V isotherm is much less common. Isotherms of this type are mainly similar to those of type III. Then, they are similar to those of type IV, with higher relative saturation values. Capillary condensation and adsorption occur in a layer of finite thickness.

Type VI has been observed when adsorption is carried out on energetically homogeneous surfaces, where the adsorbed layers form successively.

2.3.4 Desorption and regeneration

One possible way to further reduce the cost of the adsorption process is to efficiently desorb the retained substances and regenerate the adsorbent for repeat use. Zeolite offers a tremendous advantage over other adsorbents due to its tunable physicochemical properties and the ability to be regenerated without significant loss of performance at low relative temperatures (Nizam, Azhari, Azan, & Tamar, 2021). Once, the adsorption potential of the zeolite has been exhausted, and reached the saturation point, the zeolite could be regenerated and reused. The potential possibilities for regenerating saturated zeolite are feasible options for viable zeolite reuse in the wastewater treatment industry. Zeolite regeneration in a landfill depends on the adsorbed material. Several regeneration methods, including humid air oxidation, chemical and

thermal regeneration are applicable (Nizam et al., 2021). In the case of the recovery of the zeolite after adsorption of meats, the exchangeable ionic sites of the zeolites could be regenerated simply by washing them with another solution of strong cations, because the ions exchanged on the zeolites are weakly retained (Pabalan & Bertetti, 2001). Chemical regeneration can be achieved using chemical saturation of brine and salts, such as an alkaline solution of sodium chloride (NaCl) (Langwaldt, 2008), potassium chloride (KCl) (Huang et al., 2020), sodium hydroxide (NaOH) (Liu et al., 2018). Optimal NaCl should be used with neutral pH (Lata, Singh, & Samadder, 2015). Physico-chemical and thermal regeneration can also be used to regenerate saturated zeolite by the evolution of a Fenton type reaction, thermal treatment, solvent extraction, mechanical agitation and extraction with air (Deng, Elbeshbishy, & Lee, 2016). However, all of these methods are expensive. Another alternative consisted of using the combination of adsorbents and photocatalysts, a new technology that can eliminate the complete mineralization of species adsorbed by contaminants (Anastasiou, Lorentz, Stein, & Mitchell, 2014). For example, Fanourakis et al. (2020) showed that the combination of a clay base (zeolite-based) could be used to treat emerging pharmaceutical contaminants by photocatalysis with the combination of nanomaterials (grapheme or carbon nanotube) and adsorbent materials (Fanourakis, Peña-Bahamonde, Bandara, & Rodrigues, 2020). A gentler method, which does not alter the adsorbent material and allows recovery of the adsorbate, has therefore been developed (Huang et al., 2020). In this method, desorption is carried out by removing the liquid through centrifugation or filtration after the adsorption experiment and replacing this liquid with a virgin solution of the entity considered. There is therefore a passage of the molecule from the adsorbed phase to the liquid phase. In the specific case of the desorption of organic compounds, the solutions used are those of NaOH or HCl.

2.4 **Physicochemical properties of the pharmaceutical contaminant studied**

In this study, the antibiotic ciprofloxacin was used as a pharmaceutical contaminant, with >98% purity of analytical grade provided by Cadila Phamaceutical LTD (India). Table 2.3 shows the physicochemical properties of ciprofloxacin (Jara-cobos et al., 2023; David Moussa, Doubla, Kamgang-Youbi, & Brisset, 2007).

Table 2.3: Structure and properties of ciprofloxacin.

Settings	Features
Trade name	Ciprofloxacin
Systematic name	1-Cyclopropyl-6-fluoro-4-oxo acid -7-piperazin-1-yl-quinoline-3-carboxylic acid
Brute formula	$C_{17}H_{18}N_3O_3F$
Chemical structure	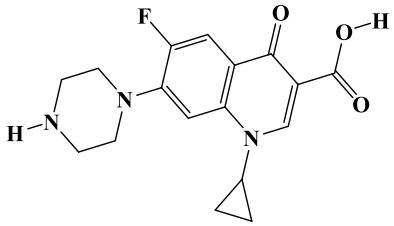
Molar mass	331.3415±0.0164 g/mol
PK_a acid	6.16
PK_b basic	8.62
Melting temperature	225-257°C
Solubility	30 mg/L in water at 25°C
Toxicity (LD_{Lo})	kg

2.5 General information on magnetite nanoparticles and its applications

2.5.1 Generality and description of the crystal structure of magnetite

Iron sesquioxides, with the formula Fe_3O_4, also called magnetites, constitute an oxide containing both ferrous Fe^{2+} and ferric Fe^{3+} ions. We can also write its crude formula as follows: $FeO.Fe_2O_3$ is a crystallized black oxide (Bharathi et al., 2020; Bhuiyan et al., 2020). In the laboratory, it is

in the form of a black powder, with a spinel structure according to the space group $Fd\bar{3}m$ and has a lattice parameter close to 0.8396 nm at room temperature (PDF sheet 04-015-8200). The spinel structure was first described by WH Bragg and Nishikawa in 1951 and owes its name to the mineral $MgAl_2O_4$ (Sanderson, Brain, Johnson, Wilson, & Solomon, 2004). Spinels have the general chemical formula AB_2X_4 where A and B are, in the case of magnetite, metal cations Fe^{2+} and Fe^{3+}. The Fe^{2+} cations occupy half of the octahedral sites, the Fe^{3+} cations occupy the other half of these sites and the tetrahedral sites (Figure 2.3). These two types of cations are organized in the same face-centered cubic network formed by oxygen anions, so they can easily move from one site to another (Sanderson et al., 2004). Thus, the general structure will not be modified by a change in the oxidation state of a cation, which explains the high sensitivity of magnetite to oxidation (Bharathi et al., 2020). Furthermore, magnetite has a permanent magnetic moment, due to the Fe^{2+} ions, the spins of the ferric Fe^{3+} cations canceling each other out. This magnetism gives it its name (Ertürk & Mattiasson, 2017).

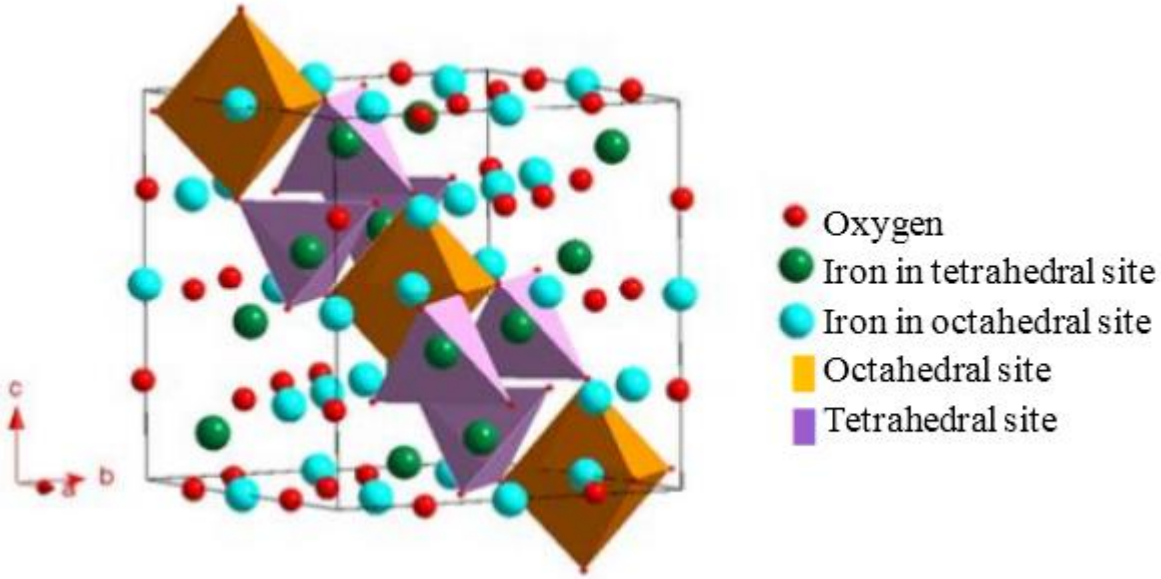

Figure 2.3: Representation of a cell of the crystallographic structure of magnetite. The octahedrons and tetrahedra materialize one of the planes (111) of the mesh.

In the remainder of this work, manuscript and unless otherwise stated, the term iron oxide used without additional precision will designate magnetite by abuse of language.

2.5.2 General methods for the synthesis of iron oxide nanoparticles

Different synthesis methods include co-precipitation, electrospinning, gas phase, hydrothermal method, membrane emulsification, microemulsion, microwave-assisted have been explored, sol-gel, green and micro-assisted have been exploited.

Co-precipitation is a simple method to synthesize iron oxide nanoparticles (IONPs) with good yield in a short reaction time. Here, ferrous and ferric alkalis are mixed in a 1:2 ratio to produce IONPs, then kept for a defined time and temperature to form a precipitate (Khalil, 2015). The main disadvantage of this method is the generation of liquid wastage and the requirement of high investment cost.

Electrospinning is a technique, generally used to produce nanofibers and nanomaterials. This technique is bio-mimicked from the method used to make cotton candy. Shi et al. (2020) synthesized magnetite fibers, in which a spinning solution was electro spun on a collector and oven-dried (Shi et al., 2020). The process requires high voltage, which is the main disadvantage.

Gas-phase synthesis can adjust the size, shape, and composition of nanoparticles by controlling process parameters. In this technique, an inert gas is bombarded with a solid precursor to create clusters of atoms deposited in a substrate (Jeyadevan, & Kennedy, 2010). The low production rate is the main disadvantage of this method (Popok & Kylián, 2020).

The hydrothermal process is generally used to synthesize nanoparticles on a large scale in less time. In this technique, solid materials at high pressure and temperature react with an aqueous solution resulting in the transformation of the precursor through crystallization. But this process requires expensive instruments, and the reaction cannot be monitored (Tercero, Röder, Fehrenbacher, Teipel, & Türk, 2014).

Membrane emulsification has many advantages such as low energy requirements, controlled droplet distribution and size (Piacentini, 2015). In this technique, an emulsion is pressurized to pass through the membrane. These droplets develop at the level of the pores until they reach the required size and detach, carried by a continuous phase circulating on the surface of the membrane containing a surfactant stabilizing the fusion of the droplets formed (Charcosset, Limayem, & Fessi, 2004). Low productivity and prolonged production are the disadvantages of this method.

The microemulsion produces a stable product with a minimum energy requirement. In this technique, a transparent and thermally stable solution with nanodroplets at the core of the

iron precursor is solubilized and precipitated, the desired size of the nanoparticles can be obtained (Okoli, Boutonnet, Mariey, Järås, & Rajarao, 2011). This technique uses many toxic surfactants, which is not desirable. Microwave-assisted synthesis is a simple technique that can quickly achieve high yield. For example, Bica et al. (2020) produced magnetite, maghemite and hematite fibers by this technique (Bica, Anitas, Anitas, Choi, & Sfirloaga, 2020). The high cost of the equipment and the inability to monitor the reaction are the main disadvantages of this technique.

The sol-gel synthesis process promises sample purity and homogeneity. After heating and stirring, the precursor is dissolved in water or alcohol to form a gel, which is then dried to obtain the product (Tadic et al., 2019). The high cost of the precursor and longer production time makes this technique undesirable. The use of ultrasound during the synthesis of nanoparticles accelerates the reaction (Low et al., 2021). Particle size and controlled crystallinity can be ensured when one of the methods described above is sonicated for a defined time (Low et al., 2022). High equipment cost and energy consumption are the main disadvantages of sonication.

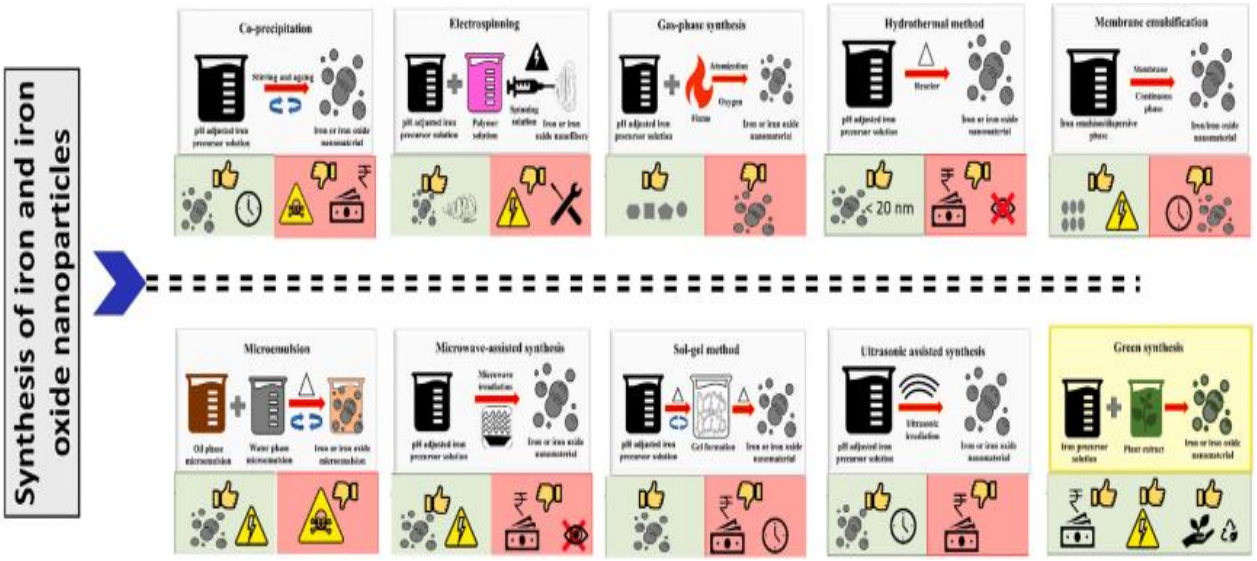

Figure 2.4: Different synthesis methods of iron and IONPs synthesis.

Table 2.4: Comparison of different synthesis methods.

Methods	Advantages	Disadvantages	- Shape, size - magnetization at saturation
Co-precipitation	-Ferrous and ferric salts, Inexpensive reagents. - Mild conditions. -Large production scale Conceivable. -Easy surface modification. - Synthesis in aqueous medium.	-Wide size distribution. -Uncontrolled oxidation. -Low reproducibility. - Aggregation of NPs.	- Sphere 10-55nm - 16 to 82 emu/g
Hydrothermal co-precipitation	- Increased size control. - Narrow size distribution. - Aqueous medium	-High temperature. -Long synthesis time. -Aggregation of NPs possible.	-Sphere 12-40nm -Disk 250-1000 nm -53 to 82 emu/g
Micro emulsions	-Increased size control. -Narrow size distribution. -Adjustable size and shape. -Well insulated particles.	-Low reaction yield. -Poor crystallinity. -Difficulties in washing surfactants.	- sphere 2-30 nm Needles 20-80 nm
Thermal decomposition	-Narrow size distribution. -High crystallinity. -Well isolated particles	-Organic solvents. -High temperature. -Phase transfer required if aqueous applications. -Low reaction yield.	-Cube,sphere, triangle, tetrapod. 3-500 -20 to 82 emu/g
Polyol solution	-Reduction of metallic salts. -Narrow size distribution. -Well insulated particles.	- High temperature. -Difficulties in washing surfactants.	-Sphere 6-100nm -50 to 69 emu/g

Sol-Gel	- Mild conditions. -Narrow size distribution. -High crystallinity.	-Long synthesis time. -The solid matrix can be difficult to eliminate.	-Sphere 4-200nm -47 to 62 emu/g

2.5.3 Green synthesis of IONPs

Green synthesis using plant extracts has gained importance. Among these advantages are: low cost of synthesis, low energy consumption and elimination of the use of toxic chemicals associated with sophisticated synthesis techniques. The profitability of the plant extract is a characteristic advantage because, they are obtained from part of the plants, dried or fresh (Pradhan et al., 2022). Extraction is carried out with polar or non-polar solvents. Preferred compounds are extracted by applying appropriate solvents with the same polarity as the biomolecules. The most commonly used solvent is water (Varghese, Zikalala, Sakho, & Oluwafemi, 2020). There are various phytochemicals originating from plant extracts, which contribute to the synthesis of nanoparticles. Each constituent has its function, which contributes to the reduction and stabilization of the nanoparticles. Flavonoids are water-dissolving secondary metabolites found in plants. The oxygen scavenging capacity of molecules present in flavonoids is precisely linked to their capacity to donate electrons (Md Ishak, Kamarudin, & Timmiati, 2019). The hydroxyl groups of terpenoids act as bioreducers for metal ions. Similarly, proteins have free amino and carboxylic groups, which can bind to metal ions to form nanomaterials. Due to the carboxylic compounds and hydroxyl groups in organic acids and alkaloids, these molecules can reduce metal ions into biofabricated nanoparticles (Bharathi et al., 2020).

Green synthesis of IONPs first consists of mixing the plant extract with iron precursors. A color change indicates a reduction of iron salts to iron ions. At alkaline pH, the color-changed solution is heated to form IONP. Figure 2.5 displays a pictorial representation of the green synthesis process. Generally, IONPs are synthesized by mixing the plant extract and iron precursor in a specific ratio and heating in a thermostat for a specified time interval. For example, the green synthesis of magnetite was carried out by mixing an iron precursor and tangerine peel extract at pH 10 producing a black precipitate characteristic of magnetite (Lingamdinne et al., 2019). Sathya et al. (2017) used coriander leaves as a reducing agent to produce magnetite nanoparticles. An equal amount of leaf extract and iron precursor solution was mixed and

sonicated keeping the pH at 6 to produce black magnetite residue (Sathya, Saravanathamizhan, & Baskar, 2017).

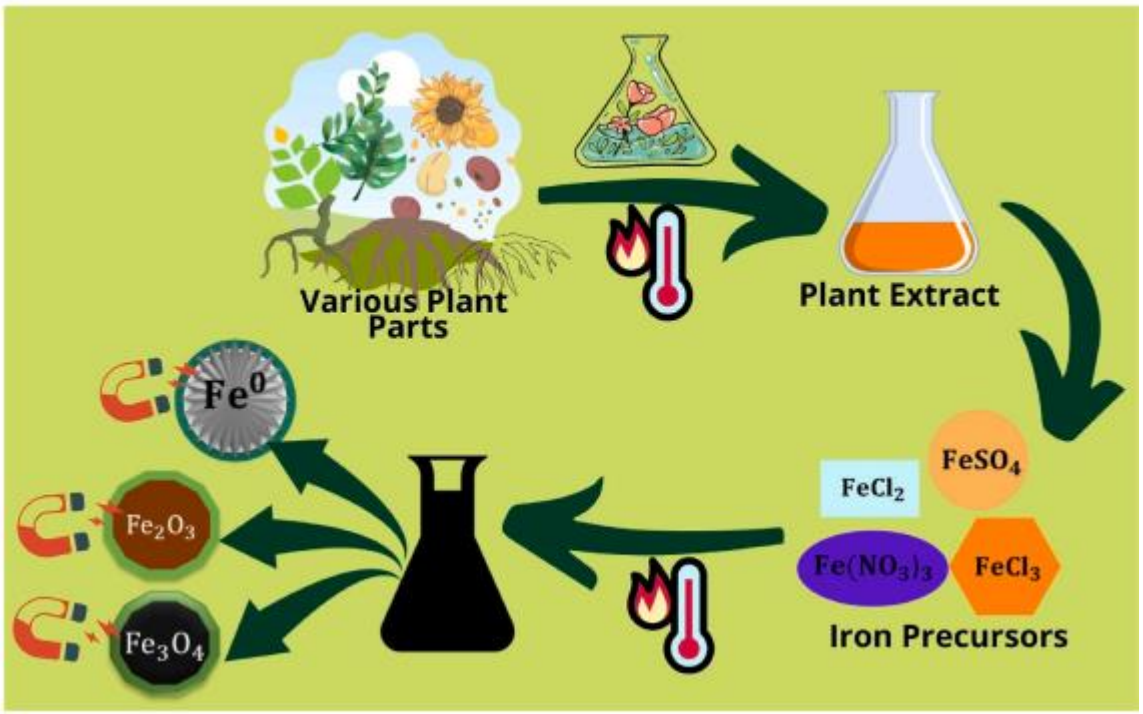

Figure 2.5: Pictorial representation of green iron synthesis and IONPs.

2.5.4 Green synthesis mechanism

The synthesis of green nanoparticles involves three major phases: reduction, growth, and termination. During the reduction phase, metal ions are reduced by the phytochemicals present in the extract. This phase takes place by the action of the electrostatic attraction force. In the growth phase, metal atoms are separated from metal precursors to form nanoparticles. During this time, the reduction of the remaining metal ions occurs. The growth phase results in stable nanoparticles, while the extended phase produces nanoparticles with imprecise morphologies (Bharathi et al., 2020). In the final termination phase, stability and capping by biomolecules are achieved (Nasrollahzadeh, Atarod, & Sajjadi, 2019). The number of biomolecules plays an important role in the final structure of the nanoparticles formed (Bharathi et al., 2020). As discussed by Vinayagam et al. (2021), the synthesis of magnetite involves three steps. Initially, Fe^{2+} ions from the precursor is reduced to Fe^0 (an unstable form) through phytochemicals in extracts. Thus, the oxidation of Fe^0 to Fe^{2+} and Fe^{3+} takes place, they undergo oxidation of the metal core during its growth and nucleation to form magnetite nanoparticles stabilized by photochemicals in the extract, such as the shown in Figure 2.6 (Vinayagam, Zhou, Pai, &

Varadavenkatesan, 2021). Figure 2.6 shows the growth mechanism of synthesized green iron and IONPs.

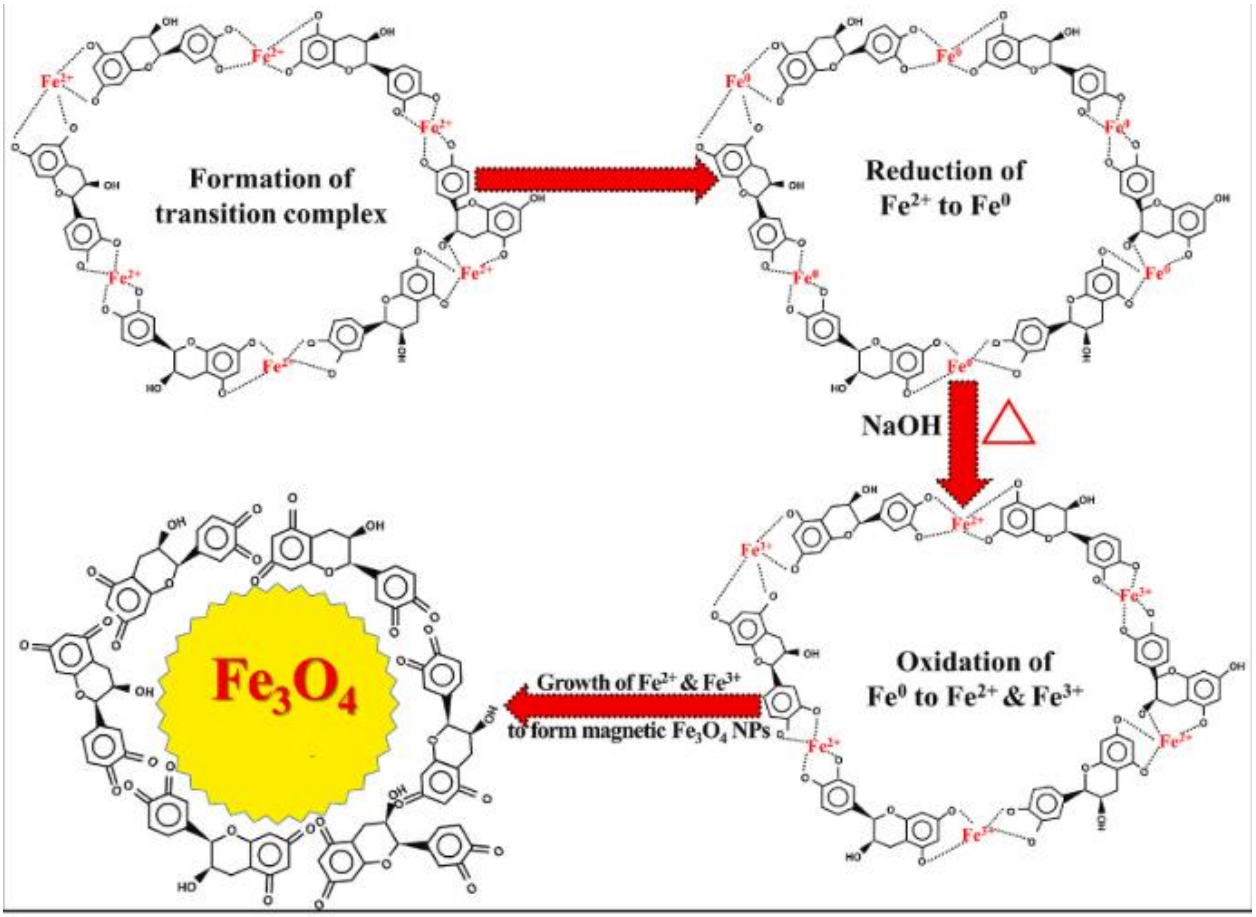

Figure 2.6: Pictorial illustration of the mechanism of formation of magnetite nanoparticles.

2.5.5 Magnetic behavior of IONPs

The magnetic nature of iron nanoparticles can be confirmed by magnetometer analysis. Superparamagnetism and high surface area are exciting properties of magnetic nanoparticles. When the residual magnetization values are low or zero, the particles are called superparamagnetic (Beheshtkhoo, Kouhbanani, Savardashtaki, Amani, & Taghizadeh, 2018). Particles have no magnetic power when the external magnetic field is separated. The higher the saturation magnetization, the higher its magnetic effect, but this value is affected due to the capping agent in green synthesis (Ali, Peng, Khan, & Sultan, 2018). Figure 2.7 the properties of nanoparticles in the presence and absence of a magnetic field.

The obtained saturation magnetization value was significantly lower in greener-manufactured iron nanomaterials (Figure 2.7b) (Das et al., 2020). For example, more

environmentally friendly iron nanomaterials using *Urtica diorica* and *Daphne mezereum* showed peak magnetization of 0.14 and 0.3 ± 0.05 emu/ g with a linear magnetization plot concluding them to be paramagnetic (Beheshtkhoo et al., 2018; Predoi, Iconaru, Predoi, Stan, & Buton, 2019). The magnetite nanoparticle synthesized using *Thunbergia grandiflora* and *Mussaenda erythrophylla* exhibited saturation magnetization of 4.7 and 5.14 emu/g on VSM analysis (Pai, Kini, Narasimhan, Pugazhendhi, & Selvaraj, 2021; Vinayagam et al., 2021) respectively. In the case of magnetite nanoparticles, the absence of hysteresis loop and low permanent magnetization below 1 emu/g confirm the superparamagnetic nature. Ferromagnetism and ferrimagnetism are two main forms of magnetism. In ferromagnetism, particles regain memory even after the magnetic field is removed. To identify these particles, an inverse magnetic field operation is applied. The presence of a hysteresis loop indicates its magnetic memory. Unlike ferromagnetic and ferrimagnetic particles do not align atoms parallel to the direction of the magnetic field rather, they show anti-alignment. Atoms with random magnetic orientation have a moment characteristic of paramagnetic particles. In the case of a diamagnetic, the particles are non-magnetic in the presence or absence of a magnetic field (Nisticò, 2021). The adaptability of superparamagnetic nanomaterials is due to their ability to react to a magnet and be functionalized with biomolecules. Nanoparticle morphologies change depending on the concentration of biomolecules generated, distinct growth and reaction environments, and precursor solutions used. The magnetic field affects the crystallinity of nanoparticles, as reported by Arenas-Alatorre et al., (2019), placing the magnet during synthesis induces crystal directions for nanoparticle growth (Arenas-Alatorre et al., 2019).

The magnetic iron nanoparticles make them more vulnerable to air, causing rust; surface modification can be done to avoid this (Nyankson et al., 2019). The agglomeration of the particles is controlled, making them stable and non-oxidized by providing the possibility of additional functionalization (Ling et al., 2019).

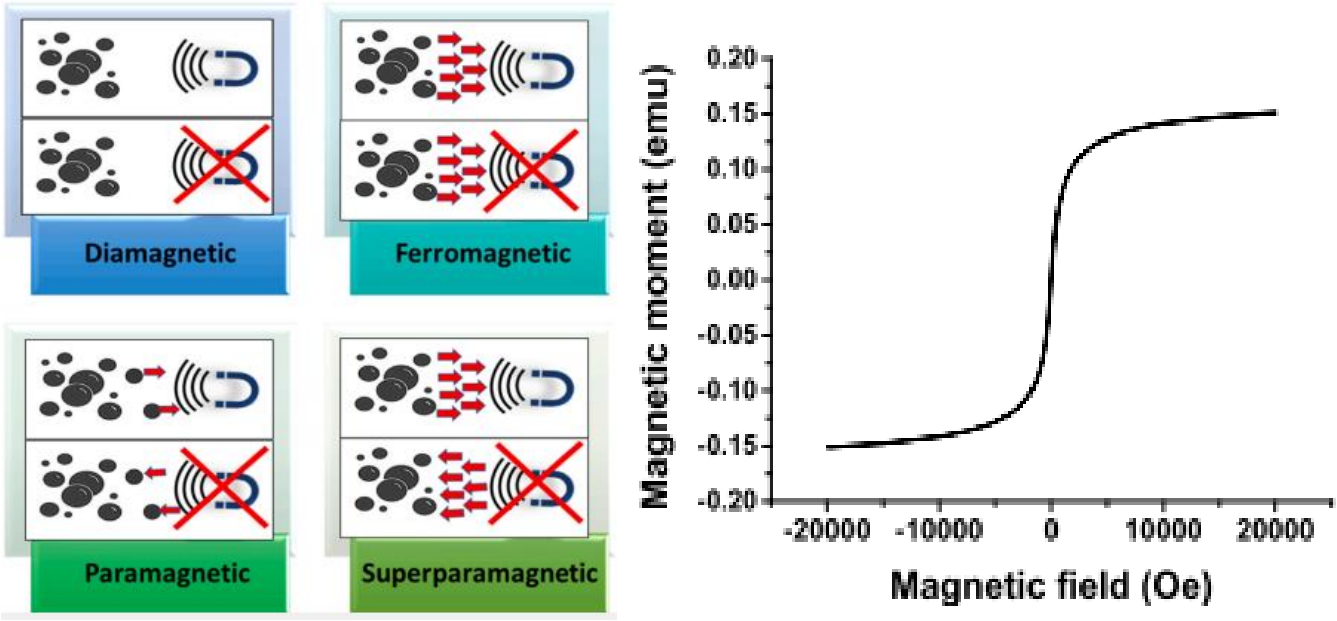

Figure 2.7: Properties of magnetic iron under the effect of the magnetic field: Magnetization curve (a), of green synthesized Fe_3O_4NP (b).

2.5.6 Application of IONPs

Iron oxide nanoparticles (IONPs) have shown tremendous applications in multidisciplinary fields. For example, it is used as a catalyst material (Zhang, Yang, & Guan, 2019), as an adsorbent in wastewater treatment (Kanagasubbulakshmi & Kadirvelu, 2017), as a pigment in manufacturing industry (Ebrahiminezhad, Zare, Ajit, Saeed, & Younes, 2018). Additionally, they are essential raw materials for coatings, gas sensors, magnetic recording devices, magnetic data storage devices, magnetic resonance imaging, bioseparation and medical applications (Aragaw, Bogale, & Aragaw, 2021). IONPs are excellent adsorbents, and can have several applications in wastewaters remediation among which we can cite: the elimination by adsorption of pharmaceutical pollutants (Abdelfatah, Fawzy, El-Khouly, & Eltaweil, 2021; Altaf et al., 2021; Stan et al., 2017), pesticides, heavy metals (Das et al., 2020; Onal, Yatkın, Aslanov, Erg, & Ozer, 2019)and dyes (Beheshtkhoo et al., 2018; Pradhan et al., 2022) .

2.6 General information on zeolite and its applications

2.6.1 History

The first discovery of zeolites was in 1756, when the Swedish mineralogist Cronstedt noticed that the mineral stilbite appeared to boil when heated. He suggested the use of the term "zeolite", which is derived from the Greek "zeo: to boil" and "lithos: stone". Currently, this word

can also be written as "zeolite" which is closer to the term used in English (Guth, Collin, & Wey, 1970)

2.6.2 General

Zeolites are crystalline and porous aluminosilicate compounds, which come from the chain of tetrahedra of SiO_4 and AlO_4, linked by oxygen atoms. This results in the formation of crystal lattices of uniform size. Oxygen neutralizes the overall negative charge induced by the compensating cation $[M^{n+}]$ (Wu, Xie, & Liu, 2018). Zeolites have the following crude formula:

$$M^{n+}_{x/n}[(AlO_2^-)x(S_iO_2)y]\ (m)H_2\,O$$

(Where M is a cation of exchangeable n valence, whether it is metallic-alkaline, alkaline-earth or transition metal, either an ammonium or a proton), Three-dimensional structure consists of a sequence of tetrahedra SiO_4 and AlO_4, connected between them by the ions O_2^- following three the rules:

i. Any sleep of a tetrahedron also belongs to another tetrahedron
ii. A given tetrahedron can only share a single vertex with another tetrahedron.
iii. It is impossible for two (or more than two) tetrahedra to AlO_4 be close: Loewenstein's principle

The structure is characterized by a regular porosity, pore size and shape, as well as microporous volume. Each structure has its own pore opening diameter, which can hinder the circulation of larger molecules inside certain materials: This is the steric phenomenon. For example, ZSM-5 zeolite cannot adsorb molecules with a size greater than 0.62 nm (Blasioli et al., 2014). The shape of the pores therefore plays a crucial role regarding the adsorption capacity and diffusion of molecular compounds inside the crystals.

The proportion of silicates and aluminates (Si/Al) indicates the hydrophilic or hydropholic nature of the zeolites. At a value greater than 8-10, it is theoretically hydrophobic (Huang et al., 2020). It is often essential to add a binder in order to bring the zeolite crystals together and create particles of a few millimeters. The formation of mesoporosity between the crystals is observed, which creates a bimodal material (Siuki et al., 2021).

Most zeolites are present in powder or grain form, but other forms are being developed in order to reduce pressure loss, increase specific surface area and develop macroporous networks. It is possible to structure them in fibers, monoliths or foams (Ma et al., 2014).

2.6.3 Types of zeolites

2.6.3.1 Natural zeolites

Zeolites occur in nature and typically fill cracks and pores in volcanic rocks, restricting the ability to form large deposits. This type of mineral deposit is therefore quite rare (Neolaka et al., 2022). Minerals such as feldspars, kaolinite, smectite, volcanic glass or even other zeolites can be used as precursor materials in the formation of zeolites, depending on the conditions of pressure, temperature and the presence of mineralizing fluids, in a dissolution-precipitation system (Deng et al., 2016). Only a few countries worldwide have exploitable reserves of zeolite, exploited only in the open air. Zeolite ore is processed in a relatively simple manner, requiring only grinding and sorting steps by particle size range (Magalhães et al., 2022). Only clinoptilolite, analcime, heulandite, laumonite, phillipsite, mordenite, chabazite, erionite, and ferrierite are known to have large sediment concentrations among the 60 varieties of natural zeolites. Unlike synthetic zeolites, natural zeolites offer a variety of mineralogical and chemical properties, crystal structure and pore size, which limits their use if more homogeneous properties are required to ensure high efficiency (Magalhães et al., 2022). Despite this, natural zeolites are more affordable than synthetic zeolites, allowing them to be used in animal feed manufacturing, water treatment, odor control, gas adsorption and addition of pozzolanic to Portland cement (Magalhães et al., 2022).

2.6.3.2 Synthetic zeolites

Chemical processes are used to produce these zeolites, resulting in uniformity and superior purity compared to natural types with respect to their lattice structures, pore sizes, and cages within their frameworks (Belachew & Hinsene, 2022). Pure chemicals rich in silica and alumina, minerals present on earth or by-products of industries can be the main raw materials used for the production of synthetic zeolites (Magalhães et al., 2022).

Depending on the temperature, pressure, concentration of reactive solutions, pH, activation process and aging period, as well as the contents of $SiO_2$and Al_2O_3raw materials, the type of zeolites formed varies (Mgbemere, Ekpe, & Lawal, 2017).

The International Zeolite Association Structure Commission (IZA-SC) identifies each type of frame with a three-letter code. Table 2.5 shows some of the major zeolites with three-letter codes based on the Si/Al ratio or phosphate level (Kianfar & Universitesi, 2020).

Table 2.5: Designation and specifications of important zeolites.

Low silica		Intermediate silica		High silica	
$\frac{Si}{Al} \leq 2$		$2 < \frac{Si}{Al} \leq 5$		$5 < \frac{Si}{Al}$	
IUPAC name	Example	IUPAC name	Example	IUPAC name	Example
ANA	Analcime	BHP	Linde Q	BEA	Zeolite β
BIK	Bikitaite	FAU	NaY	IRON	Ferrierite
CAN	Cancrinitis	IRON	Ferrierite	EMAIL	ZSM-11
EDI	Edingtonite	LTL	Linde L	MFI	ZSM-5
FAU	NaX	MAZ	Mazzite	MFS	ZSM-57
ENG	Franzinite	MEI	ZSM-18	MSO	MCM-61
PHI	Philipsite	SEA	Merlinoite	MTF	MCM-35
S.O.D.	Sodalite	MOR	Mordenite	MTT	ZSM-23
THO	Thomsonite	OFF	Offretite	MWW	MCM-22
LTA	Linde A	ITS	Stilbite	ZSM	ZSM-48

In general, for zeolites, an increase in this parameter (i.e., Si/Al from 5 to infinity) can result in a significant increase in several parameters (such as acid resistivity, thermal stability and hydrophobicity), with the exception of a few parameters (such as acid site density and cationic concentration) which decrease (Kianfar & Universitesi, 2020).

2.6.4 Methods for synthesizing zeolites

2.6.4.1 Hydrothermal method

The hygrothermal method is a method considered to be one of the least expensive. Water serves as a solvent in the process, along with sources of silicon and aluminum. Other, the reagents involved in the process are the mineralizing agent (OH^-, F^-), metal cations and a structure

directing agent (usually an organic surfactant) (Magalhães et al., 2022). Figure 2.8 illustrates the hydrothermal synthesis process. In an autoclave reactor, the reaction takes place at a high temperature and high autogenous pressure (often up to 15 bar). The product is then washed several times, filtered and oven dried. However, the method has certain drawbacks which may limit its use. Alkaline wastewater is produced at the end of the process due to high water consumption (Nizam et al., 2021). Additionally, the procedures may require a prolonged reaction. Due to advances in zeolite synthesis research, many other methods have been developed.

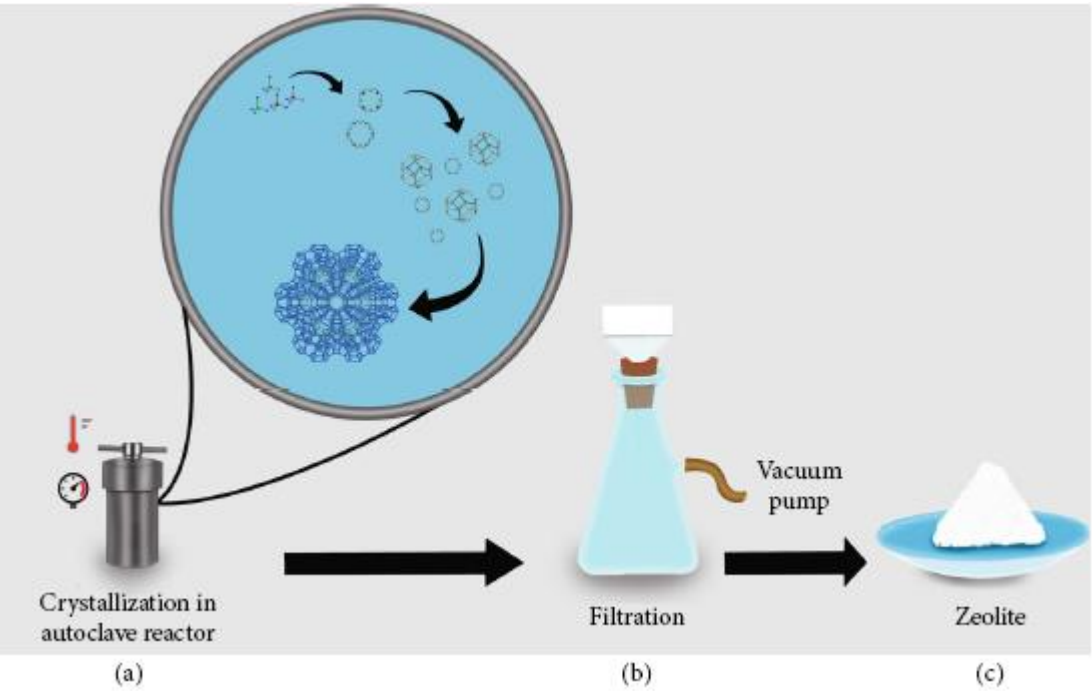

Figure 2.8: The hydrothermal synthesis process. Crystallization occurs in an autoclave (a), then the product is dried in an oven (b), and the white solid obtained is zeolite (c).

2.6.4.2 Solvothermal method

The zeolite synthesis method by solvothermal involves using a solvent (except water) to obtain the zeolite. Based on this general description, the hydrothermal method can also be considered to fall into this category, since water is by far the most common solvent. However, other solvents such as alcohols, hydrocarbons, pyridine, were effectively employed for the production of zeolite. The solvothermal method of zeolite synthesis uses different solvents, ranging from non-polar and hydrophobic solvents to polar and hydrophilic solvents (Nizam et al., 2021).

2.6.4.3 Ionothermal method

Ionothermal is another special category of solvothermal synthesis method where the solvents used are primarily ionic compounds and are not molecular in nature, unlike solvothermal solvents. Ionic liquids are solvents used in the ionothermal method of synthesizing zeolites, and their ionic nature impacts some specific characteristics, such as low vapor pressures (Nizam et al., 2021).

2.6.5 Training mechanism

Two processes are involved in the formation of zeolites, namely nucleation and crystal growth (Magalhães et al., 2022):

2.6.5.1 Nucleation

According to Arrhenius, nucleation is an activated process whose speed increases with temperature. Initial (or primary) nucleation from the labile solution can be homogeneous (spontaneous formation) or heterogeneous (impurity-induced); crystal formation is induced by secondary nucleation.

2.6.5.2 Crystal g*r*owth

At the interface between crystal and solution, zeolite crystals (or nucleates) form by condensing dissolved species (secondary building units or larger species).

The nucleation and crystallization of crystals do not necessarily form in solution, but can occur at the level of the gels present in the various mixtures.

2.6.6 Parameters influencing the synthesis of zeolites

2.6.6..1 Effect of temperature on the crystallization of zeolites

In various ways, temperature impacts zeolite production. It can influence the speed of crystallization, as well as the type of zeolite produced. In general, high synthesis temperatures result in the creation of dense phases. How quickly the reaction mixture reaches the reaction temperature also plays a crucial role. The synthesis temperature reached quickly leads to an increase in the dissolution speed of the gel, a reduction in the appearance of intermediate zeolite phases and a possible increase in the Si /Al ratio in the final product (Mgbemere et al., 2017).

2.6.6..2 Effect of adding seeds on the crystallization of zeolites

Bessa et al, (2017) examined the increase in crystallization rate by adding seeds. He found that it is possible to eliminate the induction period during the synthesis of zeolite A (LTA) by adding seeds (Bessa et al., 2017). By adding a large quantity of seeds to the reaction mixture before the formation of the gel, the effect can be further amplified (for increased homogeneity of the system). Thus, the seeds act as privileged nucleation sources. It is also possible to regulate the type of zeolite obtained by adding seeds. According to Gora and Thomson, et al (1995), the incorporation of hydroxysodality seeds into a gel, which does not lead to the formation of zeolite A (LTA), allows the crystallization of hydroxysodality.

2.6.6.3 Effect of pH

Syntheses are generally carried out in basic pH environments, generally above pH 11. Raising pH improves the rate of crystallization, but reduces the yield and leads to thermodynamically stable phases more quickly. Thanks to anions OH^-, silica and alumina are mobilized in the aqueous solution by forming silicate, aluminate and aluminosilicate anions. The composition of the zeolite (the decrease of the ratio with the increase of the pH) and the morphology of the crystals are also influenced by the alkalinity of the solution (Murali, Ismail, Rahman, & Sridhar, 2014).

2.6.6.4 Effect of structuring agents

The type of zeolite formed will certainly be determined by the nature of the cations used in the synthesis of the zeolites. These are bases which are introduced, making it possible to adjust the pH, or salts.

2.6.6.5 Effect of synthesis time

The morphology, crystal size and purity of the zeolite obtained can be influenced by the duration of zeolite synthesis. Indeed, given that zeolites are metastable phases, too rapid synthesis will result in a partial transformation of the gel into a type of zeolite. On the other hand, prolonged synthesis can lead to the appearance of more thermodynamically stable phases (such as gismondin or quartz) (Nizam et al., 2021).

2.6.6.6 Effect of the nature of the reagents and the composition of the mixture

The selection of silica and aluminum sources plays a crucial role in the production of zeolites. It will therefore take longer for highly polymerized silica to "solubilize", but the zeolite

crystals will generally be larger than those obtained with more reactive silica, which results in the formation of numerous nucleates and therefore smaller crystals (Siuki et al., 2021). As for itself, the Si/Al ratio of the reaction mixture used for the production of zeolites will influence the Si/Al ratio and the type of zeolite obtained (Abdelrahman et al., 2020).

It can be concluded that the synthesis of zeolites is influenced by many factors and each of them plays a crucial role in the formation of the desired product. In order to better understand the mechanisms of zeolite formation, it is therefore preferable to vary a single factor simultaneously.

2.7 Transformation of kaolin into zeolite

Several reasons explain the choice of kaolinite for the production of zeolite LTA. Kaolinite, which is widespread in nature, dissolves quickly in hydroxides (Ma et al., 2014). It is an affordable product with high chemical quality. According to Petrov et al. (2012), the transformation of kaolinite into zeolites begins with the destruction of the clay. The speed of this reaction varies depending on the concentration of ions OH^-, the temperature and the specific surface area of the crystals. Silicon is found in the form of silicate, SiO_4^{4-}in an alkaline environment (Petrov et al, 2012). Aluminum comes in the form of aluminate, AlO_2^- or $Al(OH)_4^-$; there remains uncertainty about its true hydrated form. We know that in an alkaline environment, the tetracoordinated Al complex is dominant, while the hexacoordinated complex is more stable in an acidic environment (Belachew, 2022).

Jean-Neyroud (1972) studied the solubility of silicon and aluminum as a function of pH. According to him, the values are extremely high in an alkaline medium, but the thermodynamic stability of a solution containing the two ions mixed is so low that the formation of a gel phase already occurs at low concentrations. Indeed, the transition from the aqueous phase to the crystalline phase does not occur until several conditions are met, and the dissolved products come together to form a gel. The gel is a complex assembly of tetrahedra $(Si, Al)O_4$ without a fixed structure and partially soluble (Shahid, Srivastava, & Sillanpää, 2021). When it is kept at a high temperature, it continuously transforms. Certain more stable combinations (rings of tetrahedrons, etc.) are formed and tend to dominate.

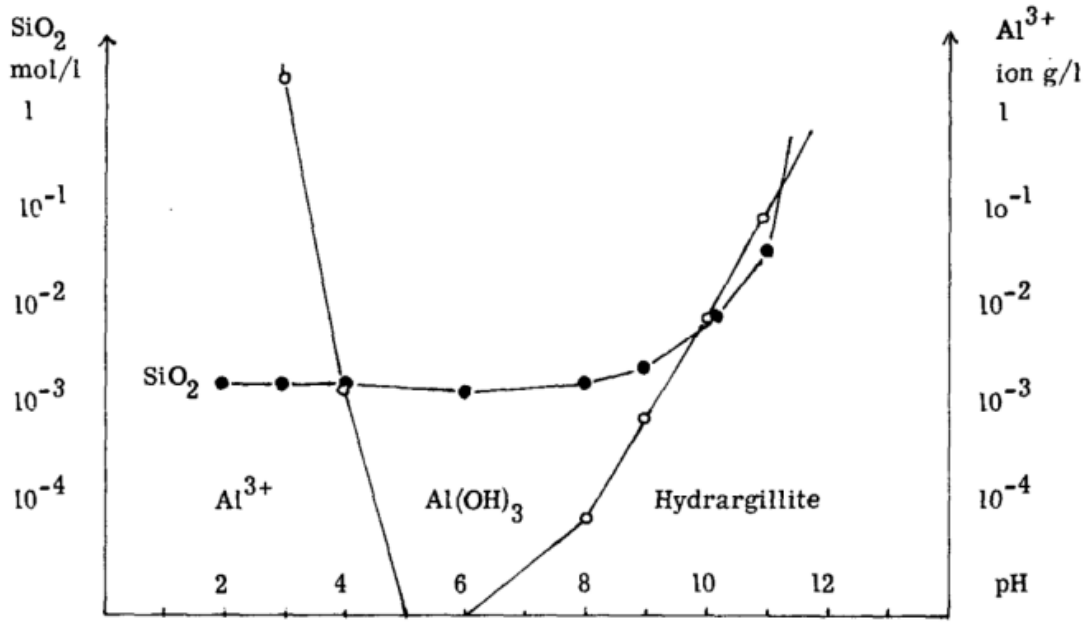

Figure 2.9: Superimposed curve of the solubility of silica and aluminum as a function of pH.

The most stable molecular arrangements are released by the gel, in equilibrium with the aqueous phase, and can react with each other and form the first crystallization nuclei (Mgbemere et al., 2017). Such a nucleus corresponds to the smallest size of the stable crystal. The probability of collision between molecules and the extreme instability of the assemblies determines the formation of nuclei. After this step, the nucleus develops by deploying molecules on its surface (Caballero, Colina, & Costa, 2007).

In summary, “the crystallization process of zeolites takes place as shown in the figure below”.

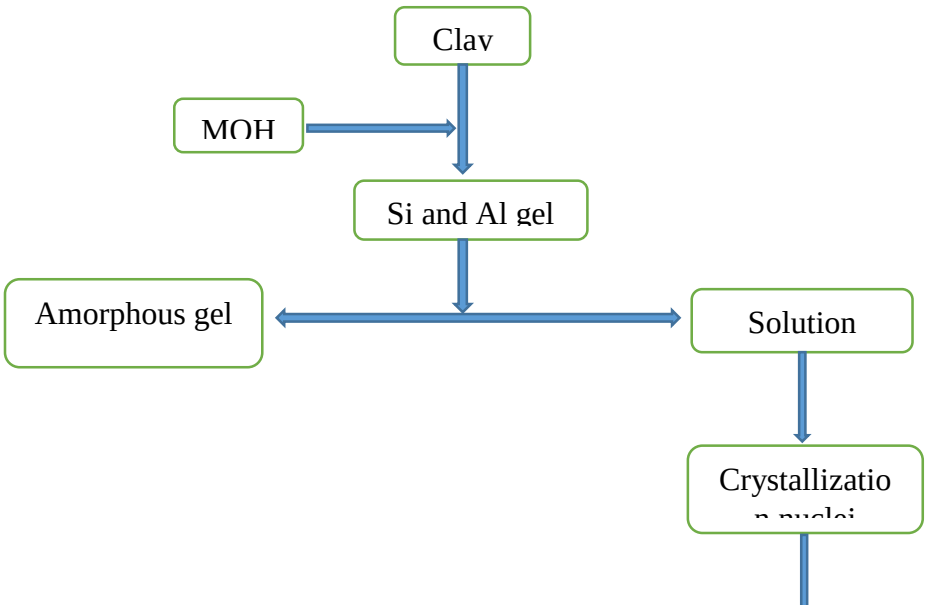

Figure 2.10 The stages of transformation of kaolinite into zeolites

2.7.1 Applications of zeolites

The very high thermal, mechanical and chemical stability of zeolites, as well as their resistance to radiation, are obtained thanks to the presence of pores and cavities in their structure, as well as the presence of an exchangeable compensating cation. These properties make zeolites effective in multiple areas. Therefore, they are commonly used as cation exchangers, adsorbents and molecular sieves for separation, as well as catalysts or catalyst supports.

2.7.1.1 Ion exchanger

The properties of zeolites are specific due to their open three-dimensional structure. The aluminosilicate framework exhibits negative charges due to the 4-coordination of aluminum, which is compensated by alkali or alkaline earth metal cations present in the channels (Profile, 2018).

Ion exchange properties differ significantly from one zeolite to another. In general, these capacities are influenced by the structure and more specifically by the Si/Al ratio. In reality, the number of tradable sites is comparable to the number of aluminums. Thus, the lower the Si/Al ratio, the higher the zeolite has a high exchange capacity (Banu, Karthikeyan, & Meenakshi, 2021).

Various other elements play a crucial role in the exchange:

i. The initial composition of the zeolite compensation cation, depending on the strength of its adsorption on the solid.
ii. The nature of the cation that we wish to put in place: some are too large to reach the zeolite and cannot be exchanged.

2.7.1.2 Adsorption, molecular sieve

Zeolite saturated with water of crystallization is usually found inside the channels and cavities of the network. Water molecules can be removed and replaced with molecules smaller than the pore size without altering the structure. However, the discovery of their abilities to selectively adsorb organic molecules led to the rise of studies on zeolites (Zavareh et al., 2018). Three factors are responsible for the adsorption properties of zeolites (Mgbemere et al., 2017):

i. Due to the presence of cations in the cavities of the zeolite structure, there is a strong electric field which favors polar (H_2O, NH_3) and polarizable (CO_2, hydrocarbon) molecules.
ii. Thanks to their large specific surface area and the perfectly adjusted dimension of the pores, the molecules can access the cavities
iii. Pore size is also important, due to the concentration effect in micropores, where molecules interact more with the walls than on a flat surface

The selectivity at the pore entrance and at the level of the internal cages is determined by the presence of fixed pores size. These adsorption characteristics are used for:

i. Dehydrate and purify gases and liquids (regulate humidity in double glazing)
ii. Elimination of H_2S in factory fumes
iii. Elimination of sulfur compounds present in certain fractions of petroleum
iv. Gas drying
v. Drying of organic solvents
vi. The high vacuum enclosure
vii. Drying in water-inhibited reactions

2.7.1.3 Separation

Zeolite has a separation capacity which is widely exploited in petrochemicals to separate various petroleum fractions. The separation of n-paraffins in a mixture containing ‘n’ and iso-paraffins on zeolite 5A is generally the most widespread method (Kora et al., 2024). Mixtures of n-hexane and 3-methylheptane can be separated by zeolite Ca-A. The separation of para and meta xylene mixture on HZSM-5 zeolite (MFI) is another example. It is also crucial to separate nitrogen and oxygen from the air on the Li-LSX zeolite (Low Silica X, Si/Al = 1, structural code FAU) (Pourazar, Mohammadi, Jafari Nasr, Javanbakht, & Bakhtiari, 2020).

2.7.1.4 Catalysis

Since the 1960s, the acidic and structural properties of zeolites have sparked keen interest in catalysis. The manufacturing sector for zeolite organic catalysts and related microporous materials continues to grow (Mgbemere et al., 2017). Different organic chemical reactions have been examined on different zeolites, and Venuto's review brings together much of the potential reactions on this type of material. These properties are therefore widely used by the oil industry for the valorization of oil fractions during refining. The gasoline fraction can be increased by cracking hydrocarbons and the octane number can be increased by forming branched products (alkylation, cracking, hydrocracking, isomerization). Methanol can also be transformed into gasoline and olefins through reactions catalyzed by zeolites (Mgbemere et al., 2017).

Table 2.6 lists the main uses of zeolites as catalysts. It is possible to classify zeolite catalysis into three categories: 1) inorganic reactions, 2) organic reactions and 3) hydrocarbon conversion (Kianfar & Universitesi, 2020). Acidity, shape selectivity, high specific surface area and structural stability are special characteristics of zeolites as catalysts, which will be discussed in more detail in the following sections.

Table 2.6: Application of zeolite as catalysis.

Inorganic reactions	Organic reactions	Hydrocarbon conversion
H_2S oxidation;	Flavoring (C_4 hydrocarbon);	Alkylation;
NO reduction of NH_3;	Alkylation (naphthalene, benzene, aniline etc.);	Cracking;
CO oxidation;	Aromatic (hydrogenation, oxidation, nitration, etc.);	Dehydration;
Decomposition of H_2O.	Chiral (enantioselective);	Fischer-Tropsch;
	Cyclohexane (oxidation, isomerization, aromatization, ring opening)	Friedel-Crafts alkylation;

2.7.1.5 Energy storage

Regarding zeolites, heat release is associated with water adsorption (Lucresse et al., 2023). It is possible to renew the adsorption/desorption cycle indefinitely and transfer the heat released through compressors or heat transfer liquids. The principle of the heat pump makes it possible to produce hot and cold thanks to this property. Due to their rigid structure, thermal stability and availability of different morphologies, zeolites can be employed to thermochemically conserve solar heat from solar thermal collectors (Lucresse et al., 2023).

2.7.1.6 In agriculture

Clinoptilolite (a natural zeolite) is used to treat soils. It offers a source of potassium that is released slowly. In case of prior ammonium loading, zeolite can play a similar role in the slow release of nitrogen (Magalhães et al., 2022). Zeolites also have the ability to be water moderators, adsorbing up to 55% of their weight in water and gradually releasing it as the plant demands. This characteristic helps avoid root deterioration and periods of moderate drought (Deepika et al., 2023) .

2.7.1.7 Acid and base

By a basic definition, a Lewis acid is an element that accepts electron pairs, while a Lewis base is a species that has an available (reactive) electron pair or delivers electrons. According to Brønsted, all acid-base reactions are characterized by the transfer of one or more protons (ion H^+). According to this theory, an acid is considered as “donor proton” and a base as an “acceptor proton”. Thus, on solid surfaces, the Brønsted acid site can transport a proton from the solid to the adsorbed molecule, while Lewis acid sites can accommodate a pair of electrons from the adsorbed molecule (Kianfar & Universitesi, 2020).

Zeolites are acidic due to the metal cations or hydroxyl ions present on their extra-framework. Aluminosilicate zeolites exhibit SiO_4neutral tetrahedra when the framework silicon atoms are positively charged $(+4)$ in tetrahedral positions (T position) and the coordinating oxygen atoms are negatively charged (-2) The charges of the corresponding tetrahedra can be changed from neutral to -1 when silicon atoms are replaced by an aluminum atom in the framework. Extra-framework metal cations or hydroxyl protons balance these negative

framework charges by creating weak Lewis acid sites or acid sites. Strong Brønsted, which play an important role in the catalytic activity of zeolite materials (Kianfar & Universitesi, 2020).

Those found on the oxygen bridges between the silicon and aluminum atoms of the framework are the first hydroxyl protons present on the zeolites. Typically, these hydroxyl groups are expressed as structural or bridging OH groups, as well as Si-OH-Al groups (Figure 2.11a). Silanol or Si-OH groups, also known as terminal OH groups, are the second type of hydroxyl groups in zeolites, which are found on the outer surface of crystal particles (Figure 2.11b). The formation of these silanol groups is mainly due to the degradation of the zeolite structure by calcination, hydrothermal treatment or treatment with strong acids (Atugoda et al., 2021).

Depending on the processing conditions, it is possible for silicon to migrate, form silanol groups or form hydroxyl groups at the extra-framework aluminum (Figure 2.11c). It sometimes happens that the zeolite framework is degraded and that there are Lewis acid sites at the level of extra-framework aluminum species and framework defects (Figure 2.11c). When these Lewis acidic sites are in the region close to the bridging OH groups, they transform into super-acidic Brønsted sites (Atugoda et al., 2021).

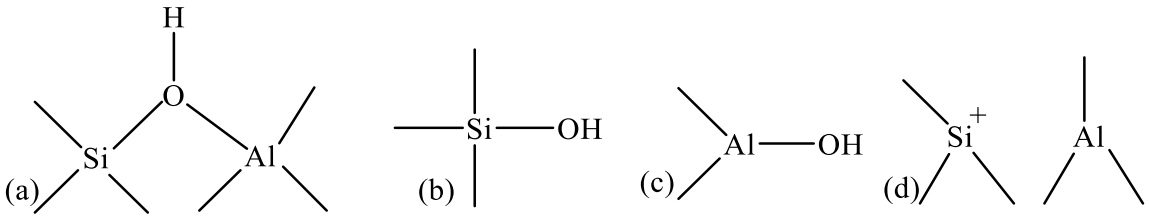

Figure 2.10: Different types of hydroxyl groups and acid sites in zeolites.

Despite the diversity of applications of acidic zeolites as solid catalysts in chemical industries, the use of these microporous and mesoporous materials as base catalyst has been less studied in the literature (Kianfar & Universitesi, 2020). These solid catalysts with essential characteristics have high potential for many crucial industrial processes (such as the Claus reaction). In zeolites, the nature of the basic sites is less precise than that of the acidic sites. This can be explained by the fact that the oxygen atoms of the basic framework or the alkali metal cations on the zeolite framework also act as weak Lewis acid sites (Kianfar & Universitesi, 2020).

2.8 Zeolite LTA

zeolites LTA (Linde Type A) are a family of synthetic zeolites. Milton et al carried out the first synthesis in 1954 (Union Carbide Corporation of the Linde Division) Milton et al,

(1954). The crystalline structure of zeolite A has no natural equivalent; it is made up of an anionic aluminosilicate structure, neutralized by alkaline or alkaline earth cations. Several gels have been used to synthesize different structure of the zeolites LTA, with mainly monovalent (Na^+, K^+, Ag^+, ...), divalent (Ca^{2+}) or even multiple cations (Ca^{2+}, Na^+), for different Si/Al ratios (Iqbal, Sattar, Haider, & Munir, 2019; Wang et al., 2019b). LTA type zeolites A were also manufactured from homogeneous aqueous solutions of sodium aluminosilicate (Hashemian, Hosseini, Salehifar, & Salari, 2013). The stacking, by the square faces, of two types of polyhedra, square-based prisms (double cycles with 4 tetrahedra) and cuboctahedra, gives rise to zeolites A as shown in Figure 2.11.

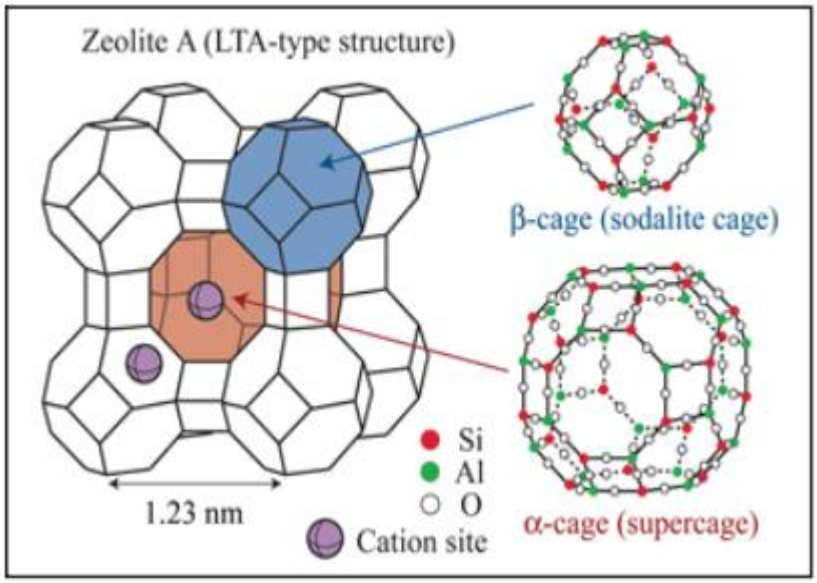

Figure 2.11: Representation of the crystal structure of zeolite LTA (Petrov & Michalev, 2012).

2.8.1 Crystallographic structure

LTA zeolites are microporous aluminosilicate crystals, composed of a regular sequence of tetrahedra TO_4, where T represents aluminum or silicon present in equal proportion and encountered alternately in the structure of the zeolite framework (Wang et al., 2019b). On a larger scale, the crystal structure of tetrahedra TO_4 appears as a crystal structure with cubic geometry (Figure 2.12). There are three categories of free volumes in this geometry. At the top of the cube are the β cages or sodalities, while the α cages or supercages are in the center, and the prisms that provide the junction between the β cages are known as D4R (Double Four-membered Ring). If we refer to the mesh parameters of zeolites LTA, the dimensions of these volumes are almost

independent of the type (Petrov & Michalev, 2012). The α and β cages, which are often considered spheres, have a diameter of 1.14 and 0.66 nm, respectively. The presence of charge compensating cations makes it possible to restore the electroneutrality of the zeolite framework due to the valence of aluminum. The chemical composition of an entire hydrated pseudo-mesh is as follows:

$$Na_{12}(AlO_2)_{12}(SiO_2)_{12}.27H_2O$$

The references encountered in the literature most often agree on a filling of a pseudo-mesh of zeolite 4A, for example, with 27 water molecules or even 28 (Petrov & Michalev, 2012). For zeolite A, the Si/Al ratio is close to 1. Thus, the overall charge of the cube is 12, and can receive up to 12 monovalent compensating cations. The position of these cations depends on their nature, but the sites are generally placed near the access windows, thus narrowing the opening.

2.8.2 Location of compensating cations

XRD made it possible to identify three types of sites for the localization of charge compensating cations in LTA zeolites (Wu et al., 2018): I sites inside the α cages , 0.04 nm from the center hexagonal access windows to the β cages , II sites in the plane of the octagonal windows between α cages at 0.12 nm from their center, III sites on one side and on the other square windows between β cages and D4R (Wu et al., 2018).

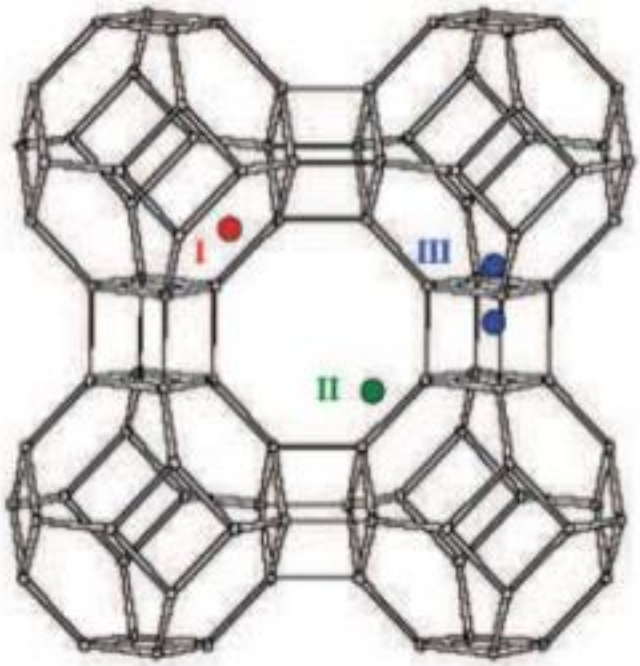

Figure 2.12: Location of cationic sites in zeolite LTA.

The location of the compensating cations considerably influences the characteristics of the zeolite LTA, in particular the occupation of type II sites. For the zeolite 5A, these II sites are unoccupied and the opening diameter of the cages is 0.5 nm, while for the 4 A zeolites, it is 0.4 nm, hence their respective names. The adsorption properties are directly affected by this difference, because for example at a temperature of 77K, the nitrogen used to measure the specific surface area can penetrate the microporous volumes of zeolite 5A, while zeolite 4A behaves like a solid non-porous with respect to it due to the inaccessibility of nitrogen for steric reasons (Bessa et al., 2017). This highlights the ability to distinguish the molecular adsorbates present in these two types of zeolites.

2.9 Evaluation of adsorption performance through computational studies

2.9.1 Evaluation of chemical reactivity within the conceptual framework of electron density functional theory.

What are the differences between stable and reactive molecules? Is it possible to predict the selectivity of a chemical reaction? Several theories have sought to address these questions. The theory of frontier orbitals (Frontier Molecular Orbital Theory) was developed by Fukui in 1952, while the theory of hard and soft acids and bases (Hard and Soft Acids and Bases) was introduced by Klopman and Pearson in 1963. In 1968. Klopman proposed a unification of these

theories based on the minimization of the interaction energy between two molecules. However, the conceptual framework has been most successful and still appears most promising in the Electron Density Functional Theory (DFT) paradigm. The original idea of DFT dates back to 1923, when Thomas Fermi and Dirac showed that the total energy of a gas of free electrons approximately depends on the electron density.

2.9.2 The foundations of DFT

2.9.2.1 The first theorem of Hohenberg and Kohn

Parr and Yang called the proof of Hohenberg and Kohn's first theorem extremely simple. If two external potentials, v(r) and v'(r), are different by more than one constant and have the same electron density, ρ(r), then we can form two Hamiltonians $\widehat{\mathrm{H}}$ and $\widehat{H'}$ with the same electron density, but whose normalized wave functions, ψ and ψ', could differ.

If we consider ψ' as a test of the Hamiltonian $\widehat{H}$:

$$\mathrm{E}_0 < (\psi'/\mathrm{H}/\psi') = (\psi'/\mathrm{H}'/\psi') + (\psi'/\mathrm{H} - \mathrm{H}'/\psi')$$

$$E_0 < E'_o + \int\rho(r)\,[v(r) - v'(r)]dr \qquad 2.1$$

Conversely, taking ψ as a test function of the Hamiltonian $\widehat{H}$,a similar equation appears:

$$\mathrm{E}'_0 < (\psi/\mathrm{H}'/\psi) = (\psi/\mathrm{H}/\psi) + (\psi/\mathrm{H}' - \mathrm{H}/\psi)$$

$$E'_0 < E_o - \int\rho(r)\,[v(r) - v'(r)]dr \qquad 2.2$$

By combining (2.1) and (2.2), we obtain $\mathrm{E_o} + \mathrm{E'_o} < \mathrm{E'_o} + \mathrm{E_o}$. Two different external potentials cannot therefore have the same electron density p(r). In this way, the electron density maintains the external potential at a constant value. Furthermore, since the total number of electrons can also be determined using the electron density, it is possible to calculate all parameters of the system using this density. The interaction energy between the electrons is therefore calculated using a functional of the electron density, F[p(r)]. It is important to remember that a functional is a type of function. The function F[p(r)] is considered "universal" because it is not conditioned by the external potential to which the system is subjected and therefore can be used for any electron density.

The electron density ρ(r) of a system of electrons subjected to a potential v(r) can be represented by the total electronic energy:

$$E_v[\rho(r)] = \int\rho(r)v(r)dr + F[\rho(r)] \qquad 2.3$$

The ν function of electronic energy highlights the fact that this function is not universal, but is conditioned by the external potential to which the electronic system is subjected.

2.9.2.2 The second Hohenbarg-Kohn theorem

Let p(r) be the prime electron density of a system. Let ρ'(r) be an electronic test function that does not correspond to the ground state electron density. According to the second Hohenberg-Kohn theorem, the variational principle is generalized as follows:

$$E[\rho(r)] < E[\rho(r')] \quad (2.4)$$

Thus, this second theorem offers a criterion for evaluating the precise electron density of a ground-state system. Indeed, the precise electron density is that which minimizes energy use. The solution must also satisfy the following condition:

$$\int \rho(r)dr = N \quad (2.5)$$

When we look for the optimal electron density based on equation (2.5), we arrive at:

$$\delta(E[\rho(r)] - \mu\int\rho(r)dr + N) = 0 \quad (2.6)$$

The constraint is represented by the Lagrange multiplier associated with u. It therefore results:

$$\frac{\delta E[\rho(r)]}{\delta \rho(r)} - \mu = 0 \quad (2.7)$$

By introducing equation (2.3) into equation (2.7) we obtain:

$$\mu = v(r) + \frac{\delta E[\rho(r)]}{\delta \rho(r)} \quad (2.8)$$

The remarkable result is that equation (2.8) shows that the sum of the external potential and the interaction potential generated by the electron density is constant at all points.

Like the majority of Lagrange multipliers, μ has a physical meaning whose discovery undoubtedly laid the foundations for the conceptual branch of the Lagrange function. We will discuss this meaning in the following paragraphs.

2.9.2.3 Descriptors of conceptual DFT

The goal of conceptual DFT is to provide a theoretical framework and precise definitions to concepts commonly employed by experimental chemists. In the canonical set [Nv(r)], the successive derivatives of energy made it possible to propose numerous descriptors of reactivity and to develop physical meanings. Even though conceptual DFT has a finite temperature version, in the following chapters we will only talk about conceptual zero temperature DFT.

2.9.2.4 The derivatives of the energy in the canonical ensemble

It is necessary to briefly discuss the differentiability as a function of the number of electrons N., an a priori discontinuous variable, when writing successive derivatives of the energy in the canonical set [Nv(r)]. In reality, a number of electrons can be called a continuous variable if we assume that it is a time average of an open system. For example, during the exchange of electrons between two free atoms. It is important, then, to emphasize that the two variables are not entirely autonomous. Indeed, a variation in the number of electrons in the system inevitably leads to a variation of the electron density, and according to the first theorem of Hohenberg-Kohn, a modification of the external potential.

Figure 2.13 shows all the successive derivatives of energy up to order 2. These derivatives can be grouped into three categories. The global quantities are derivatives with respect to A. We call “local” the derivatives which depend only on one spatial coordinate and “non-local” the derivatives which depend on two spatial variables.

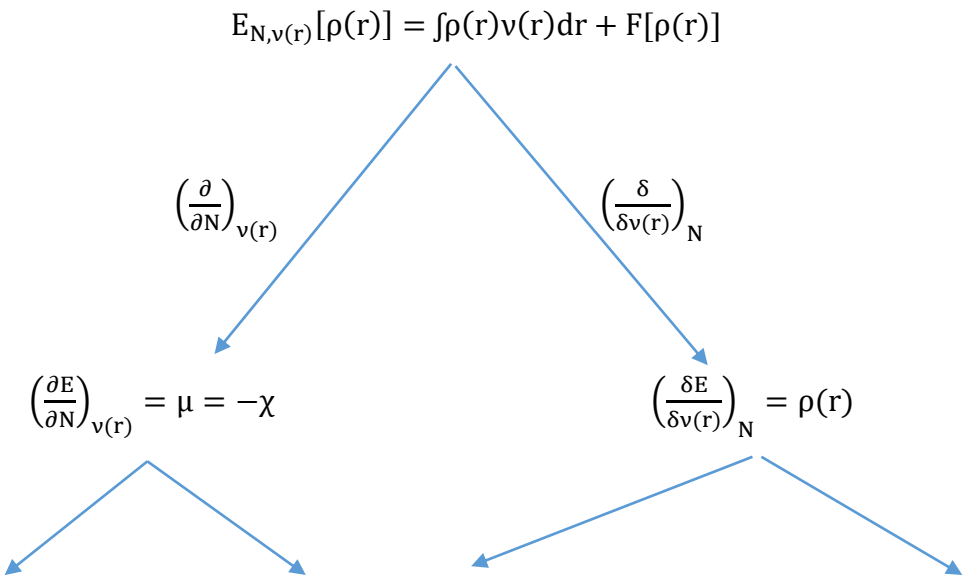

$$\left(\frac{\partial^2 E}{\partial N^2}\right)_{v(r)} = \eta \qquad \left(\frac{\partial^2 E}{\partial N\, \delta v(r)}\right) = f(r) \qquad \left(\frac{\delta^2 E}{\delta v(r)\delta v(r')}\right)_N = \chi(r, r')$$

Figure 2.13: Derivatives of the energy at 2nd order.

2.9.2.5 Overall quantities

2.9.2.5.1 Chemical potential (μ) and electronegativity (χ)

The first step towards conceptual DFT was made by identifying the Lagrange multiplier μ with electronegativity. From equations (2.3) and (2.7), we can say that the derivative of the energy with respect to the electron density at a point r in space, at constant external potential, is μ.

We have:

$$\mu = \left(\frac{\delta E[\rho(r)]}{\delta \rho(r)}\right)_{v(r)} \qquad 2.9$$

From equation (2.8), we can deduce that:

$$dE_v = \mu \int \delta\rho(r) dr = \mu dN \qquad 2.10$$

Either:

$$\mu = \left(\frac{\partial E}{\partial N}\right)_{v(r)} \text{ electronic chemical potential)} \qquad 2.11$$

On the other hand, quantity $\chi = -\left(\frac{\partial E}{\partial N}\right)$ has been identified with electronegativity since the beginning of the 1960s. We therefore opt for the following relationship:

$$\mu = -\chi = \left(\frac{\partial E}{\partial N}\right)_{v(r)} \qquad 2.12$$

The application of finite differences to relation 2.12 leads to the proposition by Mulliken.

$$\chi = -\left(\frac{I+A}{2}\right) \qquad 2.13$$

where I and A are respectively the first ionization energy and the electronegativity. This relationship is one of many relationships proposed to express electronegativity.

2.9.2.5.2 Hardness (η) and Softness (S)

In 1963, Pearson, based on research into reactions between Lewis acids and bases, divided ions and molecules into two categories. Substances described as “hard” and those described as “soft”. He points out that reactions between ions and molecules of the same category generate compounds with higher cohesion energies than reactions between reactants of different categories. It therefore suggests that "hard" acids have a preference to react with "hard" bases,

while "soft" acids have a preference to react with "soft" bases. The section devoted to the principles demonstrated using DFT will discuss this principle of “hard” and “soft” acids and bases.

Howver, it is important to remember, that in hard acids the electron acceptor atom is small and has a high oxydation number. It is difficult to excite its external electrons.

For soft acids, the electron-accepting atom has a larger size, a lower oxidation number, and can easily excite a few external electrons. Hard bases have low polarizability and high electronegativity in the electron donor atom. It is not oxidizable and has low energy empty orbitals. Finally, soft bases have atoms that provide electrons that are easily polarizable, have low electronegativity, and are easily oxidizable. Empty outer orbitals have low energy.

The energies of the frontier orbital electrons appear to be directly related to these physical characteristics. It is therefore possible to measure the characteristics of molecular orbitals in orbital theory by calculating the energy gap between the highest occupied orbital (HO) and the lowest vacant orbital (BV).

The hardness at the second derivative of the energy with respect to the number of electrons is identified by Parr and Pearson in 1983.

$$\eta = \left(\frac{\partial^2 \mathrm{E}}{\partial \mathrm{N}^2}\right)_{\nu(\mathrm{r})} = \left(\frac{\partial \mu}{\partial N}\right)_{\nu(r)} \qquad 2.14$$

Applying the finite difference approximation to equation 2.14 leads to an approximate expression for hardness:

$$\eta = \mathrm{I} - \mathrm{A} \qquad 2.15$$

In the original study by Parr and Pearson, a factor of 1⁄2 was artificially added to coincide with the operational definition of chemical potential. Taking this factor into account is increasingly common in recent scientific publications. The electronic repulsion between two electrons, one in HO and the other in BV, is responsible for this energy. Still, based on equation (2.15), it is possible to see that the hardness of an atom or molecule corresponds to the energy required for its disproportionation.

$$\mathrm{S} + \mathrm{S} \rightarrow \mathrm{S}^{+} + \mathrm{S}^{-}$$

It therefore becomes very obvious that physical hardness corresponds to the resistance of charge transfer.

Finally, the use of Koopmans' theorem provides a formula for determining hardness using molecular orbital energies, which is in agreement with molecular orbital theory.

$$\eta = E(BV) - E(OH) \quad 2.16$$

Other approaches based on equation (2.14) and/or electrostatic potential have been suggested to assess hardness. However, the previous relationship remains the most frequently used.

The physical significance of the inverse of the convexity of the curve of energy as a function of the oxidation number of an atom was addressed well before the identification of hardness as the second derivative of energy. We can therefore calculate Softness using the inverse property.

$$s = \frac{1}{\eta} \quad 2.17$$

The notions of hardness and softness have been commonly used to interpret chemical reactions.

From these global descriptors were derived indices. One of the most crucial elements is certainly the “electrophilia” index.

2.9.2.5.3 The electrophilicity index

We therefore wonder how many electrons an electrophile could accumulate, if it were immersed in a sea of free electrons. To compare the electrophilic potential of two species, it would be possible to evaluate the value of the number of electrons acquired and the resulting energy stabilization. For example, for an electrophile, we can define the fluctuation of its electronic energy during a charge transfer at constant external potential as follows:

$$\Delta E = \mu^0 \Delta N + \frac{1}{2}\eta \Delta N^2 \quad 2.18$$

Energy stabilization will be achieved when the derivative with respect to charge transfer is zero, i.e. for:

$$\Delta N_{max} = -\frac{\mu^o}{\eta} \quad 2.19$$

The energy variation becomes:

$$\Delta E = -\frac{\mu^2}{2\eta} \quad 2.20$$

Electrophilic power is therefore defined as energy stabilization due to charge transfer:

$$\omega = \frac{\mu^2}{2\eta} \quad 2.21$$

It is only if the two molecules are actually electrophilic that the comparison between two electrophilic powers makes sense. Indeed, when the chemical potential is positive, which is

common for anions, the charge acquired is negative, which means that these substances tend to drop their supernumerary electrons. To generalize this concept, it would therefore be logical to use the acquired charge rather than energy stabilization. However, much research has been carried out based on this concept.

2.9.2.5.4 Local quantities

When studying the reactivity of molecules based on global indices, deduced from electronic properties, it is necessary to rely on local indices to study selectivity. Electron density is the first local index of reactivity which represents the first derivative of energy with respect to the external potential. It is undeniable that electron density is the best indicator of purely electrostatic interactions, with a value of 38.39. On the other hand, for a covalent bond with charge transfer between the two reactants, the Fukui function is undoubtedly the best indicator.

2.9.2.5.4.1 Fukui functions

The Fukui function can be defined as the reaction of the electron density to the variation in the number of electrons. According to Scharwtz's mathematical theorem, it is necessary that the second cross derivatives of a function be equal. We can also define the Fukui function as the response of the electronic chemical potential to the variation of the external potential at a point.

$$f(r) = \left(\frac{\partial \rho(r)}{\partial N}\right)_{v(r)} = \left(\frac{\delta \mu}{\delta v(r)}\right)_{N} \quad 2.22$$

The Fukui function has the characteristic of being normalized. Indeed, we can deduce from equation (2.5) that:

$$\int f(r)dr = 1 \quad 2.23$$

It is generally accepted that this function is positive. Thus, the numerical values of the Fukui function are framed:

$$0 \leq f(r) \leq 1 \quad 2.24$$

On a purely chemical level, it is necessary to distinguish the response of the electron density when adding or removing electrons, that is to say electrophilic attacks from nucleophilic attacks. This is the reason why two different functions of Fukui have been suggested:

$$f^{+}(r) = \left(\frac{\partial \rho(r)}{\partial N}\right)^{+}_{v(r)} \quad 2.25$$

$$f^{-}(r) = \left(\frac{\partial \rho(r)}{\partial N}\right)^{-}_{v(r)} \quad 2.26$$

Significant values of the Fukui function reveal the most reactive atomic or molecular sites, that is, where the variation in electron density will be most significant when the number of electrons is changed.

We can also define in an analogous way:

$$f^{+}(r) = \left(\frac{\partial \mu}{\partial N}\right)_{N}^{+} \quad 2.27$$

$$f^{-}(r) = \left(\frac{\partial \mu}{\partial N}\right)_{N}^{-} \quad 2.28$$

The two approaches are entirely coherent, and account for complementary physical phenomena. Regarding the second definition, using equation 2.8 leads to the following expressions:

$$f^{+}(r) = 1 + \frac{\delta}{\delta v(r)}\left(\frac{\delta F[\rho(r)]}{\delta \rho(r)}\right)_{N}^{+} \quad 2.29$$

$$f^{-}(r) = 1 + \frac{\delta}{\delta v(r)}\left(\frac{\delta F[\rho(r)]}{\delta \rho(r)}\right)_{N}^{-} \quad 2.30$$

Where $\left(\frac{\delta F[\rho(r)]}{\delta \rho(r)}\right)$corresponds to the interaction potential between the electrons. Therefore, significant values of the Fukui function will be sites where the variation in the external potential results in an optimal variation in the repulsion per electron. For example, if the external potential drops at a point, the function $f^{-}(r)$ will be close to 1, if the inter-electronic repulsion potential drops considerably at that point. On the other hand, if the external potential increases at a point, the function $f^{+}(r)$ will be close to 1 if the interelectronic repulsion potential increases slightly at this point. To our knowledge, this second definition has never been used to calculate Fukui functions.

On the other hand, in the majority of chemical selectivity studies, the Fukui functions are calculated using the finite difference approximation applied to equations (2.29) and (2.30). This process leads to serious errors, because relaxation phenomena are not taken into consideration. In addition, this method depends on the results of the quantum model employed.

$$f^{+}(r) = \rho_{N_o+1}(r) - \rho_{N_o}(r) \approx \rho_{EV} 2.31$$

$$f^{-}(r) = \rho_{N_o}(r) - \rho_{N_o-1}(r) \approx \rho_{HO} \quad 2.31$$

In this estimation, the values of the Fukui functions $f^{+}(r)$ and $f^{-}(r)$are equivalent to the electron densities of the HO and BV orbitals. Frontier orbital theory uses descriptors that are second-order derivatives of the energy functional.

2.9.2.5.4.1 Local hardness and softness

While hard and soft are global parameters, experimentalists have sometimes used the terms hard and soft in relation to atoms or functional groups of a molecule to rationalize their reactivity. So to derive a local analogue to flabbiness, Parr and Yang proposed:

$$s(r) = \left(\frac{\partial \rho(r)}{\partial \mu}\right)_{v(r)} \quad 2.32$$

The correlation with the Fukui function is direct, when we apply the rule of chain derivatives:

$$s(r) = \left(\frac{\partial \rho(r)}{\partial N}\right)_{v(r)} \left(\frac{\partial N}{\partial \mu}\right)_{v(r)} = f(r)xS \quad 2.33$$

Thanks to local softness, it is possible to collect local information on the selection of a molecular site as well as an overall reactivity of the molecule. This description system is therefore perfect for evaluating the selectivity of various molecules. The majority of molecular selectivity analyzes use the local softness molecule.

2.9.2.5.5 Principle of reactivity

As mentioned previously, the Electron Density Functional Theory has helped to bring together various descriptors. In this extremely fruitful theoretical context, various principles have also been highlighted.

2.9.2.5.5 .1 Sanderson's principle of equalization of electronegativities

Following the proposal of his own electronegativity scale, which is based on the ratio between the radius of the electron density of an atom and the radius of the electron density of the corresponding rare gas, Sanderson puts forward a principle of complete equalization of electronegativities atomics in the molecule:

"When two or more atoms of different electronegativities bond to form a molecule, there is an equalization of the electronegativities within the compound."

This principle will be demonstrated autonomously by Politzer and Weinstein, as well as by Donnelly and Parr using a distinct formalism. The illustration below is taken from the work by Parr and Yang.

The molecule AB consists of two atoms or groups of atoms A and B which bond. The total energy of the system is the sum of the energy of each interacting fragment during the reaction.

$$E_I = E_A + E_B \quad 2.34$$

The optimization of energy under the effect of electron exchange leads to the relation:

$$\left(\frac{\partial E}{\partial N}\right)_{v(r)} = \left(\frac{\partial E_A}{\partial N}\right)_{v(r)} + \left(\frac{\partial E_B}{\partial N}\right)_{v(r)} = 0 \qquad 2.35$$

As the number of electrons is constant, the electron between fragments A and B can be written:

$$\partial N = \partial N_A = -\partial N_B \qquad 2.37$$

And so:

$$\mu_A^f = \mu_B^f \qquad 2.34$$

In this way, thanks to the exchange of electrons, the electronegativities of the various fragments become closer. The charge transfer between the two fragments can therefore be calculated, from this principle, without taking into account the variation in the external potential. This results in the equation:

$$\Delta N_A = \frac{(\mu_B^o - \mu_A^o)}{(\eta_A + \eta_B)} \qquad 2.35$$

Calculation of the partial charges of atoms inside molecules can be carried out through the equalization of chemical potentials, without requiring population analysis.

Since, the chemical potential is the same as an electrostatic potential and hardness corresponds to the resistance to charge transfer, equation (2.40) can be considered the molecular equivalent of Ohm's law. Furthermore, this equation confirms the intuitive idea that the dipole moment is proportional to the difference in electronegativity. Thus, it is possible to evaluate the distribution of partial charges inside a molecule using the principle of equalization of electronegativities, as well as to estimate the overall electronic properties and binding energies.

2.9.2.5.5.2 The principle of hard acids and soft bases (HSAB)

Different research into the reactions between Lewis acids and bases led RG Pearson to define substances into two categories, which were ultimately called hard or soft. The presentation of the definition of hardness recalled the physicochemical properties of hard and soft substances. According to the HSAB principle, substances belonging to the same category tend to react with each other. For example, in this reaction, recombination tends to connect the hard atoms, namely calcium and oxygen, and the two "soft" atoms, namely sulfur and copper.

$$CaS(g) + CuO(g) \rightarrow CaO(g) + CuS(g) \quad \Delta_R H^o = -125.4 KJ.mol^{-1}$$

This principle has been used by many experimental studies to study the direction of chemical or electrochemical reactions. Theoretically, it was quickly thought that the chemical bonds between

hard substances are mainly ionic, while the chemical bonds between soft substances are rather covalent. However, the only comprehensive study that seeks to understand the physical principles underlying the HSAB principle, "is barely out."

2.9.2.5.6 Kinetic theory of chemical reactivity

Since the early 1930s, various theories of reactivity have been developed.
Chemistry has been taken into account. To determine the local electrostatic field, a first method was used, the electron density amplitude in order to analyze the reactivity between two molecules as an electrostatic phenomenon. Another method employed the calculation of localization energy, that is, the energy required to force electrons to "pitch" onto a specific molecular site. In the early 1950s and 1960s, it was recognized that frontier orbitals, that is, those with the highest occupied energy and those with the lowest vacant energy, play an essential role. Thanks to this original approach which is based on molecular orbitals, Fukui and Hoffmann received the 1981 Nobel Prize in Chemistry.

Using a perturbative approach, Klopman divided chemical reactions into two different categories: those that are controlled by the local electrostatic potential and called "charge control", and those that are controlled by the overlap between the frontier orbitals of the two compounds and called “border control”.
Chemical reactivity has discovered a very promising theoretical framework in the paradigm of conceptual DFT.

2.9.2.5.7 Charge transfer between two compounds.

It is essential to be able to calculate the charge transfer between two atoms or two molecular fragments, because this allows the partial charges of the atoms within a molecule to be evaluated without resorting to population analysis. According to Sanderson's principle, equation (2.40) assumes that the external potential remains constant. This equation can be supplemented by a potential-dependent component. We only have to consider the effect of the external potential variation on the chemical potential.

2.9.2.5.8 Interaction energy

A chemical system must pass through an activation barrier, primarily electronic repulsion between reactants, in order to react. Furthermore, during the chemical reaction, some bonds are broken and others are generated. This process also requires an amount of energy. For

kinetically controlled reactions, the most stable transition state should result in the main product. All interactions likely to reduce the activation energy, that is to say stabilize the transition state, must therefore be evaluated, at least qualitatively.

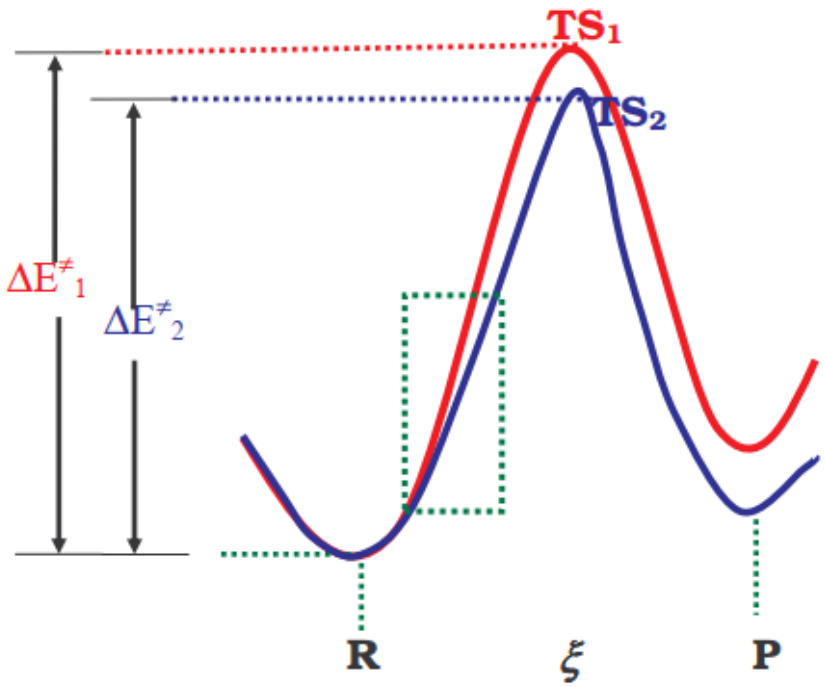

Figure 2.14: Evolution of the interaction potential energy for two different reaction paths.

These interactions are evaluated at the beginning of the reaction in most kinetic theories of reactivity and selectivity, why it is essential to be able to calculate the energetic interaction between two molecular fragments. In Figure 2.14, we establish the slope of the energy versus the degree of progress at the start of the reaction. If the reaction is under kinetic control, the lowest energy slope, that is to say the one which results in the least destabilizing interactions, results in the most stable transition state, which results in the majority product.

In the space [N,ν(r)] represented in figure 2.13, the variation of the electronic energy of a molecular fragment A can be written to the second order:

$$\Delta E_A = \mu_A^0 \Delta N_A + \int \rho_A(r)\Delta v_A(r)dr + \frac{1}{2!}[\eta_A \Delta N_A^2 + 2\Delta N_A \int f_A(r)\Delta v_A(r)dr + \iint x_A(r,r')\Delta v_A(r)\Delta v_A(r')drdr'] \quad 2.37$$

The external potential $\Delta v\ (r)$is the variation in potential felt by fragment A at point r. We can divide this variation into two parts: the variation caused by the movement of the nuclei of fragment A and the variation caused by the potential created in r by the presence of fragment B. The contribution of the nuclei and that of the electrons of fragment B is to both present in this last variation.

It is necessary to add the repulsion between the nuclei of the two fragments $\Delta v_{nn}$to evaluate the total energy variation of the AB system.

$$\Delta E = \Delta E_A + \Delta E_B + \Delta v_{nn} \quad 2.38$$

Since the number of electrons in the AB system is constant, the energy fluctuation is constant.

It is possible to divide it into three main contributions:

i. An electrostatic energy field,
ii. A covalent interaction energy,
iii. A term that refers to polarization.

$$\Delta E = \Delta E_{\text{electrostatique}} + \Delta E_{\text{transfert de charge}} + \Delta E_{\text{polarisation}} \quad 2.39$$

Depending on the descriptors derived from the energy, these different contributions can be written:

$$\Delta E_{\text{electrostatique}} = \int \rho_A(r) v_A(r) dr + \int \rho_B(r) \Delta v_B(r) dr + \Delta v_{nn} \quad 2.40$$

$$\Delta E_{\text{transfert de charge}} = -(\eta_A + \eta_B)\Delta N^2 = -\frac{\left[(\mu_B^0 - \mu_A^0) + \int f_B(r)\Delta v_B(r)dr - \int f_A(r)\Delta v_A(r)dr\right]^2}{2(\eta_A + \eta_B)} \quad 2.41$$

$$\Delta E_{\text{polarisation}} = \frac{1}{2}\left[\iint x_A(r,r')\Delta v_A(r)\Delta v_A(r')drdr' + \iint x_B(r,r')\Delta v_B(r)\Delta v_B(r')drdr'\right] \quad 2.42$$

We can notice that among all the interaction terms, the one which corresponds to charge transfer is always negative. Thus, it is a term that ensures the stability of the system. From 1978, Huheey 100 noted that charge transfer resulting in greater stabilization as the hardness of each reactant was lower. This explains why soft reactants prefer to react with soft reactants. The selectivity of the reaction is influenced by the Fukui functions when this term is important. In contrast, when the reactants are rigid, this concept of charge transfer becomes insignificant compared to the electrostatic concept. The selectivity of the reaction is influenced by the electron density when the electrostatic term is dominant. These equations allow us to obtain the same conclusions as

those of Klopman. In this way, the local selectivity index varies depending on the hardness of the reagents.

The importance of the polarization term depends on the presence of a polarizing species and a polarizable species, that is to say a hard species and a soft species. As we have seen, these exchanges are not the most favorable. On the other hand, this last interaction offers the possibility to discuss the ionic nature of a covalent bond, or the covalent nature of an ionic bond, that is, to rationalize the Fajan rules.

2.9.3 Evaluation of adsorption performance by Monte Carlo molecular simulation

2.9.3.1 Computational study

Our study focused on the Materials Studio application, which integrates numerous molecular simulation modules using the Monte Carlo method. The Metropolis method or configurational bias is used for sampling an adequate physical distribution (which is in reality that of the canonical ensemble). The Sorption module (which evaluates the thermodynamic characteristics of small molecules in a matrix) and Amorphous Cell (which creates periodic simulation cells) are used to accomplish this. Some other modules leverage simulated annealing and related techniques to improve a function, such as predicting crystal structure from molecular structure (Polymorph Predictor), predicting crystal structure from X-ray diffraction data on powder (Powder Solve) and the search for preferential sites for adsorption (Adsorption Locator).

2.9.3.2 Location of an adsorption

The adsorption localizer mimics a substrate containing an adsorbate or mixture of adsorbates of constant composition. The adsorption identification device is specially designed to study systems particularly to locate low energy adsorption sites on both periodic and non-periodic substrates, or to study preferred adsorptions of mixtures of adsorbed components. For example, the adsorption locator includes a substrate structure, such as a metal surface, as well as the structure of one or more adsorbed molecules (Akkermans, Spenley, & Robertson, 2013).

The simulation method is similar to Sorption, as it performs MC simulation of a substrate-adsorbate system. However, in the Adsorption Locator, the temperature is changed externally in order to simulate annealing of the system. The temperature is gradually increased until a high level is reached, then it is gradually decreased until the final level is reached, allowing the system to stabilize in a state of minimum energy. The process can be repeated several times

to allow the system to explore even lower energy states. The result of the Adsorption Locator consists of a lookup table that groups together all the lowest energy configurations found during the selection. They can be treated in more detail, by integrating them into quantum mechanical optimization. The energy distribution can be calculated as part of an adsorption calculation. Figure 2.15 illustrates an example of adsorption of methylene blue on the surface of zeolite 4A (001).

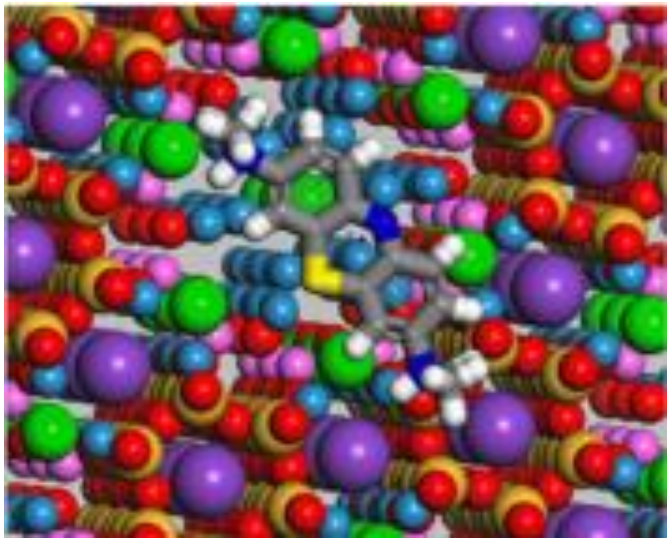

Figure 2.15: Adsorption of methylene blue on the surface of zeolite 4A (001).

2.9.3.3 Application of Adsorption Location

The Adsorption Locator module is relatively new to Materials Studio, and it has already been used in many cases to locate bonds and study their energy, such as for organic molecules on metal surfaces and nanoparticles.

Khnifira et al. (2020), used the Adsorption Locator to determine the adsorption behavior of the protonated forms of methylene blue on the surface of zeolite 4A (001) in the aqueous phase. They found low-energy adsorption sites that allow classifying protonated methylene blue molecules based on their adsorption efficiencies using adsorption and binding energies (Khnifira et al., 2022). Khnifira et al. (2020) used the same module to adsorb HF and SiF4 on the carbon graphite (111) surface (Khnifira et al., 2020).

A similar study was carried out by Musa et al. (2012), to determine the effectiveness of phthalazine derivatives in preventing corrosion of light steel. The quantum chemical calculation was carried out on the low energy adsorption sites, identified by Adsorption Locator, which made

it possible to show that phthalazone is a very effective inhibitor on the surface of Fe_2O_3 (110) (Musa, Jalgham, & Mohamad, 2012).

Liang et al. (2011), used the Adsorption Locator in their study on the formation of ZnO by biomolecules. They studied the adsorption of peptides on the (0001) and (10 $\bar{1}$0) planes of ZnO to study their ability to handle the relative growth of these surfaces (Liang, Deschaume, Patwardhan, & Perry, 2011).

CHAPTER THREE

MATERIALS AND METHODS

3.1 The materials studied

3.1.1 Origin of raw kaolins

The raw kaolins used in this study came from Fotouni. Fotouni is a village located in the Haut-Nkam department in western Cameroon (5°, 19°, 35° north latitude and 10°, 13°, 34° east longitude) (Figure 3.1a). Figure 3.1 provides information on the clay sites harvested.

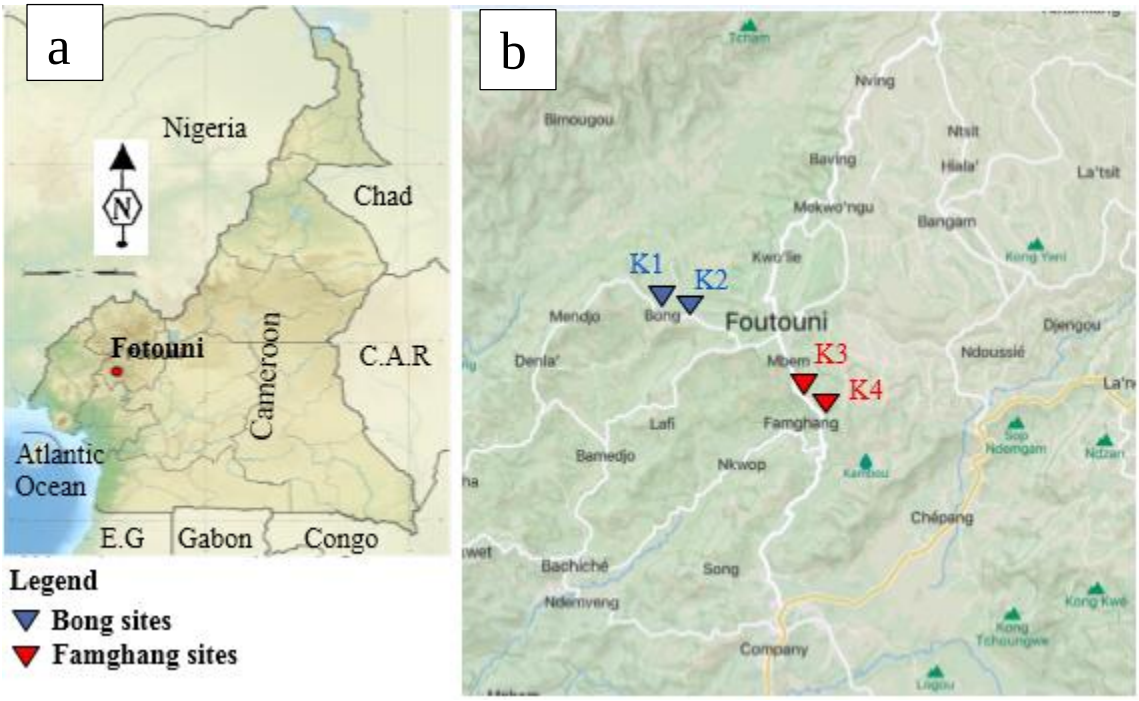

Figure 3.1: Location of Fotouni on the map of Cameroon (a), geographical map of the Fotouni clay deposit showing the localities of the samples studied (b).

In order to take into account, the varieties of materials observed, four samples were taken, mainly from long embankments of the road trench, on two sites located in the locality of Bong approximately 2 km to the South-West (samples K1 and K2) (Figure 3.2b) and the other located in the locality of Famghamg approximately 3 km South-East (samples K3 and K4) (Figure 3.2b).

The samples collected were then crushed, ground and then dried in the open air for 72 hours.

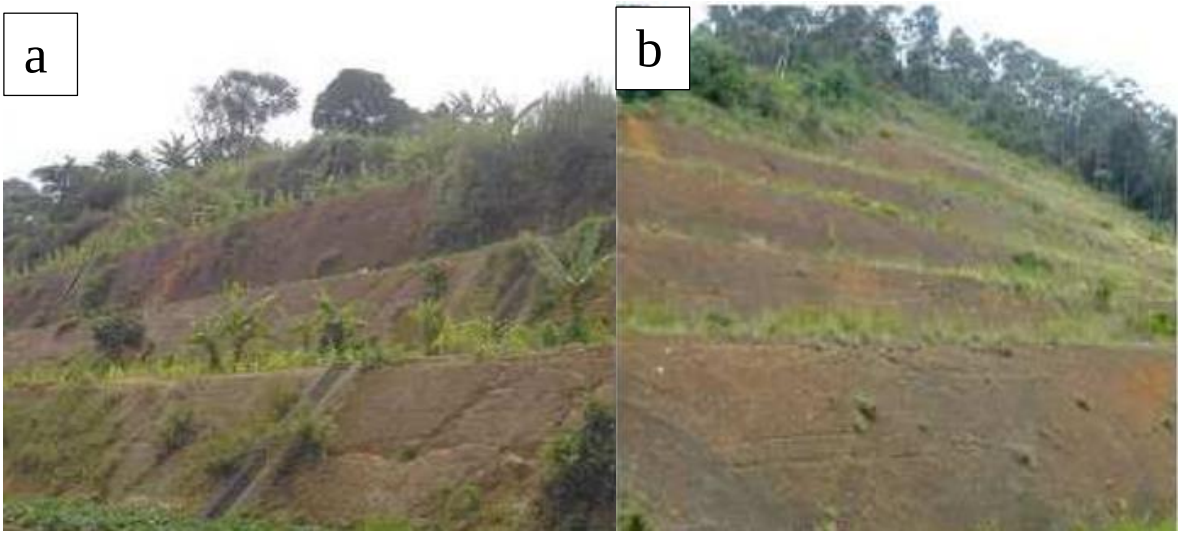

Figure 3.2: Overviews of the Bong (a) and Famghamg (b) sampling sites.

3.1.2 General information on the species *Tabernaemontana penduliflora*.

3.1.2.1 *Description of the plant*

Tabernaemontana penduliflora (TP) is a shrub or small tree 6-7 m high, available in Nigeria, Gabon, DR Congo, Central African Republic and Cameroon. In Cameroon, it is present in the Central, Eastern, Western and Southern regions. In Cameroon it is known as “Etoé” in Ewondo (Cameroonian ethnia) and releases a milky juice from all parts when cut. It is harvested from the wild for local use as medicine and a source of wood and fiber. The flowers are white, greenish or pink in sessile and subumbellate inflorescences in the high forest (Roland et al., 2022).

3.1.2.2 *Origin of* Tabernaemontana penduliflora *leaves*

The TP leaves were collected in the Central Cameroon region (GPS coordinates: Latitude 3'53'31'N, Longitude 11'13' 49"E) in February 2023 and taxonomically identified by M. Victor Nana (Botanist at the National Herbarium, Yaoundé, Cameroon). A control specimen (No. 43438/HNC) was deposited at the National Herbarium in Yaoundé, Cameroon. Figure 3.3 shows the TP leaves at collection.

Figure 3.3: Leaves of *Tabernaemontana penduliflora.*

3.1.2.3 *Composition of* Tabernaemontana penduliflora

Tabernaemontana penduliflora is a common plant found mainly in the central and southern region of Cameroon. Previous chemical work carried out on the trunk bark and leaves revealed the presence of indole alkaloids such as akuammidine, yoacangine. voacamine, voacorme anhydroyobasine-diol and flavonoids, which are the main constituents of this plant (Bitombo et al., 2021) .

3.2 Synthesis methods

3.2.1 Hydrothermal method

Hydrothermal synthesis is a method generally used for the synthesis of zeolites. It consists of the crystallization of a reaction mixture called hydrogel or more simply gel, containing a source of aluminum (Kaolin or Aluminum hydroxide), a source of silicon (Kaolin or silica gel), a mineralizing agent (Sodium hydroxide), and a solvent (demineralized water) allowing the solubilization of the structuring species (alkaline cations). The mixture obtained, after homogenization at room temperature, is brought to the crystallization temperature for a few hours.

3.2.2 Co-precipitation method

Co-precipitation is a simple method for synthesizing bio-magnetite nanoparticles. It is based on the joint precipitation in an aqueous medium of ferrous and ferric ions by adding a base (Ammonia or Sodium hydroxide) reducing and stabilizing agent (plant extract, algae, etc.). This method has the advantage of being easy to implement, even on a large scale, and allows the synthesis of nanoparticles with a quasi-spherical shape and sizes ranging from 10 to 100 nm directly in aqueous solution.

The ferrous Fe^{2+} and ferric Fe^{3+} cations are stable in an acidic medium and precipitate when the basicity of the medium increases to form iron oxide according to equation (3.1).

$$Fe^{2+}_{(aq)} + 2Fe^{3+}_{(aq)} + 8OH^{-}_{(aq)} \xrightarrow[\Delta]{} Fe_3O_{4\,(s)} + 4H_2O_{\,(l)} \qquad 3.1$$

3.2.3 Chemical reagents

All chemical reagents of analytical quality were used without prior purification for carrying out the different experiments and are presented in Table 3.1

Table 3.1: List of chemicals and solvents.

Names	Formulas	Purities (%)	Meker
Sodium hydroxide	NaOH	99.9	Sigma Aldrich
Iron(II) chloride	$FeCl_2.4H_2O$	98	Sigma Aldrich
Iron(III) chloride	$FeCl_3.6H_2O$	98	Sigma Aldrich
Sodium aluminum	$Na_2Al_2O_4$	98	Sigma Aldrich
Deionized water	H_2O	99	ACE-FUELS Laboratory
Ethanol,	EtOH	99	Sigma Aldrich

3.3 Synthesis protocol

3.3.1 Synthesis of zeolite 4A from kaolin

The synthesis was carried out in two stages, the first consisted of the transformation of raw kaolin into metakaolin by heat treatment, to facilitate the crystallization of the zeolite during the hydrothermal process; and the second step consisted of the formation of zeolite crystals.

3.3.1.1 *Calcination of raw kaolin*

The raw kaolin was crushed and reduced to powder before being sieved using a laboratory mesh sieve (75 µm aperture), and suspended with 500 mL of deionized water while stirring at room temperature. For 2 hours, the surface water and kaolin were separated by decantation and then dried for approximately 12 hours at 100 °C. The kaolin was calcined at a 900°C for 3 hours with a heating rate of 5°C/min. This process contributes to the conversion of non-reactive and highly stable kaolin into a more reactive, less stable and easily soluble metakaolin in the presence of basic solutions. Metakaolin is the phase required for the synthesis of zeolites. Equation (3.2) describes the transformation of kaolin into metakaolin.

$$Al_2Si_2O_5(OH)_4(\text{kaolin}) \rightarrow Al_2Si_2O_7(\text{metakaolin}) + 2H_2O \quad 3.2$$

The metakaolin obtained was crushed and preserved away from humidity in order to use it as a source of aluminosilicate for the synthesis of zeolite 4A.

3.3.1.2 *Synthesis of zeolite 4A by the hydrothermal method*

For the synthesis of zeolite 4A, the optimal parameters, namely crystallization time, concentration and mass, were chosen according to the literature (Mgbemere et al., 2019). Zeolite 4A was synthesized by the hydrothermal method. 4M sodium hydroxide solution was added to 6 g of metakaolin under stirring at 60 ° C at 600 rpm for about 3 hours, and then 2 g of sodium aluminum was added to adjust the amount of sodium, as shown by equation (3.3). The resulting gel was transferred to a 60 ml Teflon autoclave for crystallization at 90°C for 5 hours. The product formed was recovered, filtered and washed several times until a filtrate with a neutral pH was obtained, then dried at 90°C for 24 hours.

$$6Al_2Si_2O_7(\text{metakaolin}) + H_2O \xrightarrow{Na_2Al_2O_4} Na_{12}(AlO_2)_{12}(SiO_2)_{12}.27H_2O\ (\text{zeolite 4A}) + 6H_2O$$

3.3.2 Preparation of magnetite nanoparticles from plant extracts

3.3.2.1 *Preparation of* **Terbernaemontana penduliflora** *extract*

The leaf samples of *Terbernaemontana penduliflora* (TP) were cleaned, dried in an oven at 60 °C for 12 hours, and then ground into a fine powder. After introducing 100 ml of deionized water into 250 ml beaker containing 10 g of dried powder, the mixture was heated at 80°C for 60 minutes until the solution turned dark green. Whatman N°1 filter paper was used to filter the

mixture once after cooling to room temperature. The filtrate obtained, denoted TP, was stored at -4°C.

3.3.2.2 *Synthesis of bio-magnetite nanoparticles*

Bio-magnetite nanoparticles (Fe_3O_4) were synthesized by the co-precipitation method. In 100 mL of deionized water, 6 grams of $FeCl_3.6H_2O$and 3 grams of $FeCl_2.4H_2O$ were dissolved in a molar ratio of 2:1. The mixture was then stirred for 30 min at room temperature to ensure complete dissolution. After gradually adding 40 ml of the TP extract to the mixture, it was vigorously stirred for 30 minutes. Using 0.1 M NaOH solution, the pH was brought to between 8 and 9, and the mixture was then vigorously stirred at 80°C. After 3 hours, the color changed to black, indicating that TP- nanoparticles Fe_3O_4 were formed. After centrifugation of the black solution during four minutes at 2000 rpm, the black solid was collected and cleaned two and three times with a water-ethanol mixture. After wards being thus cleaned, the nanoparticles were dried in an oven for 24 hours at 80°C, then stored in an airtight bottle for characterization.

3.3.3 Synthesis of bio-magnetite nano composites

The bio-magnetite@zeolite 4A nanocomposites were developed by the coating method (Cao, Sun, Wang, Shen, & Dai, 2020). During the synthesis of zeolite 4A, at the crystallization stage, the temperature of the system was increased to 90 °C, then the nanoparticles $TP-Fe_3O_4$were added into the reaction solution and the mixture was stirred for 3 hours. Then, the stirring speed was controlled at 500 rpm. The product obtained was washed and dried in an oven for 24 hours to obtain the TP- Fe_3O_4@zeolite 4A nanocomposite.

To study the effect of TP-Fe_3O_4 nanoparticle charge on the adsorption and recovery capacity of as-synthesized TP-Fe_3O_4@zeolite 4A nanocomposites, a series of magnetite nanocomosite (MZ-2, MZ-4, MZ-6) were prepared by adding different mass of TP-Fe_3O_4 . 2%, 4% and 6% by weight, representing the expected loading percentages for TP-Fe_3O_4 in the TP-Fe_3O_4@zeolite 4A nanocomposite samples . Using equation (3.4), the mass percentage of TP-Fe_3O_4 was determined.

$$m_{TP-Fe_3O_4}(\%) = \frac{m_{TP-Fe_3O_4}}{m_{TP-Fe_3O_4}+m_{zeolite\ 4A}} \times 100 \qquad 3.4$$

where the masses in g of TP-$Fe_3O_4$and zeolite 4A are denoted by $m_{TP\text{-}Fe3O4}$ and $m_{Zeolite\ 4A}$, respectively.

3.4 Characterization of prepared materials

3.4.1 Physicochemical characterization techniques

Details of the characterization and measurements of the synthesized materials were obtained using the following analytical methods:

3.4.1.1 *Fourier transform infrared spectroscopy*

Fourier Transform Infrared spectroscopy (FT-IR) is a technique based on radiation-matter interactions, which allow the determination of the functional groups component the sample to be analyzed. The principle is based on the irradiation of a sample with infrared radiation. The recorded signal represents the sum of the intensities of the fringes for each frequency, which results in a curve called the interferogram. The spectra of the different samples were recorded between 400cm^{-1} and $4000\text{cm}^{-1}$with a resolution of 4cm^{-1}on a Bruker AXS spectrometer, Germany. The transmission spectra of the samples were recorded using KBr. Approximately 1 to 2% of the previously dried sample was mixed with dry KBr and the whole is crushed in a mortar then the sample is transferred to a hydraulic press and a pellet is obtained. The pellet thus obtained, having a transparent and homogeneous appearance, is inserted into the sample holder of the device for analysis.

3.4.1.2 *X-ray Diffraction*

X-ray diffraction (XRD) is a widely used technique for identifying the nature of the crystalline phases present in a sample, as well as their degree of crystallinity and particle size. The principle of this technique consists of bombarding the sample with X-rays and measuring the intensity of the X-rays which are diffracted according to the orientation of space. The diffraction peaks can be determined by Bragg's law represented by the following equation (3.5):

$$2d_{hkl}\sin\theta = n\lambda \qquad 3.5$$

Where, d_{hkl} is the distance between two crystallographic planes; θ is the angle of reflection or Bragg angle; not is the reflection order (integer) and λ is the X-ray wavelength.

The crystallographic planes being identified by the Miller indices (h.k.l), the diffraction peaks can be indexed according to these indices. On the diffractogram, the successive peaks obtained correspond to very precise angles.

The XRD analysis of the samples was carried out on disoriented powder using a Bruker D8-Advance type diffractometer, operating by reflection of $K\alpha_1$ radiation from copper (λ =1.5418Å), under a voltage of acceleration of 40 kV and an intensity of 30 mA in the angular interval [5-70°] in 2θ.

3.4.1.3 *Scanning electron microscopy*

The dimensioned adsorbent materials were examined using PHILLIPS XL0S-FEG brand scanning electron microscopy (SEM) with an accelerating voltage of 10kV. It is an imaging technique that produces high-resolution images of the surface of a sample and provides information on the morphology of the crystals as well as their size. The principle of this technique is based on an electron-matter interaction between an electron beam and the sample surface of an analyzer which emits different types of electrons, such as secondary and retro diffused electrons.

The fine particles of the samples were placed (metalized) on a carbon plate, then sputtered with a layer of Gold to increase their conductivity, before SEM analysis.

3.4.1.4 *Thermogravimetric analysis (TGA)*

The principle of thermogravimetric analysis is based on the measurement of mass loss as a function of temperature heating. Several factors intervene to control the loss of mass, note for example, the physicochemical properties of the materials studied and the operating conditions. During handling, there are several reactions that occur at different temperatures as materials decompose (Meng, Wang, Pei, Guo, & Liu, 2017). The thermogravimetric analysis (TGA) profile of the different samples clearly gives an approximation of the mass loss as a function of temperature and which is due to the release of water bound to the surface and volatile materials. TGA of the samples was carried out by a STD-Q600 thermogravimetric analyzer (TA Instruments, New Castle, USA). Approximately 30 mg of sample was subjected to carbonization under flow at N_2 a flow rate of 50 mL/min, from 25 to 800°C with a temperature rise of 10°C/min.

3.4.1.5 *Nitrogen physisorption analysis*

The specific surface area was determined from the nitrogen adsorption isotherm at relative pressures between 0 and 1 using the BET (Brunauer-EmmettTeller) method. The BET equation is given by the following relationship:

$$\frac{P}{V(P_o-P)} = \frac{1}{V_m C} + \frac{(C-1)}{V_m C}\left(\frac{P}{P_o}\right) \quad 3.6$$

This equation is called the BET linear transform of the adsorption isotherm. The values of Vm and *C* are obtained respectively from the slope and the ordinate at the origin of the line $\frac{P}{V(P_o-P)} = f\left(\frac{P}{P_o}\right)$

Where, V (cm^3/g) is the volume of gas adsorbed at standard pressure and temperature, Vm(cm^3/g) the volume of gas necessary for filling the surface of a monolayer, and *C* is the BET constant relating to the energy of adsorption in the first adsorbed layer and its value is an indication of the magnitude of the adsorbent-adsorbate interactions. If the bulk area of a gas molecule (A_{gas}) is known (16.2 $Å^2$for nitrogen), the specific surface area of the solid is obtained using the following relationship:

$$S_{BET} = \frac{V_m N_A A_{gas}}{V_m m} \quad 3.7$$

Where, N_A(mol^{-1}) is Avogadro's number; Vm (m^3/mol) the molar volume of the gas; m (kg) the mass of the solid sample. The total pore volume is estimated as the volume of N_2 adsorbed at high relative pressure (0.99). The particle size distribution of the adsorbents is determined using the Dubinin-Astakhov model (Ferdinand et al., 2022). The porosity of our different materials was determined by the liquid nitrogen adsorption-desorption method (N_2) at 77 K using a specific surface area analyzer from Novawin Quantachome (USA). Samples were degassed at 300°C for 10 hours before analysis to remove adsorbed moisture or any other impurities bound to the sample surface.

3.4.2 Determination of the pH of the point of zero charge

The pH of the point of zero charges (pHpzc) of an adsorbent material is a very important characteristic, because it determines the pH at which the net surface charge is zero. This parameter is very important in adsorption phenomena, especially when electrostatic forces are involved in the mechanisms. It was determined by introducing 0.2 g of previously dried adsorbent

and 50 mL of a decimolar solution of NaCl into different Erlenmeyer flasks. The pH of the solutions is adjusted between 2 and 10 (pHi) using a pH meter (Insmark IS128, China) through decimolar solutions of NaOH and HCl, then stirred for 48 hours at room temperature. (Sedik et al., 2022). At the end of stirring, the solutions are filtered and the pH of the filtrates are measured (pH_f). The difference between the initial and final pH ($\Delta pH = pH_f - pH_i$) is plotted against pHi. The point of intersection between the curve and the abscissa axis corresponds to the pHpzc (Yang et al., 2022).

3.5 Adsorption of ciprofloxacin

Using a batch experimental technique, the ability of adsorbent materials to remove ciprofloxacin (CIP) was demonstrated. The effects of adsorbent dosage, initial adsorbate concentration, solution pH, contact time, and temperature were determined by separate experiments. The adsorption mechanism was determined by modeling the experimental data with kinetic and isothermal models. All adsorption experiments were carried out in triplicate and average values were taken. Additionally, all solutions were prepared in deonized water.

3.5.1 Batch adsorption procedure

For the adsorption process, a stock solution containing 500 ppm ciprofloxacin (CIP) in deonized water was prepared. The adsorption tests were carried out on the different adsorbents prepared in order to compare their respective adsorption capacities.

The optimal adsorption conditions were found by examining the parameters of the adsorption process, such as initial CIP concentration (10 to 100 ppm), solution pH (4 to 10), contact time (10 at 120 min) and the adsorbent mass (10 to 50 mg). These parameter ranges were chosen based on adsorption studies (zero charge point, literature and preliminary tests). The pH of the polluted solution was adjusted using 0.1 M HCl or 0.1 M NaOH solution. The magnetic stirrer was used to stir the solution in a 500 ml Erlenmeyer flask at 200 rpm/min at room temperature. After stirring, the solutions are filtered using Whattman No. 1 paper for zeolite adsorbents, the magnetite nanocomposites were recovered from the solution using an external magnetic field (magnet) and the remaining CIP concentration was determined by the UV-Visible spectrophotometer (UV1610, China) at the maximum wavelength of 276 nm (Wei et al., 2023). Standard CIP solutions were thus prepared and then used to establish the calibration curve.

Equations (3.8) and (3.9) were used to calculate the adsorption capacity (q_e) and removal efficiency (R)of the CIP), respectively.

$$q_e = \frac{(C_o - C_e) \times V}{m} \quad 3.8$$

$$R\ (\%) = (1 \times \frac{C_e}{C_o}) \times 100 \quad 3.9$$

Where C_o, C_eV and m represent the initial pollutant concentration (ppm), equilibrium pollutant concentration (ppm), solution volume (L) and adsorbent mass (g), respectively.

3.5.2 Study of adsorption isotherms

Table 3.3 gives the different linear forms of the equilibrium isotherm models used in this work. The Langmuir isotherm is based on the assumptions that: Each adsorption site can only attach a single entity, the adsorbed entities are bound to the surface at specific and localized sites, the adsorption energy of an entity is the same for all sites, adsorption takes place in a monolayer, there is no interaction between the adsorbed molecules (Nsami & Mbadcam, 2013). The Freundlich isotherm is based on an empirical equation reflecting a variation of energies with the quantity adsorbed. It assumes that adsorption takes place on a heterogeneous surface at different adsorption energies (Nsami & Mbadcam, 2013).

Tableau 3.3: Isotherm models used in the present work.

Models	Linear shapes	Settings	References
Langmuir	$\frac{1}{q_e} = \frac{1}{K_L q_{max}} \times \frac{1}{C_e} + \frac{1}{q_{max}}$ (3.10)	q_{max}=maximum adsorption capacity (mg/g). K_L=Langmuir isthermal constant (L/mg).	(Ho & McKay, 1998)
Freundlich	$q_e = \ln K_f + \frac{1}{n} \ln C_e$ (3.11)	K_f=Freundlich constant. $1/n$=adsorption intensity	(Ho & McKay, 1998)

3.5.3 Study of adsorption kinetics

The kinetic study of adsorption processes provides information relating to the adsorption mechanism and the transfer of solute from the liquid phase to the surface of solid phase. This study was carried out using different models whose linear forms are presented in Table 3.4. The

pseudo-first-order kinetic model is based on the adsorption capacity of the material studied, because it considers that the process is of the first order compared to the concentration of free sites (Lu, Li, & Wang, 2016). The pseudo-second-order kinetic model considers that the adsorption presents a partial order 2 compared to the free sites (Li et al., 2016).

Table 3.4: Kinetic models used in the present work.

Models	Linear shapes	settings	References
Pseudo-first order	$\ln(q_e - q_t) = \ln q_e - K_1 t$ (3.12)	q_e and q_t=adsorption capacity (mg/g) equilibrium and at a time t respectively. K_1=speed constant at equilibrium (min^{-1})	(Ho & Mckay, 1999)
Pseudo-second order	$\frac{t}{q_e} = \frac{1}{K_2 q_e^2} + \frac{1}{q_e}$ (3.13)	K_2($g.mg^{-1}.mim^{-1}$) =equilibrium rate constant.	(Ho & Mckay, 1999)

3.5.4 Thermodynamic study

The adsorption phenomenon is always accompanied by a thermal process (endothermic or exothermic) (Pai et al., 2021). The variation or transformation of a system is accompanied by a variation in the Giggs free enthalpy (ΔG°), this variation depends on the initial and final states of the system (Saied et al., 2022). ΔG° is composed of the enthalpy variation (ΔH°) which expresses the interaction energies between the molecules and the surface of the adsorbent, and the entropy variation (ΔS°) which expresses the modification and the arrangement of molecules in the liquid phase on the adsorbent surface (Mohammed & Kareem, 2021).

$$\Delta G° = \Delta H° - T\Delta S° \quad 3.14$$

Measuring the heat of adsorption is the main criterion for differentiating chemisorption from physisorption (Saleh, Sari, & Tuzen, 2017). The heat of adsorption ΔH° is given by the Van't Hoff relation:

$$\ln K_C = \frac{\Delta S°}{R} - \frac{\Delta H°}{RT} \quad 3.15$$

Where $K_C$is the equilibrium constant, ΔG° is the free enthalpy change (KJ/mol), ΔH° is the enthalpy change (KJ/mol), ΔS° is the entropy change (KJ/mol/K) and T is the temperature (K). In this work, the thermodynamic studies were carried out at 25, 35 and 45 °C at a stirring speed of 200 rpm under the optimal conditions for CIP adsorption.

3.5.5 Regeneration of adsorbents

Under the ideal CIP adsorption conditions for each adsorbent, the regeneration of the synthesized adsorbents was evaluated. After each adsorption cycle, the adsorbents were stirred in a 0.1M HCl solution (To prevent the extraction of aluminum and to preserve the surface O-H groups of the zeolite) for 6 hours, then washed several times with deionized water and methanol, and dried at 60°C overnight before the next adsorption cycle. This concentration of HCl was chosen in order to achieve maximum desorption. The regeneration of the adsorbents was evaluated by carrying out successive adsorption-desorption cycles.

3.6 Computation method

3.6.1 Programs

All theoretical calculations were carried out on the electronic molecular structures of the adsorbents and adsorbates with the following module tools: DMol3, Reflex, CASTEP, Forcite and Adsorption locator included in the Materials Studio software (BIOVIA Materials studio Academic Research version 8.0 (product N ° 5CB-LUR)).

3.6.2 Adsorbents and adsorbates studied

In this study, the 3D structures of zeolite LTA and magnetite were imported into Hardware Studio software and ciprofloxacin was drawn in the 3D document of Hardware Studio.

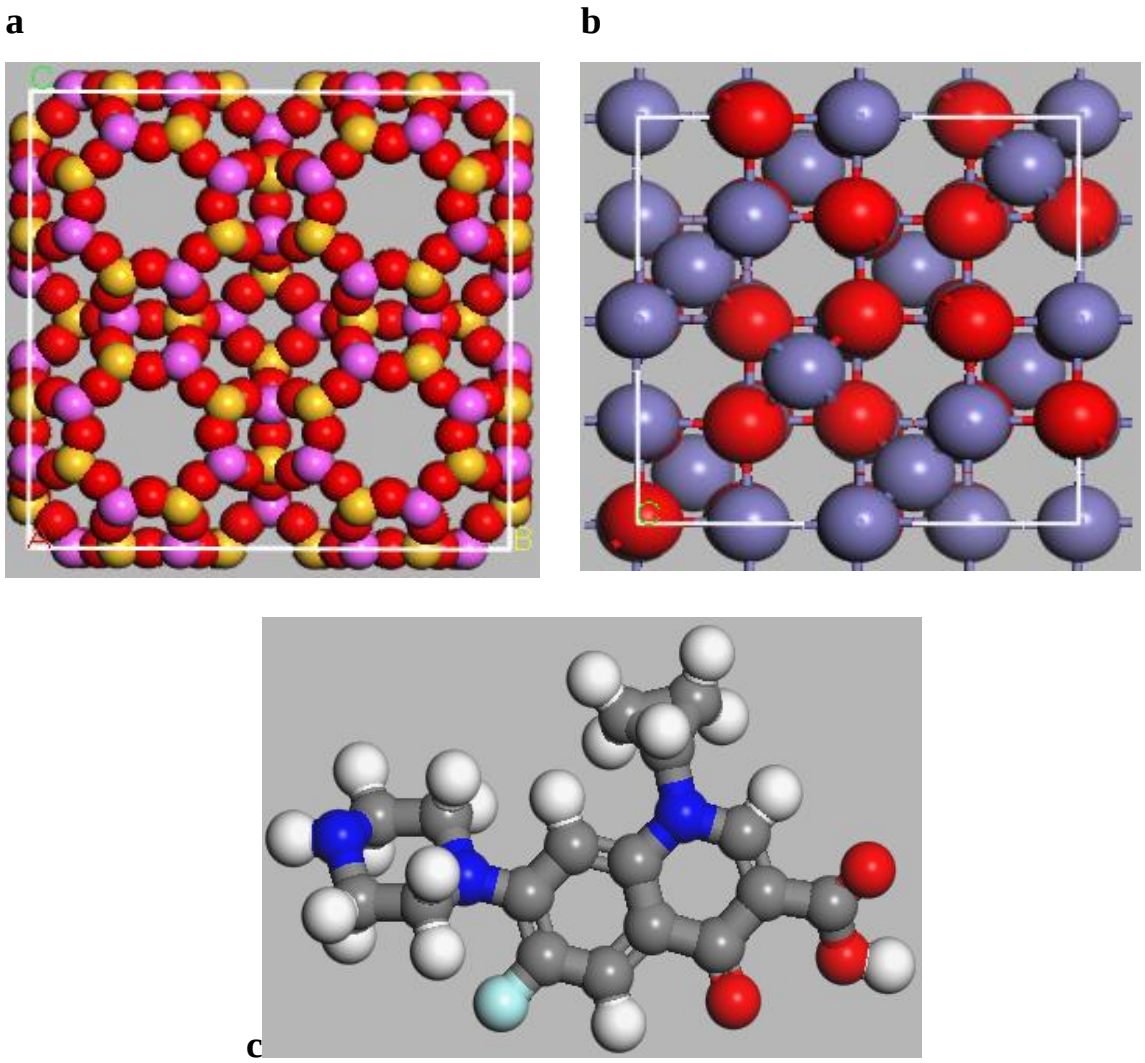

Figure 3.4: Structures of zeolite LTA (a), magnetite (b) and ciprofloxacin (c).

3.6.2.1 *Density functional theory*

Density functional theory (DFT) is a quantum computing technique that allows us to study electronic structure, in principle the precise matter. Due to its application to systems of variable size, ranging from a few atoms to several hundred, it is one of the most widely used methods in quantum calculations, both in condensed matter physics and in chemistry. quantum.

DFT is based on the theories of Hohenberg and Kohn. According to the first theorem, a single wave function corresponds to a given electron density. According to the second theorem, the functional energy of the electron density is subject to the variational principle. Therefore, according to the two theorems of Hohenberg and Kohn, the electron density of an electronic

system can be determined and the electron density of the ground state can be determined (Makkar & Ghosh, 2021).

In this study, in order to optimize the molecular structures of all compounds in the aqueous phase and to determine the chemical reactivity parameters possessed by the molecules, the DMol^3 module was used. The following parameters were selected: Generalized Gradient Approximation (GGA), double digital basis set 3.5 plus based on DND functions, K point set (gamma) 1x1x1. The COSMO control was used to include the solvation effect (aqueous phase) in the simulation and the following structural descriptors were determined: the energy of the most occupied molecular orbital (E_{HOMO}), the energy of the molecular orbital lowest unoccupied (E_{LUMO}), energy gap (ΔEgap), hardness (η), softness (σ), chemical potential (μ), electronegativity (χ), electrophile (ω), nucleophile (ε), electron donating power (ω-), electroacceptance power (ω+), retrodonation energy ($\Delta_{Eback\text{-}donation}$), transported electrons (ΔN), and indices of Fukui (Acar, 2022; Singh et al., 2021).

The useful and reliable quantum chemical parameters mentioned above can be approximately predicted using simple equations based on the ground state ionization energy and electronic affinities of atoms, ions and molecular systems, in addition to the new ideas and formulas presented in the density functional theory developed by Parr. The equations that have been mentioned are presented in the following form (Khnifira et al., 2022)

$$\mu = -\chi = -\frac{(I+A)}{2} \quad 3.16$$

$$\eta = \frac{(I-A)}{2} \quad 3.17$$

$$\sigma = \frac{1}{\eta} \quad 3.18$$

$$\omega = \frac{\chi^2}{2\eta} = \frac{\mu^2}{2\eta} \quad 3.19$$

$$\varepsilon = \frac{1}{\omega} \quad 3.20$$

In these equations, I is the ground state ionization energy and A is the ground state electron affinity of a chemical compound.

The electron donating and accepting capacities of chemical systems can be predicted and compared using two new parameters introduced by Gazquez and co-workers. The following equations present the descriptors electro-accepting power (ω+) and electro-donating power (ω-).

$$\omega^+ = \frac{(I+3A)^2}{16(I-A)} \quad 3.21$$

$$\omega^{-} = \frac{(3I+A)^2}{16(I-A)} \quad 3.22$$

Another descriptor used in corrosion and adsorption studies is the back-donation energy (ΔEback -donation). This parameter based on the chemical hardness of a compound is given as follows:

$$\Delta E_{back-donation} = -\frac{\eta}{4} \quad 3.23$$

It is important to note that the ΔN is a measure of the electronic charge that the electrophile can support. Therefore, when considering a variety of compounds, molecules with a high and positive ΔN value would be the best electrophiles.

$$\Delta N = \frac{\chi}{2\eta} \quad 3.24$$

The sites available for nucleophilic and electrophilic attacks on chemical systems are characterized by Fukui functions. The following equations provide an explanation of each index:

$$f_i(\underset{r}{\rightarrow})^{+} = q_i(N+1) - q_i(N) \quad 3.25$$

$$f_i(\underset{r}{\rightarrow})^{-} = q_i(N) - q_i(N-1) \quad 3.26$$

Where, $q_i(N+1)$, $q_i(N)$, are the $q_i(N-1)$ electron densities at point r for a compound with N+1, N, N-1 electrons respectively.

3.6.2.2 *Monte Carlo simulation*

Molecular Monte Carlo (MC) simulation is used to model the probability of different outcomes in a process that cannot be easily predicted due to the intervention of random variables. It is a method used to understand the impact of uncertainty and risk.

The CASTEP module was used to study the density of states (DOS), and the Reflex module to examine theoretical XRD.

For the MC simulation, the adsorbent material compounds (zeolite LTA and Fe_3O_4) were imported into a 3D atomistic document and optimized using the Forcite module. After optimization, the unit cell of the adsorbents was cleaved along the most stable (h, k, l) plane. The surface area of the adsorbent was optimized using the Forcite module and expanded to a supercell range (5x5), providing a large surface area for the interaction of the adsorbates and the electrolytic solution. Then, a 35 Å void was added on the C axis containing the adsorbate molecules and the water molecules. The Adsorption Locator module was used to find the most stable configurations of all complexes and the molecular descriptors involved.

The NPT (constant number of atoms, constant pressure and constant temperature) ensemble was created at 25 °C with a pressure of 1 bar, a simulation time of 500 ps and a time step of 1 fs in the cycles of annealing (the temperature cycles to be performed in the simulated annealing cycle) and 1.5×10^4 steps per cycle. The Ewald summation approach was used to deal with long- and short-range electrostatic interactions. Additionally, the Van der Waals interaction was calculated using a spline width of 1 Å and a cutoff distance of 12.5 Å.

The simulation box was used with a super cell of (5x5x5) and a 35 Å vacuum slab along the C-Axis. The Perdew-Burke-Ernzerhof (PBE) function, based on the generalized gradient approximation (GGA), was used to describe the exchange-correlation energy. It is possible to calculate the adsorption energy (Eads) of the chemical system on the surface of the adsorbents using the following equation:

$$E_{Ads} = E_{Total} + (E_{Adsorbent\ surface} + E_{Adsorbate}) \quad 3.27$$

The energy of the adsorbent-adsobate system is represented by E_{Total}, while the energy of the compounds adsorbed on the adsorbent surface is represented by $E_{Adsorbate}$. Equations (3.28) and (3.29) can be used to calculate the interaction and binding energies in a simulation complex to determine the interaction between the adsorbate and the adsorbent.

$$E_{Ads} = E_{Interaction} \quad 3.28$$

$$E_{Interaction} = -E_{Binding} \quad 3.29$$

The radial distribution function (RDF) was used to verify the interaction between molecules within the complex. The Forcite module was used to perform the RDF calculation (Sharif, Zhang, Wu, Yu, & Zhang, 2020). Furthermore, the Monte Carlo method allows calculating the distance, which evaluates the main mechanisms of adsorbate/adsorbent interaction. It is also a simple way to classify the nature of adsorption. Indeed, RDF corresponds to the probability that a given atom or molecule is distinguished from another at a distance of r (Khnifira, et al., 2022) . To study the distance between two atoms, we use the radial distribution function (g(r)) given by equation (3.30).

$$g(r) = \frac{n\,(r)}{4\pi r^2 dr} / \frac{N_B}{V} \quad 3.30$$

The average number of molecules in the area of r±dr is given by n(r), the total number of molecules B is given by N, the volume of the system is given by V and the distance between the adsorbates and the atoms on the surface area of the adsorbent is given by r.

The DFT and MC calculation methodology is summarized in the figure 3.5.

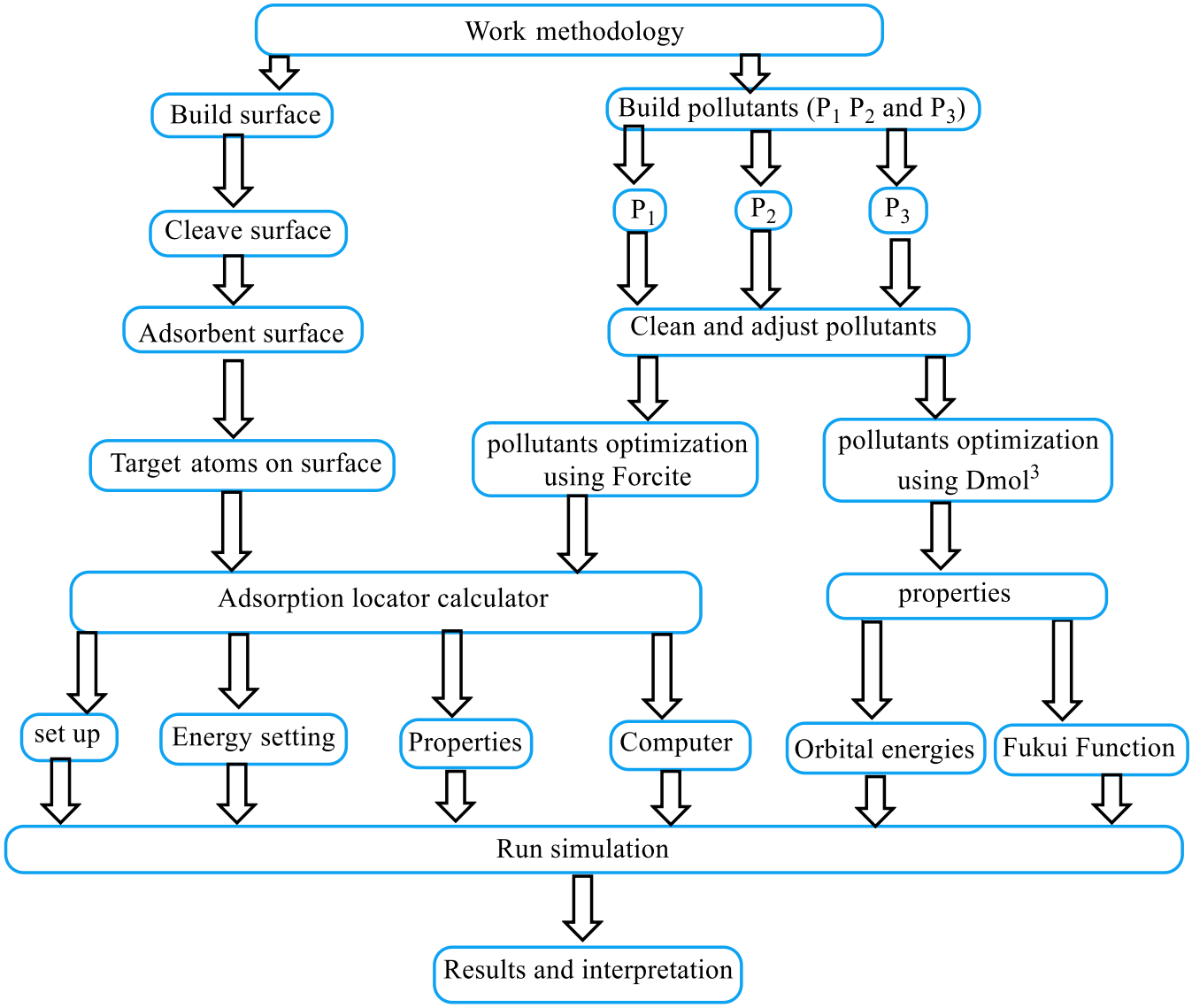

Figure 3.5: Generalized diagram of the DFT and MC calculation procedure.

CHAPTER FOUR
RESULTS AND DISCUSSIONS

4.1 Synthesis and characterization of zeolite 4A derived **from raw** Kaolin (from the locality of **Bong)** for the **elimination** of ciprofloxacin in aqueous solution

4.2 Characteristics of the synthesized zeolite 4A

4.2.1 X-ray fluorescence analysis

The hydrothermal synthesis of zeolite 4A produced an off-white solid powder. The results of an XRF analysis of the chemical compositions of zeolite 4A powders are presented in Table 4.1. The results indicate that the kaolin used had a high content of Si (51%) and Al (31%) with a Si/Al ratio of 1.65, indicating that the material was rich in Si and Al. Na content and other metals were relatively low (<1%). This makes kaolin an excellent precursor for the synthesis of zeolite 4A. Table 4.1 shows that the mass fractions of SiO_2 and Al_2O_3 decreased during the transformation of raw kaolin into zeolite 4A, indicating the dissolution of aluminosilicate in the presence of the NaOH solution (Wang et al., 2019b); the mass fraction of Na_2O increased by 18 wt%, indicating the formation of the sodium aluminum silicate gel (Belachew, 2022). Similarly, all components of kaolin can be observed in the synthesized zeolite 4A, suggesting that kaolin is stable at temperatures below 900°C. The mass fractions of Fe_2O_3, K_2O, CaO et TiO_2 within the kaolin decreased during the hydrothermal treatment, suggesting that these oxides were dissolved during the heat treatment. When preparing a zeolite type A, Wang et al. found that the content of Fe_2O_3 was lower than that of the raw material (Wang et al., 2019b). These results are consistent with those of the previous study.

Table 4.1: Analysis of the chemical composition of raw kaolin, metakaolin, and synthesized zeolite 4A.

Formula weight (%)	H_2O	Na_2O	Al_2O_3	SiO_2	Fe_2O_3	K_2O	CaO	TiO2
Raw kaolin	12.1	0.02	31.00	51.21	3,465	0.566	0.303	0.136
Metakaolin	10.9	0.00	32.29	50.95	0.906	0.912	0.828	0.474
Zeolite 4A	9.7	18.99	29.98	41.09	0.204	0.020	0.002	0.012

4.2.2 Fourier transform infrared spectroscopy analysis

The FT-IR spectra of raw kaolin, metakaolin, and synthesized zeolite 4A are shown in Figure 4.1. According to Figure 4.1a, raw Kaolin has a highly ordered structure, which explains the two clearly observable peaks in the spectrum range of 3690 to 3627 cm^{-1} caused by the stretching of the O-H bond (Zavareh et al., 2018). It can also be observed that there are many clearly defined FT-IR vibration bands in the range of 400 to 1400 cm^{-1}, due to the vibrations of Si-O, Si-O-Al and Al-OH bond (Wang et al., 2019b). The stretching vibration of Si-O units, the bending vibration of Al-OH units, the bending vibration of Si-O-Al units and the bending vibration of Si-O units in the raw kaolin structure could be assigned to vibrational bands at 1008 cm^{-1}, 912 cm^{-1}, 681 $cm^{-1}$and 535cm^{-1} (Belachew, 2022). When converting kaolin to metakaolin, these vibration bands disappeared and new vibration bands were formed at 1081 cm^{-1}, 800 cm^{-1}, and 447 cm^{-1}. According to Wang et al. (2019), the disappearance of the vibration band at 912 cm^{-1}testifies to the loss of Al-OH units (Wang et al., 2019b). This is explained by the breakage of the hydroxyl bond during calcination at high temperature. Meanwhile, a characteristic band of metakaolin is observed at 800 cm^{-1}(figure 4.1b) (Zhou, Jin, Liu, Wu, & Mei, 2014).

On the FT-IR spectrum in Figure 4.1c, zeolite 4A has a peak at 3364 cm^{-1}due to the presence of water molecules and the stretching of OH bonds on its surface (Wu et al., 2018). The bending vibration frequency of OH bonds is reported to be 1627 cm^{-1}. For the FT- IR spectrum of zeolite 4A the vibration bands at 974 cm^{-1}. and 465 cm^{-1}could be attributed respectively to the stretching vibration of Si-O or Al-O units and the vibration of Si-O-Al units in the structure of zeolite 4A, (Wang et al., 2019b). We could attribute the vibration bands to 672 cm^{-1}. and 554 $cm^{-1}$to the vibration modes of the zeolite 4A framework (Zavareh et al., 2018). According to FT-IR spectra analyses, zeolite 4A was successfully synthesized from raw kaolin and is hydrated from.

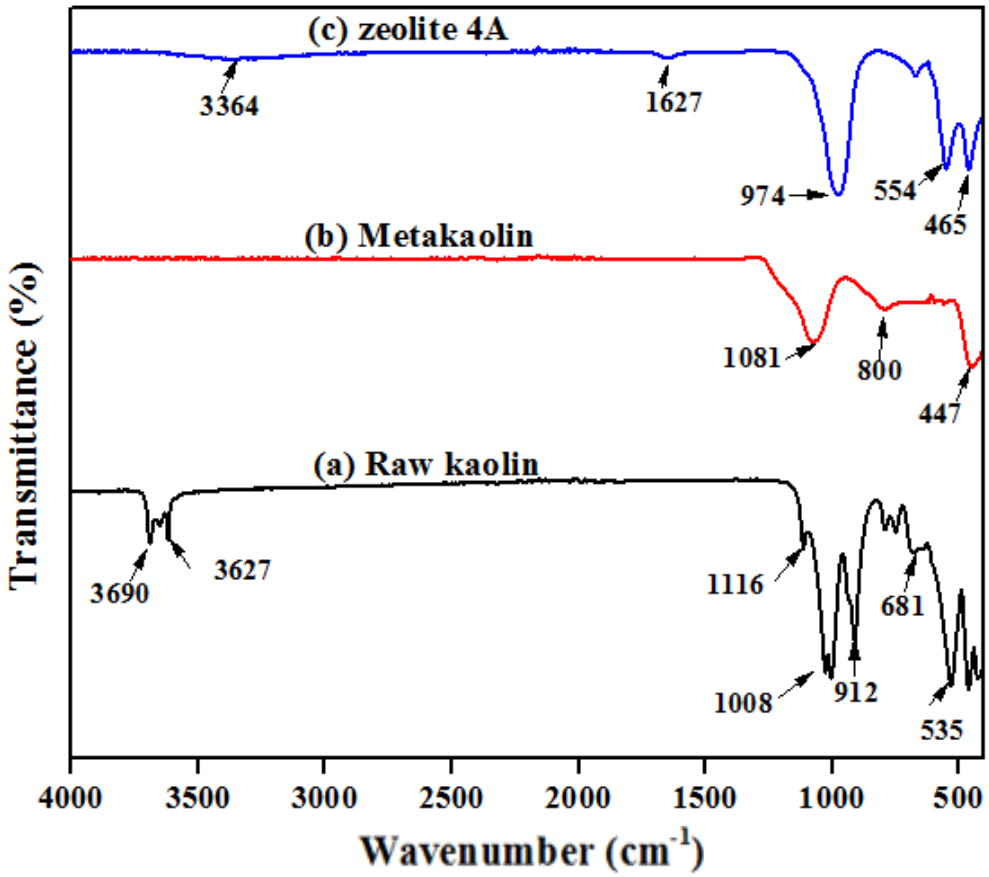

Figure 4.1: FT-IR spectra of raw kaolin (a), metakaolin (b) and synthesized zeolite 4A (c).

4.2.3 X-ray diffraction analysis

The phase analysis of raw kaolin, metakaolin, and synthesized zeolite 4A is shown in Figure 4.2. We can see that raw kaolin (Figure 4.2a) is mainly composed of illite kaolinite and quartz. However, according to the Joint Committee on Powder Diffraction Standards (JCPDS), the typical diffraction peaks of kaolinite occur at 2θ= values of 12.4° and 24.8°, which corresponds to the reference value of kaolinite single-phase (Wang et al., 2019b). Calcination observed important expected features, namely the disappearance of kaolinite diffraction peaks relative to the raw kaolin pattern, as well as the appearance of amorphous aluminosilicate, as shown in Figure 4.2b. Meanwhile, peaks typical of illite impurity and quartz are observed in the diffraction spectrum of metakaolin (Ayele, Pérez-Pariente, Chebude, & Díaz, 2015). From Figure 4.2c, it was found that the XRD pattern of the synthesized zeolite 4A is identical to those revealed in the literature, which confirms the successful synthesis of zeolite 4A. According to the reference value of single-phase zeolite 4A, the characteristic diffraction peaks of zeolite 4A are manifested

at 2θ= values of 7.2°, 10.3°, 12.6°, 16.2°, 21.8°, 24.0°, 27.2°, 29.9° and 34.2°, as shown in the XRD pattern of the synthesized zeolite 4A, according to JCPDS (Wang et al., 2019b; Zavareh et al., 2018). However, it was observed that quartz and illite, which were considered as impurities, disappeared entirely. These results highlight the crystallinity and high purity of the synthesized zeolite 4A.

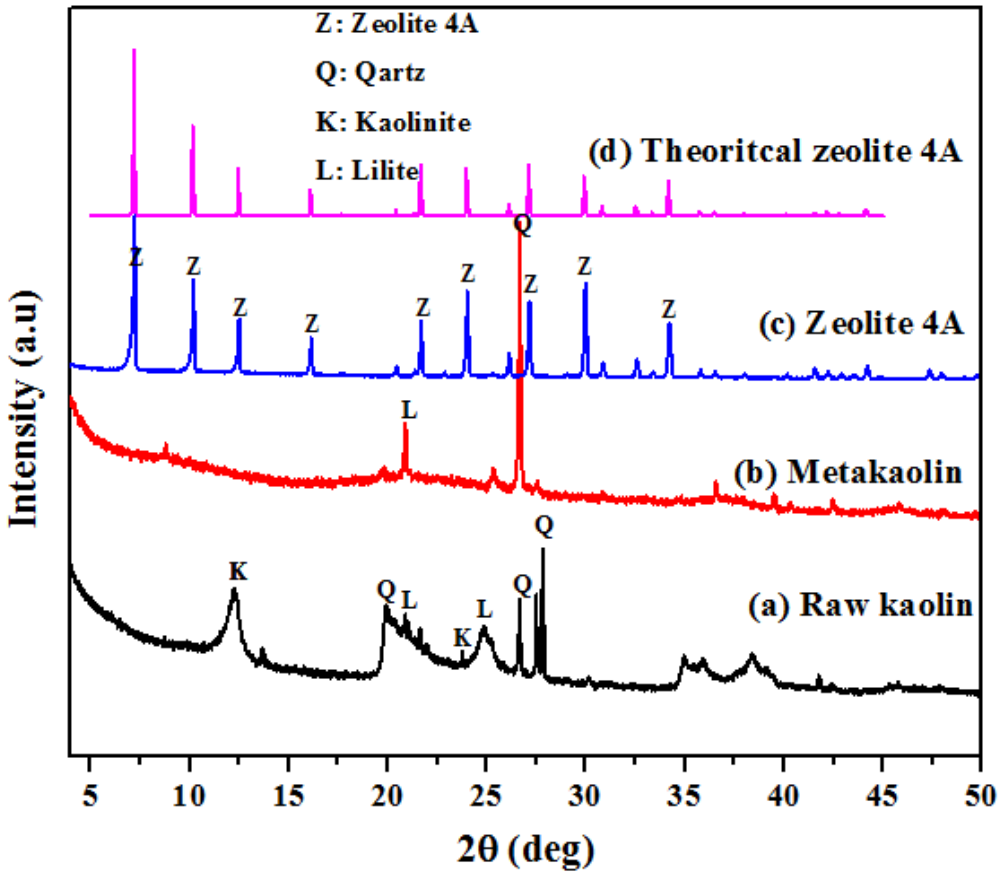

Figure 4.2: XRD pattern of raw kaolin (a), metakaolin (b), synthesized zeolite 4A (c) and theoretical 4A zeolite (d).

4.2.4 Scanning electron microscopy and energy dispersive spectrometry analyses

SEM and EDS analyses were performed on the raw kaolin, metakaolin and synthesized zeolite 4A to analyze respectively their surface morphology and composition as shown in Figure 4.3. It is noted that raw kaolin has a hexagonal lamellar structure and that metakaolin is amorphous, which suggests the presence of aluminosilicates (Araujo, Gianesi, Andrade, Valenzuela-diaz, & Freitas, 2014). The addition of the alkaline solution causes the total

disappearance of the amorphous aluminosilicate structure, followed by crystallization which results in the formation of zeolite 4A. Figure 4.3c presents a well crystallized structure with a cubic morphology and a uniform particle size distribution. This form corresponds to that of zeolite 4A described by Wang et al (Wang et al., 2019b). Additionally, Figure 4.3 (A, B, C) presents the EDS spectra of raw kaolin, metakaolin, and synthesized zeolite 4A. In the spectrum of raw kaolin and metakaolin, the peaks of the elements O, Al and Si were clearly visible. In the spectrum of zeolite 4A, we observe a new peak linked to the Na element. Which suggests that zeolite 4A is composed of O, Al, Si and Na. Using the data in Table 4.1, it is possible to see that positively charged sodium ions are present in zeolite 4A synthesized as stabilized cations.

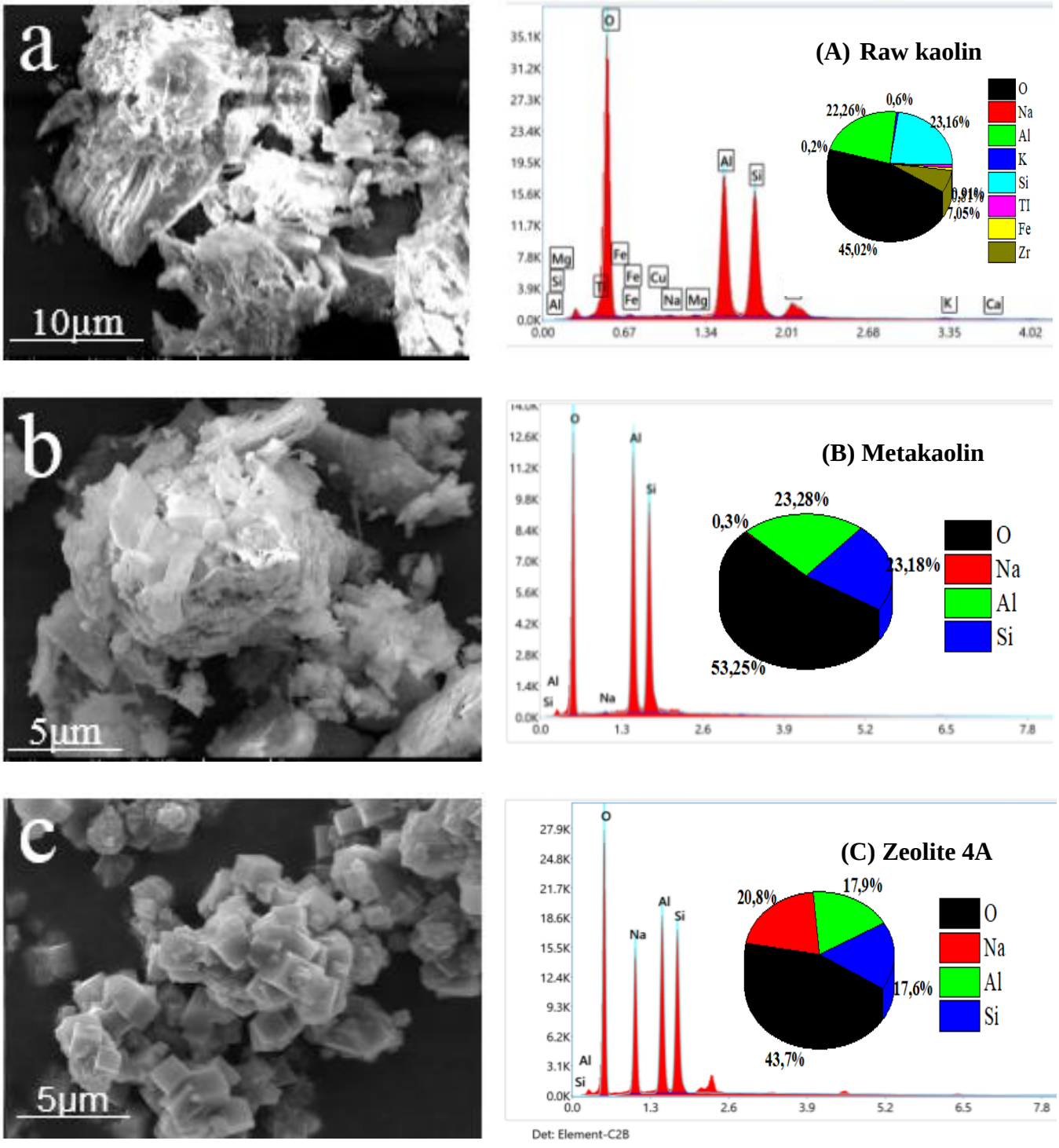

Figure 4.3: SEM and EDS images of raw kaolin (a, A), metakaolin (b, B) and synthesized zeolite 4A (c, C).

4.2.5 Magic-angle rotation and nuclear magnetic resonance for ^{27}Al and ^{29}Si in the solid-state analysis

Figure 4.4 presents the solid-state MAS-NMR spectra of ^{27}A1 and ^{29}Si of the synthesized zeolite 4A. Figure 4.4a illustrates a single resonance at approximately 58.77 ppm, suggesting that dissolved aluminum species from metakaolin are integrated into the Si-O lattice to form the $Si(OAl)_3(OSi)$ framework in solution. alkaline (Yao et al., 2018). Furthermore, the resonance full width at half maximum (FWHM) was narrow, reflecting the favorable crystallinity of zeolite 4A (Wang et al., 2019b). The typical ^{29}Si MAS-NMR resonance of zeolite 4A, which was quite clear and was around -90.75 ppm (Fig. 4.4b), proving that zeolite 4A has good lattice order (Lucresse et al., 2023).

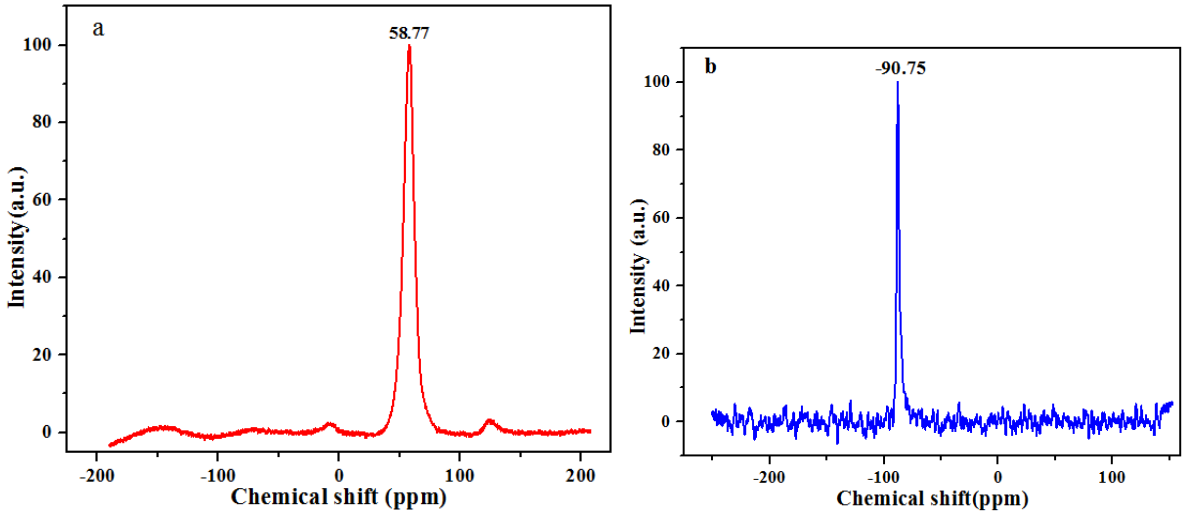

Figure 4.4: Solid-state MAS-NMR spectra of ^{27}Al (a) and ^{29}Si (b) of the synthesized zeolite 4A.

4.2.6 Thermal analysis of the synthesized zeolite 4A

The thermal stability of the synthesized zeolite 4A during heat treatment was examined, as shown in Figure 4.5. The TGA curve reveals a rapid decrease of sample mass as the temperature increases from 34 to 237 °C. On the DTG curve, we could observe the highest endothermic peak around 160 °C. This would mainly involve the total removal of free water molecules adsorbed on the zeolite 4A and the rapid expulsion of molecules such as CO_2 et le N_2 and others that were sucked into the pores of the sample (Wang et al., 2019b). The mass of the sample decreased by 11.75% due to the increase in temperature (Hashemian et al., 2013). The zeolite 4A sample then underwent a slight increase in mass up to 573°C before suddenly

flattening. In fact, the Van der Waal force of water may be related to the particular structure of cage-like pores discovered in zeolite 4A (Wang et al., 2019b). Therefore, some chemical interactions break down with increasing temperature, which would result in loss of water from the sample (Belachew & Hinsene, 2022). Ultimately, the overall weight loss rate was 14.75%. The DTG curve no longer displays a thermal peak from 573°C, demonstrating the thermal stability of the sample, and that zeolite 4A can withstand a temperature of up to 1200°C.

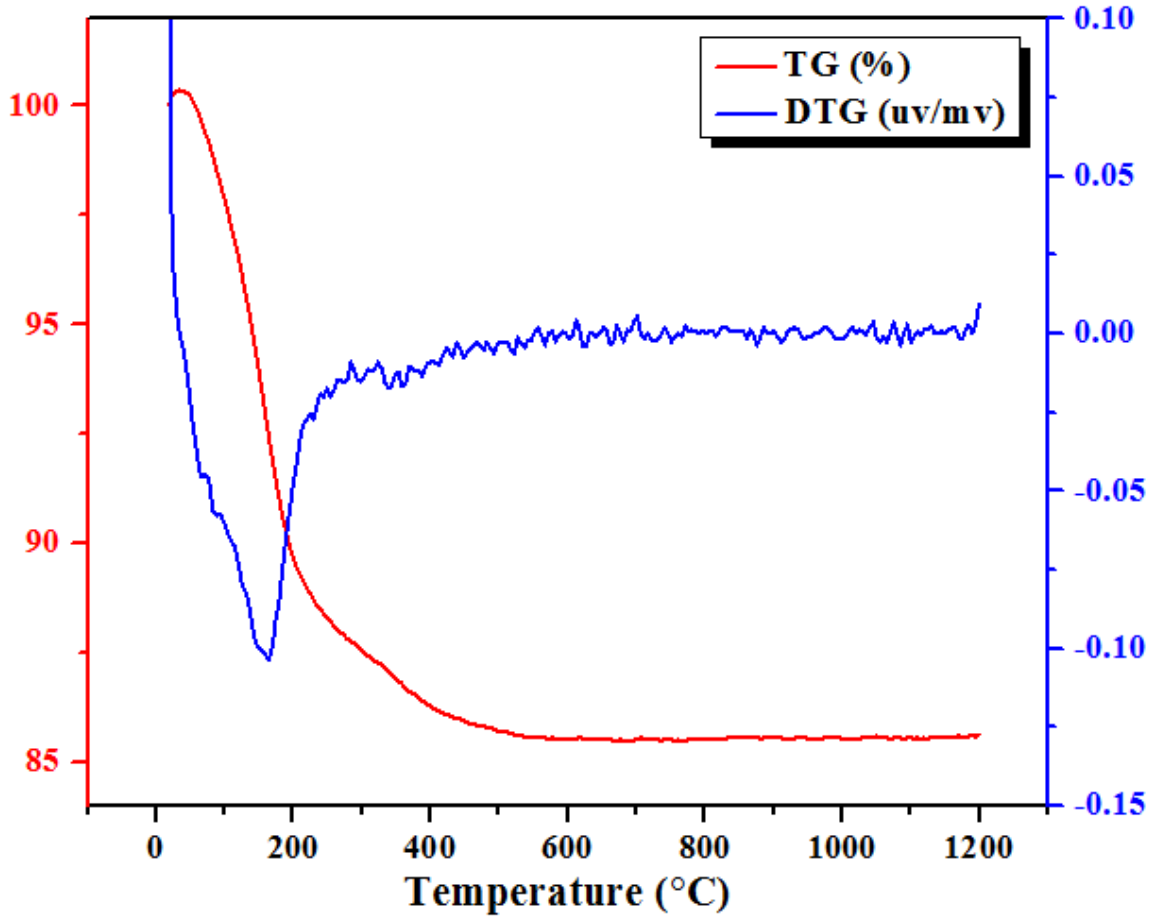

Figure 4.5: TGA/DTG curve of the synthesized zeolite 4A.

4.2.7 N_2 Adsorption-desorption isotherms

Figure 4.6a displays a type IV adsorption-desorption isotherm with a hysterisis loop, which is a typical behavior of hierarchical or mesoporous zeolites (Sivalingam & Sen, 2018). Furthermore, the sharp increase in the adsorption in the relative pressure range of P/Po=0.6-1 was attributed to the capillary condensation of gas N_2in the mesopores (Wang et al., 2019b). Figure 4.6b shows the pore size distribution of zeolite 4A obtained using the Barrett–Joyner–

Halenda (BJH) equation. It is possible to deduce that the average diameter of the pores is 13 Å. Table 4.2 summarizes the textural data of zeolite 4A. The BET surface area and mesopore volume of zeolite 4A were significantly higher compared to those of commercialized zeolite 4A. Which shows that the synthesized zeolite 4A has good characteristics for adsorption of pollutants.

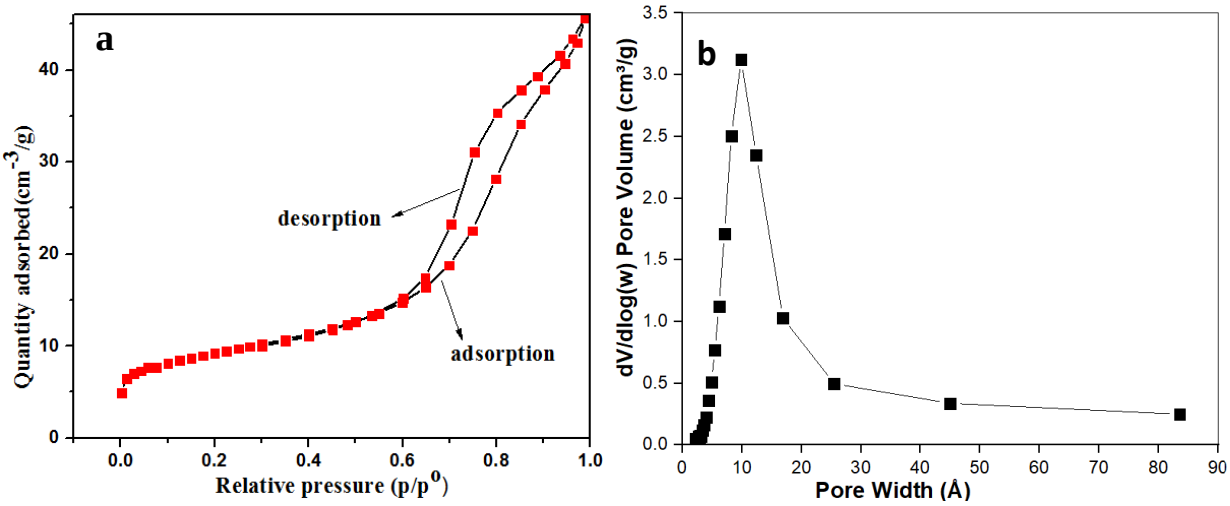

Figure 4.6: Adsorption-desorption isotherm N_2 (a) and pore size (b) of the synthesized zeolite 4A.

Table 4.2: Textural properties of synthesized zeolite 4A.

Samples	BET surface area (m^2/g)	Porous volume (cm^3/g)	Micropore surface (cm^3/g)	Nanoparticle size (nm)
Synthesized zeolite 4A	34. 2320	0.071259	7.03202	197.0432

4.2.8 Analysis of the pH of the point of zero charge on the surface of the synthesized zeolite 4A

The zero charge point pH value (pHpzc) corresponds to zero surface charge. In other words, the pHpzc determines whether the surface of the adsorbent is acidic or basic. The net charge of the adsorbent below pHpzc is positive, while it is negative above pHpzc (Sedik et al., 2022). The pHpzc value of the synthesized zeolite 4A is shown in Figure 4.7. It can be observed that the pHpzc values of zeolite 4A is 7.58, thus, at a pH value<pHpzc, the surface of zeolite 4A has a net positive charge, and at a pH value>pHpzc, the surface of zeolite 4A is negative. Indeed, at pH <7.58, the hydronium ions (H_3O^+) interact with the terminal sinalool ≡Si-OH and ≡Al-OH groups of zeolites 4A to form the cations $\equiv Si - O_2^+H$ and $\equiv Al - O_2^+H$. When the pH>7.58 the

hydroxyl ions (OH^-) interact with the terminal sinalool ≡Si-OH and ≡Al-OH groups to form the anions $\equiv Si - O^-$ and $\equiv Al - O^-$on the surface of zeolite 4A (Atugoda et al., 2021).

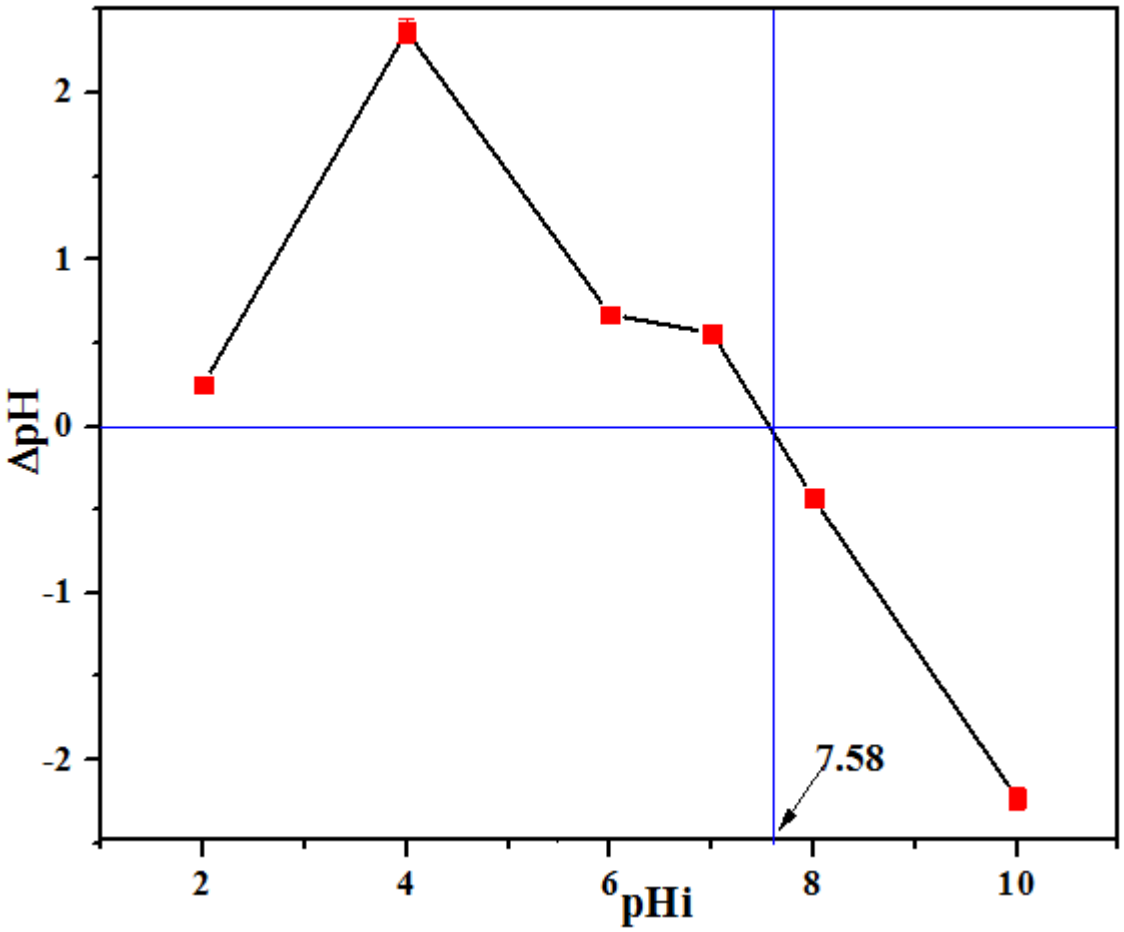

Figure 4.7: pHpzc curve of the synthesized zeolite 4A.

4.3 Study of the adsorption of ciprofloxacin by the synthesized zeolite 4A

4.3.1 Effect of pH

The change in the surface charge of the adsorbent is greatly influenced by the pH of the solution. Figure 4.8 illustrates the influence of pH on the ability of zeolite 4A to adsorb CIP. CIP presents a cationic form (CIP^+) (through the protonated amine group) at pH<6.1, a zwitterionic form ($CIP^\pm$) at pH between 6.1 and 8.7 and an anionic form (CIP^-) at pH>8.7 (Atugoda et al., 2021). It can be observed in Figure 4.8 that the CIP removal rates increase with pH until reaching a maximum efficiency of 80.79% at pH=8 and then begins to decrease. Indeed, at pH<6.1 and pH>8.7, the surface charge of zeolite 4A has the same sign as the CIP one of molecules ($CIP^+$and CIP^-). There is therefore mutual repulsion between the surface of zeolite 4A and CIP molecules,

resulting in a low CIP adsorption rate. At pH=8, the CIP molecule transforms into a zwitterion ($CIP^{\pm}$), and there is coexistence of groups $\equiv Si - O_2^+H$ and $\equiv Si - O^-$on the surface of zeolite 4A. There can therefore be a strong electrostatic interaction between the $CIP^{\pm}$and the surface of zeolite 4A. This would explain the high elimination rate observed at this pH. wakejo et al. (2022), also obtained maximum CIP adsorption at pH 8 on modified Biochar (Wakejo et al., 2022).

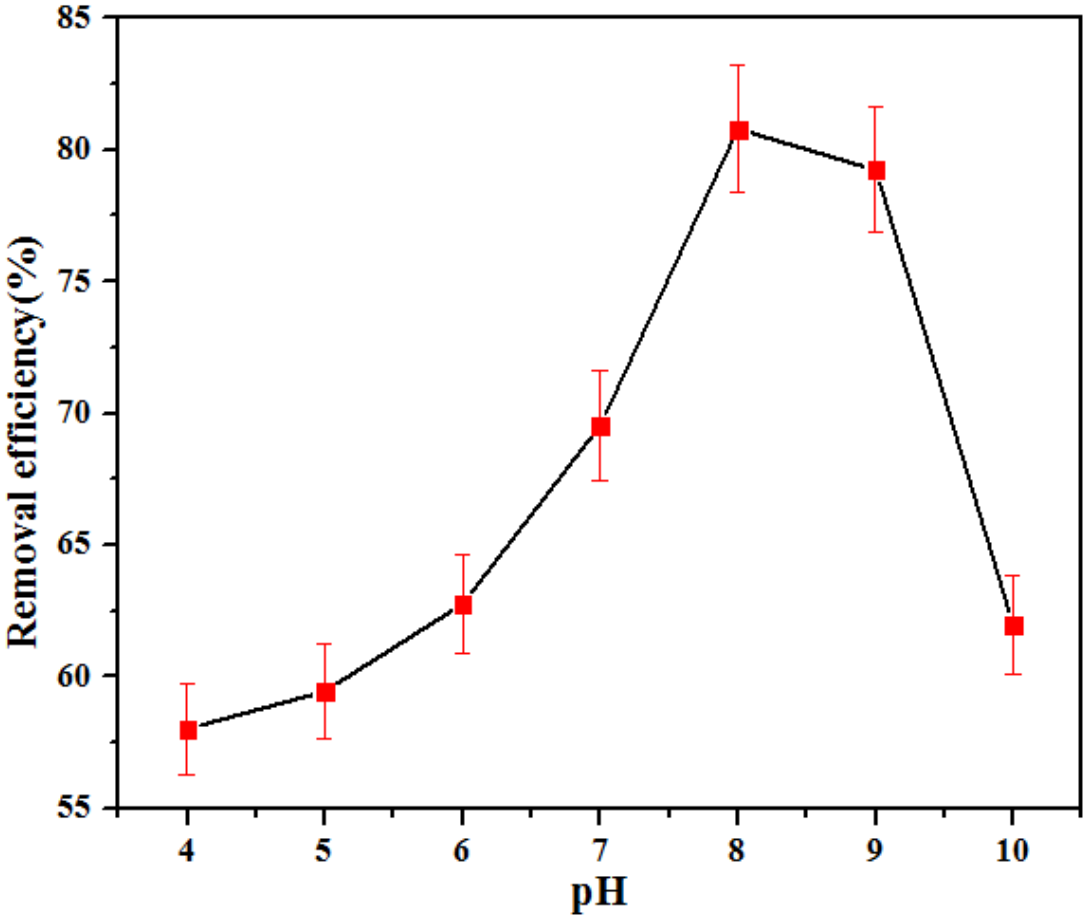

Figure 4.8: Influence of initial pH on CIP adsorption. Condition: contact time 80 mins, zeolite 4A mass 20 mg, sharking speed 200rpm, Temperature 25°C, initial concentration (CIP) 60 ppm, and error bars show ±standard deviation (3%).

4.3.2 Effect of adsorbent dose

One of the important factors affecting the adsorption efficiency is the mass of the adsorbent. The CIP removal efficiency is shown in Figure 4.9. It can be observed that the elimination efficiency of CIP increases considerably between 10 and 20 mg until reaching a maximum value of 95.34%, and they gradually decrease after a dose of 20 mg. Indeed, when the

dose of the adsorbent increases, there is a reduction in the number of active sites on the surface of the adsorbent, which leads to a reduction in the elimination efficiency of the CIP (Christopher et al., 2023). In addition, a high dose of zeolite 4A leads to the formation of flocs or aggregates which make it very difficult for CIP molecules to access the adsorption sites (Carolina et al., 2020). This explains the decrease in adsorption efficiency.

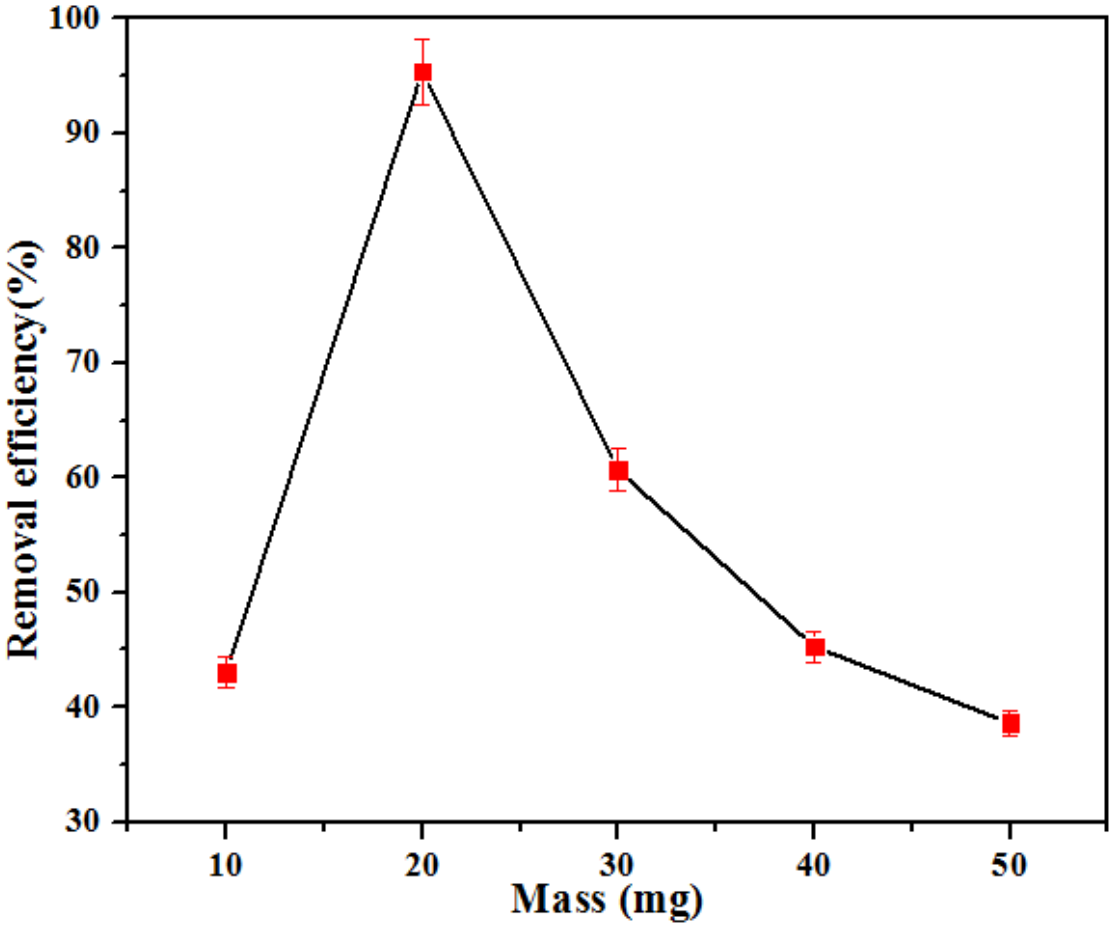

Figure 4.9:Influence of the mass of zeolite 4A on the adsorption of CIP. Condition: contact time 80 mins, pH 8 and sharking speed 200rpm, Temperature 25°C, initial concentration (CIP) 60 ppm, error bars show ±standard deviation (3%).

4.3.3 Effect of ciprofloxacin concentration

The influence of the initial CIP concentration on the removal efficiency is shown in Figure 4.10. As shown in this figure, the removal efficiency gradually increases with the initial CIP concentration between 10 and 60 ppm, with a maximum absorption capacity of 85.56%. When the concentration is greater than 60 ppm, the elimination efficiency is no longer

appreciable. Indeed, an increase in the concentration of CIP leads to an increase in collision between zeolite 4A and the CIP molecules, favoring the breakdown of the resistance forces on the surface of the pores and facilitating the diffusion of CIP (Asbollah et al., 2022). Furthermore, when the concentration of CIP is high (>60 ppm), the amount of CIP adsorbed is almost constant. This state of affairs can be explained by the difficulty of the CIP molecule to diffuse on the surface of zeolite 4A at higher concentrations. Manazir et al. (2020), reported that at a higher concentration, the adsorbed molecules or ions increase the driving force and accelerate the mass transfer between the liquid adsorbate and the solid adsorbent (Altaf et al., 2022).

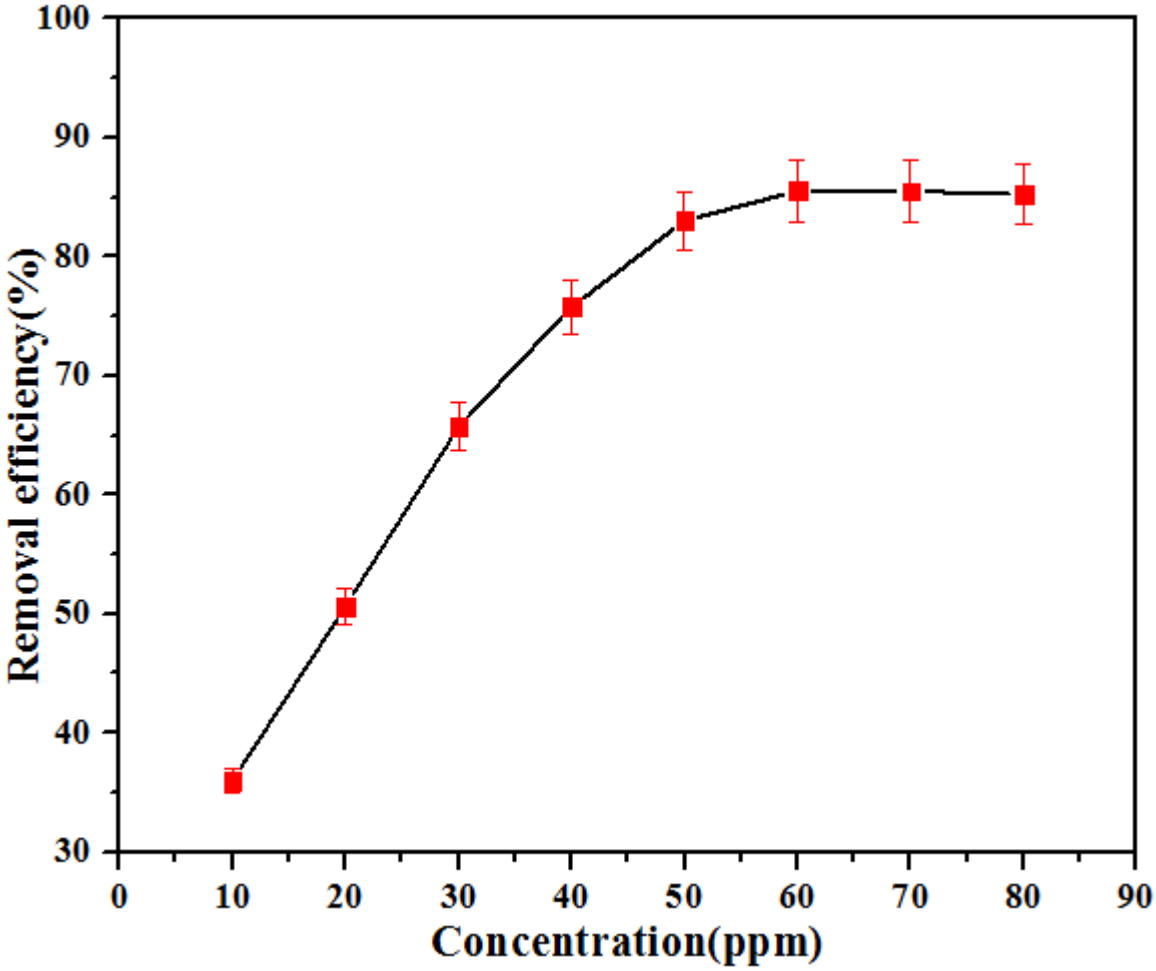

Figure 4.10: Influence of the initial CIP concentration. Condition: contact time 80 mins, zeolite mass 4A 20 mg, pH 8 and sharking speed 200rpm, Temperature 25°C, error bars show ±standard deviation (3%).

4.3.4 Effect of contact time

The adsorption process can also be affected by the contact time of the adsorbent with adsorbed molecules (Pradhan et al., 2022). Figure 4.11 presents the CIP removal efficiency as a function of contact time. It can be observed that the adsorption process is rapid for the first 40 minutes, then slows down and reaches equilibrium after 80 minutes. All available active sites of the adsorbent were unoccupied at the start of the adsorption experiment, which explains the high adsorption rate (Siipola et al., 2020). After a while, the majority of active sites contained CIP molecules, which resulted in fewer sites available for the adsorption process and lower adsorption rates. At equilibrium, the adsorbed molecules occupied the largest number of active sites and there was almost no space available for adsorption, meaning that no adsorption was carried out at equilibrium (Oliveira et al., 2024). The removal efficiency of CIP was 90.93% after 80 minutes.

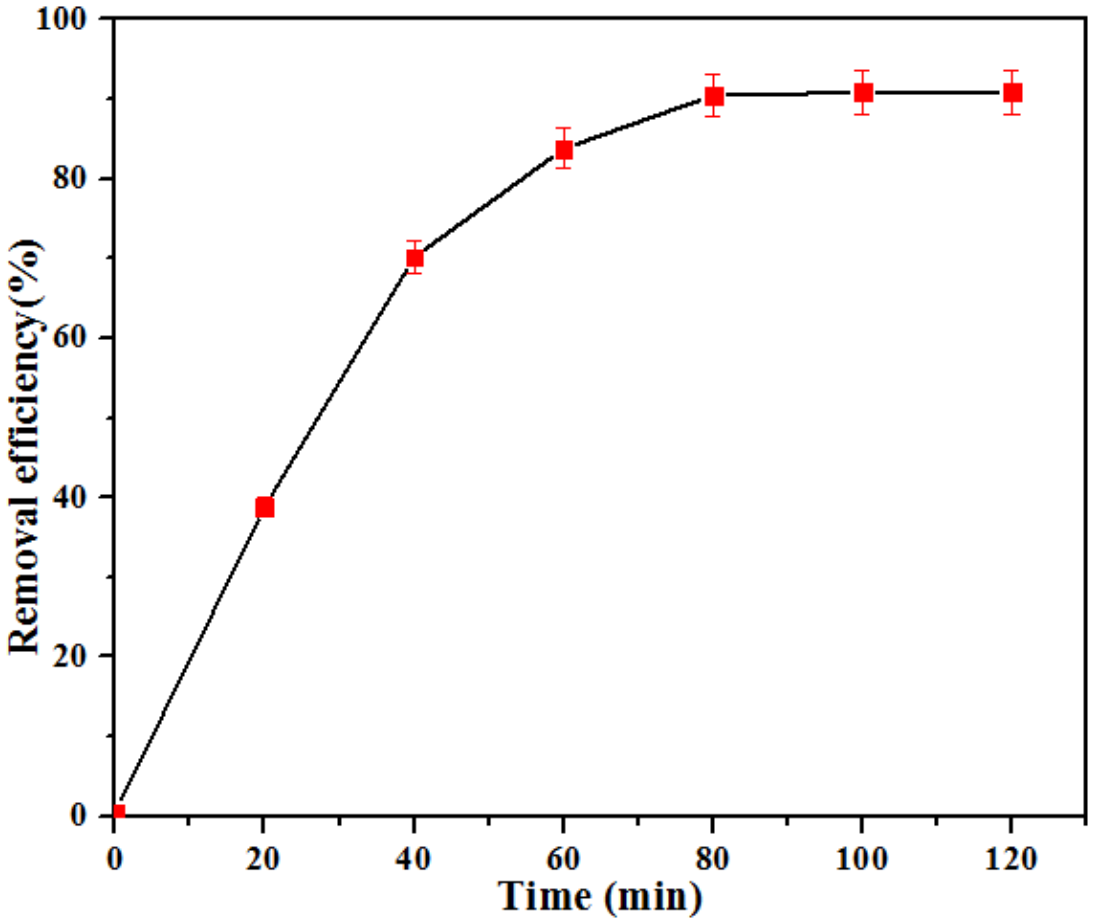

Figure 4.11: Influence of contact time. Condition: zeolite mass 4A 20 mg, pH 8 and sharking speed 200 rpm, Temperature 25°C, initial concentration (CIP) 60 ppm, error bars show ±standard deviation (3%).

4.3.5 Adsorption isotherm

It is very helpful to understand the realities of the adsorbent adsorption process. In general, adsorption isotherms are plotted using a constant solution concentration of the adsorbate in a known quantity of adsorbent. The experimental data were analyzed using different kinetic models such as Langmuir and Freundlich, and the results were presented in Figure 4.12 and Table 4.3. According to the Freundlich model, the surface of the adsorbent is considered heterogeneous and the adsorption process takes place on different layers. According to the Langmuir model, zeolite 4A has a homogeneous surface and the adsorption process takes place in a single layer. The value of the correlation coefficient for the Langmuir model (R^2=0.963) was higher compared to the value of the correlation coefficient for the Fruindlich model (R^2=0.747). This shows that

the synthesized zeolite 4A adsorbs on homogeneous monolayer surface (Altaf et al., 2022). According to the Langmuir model, the maximum adsorption capacity (q_{max}) of zeolite 4A was 87.72 mg/g for 20 mg of adsorbent. Atugoda et al. (2021), reported an adsorption of 85.65 mg/g of ciprofloxacin using 0.5 g/L of Biochar-modified zeolite (Atugoda et al., 2021). The separation factor value (R_L)was less than 1, indicating that the adsorption was favorable. The adsorption intensity (1/n), between 0 and 1, indicates the heterogeneity of the adsorbent surface and relative energy distribution (Zhang et al., 2021).

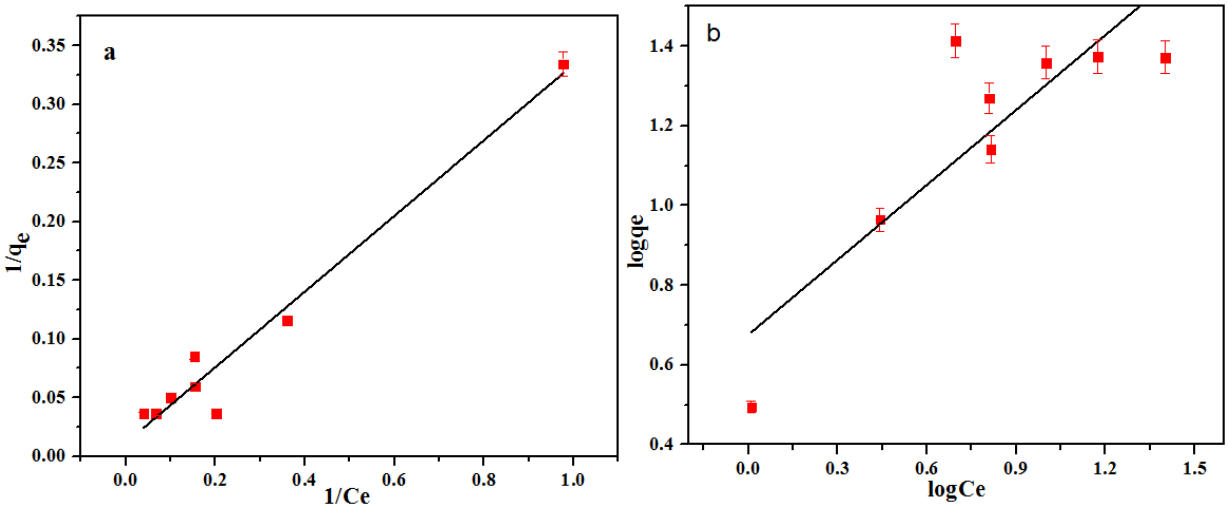

Figure 4.12: Linear isothermal models for CIP adsorption for the Langmuir (a) and Freudlich (b) models.

Table 4.3: Fitting parameters of CIP adsorption kinetic models.

Type of isothermal	Langmuir model			Freundlich model			
Parameters	K_L (L/mg)	q_{max} (mg/g)	R^2	R_L	K_F	$1/n$	R^2
Linear	0.035	87.72	0.963	0.321	4,743	0.627	0.747

4.3.6 Adsorption kinetics

The experimental data were used to study the kinetics of CIP adsorption on zeolite 4A, using pseudo-first-order (PFO) and pseudo-second-order (PSO) kinetic models. Table 4.4 presents the kinetic parameters obtained from these models. The linear fit of pseudo-first order and pseudo-second order is shown in Figures 4.13. The values R^2 of PSO are higher than those of PFO, suggesting that the adsorption was controlled by the second-order kinetic model. In

addition, the $q_{e\,Cal}$ of PSO model is very close to that of $q_{e\,Exp}$. This suggests that the adsorption capacity is determined from the adsorption rate and is independent of the adsorbate concentration (Li et al., 2022). The pseudo-second order model suggests the presence of strong interactions between the surface of zeolite 4A and the CIP (chemisorption), while the pseudo-first order model suggests the existence of weak electrostatic interactions (physisorption) (Simonin, 2016). Pseudo-second-order model fitting revealed that the rate-determining step of the adsorption process was controlled by chemisorption ($K_1 < K_2$), and this latter adsorption step becomes slower due to diffusion of molecules of CIP in micropores (Chai, Dong, Zhang, Qi, & Chen, 2022).

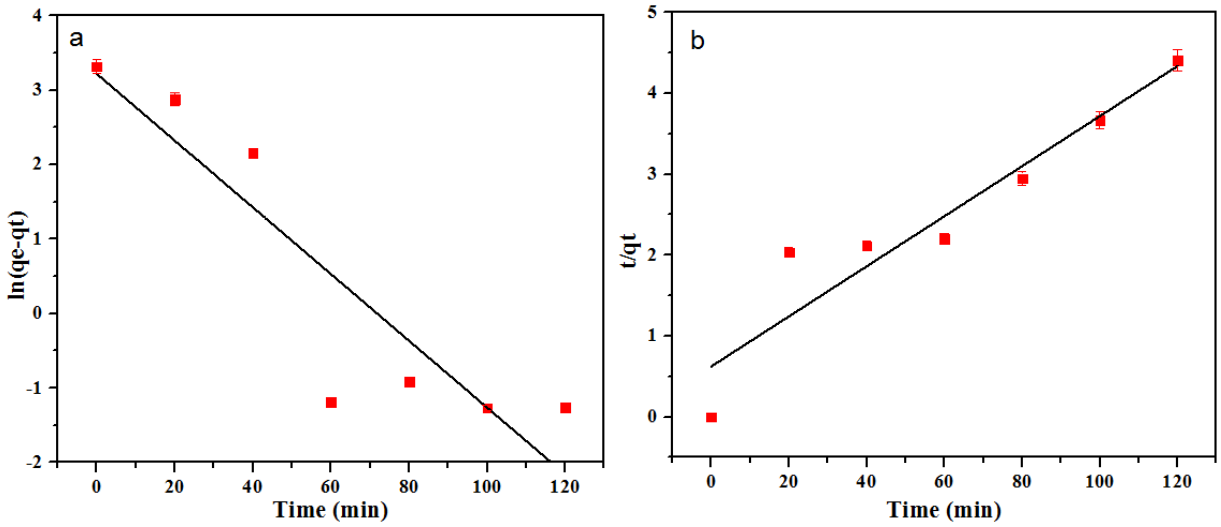

Figure 4.13: Linear fitting of pseudo-first order (a) and pseudo-second order kinetic models.

Table 4.4: Parameters and adjustment coefficients of adsorption kinetic models.

Reaction order	Pseudo-first order				Pseudo-second order		
Parameters	$q_{exp}(mg/g)$	$q_{cal}(mg/g)$	K_1	R^2	$q_{cal}(mg/g)$	K_2	R^2
Linear	27,524	24,950	-0.00037	0.821	28,362	0.001526	0.9006

4.3.7 Thermodynamic study

The study of the effect of temperature on the CIP removal efficiency is shown in Figure 4.14. It can be observed through in Figure 4.14a that an increase in temperature between 25°C and 45°C leads to an increase in the adsorption efficiency of zeolite 4A. Removal efficiency increased by 5.88%. This trend could be attributed to an increase in the diffusion rate and the

stability of adsorption sites (Zhang et al., 2021). Mohammed et al. (2021), reported that an increase in temperature promotes activation of pores and active sites favoring an increase in adsorption (Mohammed & Kareem, 2021). Figure 4.14b presents the Van't Hoff curve for the adsorption of CIP by zeolite 4A. Thermodynamic variables such as ΔG°, ΔH° and ΔS° were determined and presented in Table 4.5. It is observed that all the values of ΔG° were negative, revealing that the adsorption of CIP was favorable and spontaneous (Atugoda et al., 2020). The value of ΔH° determines the energy transfer of the adsorption process, the positive value of Δ H° reflects an endothermic process (Sabín López, Paredes Ramos, Herrero, & López Vilarinõ, 2020). The value of ΔS° reflects the affinity of the adsorbate on the surface of the adsorbent. The positive value of ΔS° indicates that the solvent molecules occupied on the surface are easily displaced by the CIP molecules improving the adsorption capacity (Atugoda et al., 2021). The value of ΔH° suggests adsorption of CIP by zeolite 4A as chemisorption (40<ΔH°<800 KJ/mol) (Belachew & Hinsene, 2022). The negative values of ΔG° and positive value of ΔH° indicate that the adsorption was favorable with increasing temperature.

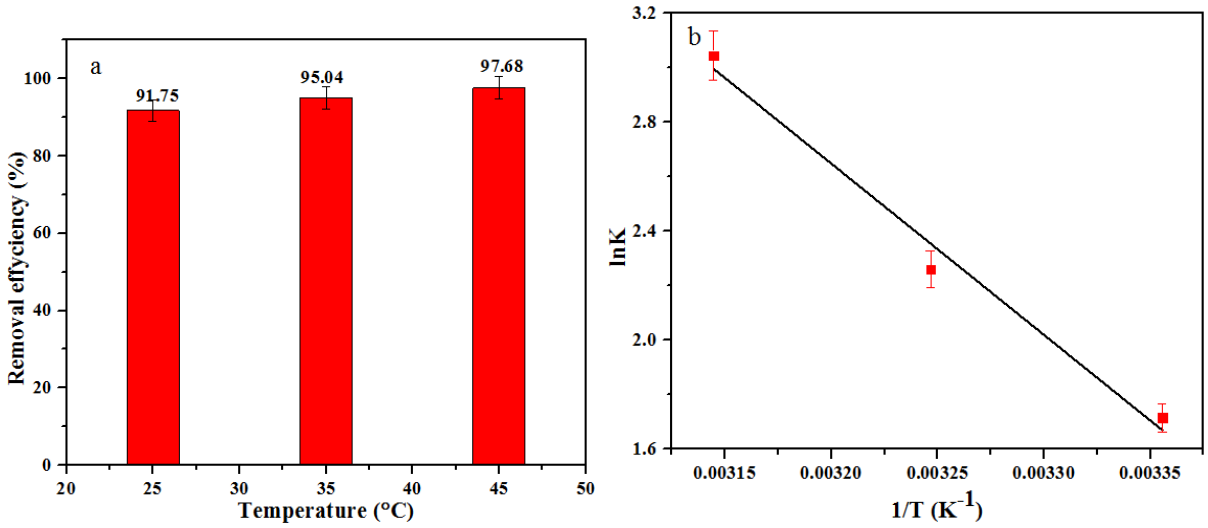

Figure 4.14: Adsorption efficiency as a function of temperature (a), Van't Hoff curve (b) for CIP removal.

Table 4.5: The thermodynamic parameters of the adsorption of CIP by the synthesized zeolite 4A.

Compound Temperature (K)	$\Delta G°\ (Kj/mol)$	$\Delta H°\ (Kj/mol)$	$\Delta S°\ (Kj/mol)$
298	-4.24993		

CIP	308	-5.78719	52.27012	0.189285
	318	-8.05136		

4.3.8 Study of the regeneration and chemical stability of zeolite 4A after adsorption of CIP.

After seven cycles, the chemical stability and reusability of zeolite 4A were analyzed and the results are recorded in Figure 4.15. Zeolite 4 A synthesized before and after adsorption shows the same vibration frequency bands (Figure 4.15a) and overlapping X-ray diffraction intensity peaks (Figure 4.15b). This means that zeolite 4A structure was not altered during adsorption. The cubic morphology of zeolite 4A after recovery is visible in the SEM image (Figure 4.15c), which corresponds to that of zeolite 4A before adsorption of CIP. These results allow us to conclude that the 4 A zeolite synthesized was chemically stable. Figure 4.15d shows the adsorption efficiency results obtained after 7 adsorption and desorption cycles. It can be seen that even after seven regeneration cycles, zeolite 4A maintains high reuse efficiency. It can be concluded that the synthesized zeolite 4A exhibits high reusability characteristics and it is chemically stable.

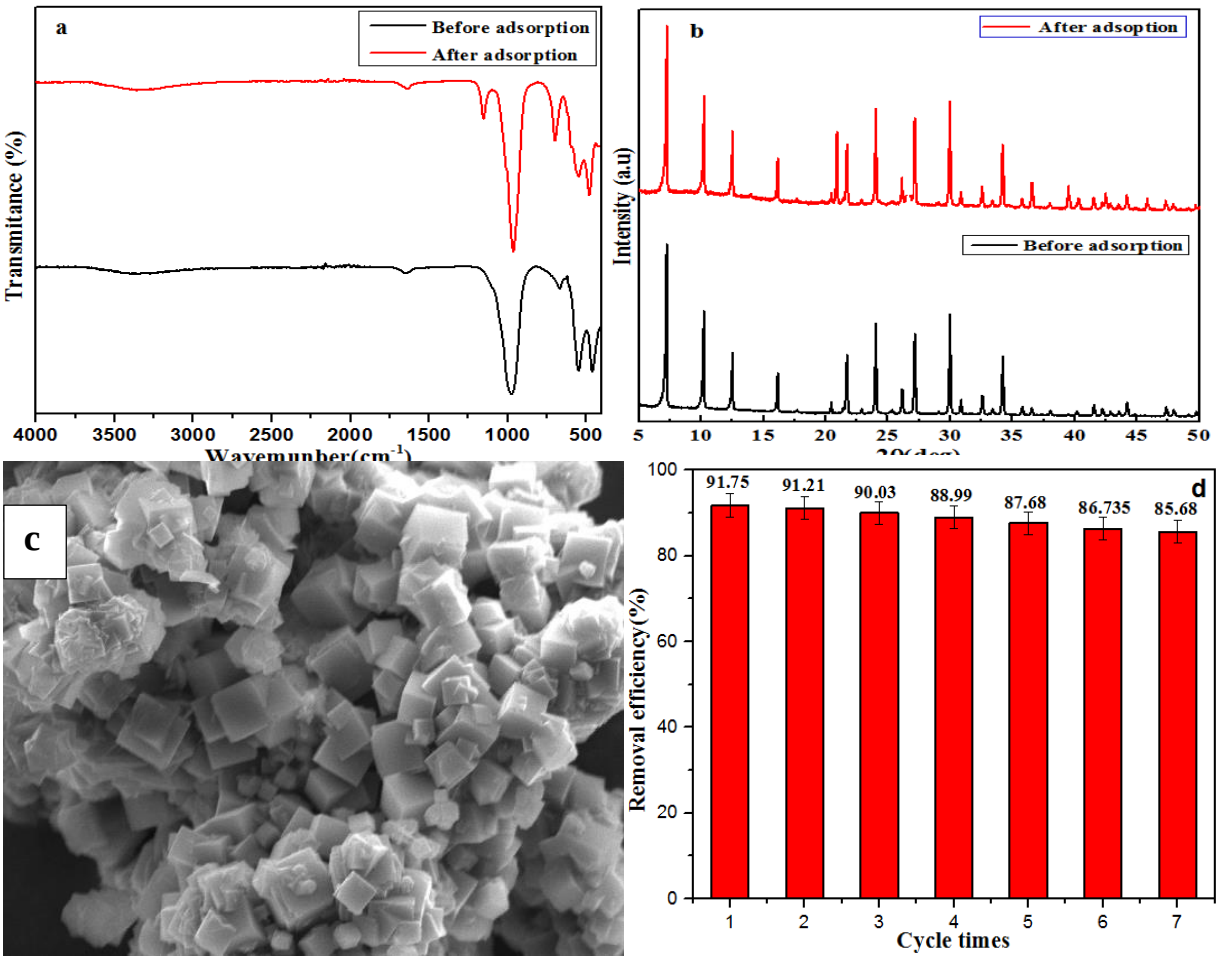

Figure 4.15: FT-IR spectrum (a), XDR patterns (b), SEM image (c) and reusability (d) of zeolite 4A after adsorption.

4.3.9 Partial conclusion

Raw kaolin from the locality of Bong in Fotouni West Cameroon is a promising source of silicon and aluminum. The hydrothermal method was used to synthesize zeolite 4A. the results of the various analyzes showed that the synthesized material was pure with high crystallinity and a homogeneous cubic morphology characteristic of zeolite 4A. The effectiveness of zeolite 4A's removal of pharmaceutical contaminants was evaluated with the antibiotic ciprofloxacin. The elimination efficiency was 91.75% with a maximum adsorption capacity (q_{max}) 87.72 mg/g obtained from the Langmuir model under optimal conditions (contact time 80 min, pH 8, initial concentration of CIP 60 ppm, dose of zeolite 4A 20 mg at 25°C). Analyzes carried out after seven

regeneration cycles showed that the synthesized zeolite 4A had a high reusability rate and was chemically stable.

4.4 Unravel the adsorption mechanism of ciprofloxacin on the surface of zeolite 4A (001) in aqueous solution

Molecular stimulation provides an effective way to examine the sorption mechanism based on experimental results. In order to effectively predict the existing and stable form of CIP molecules in aqueous media and their adsorption mechanism to improve the design of adsorbents, DFT and MC methods were used. The objective of this study was to assess the reactivity and stability of CIP molecules in aqueous solution and detect its interaction mechanism on the surface of zeolite 4A (001).

4.4.1 Study of the functional density theory of ciprofloxacin molecules in aqueous phase

In general, ciprofloxacin exhibits a high proton exchange probability (H^+) in aqueous solution (Chohan et al., 2019) as shown in Figure 4.16. It is therefore essential to award a great attention to the different forms and physicochemical characteristics of these chemical systems.

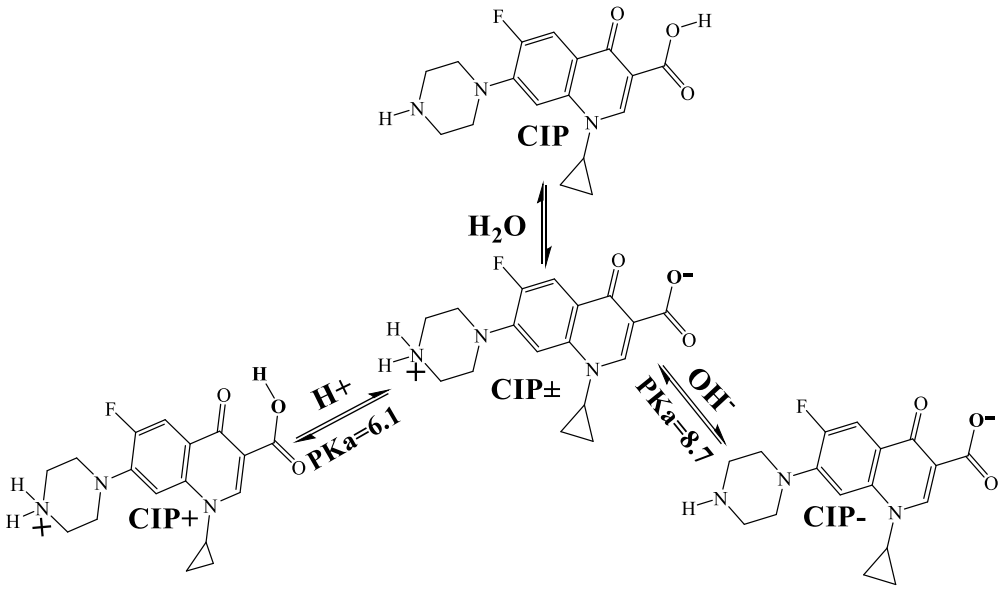

Figure 4.16: Different molecular structures of CIP in aqueous solution.

4.4.1.1 *Electronic distribution*

The GGA/PPE method made it possible to obtain the optimized structures and orbitals (HOMO and LUMO) of ciprofloxacin molecules in order to determine their reactivities, identify their electrophilic and nucleophilic sites, and study their behavior on the surface of zeolite 4A

(001). The optimized, LUMO and HOMO structures of ciprofloxacin molecules are shown in Figure 4.17. In the structures of the LUMO orbitals of the four compounds studied, the electrons are uniformly distributed on the six-membered rings carrying the Fluorine atom and the ketone group. Which suggests that these four compounds can easily receive electrons through these regions. Thus, they can be attacked by nucleophilic centers (Yang et al., 2022). The low electron density around these two rings may be due to the fact that they are linked to the Fluorine atom and the carboxylic acid group which are electron attractors. In the structures of the HOMO orbitals of the CIP and CIP+ compounds, the electrons are mainly delocalized on the heterocycle carrying two nitrogen atoms and on the six-membered ring carrying the Fluorine atom. While in the structures of the HOMO orbitals of the CIP± and CIP- compounds, the electrons are highly concentrated on the carboxylate and ketone groups. This indicates a strong capacity of these compounds to transfer electrons to electrophilic centers via these groups (Hassan, Sajid, Tanimu, Abdulazeez, & Alhooshani, 2021). These centers are active sites for nucleophilic reactions and can ensure the formation of chemical bonds (coordination bond) with empty orbitals of the adsorbent surface (Khnifira et al., 2022). In general, it can be observed that the CIP± and CIP- compounds have a high donating power, due to the transformation of the carboxylic acid group into a carboxylate, thus making this group very rich in electrons.

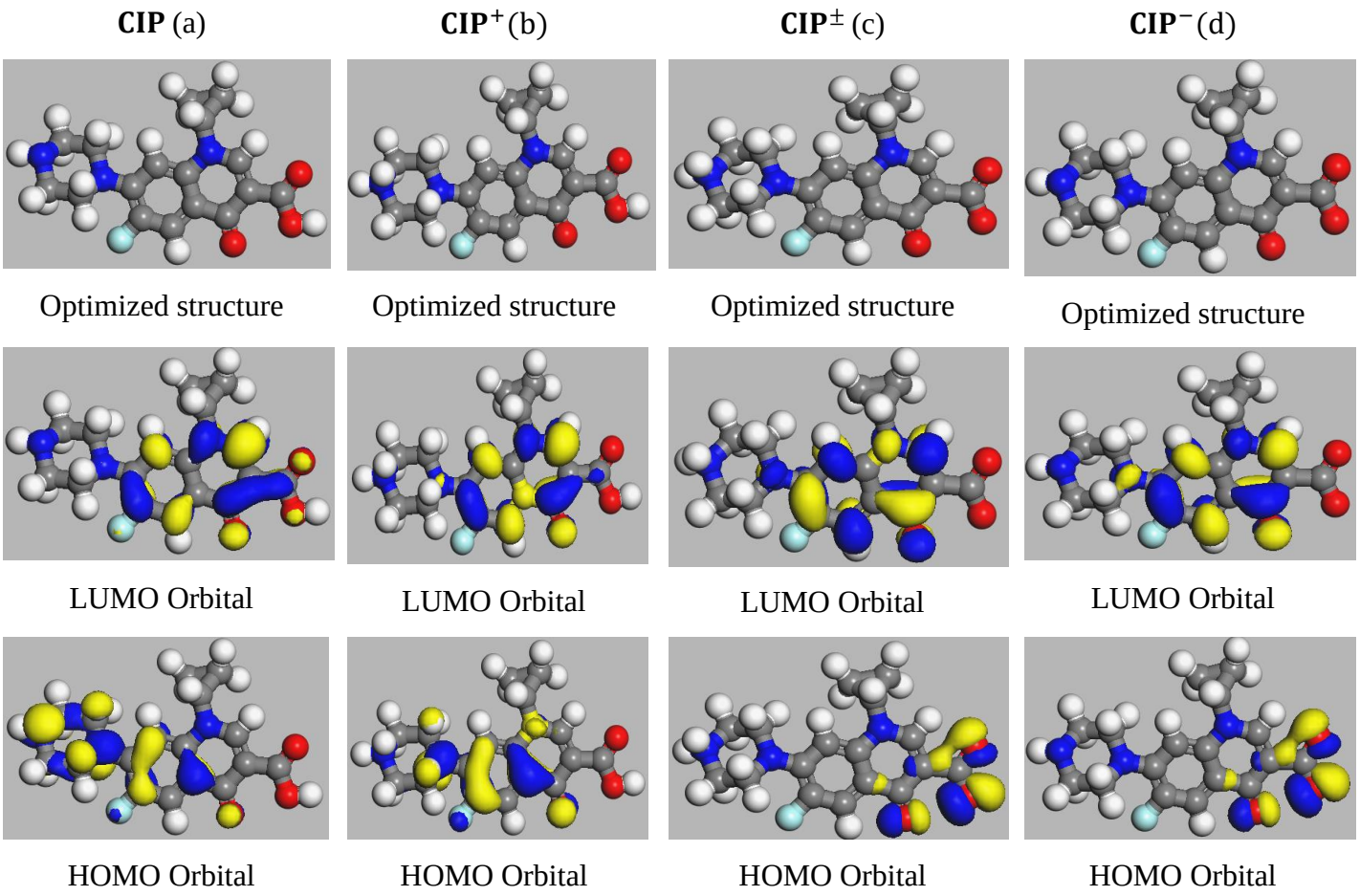

Figure 4.17: Quantum descriptors of CIP (a), CIP+ (b), CIP± (c), and CIP- (d), compounds. Legend of atoms: Gray=C, Red=O, White=H. Yellow and blue isosurface represent electron density: yellow regions represent electron loss and blue regions represent electron buildup.

4.4.1.2 *Description of quantum chemical parameters and reactivity indices*

The essential quantum descriptors are the energies of the HOMO (E_{HOMO}), LUMO (E_{LUMO}) orbitals and the gap energy (ΔEgap). A high HOMO energy value reflects the ability of the molecule to provide electrons and a low LUMO energy value reflects the ability to receive electrons (Acar, 2022). Lower adsorption of molecules on the adsorbent surface is associated with high values of ΔEgap, while lower values demonstrate more efficient adsorption of the molecule on the absorbing surface (Khnifira et al., 2022; Yang et al., 2022). Table 4.6 presents the quantum chemistry descriptors of the compounds studied.

Table 4.6: Quantum chemistry parameters of ciprofloxacin molecules in aqueous phase.

Parameter	CIP	CIP^+	$CIP^\pm$	CIP^-
E_{HOMO}	-5.298	-5.655	-4.362	-4.575
E_{LUMO}	-2.455	-2.564	-3.405	-2.065
ΔE_{gap} (eV)	2.843	3.091	0.957	2.51
χ (eV)	3.877	4.110	3.884	3.32
μ (eV)	-3.877	-4.110	-3.884	-3.32
η (eV)	1.421	1.546	0.479	1.255
σ (eV^{-1})	0.703	0.647	2.090	0.797
(ω)	5.286	5.467	15.759	4.391
(ε)	0.189	0.183	0.063	0.228
(ω^+)	3.525	3.602	13.877	2.888
(ω^-)	7.402	7.712	17.761	6.208
ΔN	1.364	1.330	4.058	1.323
$\Delta E_{Back-donation}$	-0.355	-0.386	-0.120	-0.314
Dipolar moment (Debye)	8.000	12.570	46.958	14.243
Total energy (eV)	-1147.524	-1147.981	-1147.511	-1148.014

According to table 4.6, the energies of HOMO evolve in the following order: CIP± > CIP- > CIP > CIP+. The CIP± compound has the highest HOMO energy (-4.362 eV), suggesting that it has the highest ability to deliver electrons to the adsorbing surface. Likewise, the values of the LUMO energies of CIP± observed are lower than those of the other compounds. This suggests that the CIP± compound has a higher electron acceptance capacity than the other compounds. The E_{LUMO} values of the molecules examined increase as follows: CIP->CIP> CIP+> CIP±. It should be noted that the ability of a compound to interact with the adsorbent surface is linked to its electron donating capacity. Therefore, the electron donating capacity can be classified in the following order: CIP±>CIP->CIP+>CIP. In addition, the CIP± compound presents the lowest gap energy value (ΔEgap =0.957 eV). Which has high reactivity, chemical stability and higher adsorption efficiency at the adsorbent surface compared to other compounds (Khnifira et al., 2022).

Electronegativity (χ) is used to measure a molecule's ability to attract electrons. Its low value suggests a high potential for the compound to release electrons. Electronegativity values are in the following order: CIP+ > CIP > CIP±>CIP-. The high electronegativity value of CIP+ reflects its high capacity to retain electrons, which may lead to its poor adhesion on the adsorbent surface (Singh et al., 2021).

According to Bhomick et al. (2023), the dipole moment of a compound increases with its polarity and vice versa. In addition, the increase in the dipole moment is linked to the increase in adsorption (Bhomick et al., 2023). All compounds studied have a positive dipole moment, demonstrating that they are all polar and can adsorb. The increasing dipole moment values in the following order: CIP±>CIP-> CIP+>CIP, which suggests that the CIP± compound will be more adsorbed on the adsorbent surface.

Chemical hardness is a parameter reflecting the stability of a chemical system and representing the resistance to polarization of electronic clouds of atoms, ions or molecules (Yang et al., 2022). Hard molecules have higher stability (low η) than soft molecules. Chemical hardness is in the following order: CIP+>CIP>CIP->CIP±. According to these results, it is therefore concluded that the CIP± compound (η = 0.479 eV) is the most stable compound compared to the others.

We can also describe the stability and reactivity of a molecular system based on softness (σ). A soft compound has a fairly high ΔEgap value while a soft compound has a fairly low Δ Egap value (Khnifira et al., 2022). The reactivity of a hard compound is lower than that of a soft compound because it cannot easily transmit electrons to the receptor. According to Table 4.6, it is observed that the σ value of the CIP± compound (σ = 2.090 eV) is higher compared to other species. Thus, it is more reactive, stable and absorbs more at the adsorbent surface.

ΔEback-donation values below zero suggest that electron transfer has energetic advantages for all compounds studied (M. Khnifira., W. Boumya., J. Attarki., A. Mahsoune., M. Sadiq., M. Abdennouri., 2022). Nucleophilicity (ε) and electrophilicity (ω) are considered by chemical descriptors as parameters which quantitatively define the nature of the attack of a molecule. The electron-donor (ω-) and electron-acceptor (ω+) powers of a system or molecule are closely linked. Compounds with high ω+ value are good electron acceptors, while compounds with high ω- value are good electron density donors (Singh et al., 2021).

ΔN value has also been mentioned to evaluate the ability of a chemical system to transport electrons to the surface of the adsorbent (Khnifira et al., 2022). The electron transfer potential of a molecule with a positive value of ΔN (ΔN>0) is higher, while a molecule with the opposite tendency is characterized by a negative value of ΔN (ΔN<0) (Khalil, 2003; Sedik et al., 2022). The ΔN values are positive for all systems, suggesting that these molecules have an ability to transport electrons into the empty orbitals of the adsorbent through a chemical bonding process (Nwanonenyi et al., 2020). In this way, all molecules examined exhibit a tendency to exchange electrons. Furthermore, the ΔN value of +4.058 suggests that CIP± is a strong electron donor. From the results mentioned above, it is possible to conclude that the studied compounds can be perceived as Lewis bases and can therefore establish coordination bonds with the empty orbitals of the adsorbent surface. In addition, the ciprofloxacin molecule is stable and reactive in the aqueous phase in the form of zwitterion (CIP±).

4.4.1.3 *Local responsiveness based on Fukui indices*

Fukui indices play a crucial role in detecting nucleophilic reagents and electrophilic centers present in the same compound. The electrophilic and nucleophilic attack index of the studied compounds is measured by the maximum threshold values of fk- and fk+, which are calculated using the Fukui function distribution (Belachew & Hinsene, 2022; Li, Huang, Du, Liu, & Hu, 2020). Table 4.7 lists the electron-accepting capacity of chemical systems, which is calculated from high values of fk+, and the electron-donating capacity of chemical systems, which is measured from high values of fk−. Regarding the CIP are the atoms O_2, N_6, N_7, C_{14} and C_{23} are the most electron-rich sites with high values of fk−, thus they are the most active sites in electrophilic attack. Atoms O_2, O_4, C_{12}, C_{19}, C_{23} and C_{24} have high fk+ values, indicating that these atoms are nucleophilic attack centers. For CIP+, the O_2, N_6, C_{13}, C_{14} and C_{23} atoms are nucleophilic sites and the electrophilic sites are the O_2, C_{12}, C_{14}, C_{19}, C_{22} and C_{23} atoms. Regarding CIP± and CIP-, the atoms O_2, O_3, O_4 and C_{24} are indicators of the electrophilic attack sites, while the nucleophilic attack sites are the atoms O_2, C_{12}, C_{14}, C_{15}, C_{19}, C_{22} and C_{23}. As shown in Table 4.7, the molecules studied have different electrophilic and nucleophilic attack centers, which could favor their interactions with the adsorbent surface. The analysis of the highest values of fk- of the compounds studied allows us to conclude that the electron donation effect evolves in the following order: CIP±>CIP->CIP+>CIP. These electron-rich centers are

mainly found on oxygen and nitrogen atoms. These atoms are nucleophilic centers that send electrons to the empty molecular orbital of the adsorbent to create coordination bonds, while the carbon atoms are the electrophilic sites through which the system accepts the electron to create feedback bonds to the adsorbent surface (Bouayad et al., 2018). Fukui's function indicators agree with quantum indicators.

Table 4.7: Distribution of Fukui indices in aqueous phase.

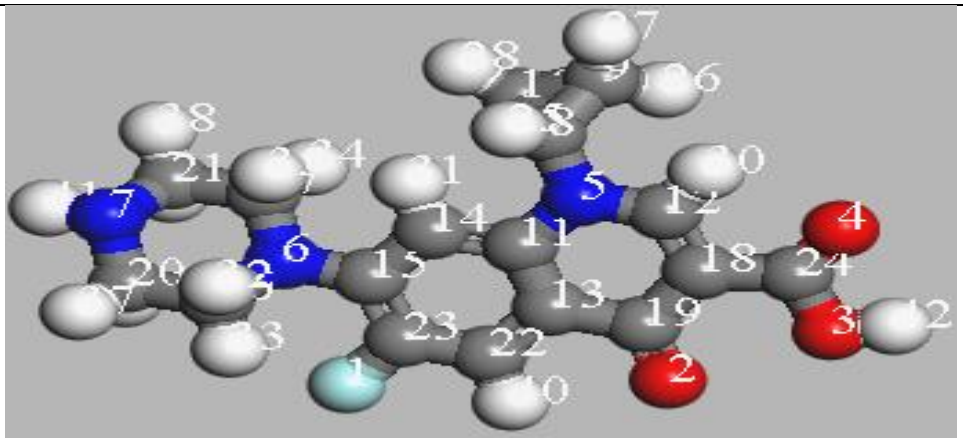

Atoms	CIP		CIP^+		$CIP^\pm$		CIP^-	
	f_k^-	f_k^+	f_k^-	f_k^+	f_k^-	f_k^+	f_k^-	f_k^+
F_1	0.023	0.025	0.04	0.026	0.008	0.026	0.008	0.026
O_2	**0.041**	**0.076**	**0.084**	**0.089**	**0.097**	**0.098**	**0.101**	**0.099**
O_3	0.004	0.022	0.006	0.014	**0.329**	0.02	**0.326**	0.021
O_4	0.011	**0.046**	0.019	0.034	**0.161**	0.019	**0.162**	0.02
N_5	-0.001	0.012	0.006	0.013	0.003	0.01	0.004	0.012
N_6	**0.094**	0.013	**0.106**	0.012	0.005	0.011	0.006	0.015
N_7	**0.093**	0.001	-0.002	-0.001	0	-0.002	0	0.001
C_8	-0.008	-0.018	-0.011	-0.018	-0.007	-0.016	-0.007	-0.017
C_{11}	0.022	0.022	0.037	0.025	0.013	0.029	0.013	0.029
C_{12}	0.015	**0.168**	0.023	**0.139**	0.031	**0.095**	0.031	**0.099**
C_{13}	**0.043**	0.011	**0.063**	0.007	0.009	0.009	0.009	0.008
C_{14}	**0.048**	0.06	**0.047**	**0.071**	0.01	**0.072**	0.01	**0.067**
C_{15}	0.017	0.025	0.031	0.038	0.012	**0.054**	0.012	**0.051**
C_{16}	-0.023	-0.007	-0.018	-0.008	-0.002	-0.009	-0.003	-0.01
C_{17}	-0.028	-0.011	-0.022	-0.011	-0.002	-0.007	-0.003	-0.01
C_{18}	0.011	0.024	0.024	0.02	0.008	0.018	0.007	0.017
C_{19}	0.018	**0.067**	0.029	**0.082**	0.036	**0.091**	0.035	**0.093**
C_{22}	0.026	0.06	0.036	**0.079**	0.008	**0.102**	0.008	**0.097**
C_{23}	**0.042**	**0.049**	**0.065**	**0.042**	0.013	**0.042**	0.013	**0.043**
C_{24}	0.009	**0.045**	0.015	0.032	**0.128**	0.023	**0.125**	0.023

The DFT results show that in the gas phase, ciprofloxacin is stable, reactive in the form of zwitterion (CIP±), the oxygen, nitrogen and carbon atoms are responsible for its interaction with the adsorbent surface.

4.4.2 Theoretical X-ray diffraction analysis of zeolite LTA

It is known that each material has a particular crystal field intensity. The XRD characterization technique is used to verify purity, identify the crystalline phases of a material, and ensure that the material used conforms to the description in the literature. The results of XRD analysis of zeolite LTA imported into Material Studio software were obtained using the Reflex module, as shown in Figure 4.15. According to Figure 4.18, the diffraction peaks are observed at reference values of single-phase zeolite 4A (Wang et al., 2019b), namely 7.3°; 10.4°; 12.8°; 16.3°; 21.9; 24.2°; 27.8° and 34.3°. These values can also be confirmed by the experimental results of the synthesized zeolite 4A (Figure 4.2). From these results, we can confirm that the studied zeolite LTA is identical to zeolite 4A.

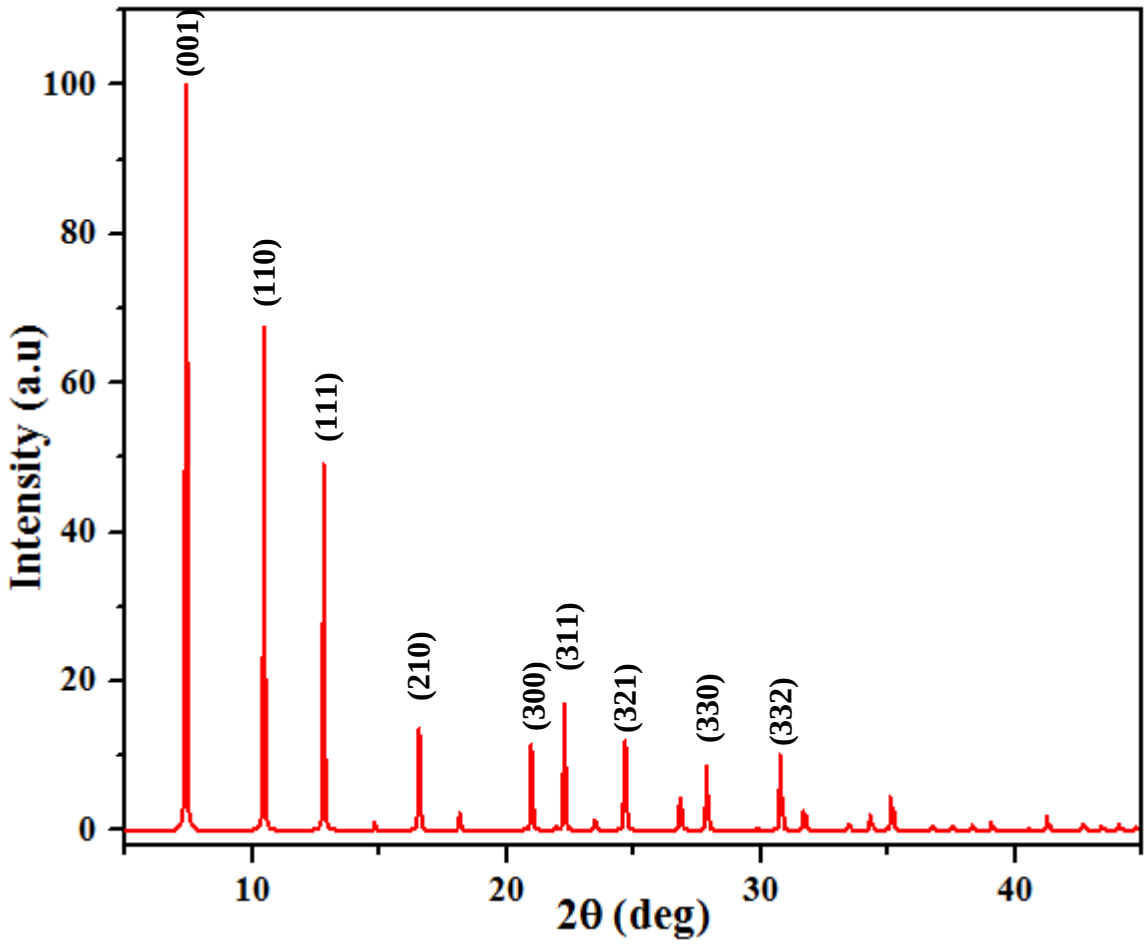

Figure 4.18: X-ray difraction of zeolite LTA.

4.4.3 Monte Carlo molecular modeling

4.4.3.1 ***Adsorption of CIP, CIP±, CIP-, and CIP+ on the surface of zeolite 4A (001)***

The evaluation of the interaction between the studied compounds (CIP±, CIP-, CIP, CIP+) on the surface of zeolite 4A (001) was carried out using the MC simulation technique. The results obtained are presented in Figure 4.19. We can clearly visualize the equilibrium configuration of the compounds studied on the zeolite surface through the top and side views. It is clearly observed that all the molecular structures of the studied compounds are adsorbed on the zeolite surface, mainly by the oxygen and nitrogen atoms, as well as by the aromatic ring. As shown in Figure 4.19, the compounds studied are placed parallel to the surface of zeolite 4A(001) in all systems. Furthermore, the compounds are adsorbed in a quasi-planar manner in the aqueous solvent molecules, with maximum contact on the zeolite surface, reflecting strong interaction between the adsorbent and the adsorbate. The parallel and planar position of the compounds

studied on the surface of zeolite 4A indicates that adsorption is controlled by the chemisorption process (Khnifira et al., 2022).

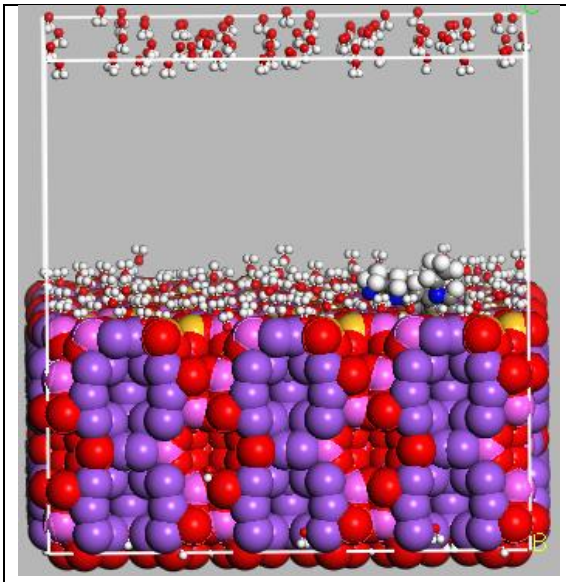

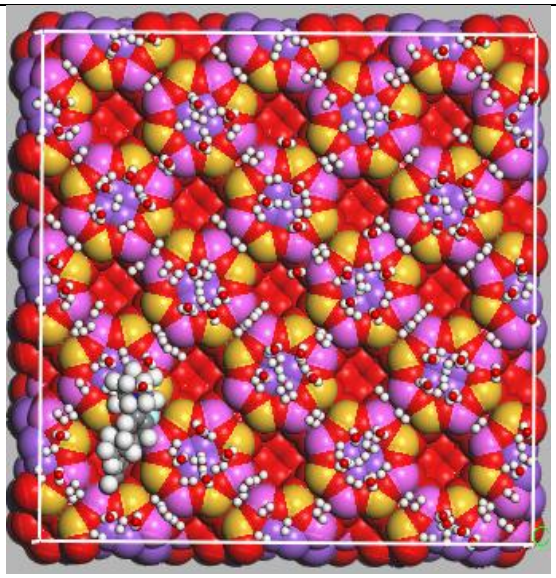

350 H_2O , CIP /zeolite 4A (001)(has)

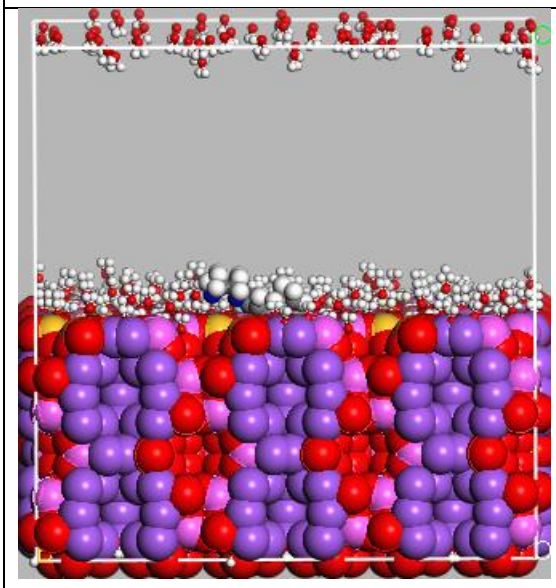

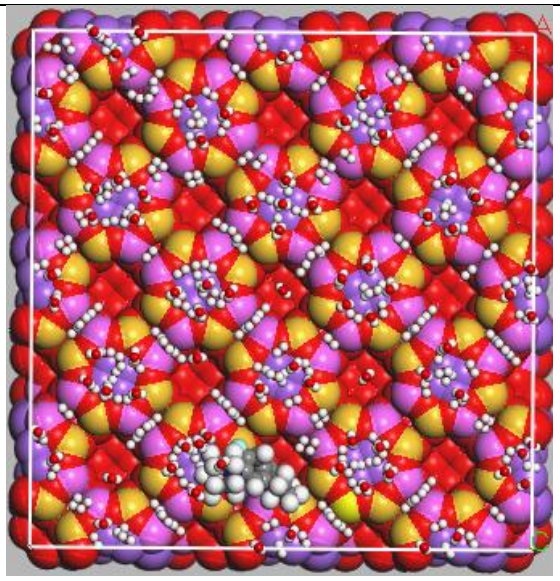

350 H_2O , CIP^+ /zeolite 4A (001)(b)

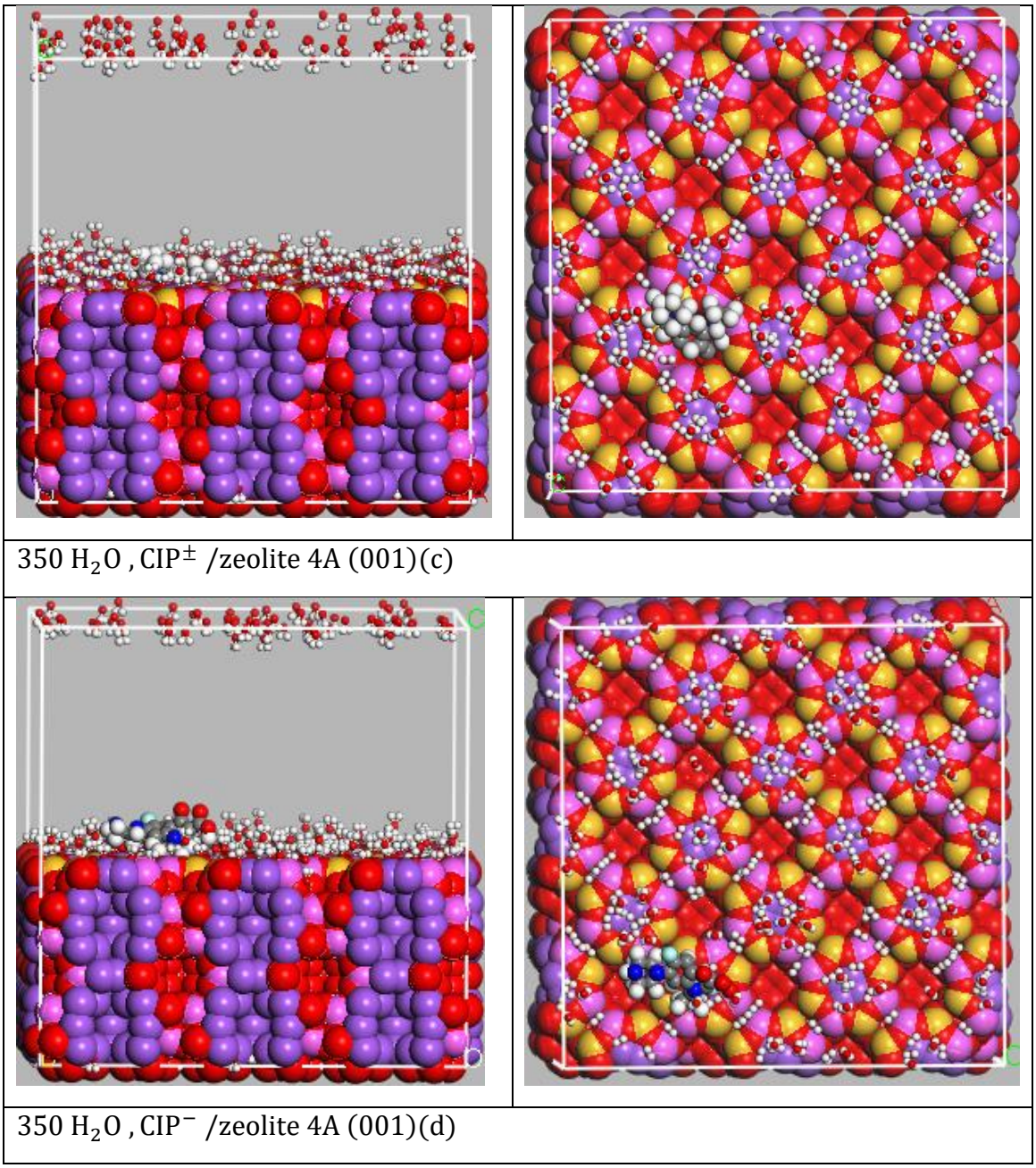

Figure 4.19: Side view (left) and top view (right) of the most stable low-energy configuration for adsorption of CIP (a), CIP+ (b), CIP± (c) and CIP-compounds on the surface of zeolite 4A (001) in aqueous medium at 298 K.

4.4.3.2 *Dynamic descriptors*

The values of the dynamic descriptors of the four compounds studied are presented in Table 4.8. The comparison of the individual adsorption energies (Ead⁄dNi) of the compounds studied and that of water show that the adsorption energies of the compounds studied are not

close. In Revenge, the individual adsorption of the compounds studied is high compared to that of water. These results suggest that water molecules promote the adsorption of CIP±, CIP, CIP- and CIP+ on the surface of zeolite 4A (001). Furthermore, in Table 4.8 we see that the deformation energies are all positive, which suggests that the water molecules and the compounds studied did not undergo deformation during the adsorption process (Kondori, Zendehboudi, & James, 2019). The negative values of total energy (E_{Tot}) confirm that adsorption was favorable for all compounds on the surface of zeolite 4A. Similarly, the values of adsorption energies (E_{Ads}) were negative, suggesting that the adsorption of CIP±, CIP, CIP- and CIP+ can occur spontaneously.

Although all complexes have similar adsorption energy values, the strong negative value of adsorption energy for CIP± suggests that the CIP±@zeolite 4A complex is more stable and that CIP± is strongly adsorbed on the surface of the zeolite (001) compared to the others (Boumya et al., 2021). In addition, the adsorption energy of the zeolite/molecule complex is established as a function of the order of the quantum descriptors. This underlines the importance of the porous structure of the zeolite which plays a primordial role in the adsorption of these compounds. Heteroatoms such as nitrogen and oxygen, as well as the "pi" electrons of the aromatic ring contribute effectively during the interaction between the zeolite and the ciprofloxacin molecules.

Table 4.8: Parameters of the dynamic descriptors of the most stable configurations of CIP±, CIP-, CIP, and CIP+ on the surface of zeolite 4A (001) (in Kcal/mol).

Compounds	E_{Tot}	E_{Ads}	RAE	$E_{Deformation}$	H_2O dEad/dNi	Ead/dNi
CIP	-126.31	-127.29	-165.47	38.17	-0.72	-13.66
$CIP^{\pm}$	-129.08	-129.50	-167.94	38.44	-0.18	-28.87
CIP^{-}	-128.99	-129.44	-167.89	38.45	-0.24	-27.76
CIP^{+}	-126.91	-127.31	-165.63	38.33	-0.18	-12.22

4.4.3.3 *Binding energy*

MC simulation was also used to study the mode of action of the molecular system on the surface of zeolite 4A (001) in aqueous phase. Table 4.9 presents the obtained values of binding, interaction and electrostatic energies. It can be observed that the interaction and electrostatic energies are negative indicating that the adsorption of the CIP molecules on the zeolite surface can be carried out in two ways: by electrostatic interaction between the surface charge of the CIP

molecules and the surface of the zeolite (physisorption) and/or by ion exchange between the compensating sodium ions and the active Lewis sites generated by the oxygen atoms (chemisorption) (Mahmoud et al., 2018; Wei, Gui, Kang, Wang, & Tang, 2018). Positive values of binding energies indicate very stable interaction and an exothermic reaction (Khnifira, et al., 2022) . The increase in binding energies follows the order: CIP±>CIP->CIP>CIP+. Which indicates that the CIP±@zeolite 4A complex is the most stable, therefore, the binding energy of CIP± increases with the interaction force with the surface of zeolite 4A.

Table 4.9: Interaction, binding and electrostatic energies of the 4A molecule/zeolite complexes in (Kcal/mol).

Compounds	$E_{Interaction}$	$E_{Binding}$	$E_{Electrostatic}$
CIP	-126.96	126.96	-73.83
$CIP^{\pm}$	-129.06	129,06	-75.27
CIP^{-}	-128.93	128.93	-76.26
CIP^{+}	-126.90	126.90	-74.40

4.4.3.4 *Analysis of the total density of state*

To further our understanding of the electronic interactions between the zeolite 4A (001) surface and ciprofloxacin molecules, we evaluated the density of states (DOS) of the surface atoms in their most stable configuration. One can evaluate the type of electron transfer during the adsorption procedure by comparing the DOS curves after and before the adsorption process. Zeolite 4A and molecules/zeolite 4A complexes were subjected to density of state calculations to study the impact of CIP±, CIP+, CIP and CIP- adsorption on the surface of zeolite 4A (001). The results obtained are illustrated in Figure 4.20. The DOS peaks of isolated zeolite 4A are mainly composed of 3S and 3P orbitals, as shown in Figure 4.20. After adsorption, the s and p orbitals of zeolite 4A shift to the left, resulting in a lower of energy due to redistribution and charge transfer (El-Mansy, El-Bana, & Fouad, 2017). Furthermore, the shifted peaks have a higher intensity than the isolated surface of zeolite 4A (before adsorption). This process confirmed that the impacted orbits play a role in the interaction process and the reduction in total energy indicates that it consolidates in the complexes obtained (Wei et al., 2018). All complexes experienced peaks close to the Fermi level, but those of isolated zeolite 4A were more intense, suggesting a strong interaction between the zeolite and the compounds studied. Beyond the Fermi

energy, all structures experience a significant transformation after being adsorbed. This transformation may be due to the fact that low energy electrons were transported from the molecules to the surface of the zeolite (Khnifira et al., 2022). After adsorption, the state density diagrams of CIP and CIP+ showed a slight decrease in the intensities of the complex peaks. This indicates a weak transfer of electrons towards the surface of the zeolite. While the DOS diagrams of CIP- and CIP±, a strong decrease in peak intensities is observed, illustrating the low energy electrons were strongly transferred onto the zeolite surface, suggesting that these compounds are strongly adsorbed on the zeolite surface. By comparing the intensities of the peaks and DOS curves after and before adsorption, we can say that the electrons are efficiently transferred to the zeolite surface in the order: CIP±>CIP->CIP>CIP+.

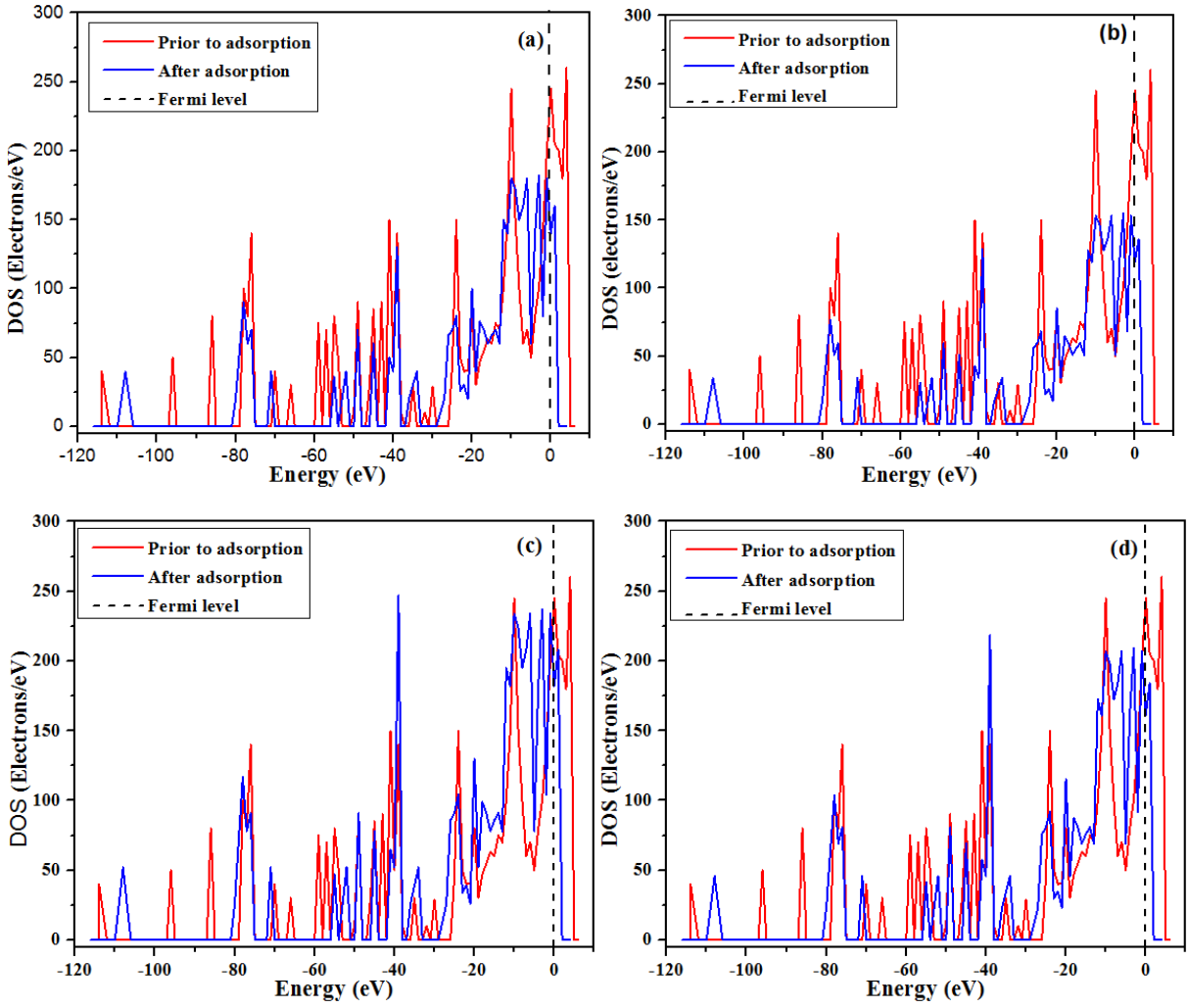

Figure 4.20: Density of states (DOS) before and after adsorption of CIP- (a), CIP± (b), CIP+ (c) and CIP (d) on the surface of zeolite 4A (001) in aqueous phase.

4.4.3.5 *Radial distribution function*

The results of simulation studies were analyzed using the radial distribution function (RDF) to examine the distance between the different compounds studied and the surface of zeolite 4A (001), in order to deepen our understanding on the nature of the bond formed during the adsorption process. In general, peaks located at a distance greater than 3.5 Å are related to electrostatic interaction, while peaks located at a distance less than 3.5 Å are directly related to chemisorption (Khnifira, et al., 2022 Sharif et al., 2020) . Figure 4.21 shows the RDF plots of each compound studied with the surface of zeolite 4A (001).

For all compounds studied, the most intense peaks are observed at a distance less than 3.5 Å, as shown in Figure 4.21. which suggests that all these studied species are strongly bound to the surface of zeolite 4A by chemisorption. All species show low intensity peaks at a distance greater than 3.5 Å, indicating weak electrostatic interaction (physisorption). Furthermore, the intensity of the peaks varies depending on the complex formed, with a value of 23.34 for CIP±, 21.93 for CIP-, 20.91 for CIP and 20.21 for CIP+. This demonstrates a stronger interaction between the CIP± and the surface of the zeolite. The order of binding energy according to the maximum intensity values is: CIP±>CIP->CIP>CIP+. The RDF results confirm that the studied compounds adsorb on the zeolite surface by the chemisorption and physisorption processes with a predominance of chemisorption.

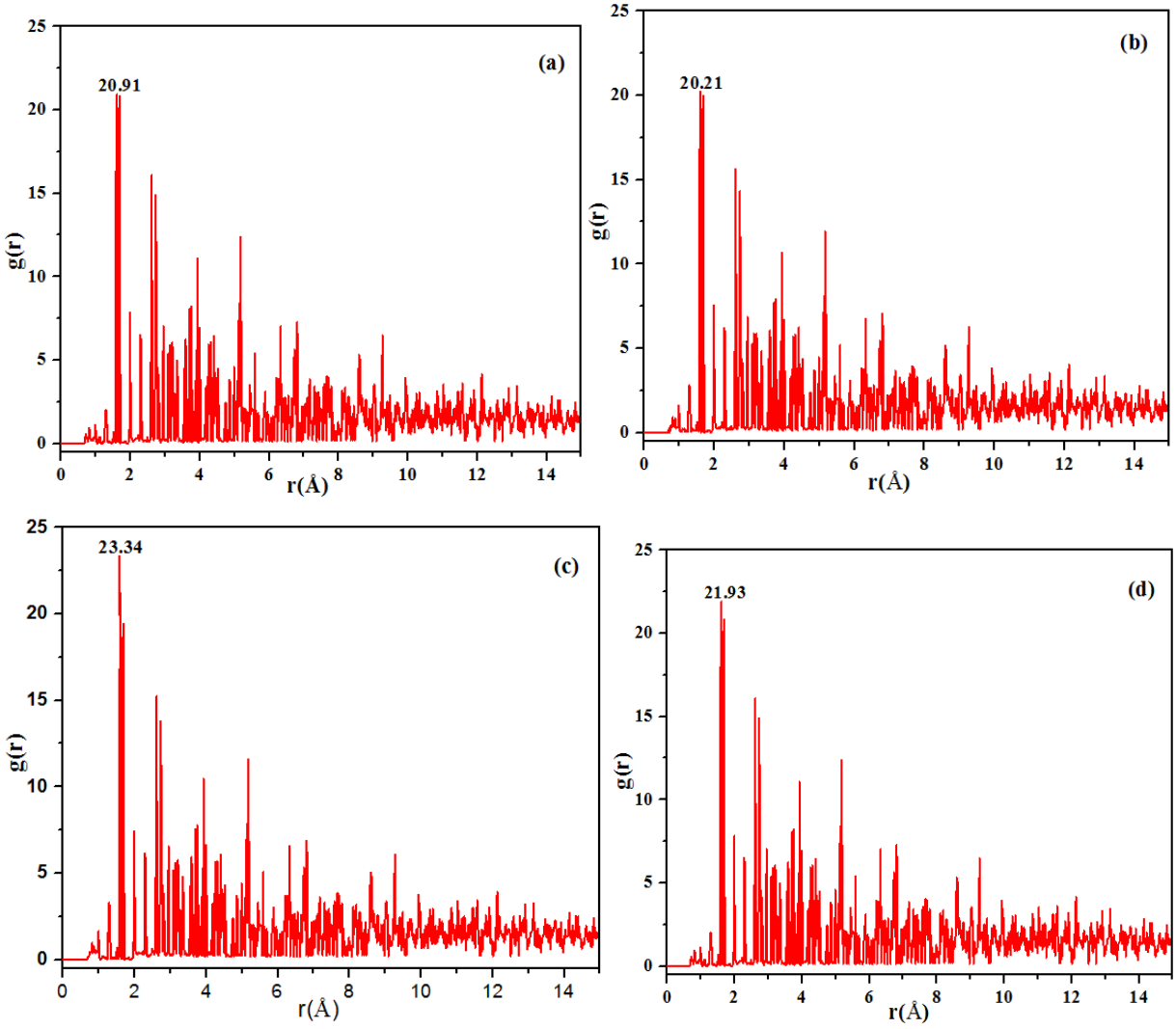

Figure 4.21: Radial distribution function as a function of the distance between CIP (a), CIP+ (b), CIP± (c) and CIP- (d) and the surface of zeolite 4A (001).

4.4.3.6 *Effect of temperature on adsorption energy*

Adsorption energy is used to subtly describe the adsorption process. Therefore, adsorption energy can provide us with an easy method to classify the adsorption capacities of molecular systems (Singh et al., 2021). The studied molecules were adsorbed on the surface of zeolite 4A (001) at different temperatures in an aqueous solution, as shown in Figure 4.22.

The fact that the adsorption energy is negative confirms the exothermic and spontaneous nature of the adsorption process at all temperatures (Kondori et al., 2019). This implies that the molecules are attracted on the zeolite surface via the physisorption and/or chemisorption process. The value of adsorption energy (high negative value) leads to an increase in the interaction force,

which leads to an increase in adsorption capacity (Boumya et al., 2021). Thus, adsorption is more favorable for CIP± than the other compounds at all temperatures. Furthermore, Figure 4.22 shows that the absorption energy for all complexes increases with temperature. An increase in temperature results in activation of the adsorbent surface or activation of certain active sites, resulting in increased adsorption (Atugoda et al., 2020).

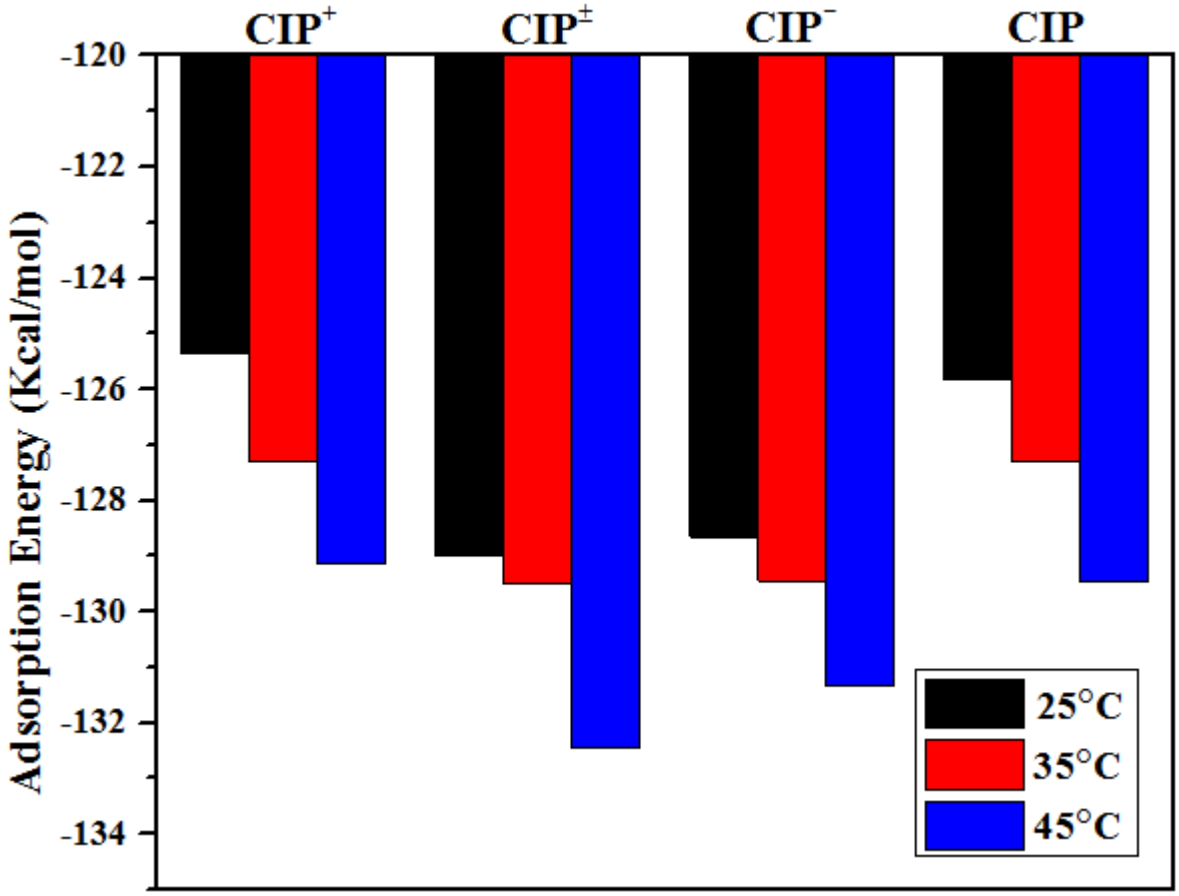

Figure 0.22: Influence of temperature on adsorption energy.

4.4.4 Partial conclusion

The DFT study made it possible to examine the electronic and structural characteristics of ciprofloxacin molecules. The DFT results revealed that in the aqueous phase, the ciprofloxacin molecule is stable, reactive in the form of zwitterion. Also, the oxygen, nitrogen atoms and the aromatic ring were responsible for the reactivity of ciprofloxacin. The MC simulation made it possible to decelerate the mode of interaction of ciprofloxacin molecules on the surface of zeolite 4A (001). The MC simulation results showed that the ciprofloxacin molecules on the surface of

zeolite 4A were favorable and spontaneous and the interactions occurred via chemisorption and physisorption processes. Thus, these results demonstrate that zeolite 4A is an effective adsorbent agent for eliminating ciprofloxacin.

4.5 Green synthesis of bio-magnetite@zeolite 4A nanocomposites for elimination of ciprofloxacin in aqueous solution

4.5.1 Characteristics of zeolite 4A, bio-magnetite nanoparticles and synthesized nanocomposites

4.5.1.1 *X-ray fluorescence analysis*

Table 4.10 presents the chemical composition of zeolite 4A and the synthesized nanocomposites. It can be observed that zeolite 4A is mainly composed of SiO_2 (40.01%), Al_2O_3 (37.70%) and Na_2O (19.61%). The ratio SiO_2/Al_2O_3 is approximately 1, this value corresponds to that of zeolite 4A as reported by Wang et al. (2019). In addition, the content of K_2O, TiO_2 and Fe_2O_3 is less than 1. This low content is due to the dissolution of these oxides during heat treatment (Mgbemere et al., 2019). It can also be seen that after the synthesis of the nanocomposites, the ratio SiO_2/Al_2O_3remained constant. This implies that the SiO_2 et Al_2O_3 oxides remained stable during the synthesis process. We can also notice that the content Fe_2O_3 has increased as well as the appearance of the group CH_2,which indicates the presence of bio-magnetite nanoparticles (TP-Fe_3O_4) in the zeolite framework.

Table 4.10: Chemical composition of zeolite 4A and synthesized nanocomposites.

Formula weight (%)	SiO_2/Al_2O_3	H_2O	CH_2	Na_2O	Al_2O_3	SiO_2	K_2O	CaO	TiO_2	Fe_2O_3
MZ-6	~1	10.0	16.05	16.14	24.34	26.91	0.051	0.022	0.68	6.62
MZ-4	~1	12.0	15.21	15.99	24.12	26.73	0.056	0.023	0.66	5.41
MZ-2	~1	12.0	13.05	16.03	24.17	26.37	0.052	0.021	0.62	3.31
zeolite 4A	~1	11.7	/	19.61	37.7	40.01	0.056	0.022	0.65	0.22

4.5.1.2 *Analysis by Fourier transform infrared spectroscopy*

Figure 4.23 presents the FT-IR spectra of zeolite 4A, bio-magnetite and synthesized nanocomposites. The spectrum of zeolite 4A presents a band at 3364 cm^{-1}resulting from the OH retirement mode of water within zeolite 4A (Mgbemere et al., 2019). The band at 974 cm^{-1}describes the internal vibration due to asymmetric Si-O or Al-O stretching bond (Du, Long, Liu, & Li, 2020). In addition, the band located at 559 cm^{-1}can be attributed to internal

vibrations of the zeolite framework. While the bands located at 455 $cm^{-1}$and 364 cm^{-1}respectively indicate the presence of internal vibration of the tetrahedra $SiO_4$and $AlO_4$with a bending mode of the sodality cages in zeolite 4A (Belachew & Hinsene, 2022). On the spectrum of bio-magnetite nanoparticles (TP-Fe_3O_4), the absorption band located at 435 $cm^{-1}$is responsible for the bonds $Fe^{2+} - O - Fe^{3+}$ within the magnetite (Demirezen & Yilmaz, 2018). Altaf et al. (2021), reported that the formation of magnetite can be recognized by the band around 434 cm-1 (Altaf et al., 2021). The bands located at 770 $cm^{-1}$and 673 cm^{-1}indicate the presence of the connection$Fe^{3+} - O$ et $Fe^{2+} - O$ (Jahangirian et al., 2013; Tran et al., 2021) . The absorption frequencies at 2090 $cm^{-1}$and 1630 cm^{-1} indicate the presence of Flavonoids and alkaloids as reported by bitombo et al. (2021) (Bitombo et al., 2021) . By comparing the spectra, we notice that the characteristic bands of zeolite 4A and the bio-magnetite nanocomposite appear on the spectra of the nanocomposites. This observation could demonstrate the success of the synthesis of TP-Fe_3O_4@zeolite 4A nanocomposites.

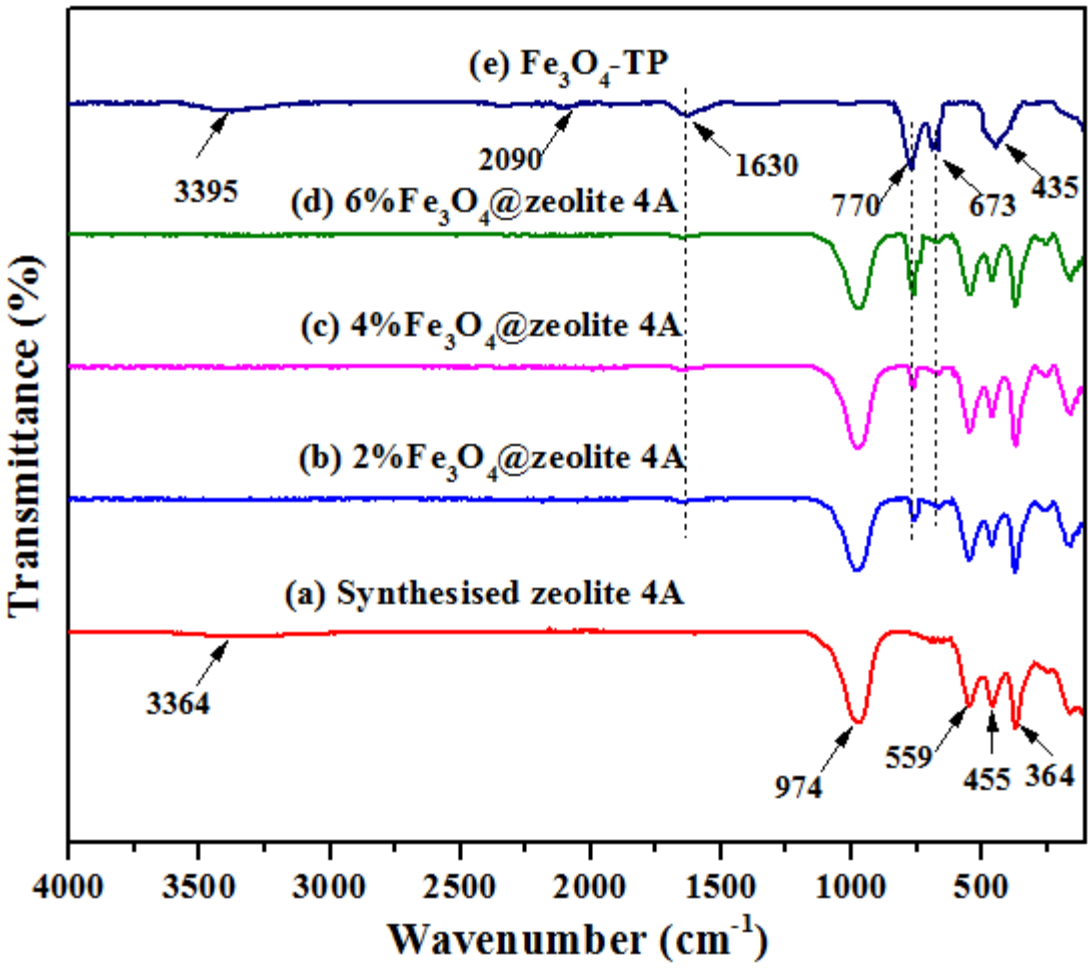

Figure 4.23: FT-IR spectra of synthesized zeolite 4A (a), MZ-2 (b), MZ-4 (c), MZ-6 and TP-Fe_3O_4(d).

4.5.1.3 *X-ray diffraction analysis*

XRD analysis was carried out to examine the purity and identify the crystalline phases present in the synthesized materials and the results are depicted in Figure 4.24. Figure 4.24(b) shows well-resolved images at 2θ~7.2°, 10.3°, 12.3°, 16.2°, 21.7°, 24.1°, 27.2°, 30.0° and 34.2°, which are basically consistent with the model Standard XRD of single-phase zeolite 4A in pure crystalline phase (Du et al., 2020), and these diffraction peaks corresponding to the (001), (110), (111), (210), (300), (311), (321), (330) and (332) planes respectively. These maximum values were attributed to zeolite 4A (JCPDS n°: 39-222). Wang et al. (2019), also reported similar results for zeolite 4A synthesized from kaolin by hydrothermal method (Wang et al., 2019b). Figure 4.24(f) shows the diffraction images at 2θ~18.7°, 31.2°, 35.8°, 43.64°, 53.6°, 57.2° and

62.9° corresponding to the (111), (200), (311), (400), (422), (511) and (440) planes of the crystalline phase of magnetite (JCPDS#00-065-0731) (Tran et al., 2021) . Altaf et al. (2021), reported similar peaks for magnetite synthesized by the co-precipitation method (Altaf et al., 2021). It is observed that the diffraction peaks of the Fe_3O_4isolated zeolite 4A and TP- overlap with those of the nanocomposites, which confirms the incorporation of TP- Fe_3O_4 into the structure of the zeolite 4A and their stabilities.

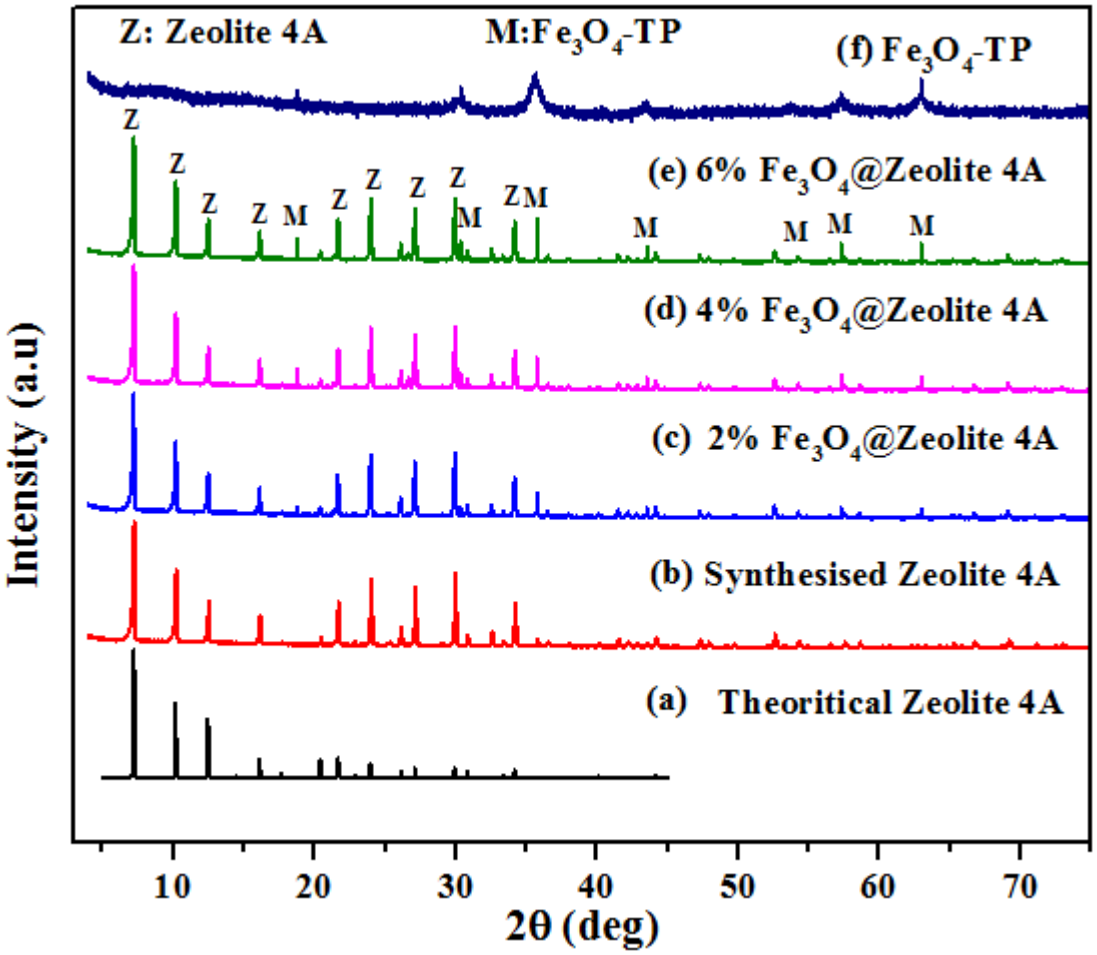

Figure 4.24: XRD pattern of theoretical zeolite 4A (a), synthesized zeolite 4A (b), MZ-2 (c), MZ-4 (d), MZ-6 (e) and TP-Fe_3O_4(f).

4.5.1.4 *Scanning electron microscopy and energy dispersive spectrometry*

SEM images of zeolite 4A, bio-magnetite and MZ-6 nanocomposite are shown in Figure 4.25. The structure observed in Figure 4.25a exhibits effective dispersion, high crystallinity and a cubic morphology with an average cube diameter of 5µm. This morphology corresponds to the

one of zeolite 4A as described by Kora et al (Lucresse et al., 2023). EDS analysis confirmed that oxygen, sodium, silicon and aluminum are the main components of the synthesized zeolite 4A Figure 4.25A). In addition, the Si/Al ratio is approximately 1, which corresponds to an ideal value for zeolite 4A (Tran et al., 2021). Figure 4.25b shows irregular agglomerated and approximately spherical particles with a diameter of 100 nm characteristic of magnetite nanoparticles (Bica et al., 2020). The EDS spectrum of TP-Fe_3O_4 nanoparticles (Figure 22B) confirmed that iron, oxygen and carbon were essential components of TP-Fe_3O_4 nanoparticles. In addition, the Fe/O ratio was approximately 0.76, which corresponds perfectly to the stoichiometric ratio (Fe/O=0.75) of magnetite (Fe_3O_4) (Tran et al., 2021) . The three nanocomposites showed almost identical SEM images and EDS spectra, so we only exposed those of the MZ-6 nanocomposite. Figure 4.25c shows the MZ-6 nanocomposite sample, which exhibits homogeneous adhesion of magnetite nanoparticles to the surface of zeolite 4A. We can also see that the nanocomposite retains the crystal structure of zeolite 4A and still exhibited good crystallinity. On the EDS spectrum (Figure 25C), the nanocomposites were confirmed to be composed of Si, Al, O, Fe, C, and Na, with atomic percentages of 9.9%, 8.2%, 40.9%, 5.2%, 26.6% and 7.2% respectively. The high oxygen levels demonstrate that all components are present in oxide form (Pai et al., 2021). Following the SEM and EDS analyses, we can deeply say that the magnetite nanocomposites were successfully synthesized.

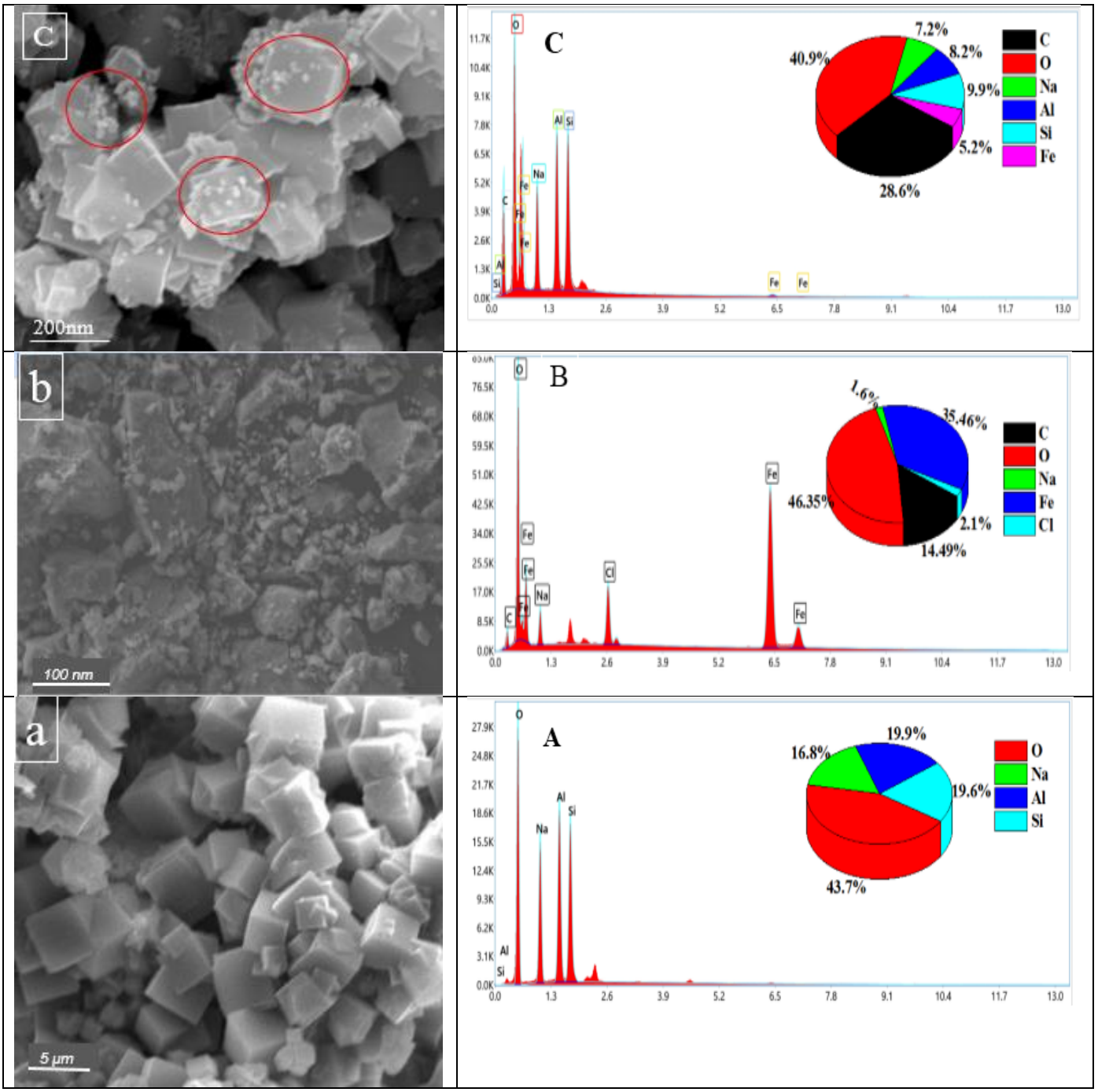

Figure 4.25: SEM and EDS images of synthesized zeolite 4A (a, A), TP- Fe_3O_4 (b, B) and MZ-6 (c, C).

4.5.1.5 *Magic-angle rotation and nuclear magnetic resonance analysis for ^{27}Al and ^{29}Si in the solid state of zeolite 4A and nanocomposite*

Nuclear magnetic resonance spectroscopy analysis provides additional information on the magnetic phase of iron oxides (Samrot, Durga, Chamarthy, & Sahithya, 2018) as well as on the structure of aluminosilicate zeolite materials (Lucresse et al., 2023). This involves analyzing the chemical environment of a particular atomic nucleus. The solid-state MAS-NMR spectra of ^{29}Si and ^{27}Al of zeolite 4A and nanocomposite are shown in Figure 4.26. A single resonance was observed at -89.61 ppm (Figure 4.26a), which corresponds to the ^{29}Si resonance for the perfectly crystallized 4A zeolite reported previously (Wang et al., 2019b). A unique signal at 56.92 ppm is observed in the MAS-NMR spectrum of the synthesized zeolite 4A (Figure 26b), which corresponds to a tetrahedrally coordinated aluminum atom present in the structure of the zeolite 4A (Microcalorimetrie et al., 2006). This chemical shift can also be explained by the fact that dissolved aluminum from metakaolin was introduced into the Si-O lattice with four coordinates, thus creating the structure $Si(OAl)_3(OSi)$ in an alkaline medium (Wang et al., 2019b). A single resonance (56.92 ppm) was presented, which demonstrates favorable crystallinity of zeolite 4A (Lucresse et al., 2023). We can observe the appearance of new peaks on the different graphs of the nanocomposite, which indicates the presence of iron, because iron has an impact on the magnetism present during NMR measurements (Samrot et al., 2018). These new peaks confirm the presence of the magnetic phase in the structure of zeolite 4A and could correspond to the E_g, T_{2g} and A_{1g} modes of the magnetic phase (Onal et al., 2019). These results also demonstrate the successful synthesis of the magnetite nanocomposite and that they are paramagnetic.

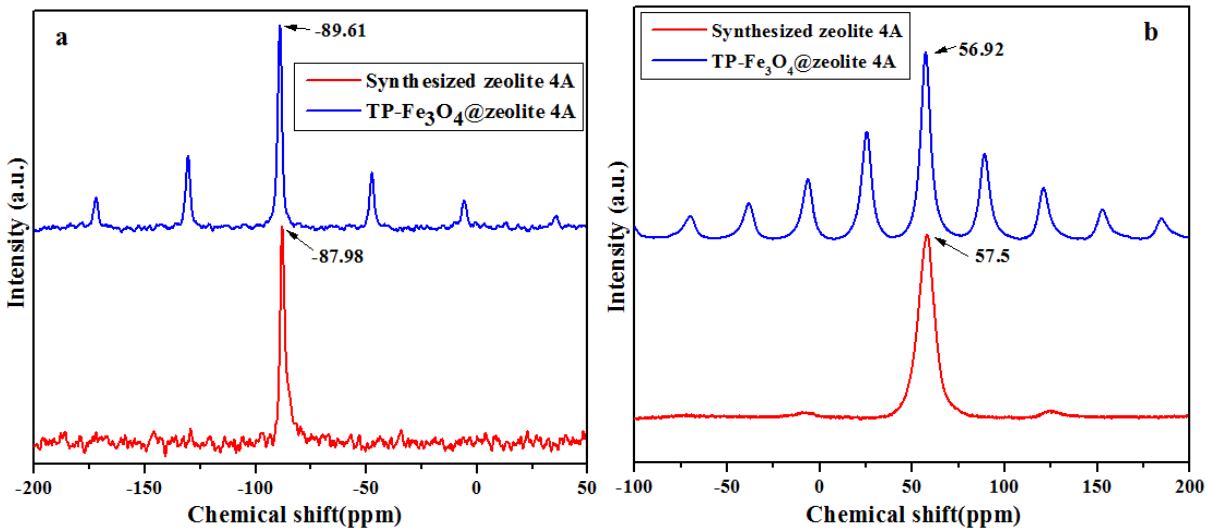

Figure 4.26: Solid-state MAS-NMR spectra of ^{27}Al (a) and ^{29}Si (b) of the zeolite 4A and the synthesized magnetite nanocomposite.

4.5.1.6 *N_2 adsorption-desorption isotherms*

Figure 4.27a presents the N_2 adsorption-desorption isotherm of the as-synthesized materials, which illustrates common Type IV isotherm, and the presence of a significant hysteresis loop testifies to the presence of mesoporosity (Abdelrahman et al., 2020). The rapid increase in adsorption capacity to $0.6 < P/Po < 1$ indicates that there are a large number of mesopores compared to micropores in the sample, which may be due to the incorporation of TP-Fe_3O_4 nanoparticles. The N_2 adsorption-desorption isotherm graph for the isolated TP-Fe_3O_4 nanoparticle shows absence of hysteresis loop which shows that the deposition of TP-Fe_3O_4 on zeolite 4A improves the porosity throughout the nanocomposite. Figure 4.24b illustrates the pore size distribution of the synthesized materials. It is observed that the pore size increases with the weight of the magnetite nanoparticles, we also observe the appearance of a single peak (band) around 9Å illustrating a monomodal distribution and a strong mesoporosity. From Table 4.11, we notice that the total specific surface area, the surface area and the volume of the micropores increase strongly as the weight of the TP-Fe_3O_4 nanoparticles increase. This can be explained by the fact that the incorporation of magnetite into the structure of zeolite 4A creates new pores and additional actives sites (surface area) on the as-synthesized nanocomposites. Similar results have been reported previously (Tran et al., 2021) . The incorporation of TP-Fe_3O_4into the cage of

zeolite 4A resulted in an increase of its specific surface area and pore volume. By improving its textural characteristics, the absorption capacity of zeolite 4A can increase.

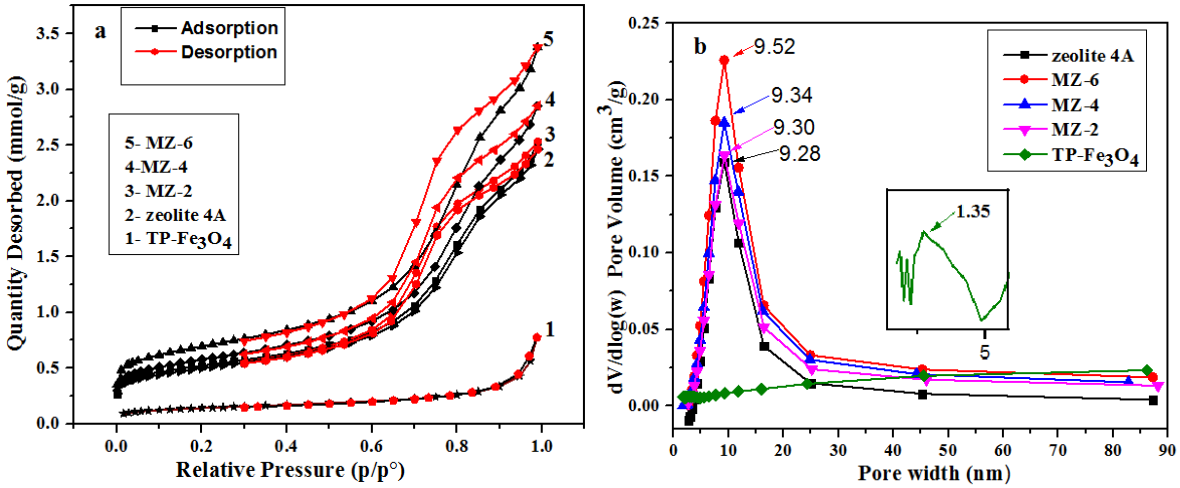

Figure 4.27: N_2 adsorption-desorption isotherm (a) and pore size (b) of zeolite 4A synthesis.

Table 4.11: Textural properties of synthesized zeolite 4A.

Samples	TP-Fe_3O_4	Zeolite 4A	MZ-2	MZ-4	MZ-6
BET surface area (m^2/g)	10.959	38.443	39.944	43.969	53.258
Microspore area (m^2/g)	2.451	10.210	11.536	10.505	15.380
External surface area (m^2/g)	8.508	28.233	28.408	3.464	37.878
Total pore volume (cm^3/g)	10.959	0.079	0.082	0.092	0.109

4.5.1.7 *pH of the point of zero charge on the surface of the synthesized zeolite 4A*

Figure 4.28 presents the pHpzc of zeolite 4A and the synthesized nanocomposites. It appears that the pHpzc of MZ-2, M-4 and MZ-6 are respectively 7.50, 7.47 and 7.41 while that of zeolite 4A is 7.75. Compared to zeolite 4A, the pHpzc values of the nanocomposites are low. This could be attributed to a decrease in basicity due to the addition of TP-Fe_3O_4 nanoparticles which have a predominantly acidic surface (Ling et al., 2019). This difference between the pHpzc values of the nanocomposites and zeolite 4A allows us once to say that these nanocomposite materials have new properties.

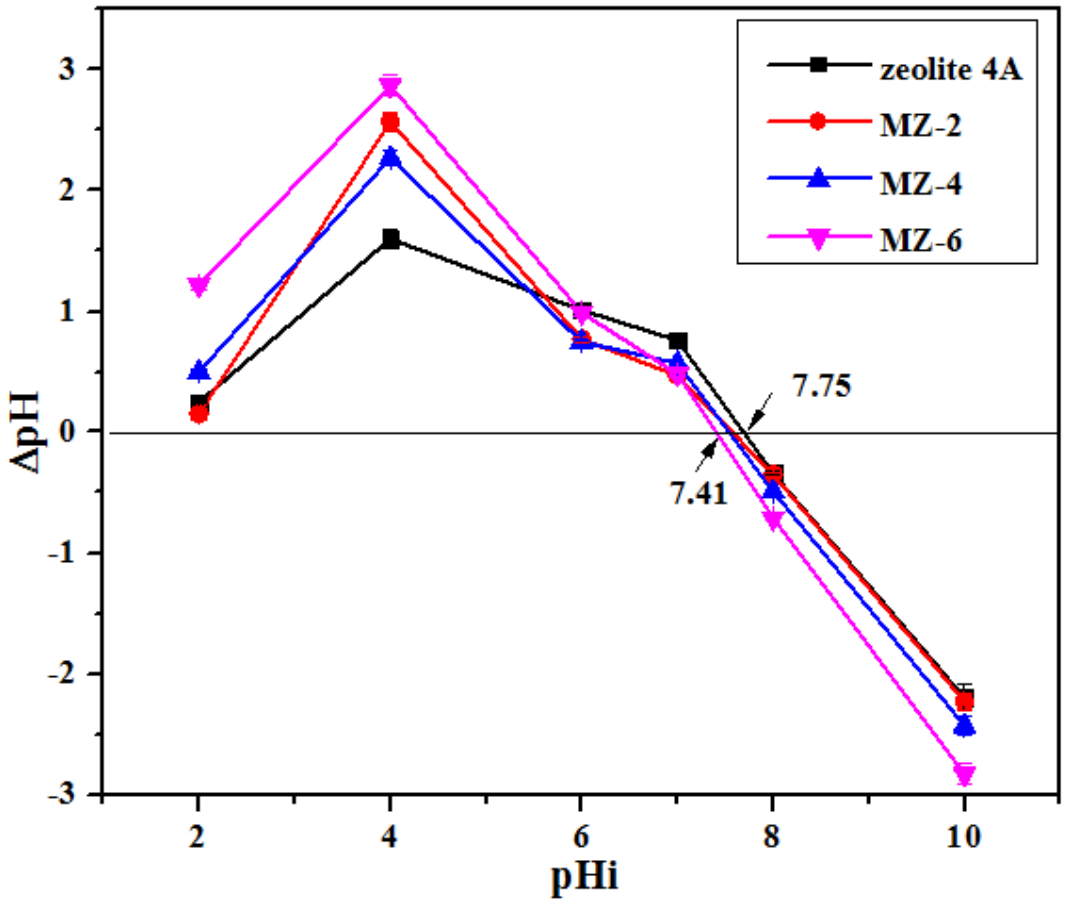

Figure 4.28: pHpzc curve of zeolite 4A and synthesized nanocomposites.

4.5.2 Study of the ciprofloxacin adsorption by zeolite 4A and synthesized nanocomposites

4.5.2.1 *Effect of pH*

Figure 4.29 shows the evolution of CIP adsorption as a function of pH. It can be observed that an increase in pH results in a gradual increase of CIP adsorption, until reaching maximum adsorption efficiency at pH 8 for all adsorbents. However, MZ-6 nanocomposite showed significantly higher adsorption efficiency (95.71%) at pH 8 compared to zeolite 4A (85.79%). Such adsorption behavior can be explained by the surface charge potential of TP-Fe_3O_4 in the zeolitic framework. According to Atugoda et al. (2020), ciprofloxacin has amphoteric properties, which gives him two dissociation constants, namely pKa1 = 6.1 and pKa2 = 8.7 (Atugoda et al., 2020). Adsorption of CIP is very weak at a very low pH (acidic environment) because there are electrostatic repulsions between the surface of the protonated adsorbent (≡Si-OH_2^+) and the CIP+. The nanocomposites maintain a more positive surface in an acidic environment, which

considerably reduces sorption compared to zeolite 4A. By improving the pH, the cationic CIP (CIP+) transforms into its zwitterionic form (CIP±), resulting in a gradual increase in adsorption. Due to the strong electrostatic attraction, the interaction between CIP± and nanocomposites becomes significant at pH 8.0, where maximum adsorption is achieved (Song et al., 2019). The adsorption of CIP is more significant at pH 8 due to the presence of the positive (≡Si-O H_2^+) and negative (≡S-O^-) silanol groups on the surface of the adsorbents (Atugoda et al., 2021)and the presence of numerous active sites (O^{2-} et Fe^{2+}/Fe^{3+}) in the TP-Fe3O4 makes it possible to electrostatically adsorb the positive polarized poles of the CIP. Under alkaline conditions (pH > 8.7), the surface of zeolite 4A and nanocomposites become negative due to the presence of the negative silanol groups (≡S-O^-), which creates repulsive forces between the anionic CIP (CIP-) and therefore reduces adsorption process.

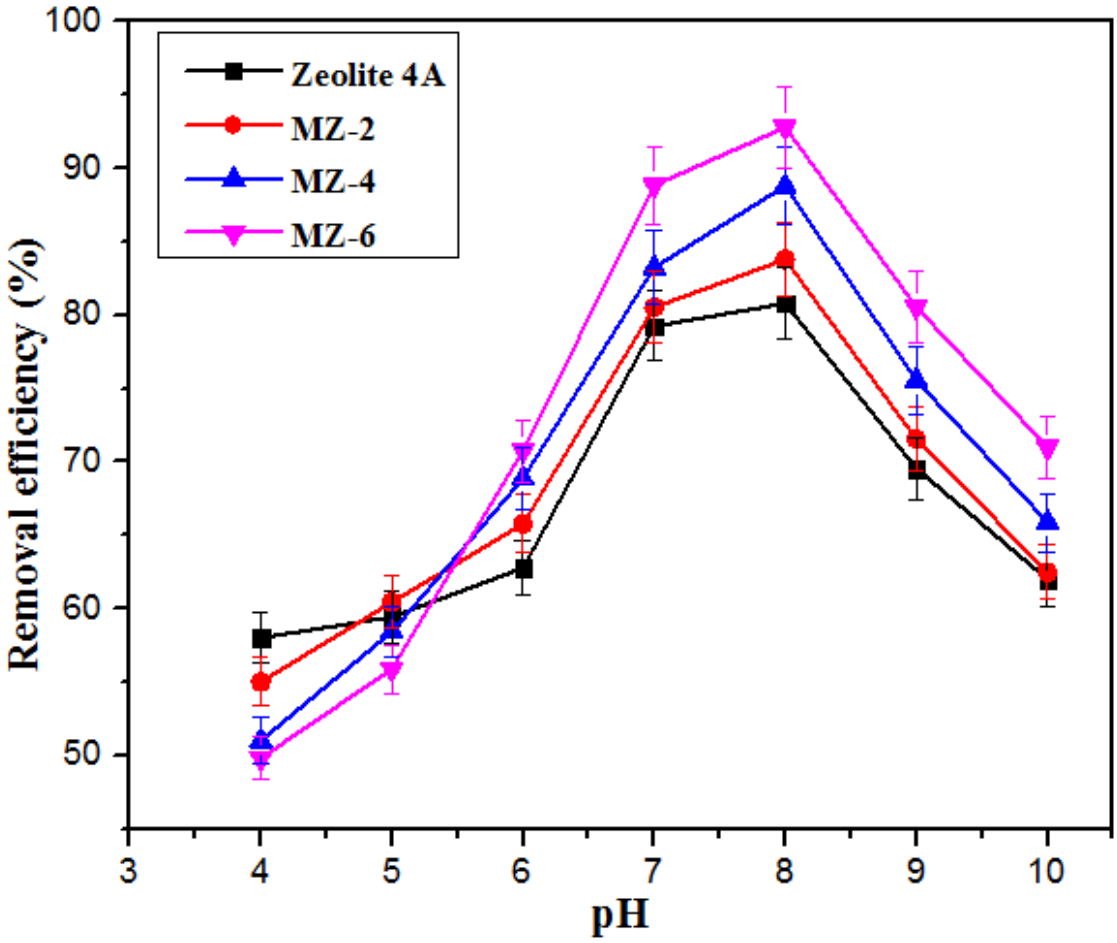

Figure 4.29: Influence of initial pH on CIP adsorption. Condition: contact time 80 mins, zeolite mass 4A 20 mg, nanocompsites mass 10 mg, sharking speed 150rpm, Temperature 25°C, initial concentration (CIP) 90 ppm, and error bars show ±standard deviation (3%).

4.5.2.2 *Effect of adsorbent dose*

The impact of adsorbent mass on CIP removal was examined by varying adsorbent mass, and the results are shown in Figure 4.30. The elimination rate of zeolite 4A increased from 10 mg to 20 mg, then decreased sharply. However, when nanocomposites are used, a gradual decrease in CIP removal efficiency is observed as the mass of the nanocomposites increases. Indeed, agglomeration of adsorbent particles can occur at low masses. There is a formation of flocs or aggregates which prevent CIP molecules from reaching the adsorption sites and decrease the number of active sites present on the surface of the adsorbents, inducing a decrease of the adsorption process (Wakejo et al., 2022). Otherwise, we can clearly see that the addition of TP-Fe_3O_4 nanoparticles increases the adsorption capacity of zeolite 4A. The maximum adsorption

efficiency is reached with a mass of 10 mg (97.73 %) for the MZ-6 nanocomposite unlike that of zeolite 4A which is 85.20% for 20 mg.

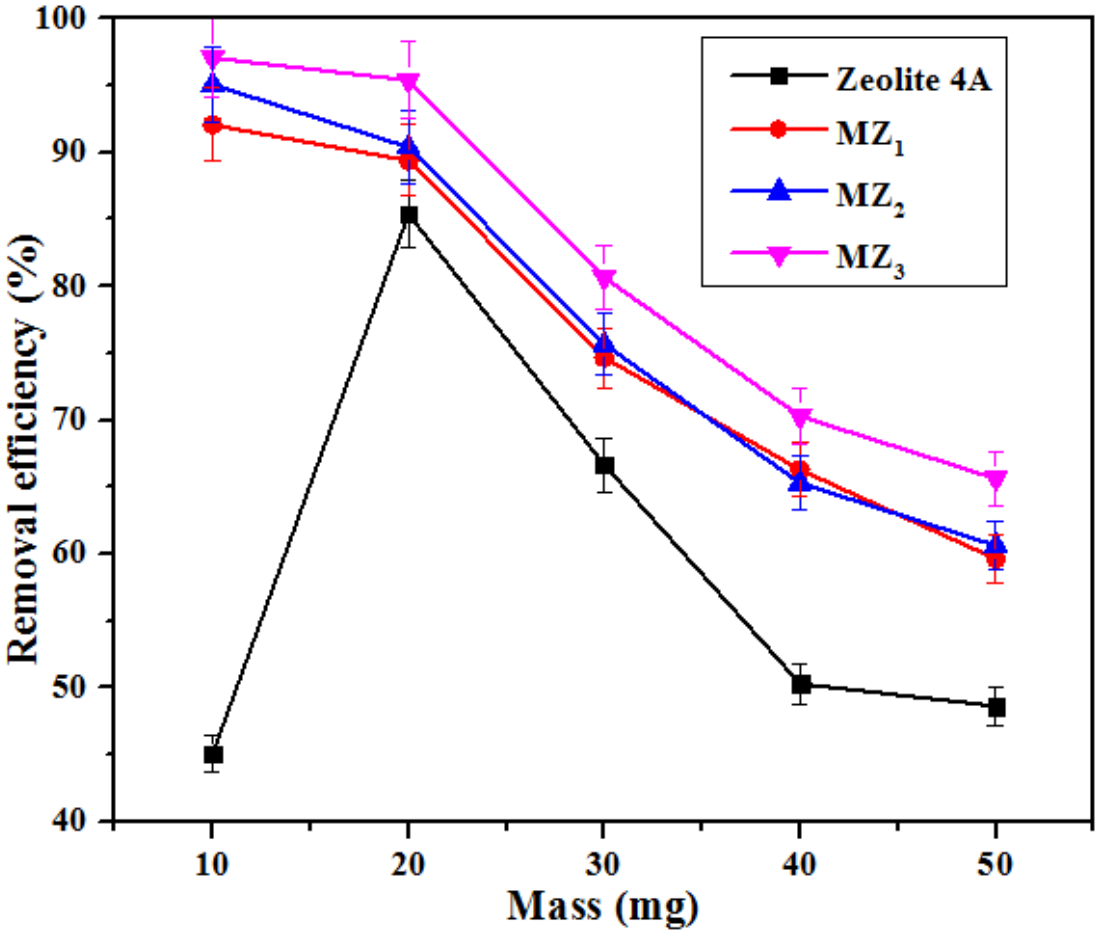

Figure 4.30: Influence of the mass of the adsorbents on the adsorption of CIP. Condition: contact time 80 mins, pH 8, sharking speed 150 rpm, Temperature 25°C, initial concentration (CIP) 90 ppm, and error bars show ±standard deviation (3%).

4.5.2.3 *Effect of ciprofloxacin concentration*

The influence of the initial CIP concentration on the removal efficiency was studied and the results are shown in Figure 4.31. It can be observed that the removal efficiency of CIP increases rapidly as a function of the initial concentration, reaching 60 ppm for zeolite 4A and 90 ppm for MZ-6 nanocomposite. The increase in the concentration of the pollutant causes an increase in driving force (concentration gradient), triggering a transfer of CIP molecules from the aqueous medium onto the surface of the adsorbents (Khan et al., 2020). Then, a slight decrease in the CIP elimination rate is recorded. This may be due to the reduction in resistance

forces caused by the accumulation of CIP on the surface of the adsorbents, including the mass transfer of CIP between the solid and liquid phases (Wakejo et al., 2022). Atugoda et al. (2020), obtained similar results when studying the effect of the initial concentration of CIP on microplastic polyethylene (Atugoda et al., 2020). The CIP removal efficiency increased from 89.78% for zeolite 4A to 97.52% for MZ-6 nanocomposite once equilibrium was reached. This increase in concentration and elimination rate observed highlights the impact of the TP-Fe_3O_4 charge in the structure of zeolite 4A.

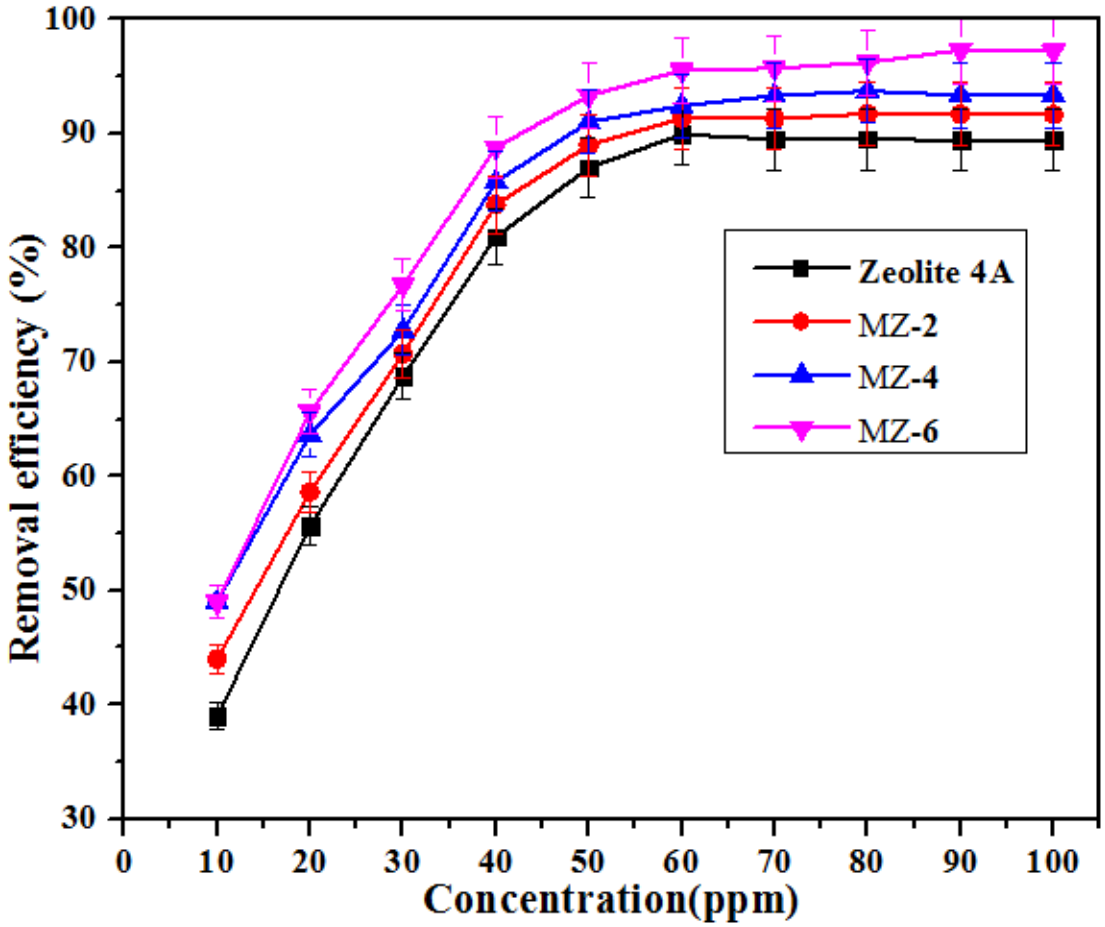

Figure 4.31: Influence of the initial CIP concentration. Condition: contact time 80 mins, zeolite mass 4A 20 mg, nanocompsites mass 10 mg, pH 8, sharking speed 150rpm, Temperature 25°C, and error bars show ±standard deviation (3%).

4.5.2.4 *Contact time effect*

The adsorption process was also affected by the contact time of adsorbents with the CIP molecule. As shown in Figure 4.32, the CIP adsorption rate was rapid during the first 60 minutes

for the nanocomposites and 80 minutes for zeolite 4A. The increase in contact time favors the access of CIP molecules to the active sites of the adsorbents until equilibrium (Atugoda et al., 2021). At equilibrium, the adsorbed molecules occupied the largest number of active sites and there was almost no space available for connection, meaning that no adsorption was carried out at equilibrium (Altaf et al., 2022). Beyond the equilibrium time, there was no significant uptake of CIP. The number of active sites decreases with time and eventually the adsorbent becomes saturated (Khan et al., 2020). Adsorption at this stage becomes slower due to the weak diffusion of the CIP molecules into the pores. Indeed, the incorporation of TP-Fe_3O_4 nanoparticles into the zeolite framework made it possible to increase the number of active sites and the specific surface area. This made it possible to increase the speed, reduce the reaction time and improve the adsorption efficiency. The maximum equilibrium removal efficiency was 90.74% for zeolite 4A and 98.97% for MZ-6 nanocomposite.

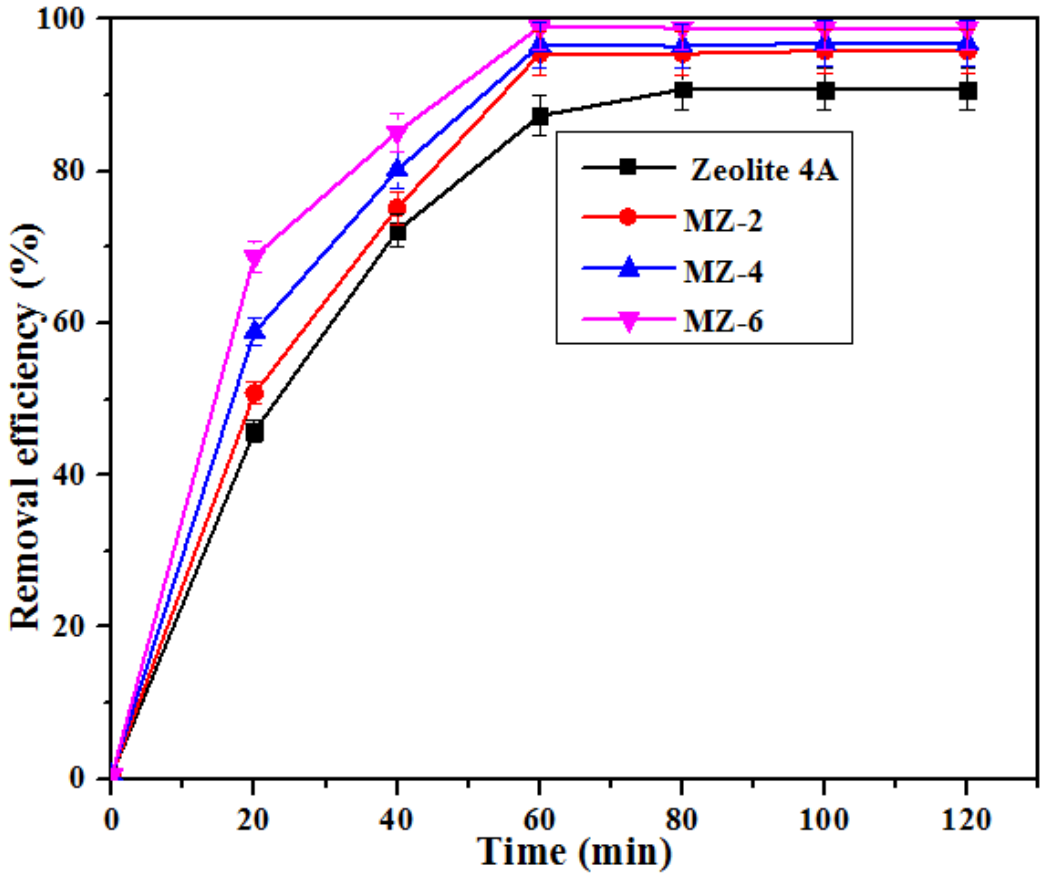

Figure 4.32: Influence of contact time. Condition: zeolite mass 4A 20 mg, nanocompsites mass 10 mg, pH 8, sharking speed 150 rpm, Temperature 25°C, initial concentration (CIP) 90 ppm, and error bars show ±standard deviation (3%).

4.5.2.5 *Adsorption isotherm*

The importance of isothermal models in adsorption processes lies in their ability to provide maximum sorption capacity and the expected interactions between adsorbent and the adsorbate (Wakejo et al., 2022a). Two isotherm models were investigated in this study in order to interpret and describe the CIP adsorption data, namely Langmuir and Freundlich. The adsorption isotherm parameters were evaluated and presented in Table 4.12. The plots of the CIP adsorption isotherm can also be observed in Figure 4.33. The adsorption capacity of CIP increased with concentration because the binding sites can be easily contacted with the adsorbate. Once the active sites are saturated at a specific concentration, adsorption remains the same as the initial concentrations (Wakejo et al., 2022). The maximum adsorption capacities calculated according to the Langmuir model were 95.24 mg/g and 175.44 mg/g for zeolite 4A and MZ-6 nanocomposite respectively. Based on the Langmuir isotherm, the R_L calculated value makes it possible to determine the type of isotherm and its nature: (i) irreversible isotherm (R_L=0), (ii) favorable isotherm (0< R_L<1), (iii) linear isotherm (R_L= 1) and unfavorable isotherm (R_L> 1) (Atugoda et al., 2021). In this study, the residual reduction ratios were less than 1, demonstrating that the CIP adsorption process by zeolite 4A and MZ-6 nanocomposite was favorable. In this study, the Langmuir model seems more suitable because its correlation coefficients (R^2=0.976 and 0.991) are slightly higher than those of Freundlich (R^2=0.814 and 0.903), which suggests that the adsorption process was a monolayer adsorption on a homogeneous surface (Mohammed et al., 2021). The Freundlich constant, 1/n was between 0 and 1, which indicates a more intense interaction between the adsorbents and the sorbate, which characterizes chemisorption.

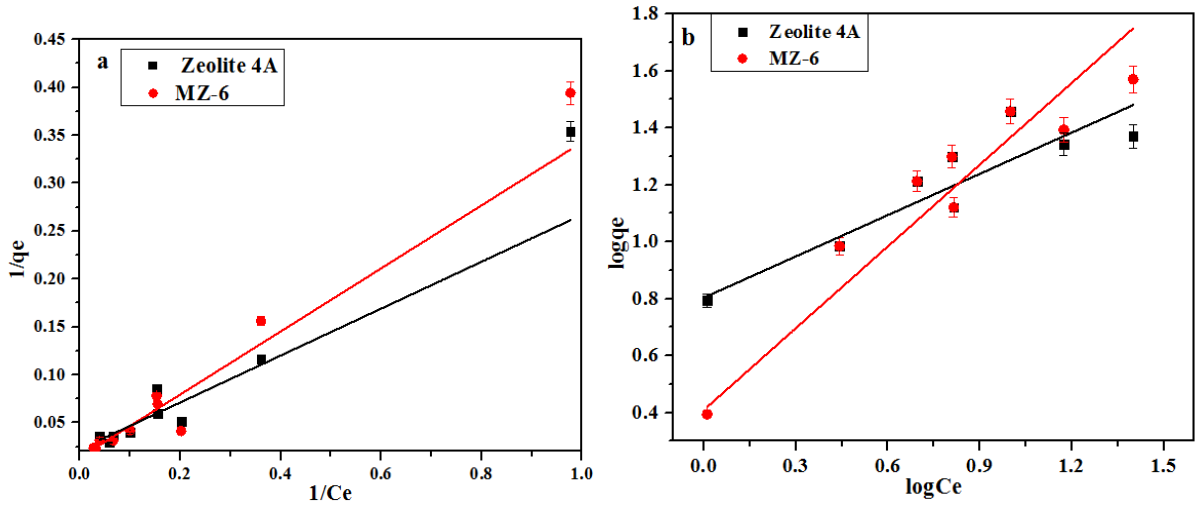

Figure 4.33: Linear models of Langmuir (a) and Freundlich (b) isotherms for CIP adsorption.

Table 4.12; Fitting parameters of CIP adsorption kinetic models.

Type of isothermal	Settings	Zeolite 4A	MZ-6
Langmuir model	K_L (L/mg)	0.031	0.015
	q_{max}(mg/g)	95.238	175,439
	R_L	0.353	0.435
	R^2	0.976	0.991
Freundlich model	K_F	6,773	3,434
	1/n	0.463	0.8113
	R^2	0.814	0.903

4.5.2.6 *Adsorption kinetics*

The contact time influences the adsorption of CIP on the adsorbents synthesized according to the kinetic study. Table 4.13 presents the results of the CIP adsorption kinetic parameters, while Figure 4.34 illustrates the kinetic models. The regression coefficients of the pseudo-second-order model are the highest compared to those of the pseudo-first-order model, as shown in Table 4.13. Additionally, $q_{e_{cal}}$ using a pseudo-second-order kinetic model is closer to $q_{e_{exp}}$. This indicates that the pseudo-second-order model was best fitted to the CIP experimental data, which involves both physical and chemical interaction (Tran et al., 2021). Chemisorption involves a covalent bond through electron sharing between the orbiting surfaces and the CIP molecule (Boumya et al., 2021). More specifically, it is possible that the n-π

interaction, complexation reaction and hydrogen bonding take part in the chemisorption process. Similar results have been reported in the literature (Dumitru et al., 2024; Pai et al., 2021).

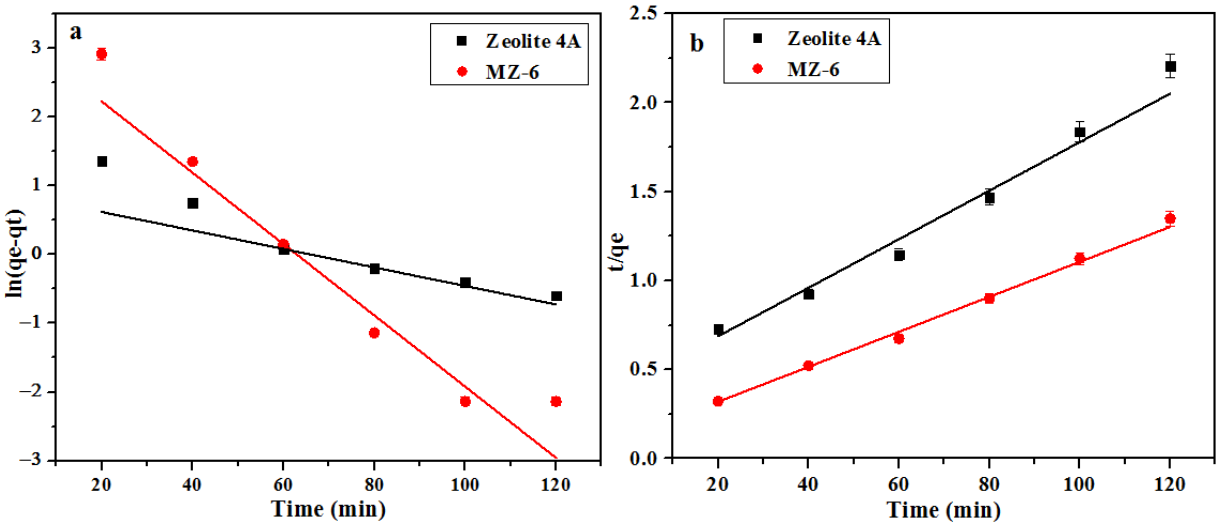

Figure 4.34; Linear fitting of pseudo-first order (a) and pseudo-second order (b) kinetic models.

Table 4.13: Parameters and adjustment coefficients of adsorption kinetic models.

Reaction order	Settings	Zeolite 4A	MZ-6
Pseudo-first order	$q_{exp}(mg/g)$	52.32	90.31
	$q_{cal}(mg/g)$	20,356	26,250
	K_1	-0.00011	-0.00043
	R^2	0.857	0.934
Pseudo-second order	$q_{cal}(mg/g)$	67.114	101,729
	K_2	0.00065	0.00079
	R^2	0.973	0.995

4.5.2.7 *Thermodynamic study*

The results of evaluating the impact of system temperature on the adsorption efficiency of CIP are shown in Figure 4.35. Figure 4.35a shows a 6.4% increase in removal rate between 298 K to 318 K for zeolite 4A. While the elimination rate with MZ-6 nano composite increases by 0.63% between 298 K to 308 K, then decreases by 3.36% between 308 K to 318 K. This decrease can be explained by the fact that an increase in temperature can lead to the destruction of the nanocomposite by breaking the bonds between the TP- Fe_3O_4 nanoparticles and the zeolite 4A, or a reduction of certain active sites on the surface of the nanocomposite. The Van't Hoff

curve was used to evaluate the thermodynamic parameters of CIP adsorption by the synthesized adsorbents, and the values of the obtained parameters are presented in Table 4.14. The ΔG° values were all negative, suggesting that the adsorption reactions of CIP on zeolite 4A and MZ-6 nanocomposite were both spontaneous (Boumya et al., 2021). The energy transfer of the adsorption process is measured by ΔH°, a negative value means the reaction is exothermic, while a positive value means the reaction is endothermic (Atugoda et al., 2021). According to Gokulan et al. (2019), the negative ΔS° testifies to the affinity of CIP towards the surface of the MZ-6 nanocomposite, while the positive entropy indicates that the solvent molecules present on the surface are easily displaced by the CIP molecules, which improves the adsorption capacity (Gokulan et al. 2019). Zeolite 4A has the value of negative free energy and positive enthalpy, which indicates that adsorption is beneficial with increasing temperature.

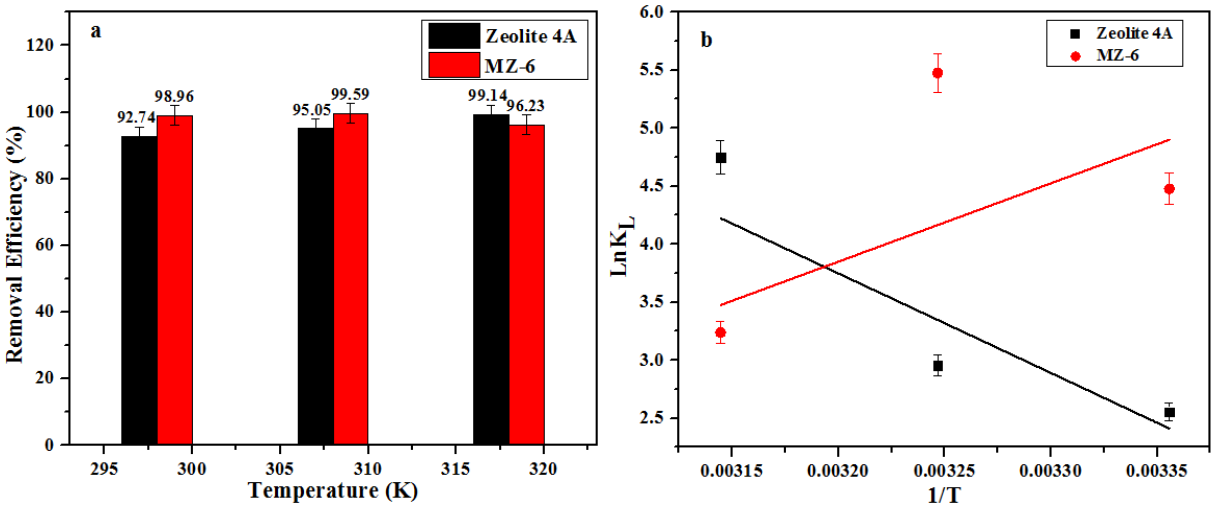

Figure 4.35: Adsorption efficiency versus temperature (a), Van't Hoff curve (a) for CIP removal on zeolite 4A and nano composite MZ-6.

Table 4.14: Thermodynamic parameters of CIP adsorption on zeolite 4A and MZ-6 nanocomposite.

Adsorbents	Temperature (K)	ΔG°(KJ/mol)	ΔH°(KJ/mol)	ΔS°(KJ/mol)
Zeolite 4A	298	-6.330		
	308	-7.562	7.366	0.260
	318	-1.560		
MZ-6	298	-11.092		
	308	-14.022	-56.126	-0.148
	318	-8.564		

4.5.2.8 *Study of the regeneration and chemical stability of zeolite 4A after adsorption*

To evaluate the possibility of reuse the adsorbents, up to seven adsorption-desorption cycles were carried out. According to Figure 4.36a, after seven cycles, a decrease of 6.44% in the adsorption efficiency is observed for zeolite 4A and 38.62% for the MZ-6 nanocomposite. The adsorption and regeneration efficiency may decrease due to the reduction in the amount of adsorbents during the washing and drying processes. The results obtained indicates that there could be formation of chemical bonds (which confirms the results given by the study of pseudo-second order kinetic models). in addition to the electrostatic interaction during adsorption, so that the saturated adsorbent cannot be completely regenerated. FT-IR and SEM analysis were used to evaluate the chemical stability of the adsorbents. The FT-IR curve (Figure 4.36b) does not show any significant modification, but two new peaks are observed at 1149 $cm^{-1}$and 700 cm^{-1}, which can be attributed to the formation of Si-OH and Al-OH groups resulting from hydrolysis. of the Si-O-Al bond (Djioko et al., 2024). Additionally, SEM images (Figure 4.36c and 4.36d) confirm that the morphology of the adsorbents was retained after seven cycles, with the crystal structures remaining intact, suggesting that the adsorbents were chemically stable.

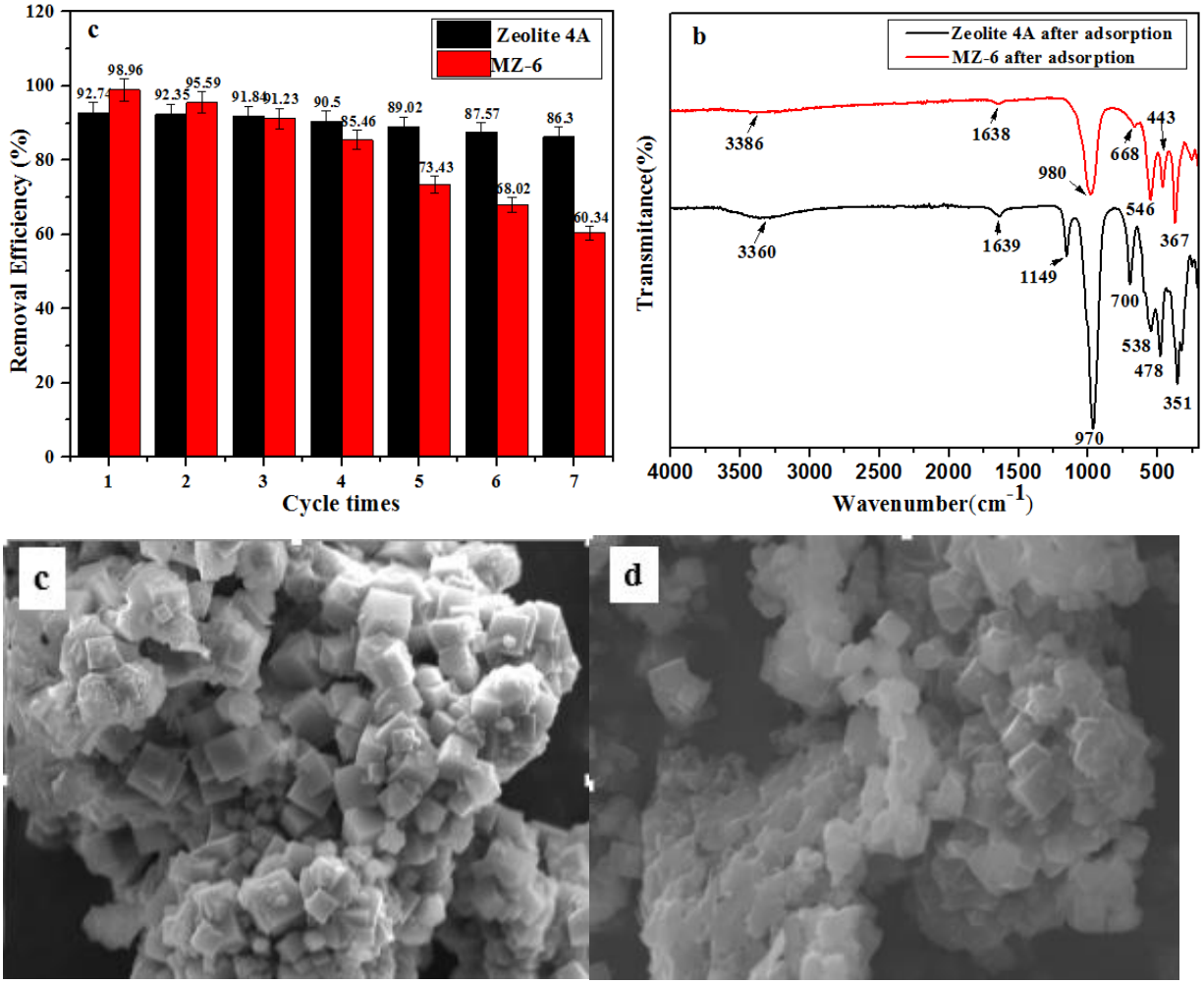

Figure 4.36: Reusability efficiency (a) FT-IR spectrum (b), SEM image (c and d) of zeolite 4A and MZ-6 nanocomposite after adsorption.

4.5.3 Investigation of the interaction mechanism of CIP molecules on the surface of zeolite 4A (001) and the magnetite@zeolite 4A composite

4.5.3.1 *Monte Carlo molecular simulation*

We can effectively explore the adsorption mechanism using Monte Carlo molecular simulation. It was carried out with the aim of predicting the adsorption of CIP molecules on the surface of zeolite 4A (001) and MZ (001) composite. According to the DFT conclusions, it is possible to adsorb all CIP molecules on the adsorbent surface and that CIP molecules are more reactive and stable in a neutral medium (CIP±), followed by the basic medium (CIP-) and finally the acidic medium (CIP+) (table 4.6). The basic adsorption energy configurations of CIP

molecules on zeolite 4A (001) and ZM (001) composite are shown in Figures 4.37 and 4.38. It can be seen that the orientations of the CIP molecules on the surfaces studied vary depending on the environment. In acidic and basic environments, they have an almost perpendicular orientation, which suggests electrostatic repulsion and the decrease in adsorption capacity (Khnifira et al., 2022). While in neutral medium, CIP molecules exhibit a parallel and flat orientation, exposing as many heteroatoms as possible (O and N) on the adsorbing surfaces. Which suggests a strong interaction between the CIP molecule and the surfaces studied (Khnifira et al., 2022). In addition, very short distances are observed between the CIP molecules and the adsorbent surfaces in a neutral environment, Thhis could suggests the CIP molecules interact on the surface of the adsorbents via chemisorption (Djioko et al., 2024). However, we observe that the CIP molecules are more bound to the MZ composite in a neutral medium, which shows that the CIP molecules have a high affinity with the MZ composite in this medium.

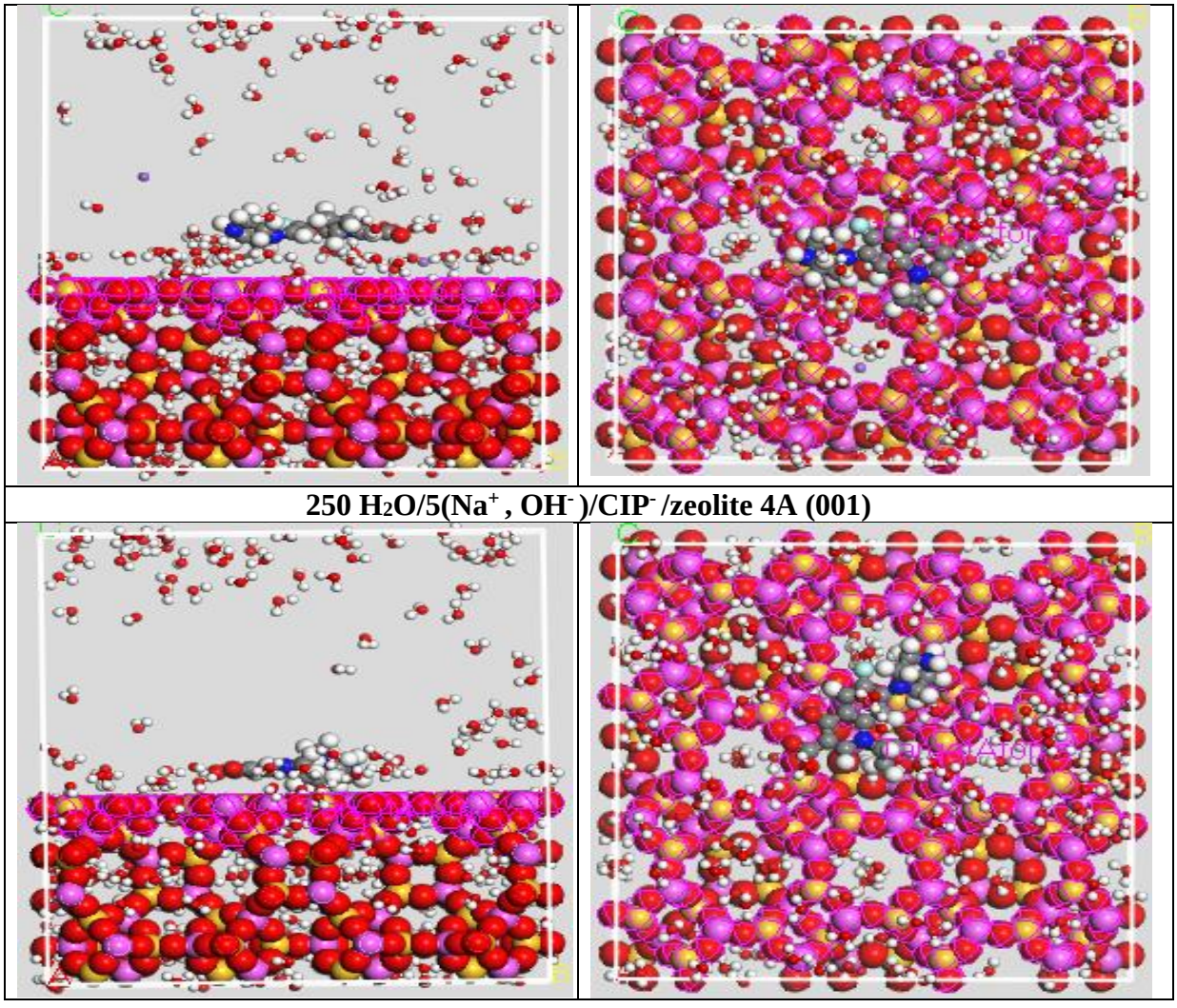

250 H_2O/5(Na^+ , OH^-)/CIP^- /zeolite 4A (001)

250 H_2O/CIP $^{\pm}$ /zeolite 4A (001)

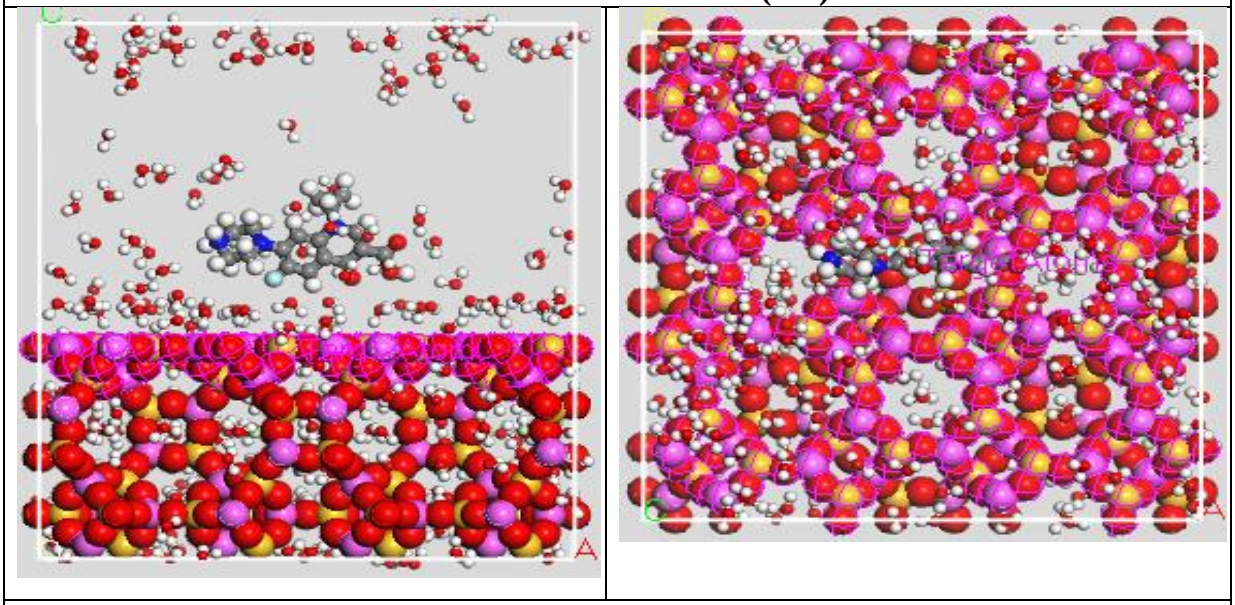

250 H $_2$ O/5(H_3O^+, Cl^-)/CIP^+ /zeolite 4A (001)

Figure 4.37: Side view (left) and top view (right) of the most stable low energy configuration for the adsorption of CIP molecules on the surface of zeolite 4A (001) in various aqueous media at 298 K.

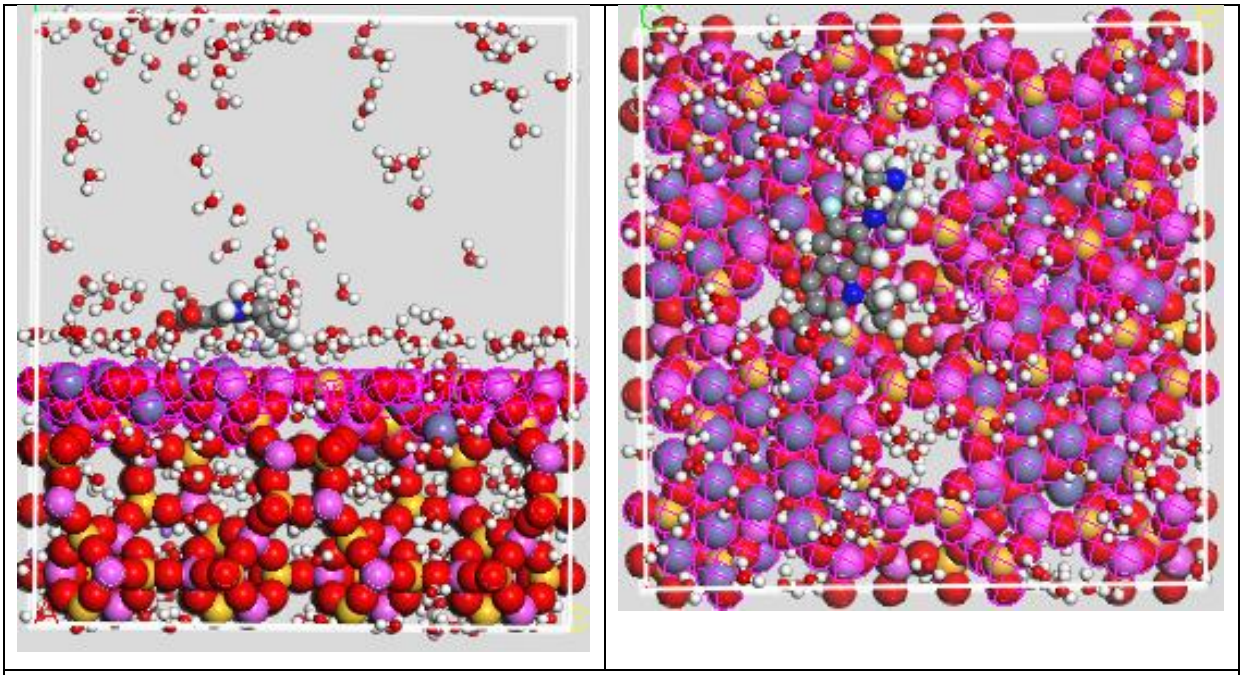

250 H_2O/5(Na^+, OH^-) /CIP^- / MZ (001)

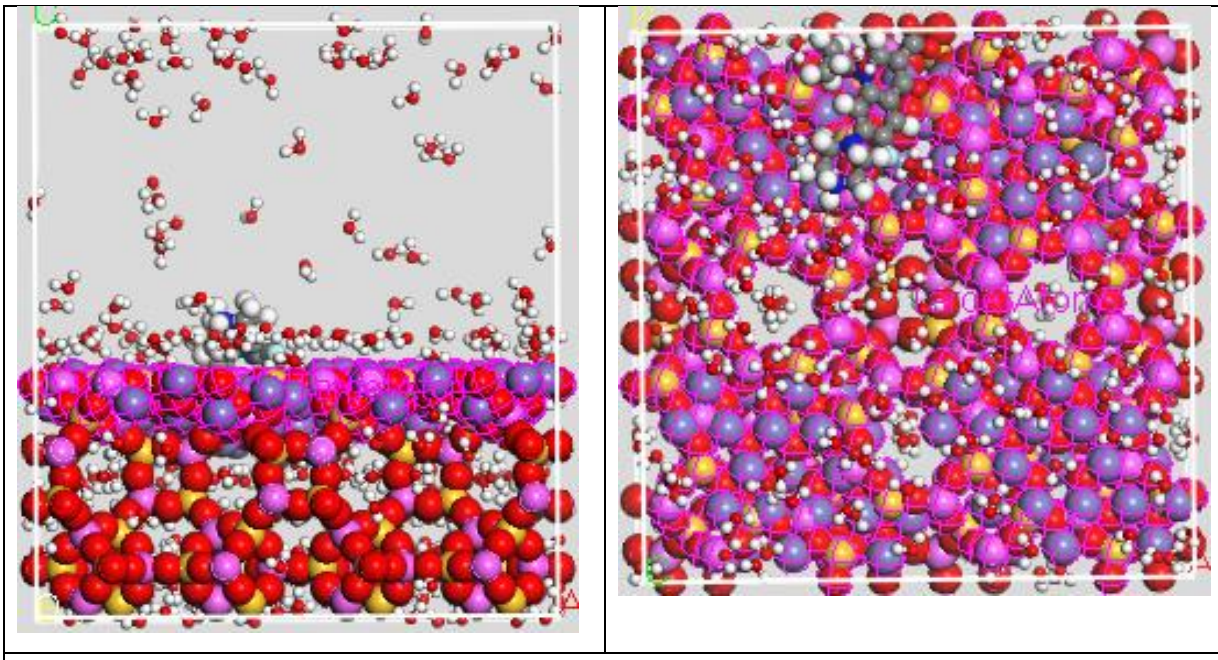

250 H_2O/CIP $^{\pm}$ / MZ (001)

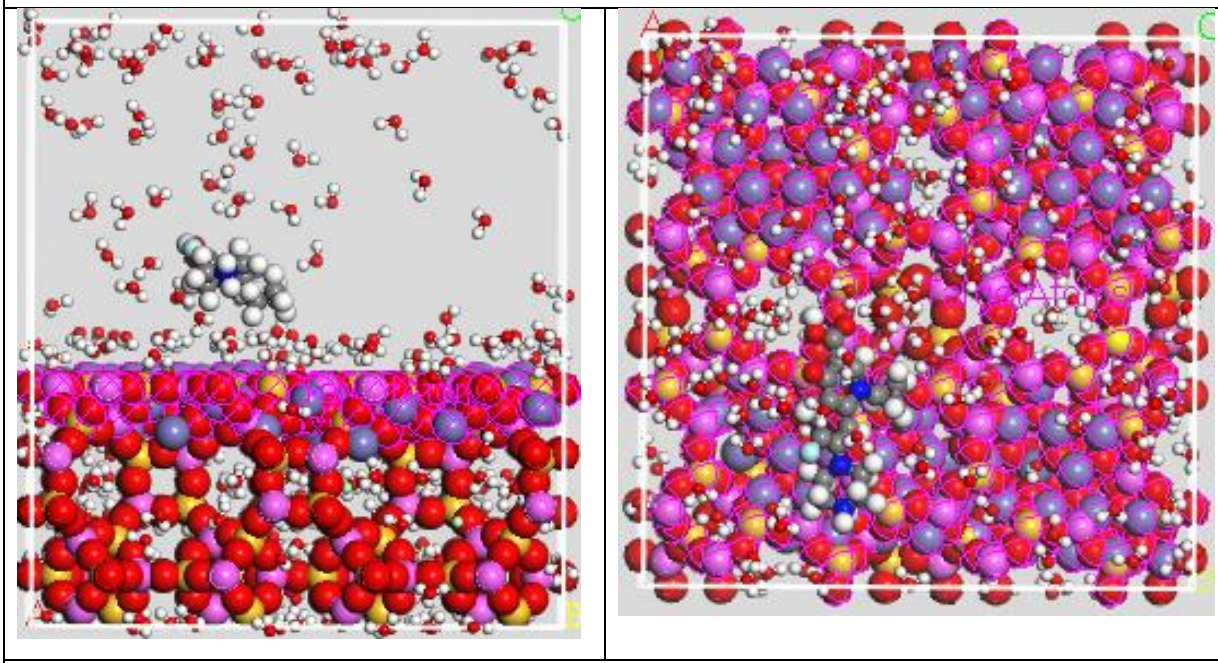

250 H_2O/5(H_3O^+, Cl^-)/CIP^+ / MZ (001)

Figure 4.38: Side view (left) and top view (right) of the most stable low energy configuration for the adsorption of CIP molecules on the surface of composite MZ (001) in various aqueous media at 298 K.

4.5.3.2 *Dynamic descriptors*

The calculated energies of the dynamic parameters are presented in Table 4.13. It is possible to see that all the values of the total energy (E_{Tot}) are negative, which confirms favorable adsorption for all the systems analyzed (Singh et al., 2021). Furthermore, all values $E_{Ads}$are negative, which confirms that the adsorption process is exothermic and spontaneous (Djioko et al., 2024). This also means that CIP molecules adhere to the surface of the adsorbents, resulting in physical and/or chemical adsorption. In general, high adsorption is observed when the adsorption energy (E_{Ads}) of the adsorbate on the adsorbent surface is more negative (Barour et al., 2023). Adsorption is higher in an acidic medium, followed by basic medium on all the absorbent surfaces studied, as shown in Table 4.15. The high levels of strain energy (E_{Def}) and individual energy (Ead/dNi) of hydronium ions (H_3O^+) and hydroxides (OH^-) explain these high values of E_{Ads}in these two environments. However, the different individual energies of the CIP molecules (CIP: dEad/dNi) allow us to better understand their individual adsorption capacity on the surface of the adsorbents studied. The individual energies of the CIP molecules indicate that they are most adsorbed in a neutral medium (CIP±), then in a basic medium (CIP-) and finally in an acidic medium (CIP+). Indeed, due to their increased reactivity (high Ead/dNi), the Hydronium ions attach more quickly to the surface of the adsorbent, then repel the CIP+ molecules, which leads to a reduction of the adsorption capacity in a acidic medium, it is the same for the basic medium.

Table 4.15: Parameters of the dynamic descriptors of the most stable configurations of the CIP on the surface of zeolite 4A (001) and the composite (in Kcal/mol).

	Media	E_{Tot}	E_{Ads}	RAE	E_{Def}	dE_ad/N_i			
						CIP	H_2O	H_3O^+	N_aOH
Zeolite 4A	Acid	-552.57	-985.07	-883,95	-896.05	-98.99	-0.32	-177.38	/
	neural	-544.73	-999,15	-860.59	-138,53	-104,5	-0.33	/	/
	Basic	-540.27	-104.48	-855.99	-188.80	-99.51	-0.32	/	-10.74
MZ	Acid	-543.80	-982.58	-859.44	-896.55	-102.12	-0.34	-177.54	/
	neural	-668,32	-102.27	-885.03	-138.40	-109.17	-0.41	/	/
	Basic	-666,64	-107.12	-882,49	-188.04	-105.37	-0.32	/	-10,79

4.5.3.3 *Probability demerge distribution*

The probability energy distribution was examined to describe the distribution of interaction energies between adsorbates and adsorbents, to better understand the behavior and mechanism of adsorption and/or repulsion of CIP molecules on the adsorbents surface studied. The energy distribution during adsorption of CIP molecules on the surface of adsorbents in different reaction media is shown in Figure 4.39. In an acidic environment, it has been observed that hydronium ions (H_3O^+) exhibit greater stability and reactivity than CIP+ molecules. Hydronium ions have a highest interaction energy of -1776.30 Kcal/mol and -1787.41 kcal/mol, as well as a highest probability energy distribution P(E) of 0 .71 and 0.58 respectively on the surface of zeolite 4A and the MZ composite. Surface protonation of adsorbents leads to a decrease in active sites and high electrostatic repulsion of CIP+ compounds (Kora et al., 2024). On the other hand, in a basic environment, hydroxide ions (OH^-) react more strongly than CIP- molecules, with high P(E) values of 0.81 and 0.98 respectively on the surface of zeolite 4A and MZ nanocomposite. CIP- molecules exhibit higher stability than hydroxide ions (OH^-), with high interaction energies of -99.51 Kcal/mol and -106.46 Kcal/mol respectively on the surface of zeolite 4A and composite MZ. This results in a slight drop of adsorption capacity in a basic medium (Mwendapole & Gang, 2022). CIP± molecules exhibit great reactivity and high stability in a neutral environment. The adsorption of CIP± molecules on the surface of the adsorbents is

not affected by the other species present in solution. This leads to an increase in interaction energies and a strong probability energy distribution, leading to an increase in the adsorption capacity of CIP±. On the other hand, an overabundance of hydronium ions (H_3O^+) or hydroxide ions (OH^-) will oppose the CIP molecules on the various adsorption sites, which will reduce the adsorption capacity.

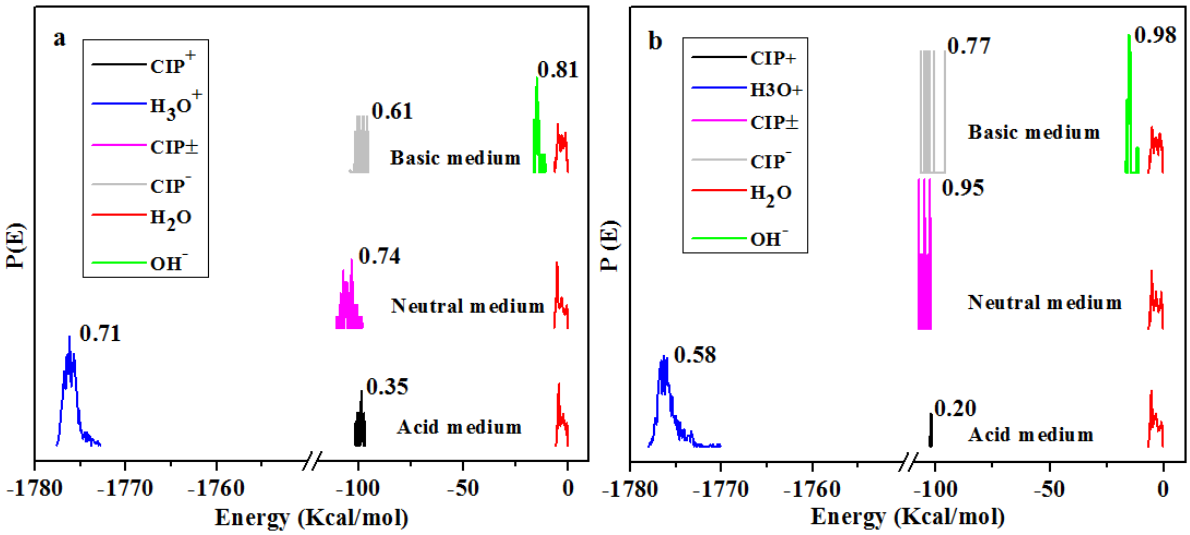

Figure 4.39: Probability energy distribution of CIP on the surface of zeolite 4A (001) and MZ (001) composite in various media.

4.5.3.4 *Radial distribution function*

The results of the simulation study were analyzed by measuring the interaction distance of CIP molecules and the adsorbent surface area using the peer correlation function (g(r)), or the radial distribution function (RDF). (Fouda et al., 2019). The peer correlation function g(r) was calculated to better understand the type of bond created between the CIP molecules and the surface of zeolite 4A and MZ composite, using equation (3.30).

Khnifira, Hamidi, et al., (2022) reported that peaks that appear at a distance less than 3.5 Å are related to an intense interaction called chemisorption, while peaks that manifest at a distance greater than 3.5 Å are linked to a weak interaction called physisorption. The most intense peaks are located at a distance r less than 3.5 Å, as demonstrated by the RDF traces (Figures 4.40a and 4.40b), which suggests a predominance of chemisorption. The heteroatoms (N and O) present in CIP molecules have the ability to transport electrons to the surface of the adsorbents and create chemical bonds, which could explain this strong interaction. The intensity and distance of the

high intensity peaks are not identical on the zeolite and the MZ composite, even though they emerge at a distance of less than 3.5 Å. An intensity of 60.27 and 71.41 is observed in acidic medium at a distance r of 2.77 Å and 2.87 Å respectively. In a basic medium, there is an intensity of 71.78 and 85.12 at a distance r of 2.03 Å and 1.73 Å respectively. While in neutral medium, the CIP molecules present an intensity of 90.86 Å and 101.37 Å respectively at a distance r of 1.61 Å and 1.59 Å on the surface of zeolite 4A and MZ composite. It appears from these results that the interaction between the CIP molecules and the surface of the adsorbents is more intense in a neutral environment. In addition, a more intense interaction and a shorter adsorbate-adsorbent distance can be seen between the CIP molecules and the surface of the MZ composite. This suggests that CIP molecules have some affinity on the MZ composite compared to the zeolite 4A. Indeed, the low energy empty orbitals of the ions $Fe^{3+}$and Fe^{2+}in the magnetite nanoparticle make it possible to receive doublets of free electrons given up by the heteroatoms of the CIP molecules in order to create coordination bonds. The presence of electrostatic interactions (Physisorption) is illustrated by the peaks observed in a neutral medium at a distance of 5.91Å and 4.24Å at low intensities. These results corroborate with those on the study of adsorption kinetics.

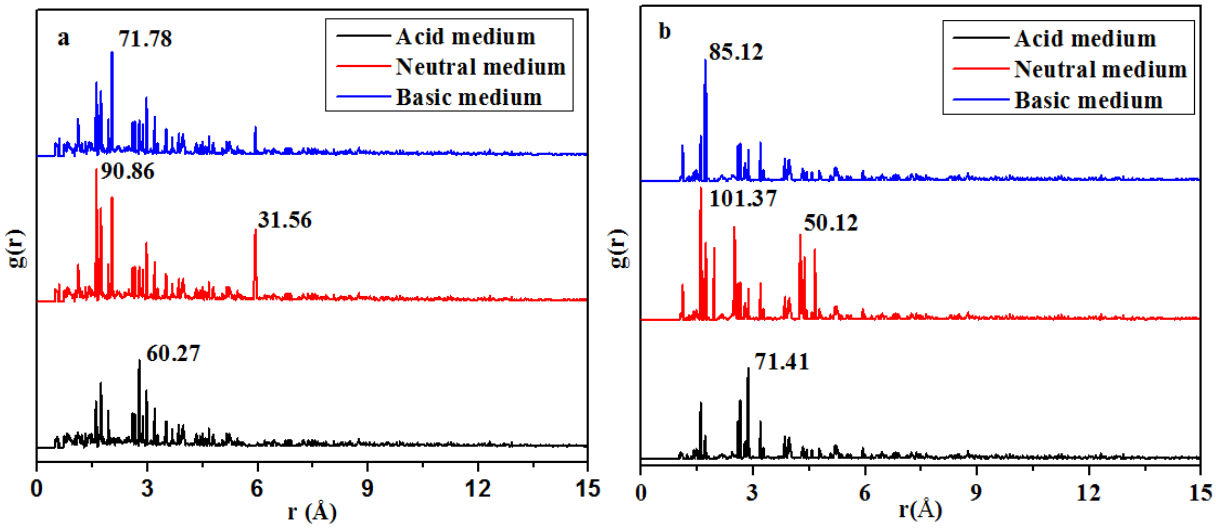

Figure 4.40: Radial distribution function as a function of the distance between CIP molecules and the surface of zeolite 4A (001) (a) and composite (001) (b).

4.5.3.5 *Effect of temperature on adsorption energy*

According to Li et al. (2018), adsorption energy corresponds to the energy released when a compound molecule is adsorbed on the surface of an adsorbent (According to Li et al. 2018). According to El-Mansy et al. (2017), adsorption energy provides an easy method to classify the adsorption capacities of molecular complexes (El-Mansy et al. 2017). The adsorption energies of CIP molecules on the surface of zeolite 4A (001) and MZ (001) composite in a neutral medium at various temperatures are shown in Figure 4.30. The negative adsorption energies illustrate spontaneous and favorable adsorption at any temperature on the surface of the adsorbents studied. On the surface of zeolite 4A, the adsorption energies of CIP are -999.15 Kcal/mol, -1060.08 Kcal/mol and -1136.26 Kcal/mol at 298K, 308K and 318K respectively. This demonstrates that increasing the temperature increases the adsorption capacity of CIP on the zeolite surface. Indeed, the pores of the zeolite expand when the temperature increases, which leads to an increase in the degree of randomness of the system (Lucresse et al., 2023). The MZ composite shows a decrease in adsorption energy at 318 K, suggesting a decrease in adsorption capacity at this temperature. This can be explained by the fact that at 318 K the MZ composite is unstable, which creates a reduction of some active sites. These results are in agreement with the thermodynamic analysis (Figure 4.41).

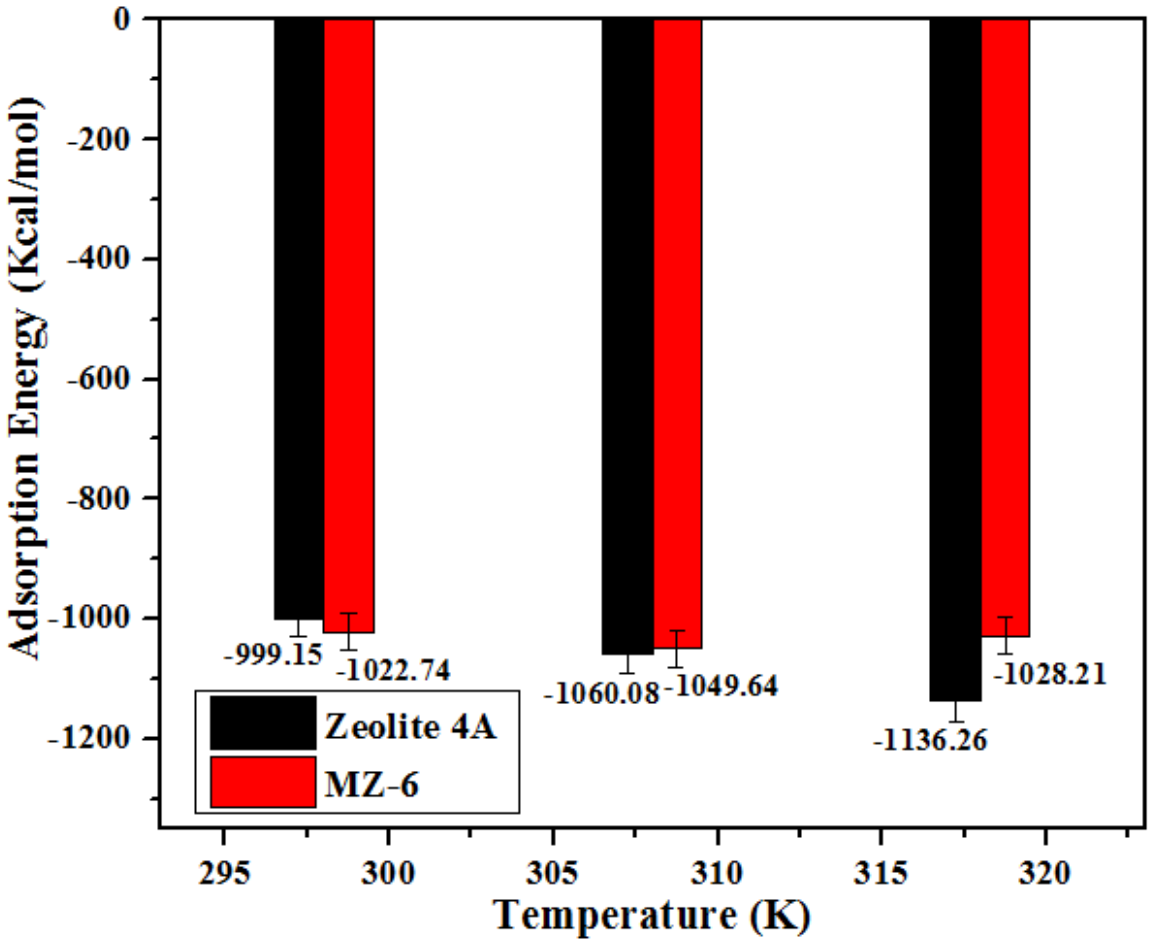

Figure 4.41: Influence of temperature on adsorption energy.

4.5.4 Proposal of the adsorption mechanism of CIP

The prepared adsorbents demonstrated satisfactory results on CIP removal in aqueous solution. Figure 4.42 presents the adsorption mechanism of CIP± on the surface of zeolite 4A and MZ nanocomposite. The FT-IR spectra after adsorption made it possible to predict the molecular interactions between the functional groups of the CIP and those on the surface of the zeolite 4A and the nanocomposite (Figure 4.36b). By observing these spectra, we can see a slight shift in the absorption bands and the appearance of a few additional bands, notably at 1149 $cm^{-1}$and 700 cm^{-1}, due to the formation of the ≡Si-OH and ≡Al-OH groups due to the hydrolysis of the ≡Si-O-Al≡ group (Atugoda et al., 2021). The Si-OH and Al-OH groups are protonated in an acidic medium (Si-$OH_2^+$and Al-OH_2^+), while in a basic medium, they are deprotonated (Si-O^- and Al-O^-). In a neutral environment, the protonated and deprotonated forms of the ≡Si-OH and ≡Al-OH groups grow and coexist, resulting in strong electrostatic interactions

between the CIP± and the surface of the zeolite 4A and the one of nanocomposite (Atugoda et al., 2021). The two bands at 668 cm^{-1} and 443 cm^{-1} of the nanocomposite FT-IR spectrum after adsorption (Figure 4.36b) reveal an efficient reaction of the Fe^{3+}-O and Fe^{2+}-O groups during the adsorption of CIP. According to the DFT results, it was demonstrated that the heteroatoms (O and N) and the aromatic ring of the CIP± molecule present a high electron density (Lewis basis) and can donate free electronic doublets to the empty atomic orbitals of the CIP± molecule, ions $Fe^{3+}$and Fe^{2+}(Lewis acid) in order to form coordination bonds. The RDF spectrum confirmed the formation of chemical bonds and electrostatic interactions. The diffusion of pores inside the nanocomposite channels could be another element promoting better adsorption.

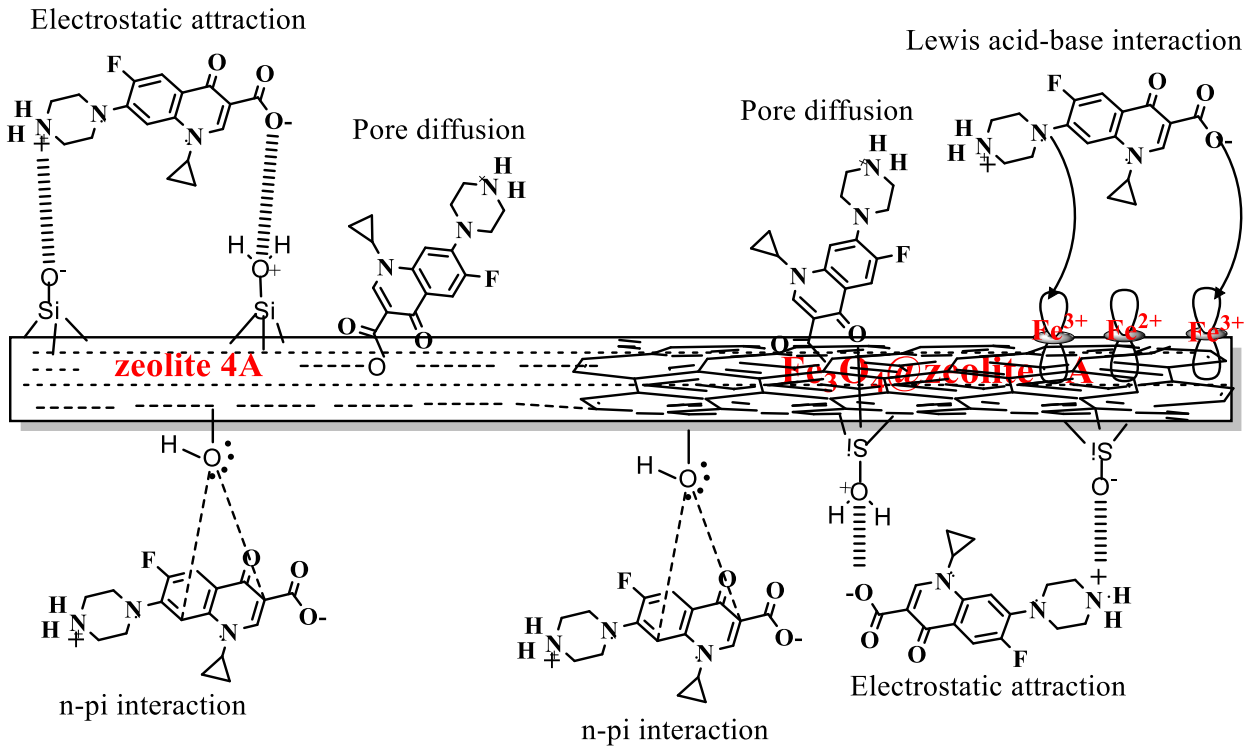

Figure 4.42: Adsorption mechanisms of CIP± on the surface of zeolite 4A and MZ nanocomposite.

4.5.5 Partial conclusion

In this part, we successfully synthesized a crystalline zeolite 4A from the raw kaolin of Famgamg using a hydrothermal synthesis method, the magnetite nanoparticles using the TP sheets as a reducing and stabilizing agent finally, we have incorporated the magnetite nanoparticles into the zeolite framework to form the bio-magnetite@zeolite 4A nanocomposite, as demonstrated by the

characterization results. At the end of the study of CIP adsorption on our different materials, it is interesting to note that the specific surface is not the most important factor influencing adsorption, but rather the surface chemistry (presence of sinalol group on the surface of the zeolite). The maximum CIP adsorption was obtained for the nanocomposites at pH 8 a relatively short equilibrium time (60 minutes), a mass of 10 mg and an initial CIP concentration 90 ppm. Unlike zeolite 4A, where the maximum adsorption of CIP was obtained at pH 8, contact time 80 minutes, initial CIP concentration 60 ppm with a mass of 20 mg at 25 °C. It was also noted at the end of the kinetic and MC study that the CIP adsorption mechanism by the different adsorbents was dominated by the chemisorption phenomenon. The regeneration study carried out on the most convincing adsorbents showed that they could be used at least seven times. Finally, the theoretical study confirmed that in the aqueous phase, the CIP molecules have more affinity with the surface of the nanocomposite, that the reaction between the CIP and the adsorbent surfaces were favorable, spontaneous and exothermic. In addition, the CIP molecules were more stable and reactive in a neutral environment.

4.5.6 Comparison of the adsorption capacity of CIP with other adsorbents

The adsorption capacity of CIP by zeolite 4A, nanocomposites 6%TP-Fe_3O_4@zeolite 4A and other adsorbents was compared and reported in **Table 4.16.** The data presented reflect satisfactory adsorption capacity values compared to other adsorbents. Although the adsorption capacity of CIP for activated carbon is slightly higher than that of the nanocomposite synthesized in this study, activated carbon is 20 times more conductive than clay materials (Hartig, Ernst, & Jekel, 2001), resulting in a negligible gain in conductivity value. In return, the value of q_{max} was higher than that of zeolite 4A, nanocomposite TP-Fe_3O_4@zeolite 4A and other adsorbents reported in the literature. As a result, the nanocomposite TP-Fe_3O_4@zeolite 4A can be considered as a catalyst for the removal of CIP.

Table 4.16: Comparison of different adsorbent materials' maximal Langmuir adsorption capabilities for the elimination of CIP

adsorbents	Antibiotics	Adsorption capacity (mg/g)	References
Al-dispersed bamboo activated carbon	CIP	93.6	(Guellati, Maachi, & Chaabane, 2022)
Zeolite modified seaweed	CIP	90.0	(Atugoda, Gunawardane, Ahmad, & Vithanage, 2021)
Chitosan-based Cryostructured composites	CIP	5.15	(Dumitru, Neagu, Miron, In, & Dur, 2024)
Bentonite Clay	CIP	114.4	(Antonelli, Malpass, Da Silva, & Vieira, 2020)
Magic activated carbon/chitosan nanocomposite	CIP	90	(Tu, Sena, Kerkez, & Abdel, 2017)
Activated carbon from biomas wastes	CIP	244.0	(Sun et al., 2016)
Silica arogels modified with vinyl	CIP	47.8	(Sert, Koç, Len, Almásy, & Dudás, 2025)
Zeolite 4A	CIP	95.24	This study
TP-Fe3O4@zeolite 4A nanocomposite	CIP	175.44	This study

CHAPTER FIVE
CONCLUSION AND RECOMMENDATION

5.1 General conclusion

The objective of this work was to develop bio-magnetite@zeolite 4A nanocomposites to from local materials and then use them as adsorbents for the efficient removal of pharmaceutical contaminants in aqueous solution. In this context that we harvested raw kaolin in two localities (Bong and Famgamg) in the village of Fotouni (West Cameroon). The latter can be converted into products with very high added value such as zeolite 4A with many environmental applications. Zeolite 4A was synthesized by hydrothermal method and bio-magnetite nanoparticles by co-precipitation using TP plant extracts as stabilizing and reducing agents. Zeolite 4A and bio-magnetite nanoparticles were combined with the aim of obtaining composite nanomaterials. All the materials thus prepared were characterized by different techniques and then their adsorption capacities were evaluated with respect to ciprofloxacin in aqueous solution. Through this study, the following conclusions were obtained:

i. It appears that the zeolite 4A synthesized was pure and hydrated, with a homogeneous cubic morphology. We noticed that they had a relatively mesoporous specific surface area with a value of 34,232 $m^2/g$for zeolite 4A derived from Kaolin (from the locality of Bong) and 38,443 $m^2/g$for zeolite 4A derived from Kaolin (from the locality of Famgamg). The nanocomposites combining the attractive properties of zeolite 4A and the magnetite nanoparticles (TP-Fe_3O_4) were prepared and the results of the various analyzes allowed us to see that a new paramagnetic material was obtained. It was observed that the nanocomposite exhibited homogeneous adhesion of magnetite nanoparticles to the surface of zeolite 4A, and the crystal structure of zeolite 4A was retained. The specific surface area of the nanocomposites increased with the weight of TP-Fe_3O_4, either 339,944 m^2/g, 43,969 $m^2/g$and 53,258 $m^2/g$for the MZ-2, MZ-4 and MZ-6 nanocomposites respectively.

ii. Following the application of different materials for the adsorption of ciprofloxacin, it was interesting to note that the specific surface area is not the most important factor influencing adsorption, but rather the surface chemistry (presence of the ≡Si-OH, ≡Al-OH groups and the empty orbitals of the iron ions). The maximum adsorption for zeolite

4A was obtained at pH 8, a contact time 80 minutes, an initial concentration of CIP 60 ppm and a dose of zeolite 4A of 20 mg at 25°C. The removal efficiency was 91.75% and 90.74% with a maximum adsorption capacity (q_{max}) 87.72 mg/g and 95.24 mg/g obtained from the Langmuir model for zeolite 4A derived from Kaolin (from the locality of Bong and Famgamg respectively). For the MZ-6 nanocomposite, the maximum adsorption for zeolites 4A was obtained at pH 8, a contact time of 60 minutes, an initial CIP concentration 90 ppm and a MZ-6 dose of 10 mg at 25°C. the removal efficiency was 98.78% with a maximum adsorption capacity (q_{max}) 175.44 mg/g.

iii. The study of regeneration (seven adsorption-desorption cycles) carried out on zeolites 4A and the MZ-6 nanocomposite showed that they could be used several times.

iv. Isotherm studies suggested that the Langmuir isotherm was the most suitable; suggesting that the CIP adsorption process was a monolayer adsorption on a homogeneous surface.

v. Kinetic and equilibrium studies allowed us to see that the adsorption mechanism of CIP by our different adsorbents was dominated by the chemisorption phenomenon.

vi. Thermodynamic studies indicated spontaneous and exothermic adsorption for zeolite 4A, but and endothermic process for nanocomposites.

vii. Finally, the DFT study made it possible to examine the electronic and structural characteristics of ciprofloxacin molecules. The DFT results revealed that in the aqueous phase, the CIP molecule is stable, reactive in the form of zwitterion (CIP±) and oxygen, nitrogen atoms and the aromatic ring were responsible for this reactivity. The MC simulation made it possible to decelerate the mode of interaction of the ciprofloxacin molecules on the surface of zeolite 4A (001) and MZ (001) composite. The MC simulation results showed that the adsorption of CIP molecules on the surface of zeolite 4A and MZ were favorable and spontaneous and the predominant interaction was chemisorption. In addition, the CIP molecules had more affinities with the surface of the MZ composite.

From the above, the results obtained are sustainable and reproducible. Innovative and original, in particular because they emphasize the valorization of local materials for the preservation of the environment.

5.2 Recommendations

The main perspectives relating to this work are as follows:

i. Investigations should be carried out to produce 4A zeolites and magnetite nanoparticles with even higher specific surface areas through different methods and compare their characteristics with those obtained in this work.
ii. Study the performance of the adsorbents prepared in this work with respect to other pollutants such as metals and dyes
iii. To study the performance of the adsorbents prepared in this work with respect to real wastewater. The presence of the other chemical species in the actual wastewater could affect the adsorption mechanisms in different ways. It is important to consider the presence of these elements to apply magnetite@zeolite nanocomposites in large-scale industrial applications.
iv. Finally, carry out adsorption experiments in continuous mode (column) in order to simulate water purification systems.

5.3 Contribution to knowledge

In this study, we were able to show that:

i. Raw kaolin from the Fotouni Locality can be used as a precursor during the synthesis of zeolites
ii. when zeolite is transformed into a magnetic composite, it facilitates its recovery after adsorption and increases its adsorption capacity.
iii. DFT and MC methods can effectively predict the interaction mechanisms of organic pollutants at the adsorbent surface, as well as the behavior of a compound in aqueous solution.

Generally speaking, this study aimed to effectively combat environmental pollution.

PUBLICATIONS FROM THE STUDY

Article Publications

Kamgang Djioko, F. H., Fotsop, C. G., C., Kamgang, G., Nwanonenyi, S. C., Oguzie, E. E., & Madu, C. A. (2024). Efficient removal of pharmaceutical contaminant in wastewater using low-cost zeolite 4A derived from kaolin: Experimental and theoretical studies. *Materials Chemistry and Physics*, 315, 128994 https://doi.org/10.1016/j.matchemphys.2024.128994

Kamgang Djioko, F. H., Fotsop, C. G., Kamgang Youbi, G., Nwanonenyi, S. C., Madu,C.A., C., & Oguzie, E. E. (2024). Applied Surface Science Advances Unraveling the sorption mechanisms of ciprofloxacin on the surface of zeolite 4A (001) in aqueous medium by DFT and MC approaches. *Applied Surface Science Advances*, 19, 100542. https://doi.org/10.1016/j.apsadv.2023.100542

Article Submitted

Kamgang Djioko, F. H., Fotsop, C. G., Kamgang Youbi, G., Nwanonenyi, S. C., Madu,C.A., C., & Oguzie, E. E. (2024).. Green synthesis of bio-magnetite@zeolite 4A nanocomposites for elimination of antibiotics in aqueous solution: experimental, DFT and MC approaches. Journal of inorganic and oranometallic polymers and materials

REFERENCES

Abdelfatah, A. M., Fawzy, M., El-Khouly, M. E., & Eltaweil, A. S. (2021). Efficient adsorptive removal of tetracycline from aqueous solution using phytosynthesized nano-zero valent iron. *Journal of Saudi Chemical Society*, *25*(12), 101365. https://doi.org/10.1016/j.jscs.2021.101365

Abdelrahman, E. A., Alharbi, A., Subaihi, A., Hameed, A. M., Almutairi, M. A., Algethami, F. K., & Youssef, H. M. (2020). Facile fabrication of novel analcime/sodium aluminum silicate hydrate and zeolite Y/faujasite mesoporous nanocomposites for efficient removal of Cu(II) and Pb(II) ions from aqueous media. *Journal of Materials Research and Technology*, *9*(4), 7900–7914. https://doi.org/10.1016/j.jmrt.2020.05.052

Acar, E. T. (2022). An experimental and theoretical investigation of cationic azine dye adsorption on natural sepiolite in single and multi-component systems. *Chemical Engineering Research and Design*, *187*, 507–515. https://doi.org/10.1016/j.cherd.2022.09.013

Akkermans, R. L. C., Spenley, N. A., & Robertson, S. H. (2013). Monte carlo methods in materials studio. *Molecular Simulation*, 39, 1153–1164. https://doi.org/10.1080/08927022.2013.843775

Ali, I., Peng, C., Khan, Z. M., & Sultan, M. (2018). Green Synthesis of Phytogenic Magnetic Nanoparticles and Their Applications in the Adsorptive Removal of Crystal Violet from Aqueous Solution. *Arabian Journal for Science and Engineering*. 43, 6245–6259. https://doi.org/10.1007/s13369-018-3441-6

Altaf, M., Najam, T., Shahzad, K., Ahmad, M., Hussain, T., Khurram, M & Shah, A. (2022). Heterointerface engineering of water stable ZIF-8 @ ZIF-67 : Adsorption of rhodamine B from water. *Surfaces and Interfaces*, 34, 102324. https://doi.org/10.1016/j.surfin.2022.102324

Altaf, S., Zafar, R., Zaman, W. Q., Ahmad, S., Yaqoob, K., Syed, A., Asim,J.B & Arshad, M. (2021). Removal of levofloxacin from aqueous solution by green synthesized magnetite

(Fe_3O_4) nanoparticles using *Moringa oleifera*: Kinetics and reaction mechanism analysis. Ecotoxicology and Environmental Safety, 226, 112826. https://doi.org/10.1016/j.ecoenv.2021.112826

Amin, U. R., Farid, U. K., Waheed, U. R & Sanum, S. (2018). Synthesis and characterization of zeolite 4A using swat kaolin. *Journal of Chemical Technology and Metallurgy*, 53, 5, 2018, 825-829.

Anastasiou, E., Lorentz, K. O., Stein, G. J., & Mitchell, P. D. (2014). Prehistoric schistosomiasis parasite found in the Middle East. *The Lancet Infectious Diseases*, *14*(7), 553–554. https://doi.org/10.1016/S1473-3099(14)70794-7

Anchique, L., Alc, J. J., Ramos-hernandez, A., Maximiliano, M., Mora, J. R., Rangel, N.,& Edgar, M. (2021). *Predicting the Adsorption of Amoxicillin and Ibuprofen on Chitosan and Graphene Oxide Materials : A Density Functional Theory Study*. *Polymers.* 17;13(10):1620. https://doi: 10.3390/polym13101620

Antonelli, R., Malpass, G. R. P., Da Silva, M. G. C., & Vieira, M. G. A. (2020). Adsorption of ciprofloxacin onto thermally modified bentonite clay: Experimental design, characterization, and adsorbent regeneration. *Journal of Environmental Chemical Engineering*, *8*(6), 104553. https://doi.org/10.1016/j.jece.2020.104553

Bitombo, A. N., Zintchem, A. A. A., Atchadé, A. D. T., Mbabi Nyemeck II, N., Bikobo, D. S. N., Pegnyemb, D. E., & Bochet, C. G. (2021). Antiplasmodial activities of indole alkaloids from *Tabernaemontana penduliflora* K. Schum (Apocynaceae). *Fitoterapia*, 153, 104941. doi:10.1016/j.fitote.2021.104941

Apocynaceae, T. S., Naidoo, C. M., Naidoo, Y., Dewir, Y. H., Murthy, H. N., El-hendawy, S., & Al-suhaibani, N. (2021). Major Bioactive Alkaloids and Biological Activities of Tabernaemontana Species. *Plants* 10(2), 431-458. http:// doi: 10.3390/plants10020313

Aragaw, T. A., Bogale, F. M., & Aragaw, B. A. (2021). Iron-based nanoparticles in wastewater treatment: A review on synthesis methods, applications, and removal mechanisms. *Journal of Saudi Chemical Society*, *25*(8), 101280. https://doi.org/10.1016/j.jscs.2021.101280

Araujo, E., Gianesi, C., Andrade, B., Valenzuela-diaz, F. R., & Freitas, R. De. (2014). Synthesis and Characterization of Zeolite NaP Using Kaolin Waste as a Source of Silicon and Aluminum 2 . *Material and Methods*. *17*, 174–179.

Arenas-Alatorre, J., Tehuacanero C., S., Lukas, O., Rodríguez-Gómez, A., Hernández Reyes, R., Tapia-del León, C., & Lara V., J. (2019). Synthesis and characterization of iron oxide nanoparticles grown via a non-conventional chemical method using an external magnetic field. *Materials Letters*, *242*, 13–16. https://doi.org/10.1016/j.matlet.2019.01.098

Asbollah, M. A., Syaadii, M., Sahid, M., & Waatriah, E. (2022). Dynamics and thermodynamics for competitive adsorptive removal of methylene blue and rhodamine B from binary aqueous solution onto durian rind. *Environmental Monitoring and Assessment*. 94(645), 301-342. https://doi.org/10.1007/s10661-022-10332-0

Asghar, A., Nemati, O., Alidadi, H., Yazdani, M., Asghar, A., Fezabady, N., & Taghavi, M. (2019). Optimization of ciprofloxacin adsorption from synthetic wastewaters using γ-Al_2O_3 nanoparticles : An experimental design based on response surface methodology. *Colloid and Interface Science Communications*, *33*, 100212. https://doi.org/10.1016/j.colcom.2019.100212

Ashiq, A., Adassooriya, N. M., Sarkar, B., Upamali, A., Sik, Y., & Vithanage, M. (2019). Municipal solid waste biochar-bentonite composite for the removal of antibiotic cipro fl oxacin from aqueous media. *Journal of Environmental Management*, *236*, 428–435. https://doi.org/10.1016/j.jenvman.2019.02.006

Atugoda, T., Gunawardane, C., Ahmad, M., & Vithanage, M. (2021). Chemosphere Mechanistic interaction of ciprofloxacin on zeolite modified seaweed (Sargassum crassifolium) derived biochar : Kinetics , isotherm and thermodynamics. *Chemosphere*, *281*, 130676. https://doi.org/10.1016/j.chemosphere.2021.130676

Atugoda, T., Wijesekara, H., Werellagama, D. R. I. B., Jinadasa, K. B. S. N., Bolan, N. S., & Vithanage, M. (2020). Adsorptive interaction of antibiotic ciprofloxacin on polyethylene microplastics: Implications for vector transport in water. *Environmental Technology and Innovation*, *19*, 100971. https://doi.org/10.1016/j.eti.2020.100971

Ayele, L., Pérez-Pariente, J., Chebude, Y., & Díaz, I. (2015). Synthesis of zeolite A from Ethiopian kaolin. *Microporous and Mesoporous Materials*, *215*, 29–36. https://doi.org/10.1016/j.micromeso.2015.05.022

Banu, H. A. T., Karthikeyan, P., & Meenakshi, S. (2021). Synthesis and characterization of Ce(III) decorated Duolite resin and its removal performance of toxic anions from aqueous solutions. *Environmental Chemistry and Ecotoxicology*, *3*, 8–16. https://doi.org/10.1016/j.enceco.2020.11.002

Beheshtkhoo, N., Kouhbanani, M. A. J., Savardashtaki, A., Amani, A. M., & Taghizadeh, S. (2018). Green synthesis of iron oxide nanoparticles by aqueous leaf extract of Daphne mezereum as a novel dye removing material. *Applied Physics A: Materials Science and Processing*, *124*(5), 0. https://doi.org/10.1007/s00339-018-1782-3

Belachew, N., & Hinsene, H. (2022). Preparation of Zeolite 4A for Adsorptive Removal of Methylene Blue: Optimization, Kinetics, Isotherm, and Mechanism Study. *Silicon*, *14*(4), 1629–1641. https://doi.org/10.1007/s12633-020-00938-9

Bessa, R. de A., Costa, L. de S., Oliveira, C. P., Bohn, F., do Nascimento, R. F., Sasaki, J. M., & Loiola, A. R. (2017). Kaolin-based magnetic zeolites A and P as water softeners. *Microporous and Mesoporous Materials*, *245*, 64–72. https://doi.org/10.1016/j.micromeso.2017.03.004

Bharathi, D., Preethi, S., Abarna, K., Nithyasri, M., Kishore, P., & Deepika, K. (2020). Bio-inspired synthesis of flower shaped iron oxide nanoparticles (FeONPs) using phytochemicals of *Solanum lycopersicum* leaf extract for biomedical applications. *Biocatalysis and Agricultural Biotechnology*, *27*, 101698. https://doi.org/10.1016/j.bcab.2020.101698

Bhomick, P. C., Supong, A., Kumar, S., Sema, A. I., Merry, T., & Sinha, D. (2023). Utilization of Pinus kesiya and Schima wallichii Biomass - Derived Activated Carbon for Methylene Blue Removal : Adsorption Performance and Mechanistic Insights. *Water Conservation Science and Engineering* 8, 48 (2023). https://doi.org/10.1007/s41101-023-00220-0

Bhuiyan, M. S. H., Miah, M. Y., Paul, S. C., Aka, T. Das, Saha, O., Rahaman, M. M., …

Ashaduzzaman, M. (2020). Green synthesis of iron oxide nanoparticle using Carica papaya leaf extract: application for photocatalytic degradation of remazol yellow RR dye and antibacterial activity. *Heliyon*, *6*(8), e04603. https://doi.org/10.1016/j.heliyon.2020.e04603

Bica, I., Anitas, E. M., Anitas, E. M., Choi, H. J., & Sfirloaga, P. (2020). Microwave-assisted synthesis and characterization of iron oxide microfibers. *Journal of Materials Chemistry C*, *8*(18), 6159–6167. https://doi.org/10.1039/c9tc05687d

Blasioli, S., Martucci, A., Paul, G., Gigli, L., Cossi, M., Johnston, C. T., … Braschi, I. (2014). Removal of sulfamethoxazole sulfonamide antibiotic from water by high silica zeolites: A study of the involved host-guest interactions by a combined structural, spectroscopic, and computational approach. *Journal of Colloid and Interface Science*, *419*, 148–159. https://doi.org/10.1016/j.jcis.2013.12.039

Bouayad, K., Rodi, Y. K., Elmsellem, H., El Ghadraoui, E. H., Ouzidan, Y., Abdel-Rahman, I., … Chetouani, A. (2018). Imidazo[4,5-b]pyridines as a new class of corrosion inhibitors for mild steel: Experimental and DFT approach. *Moroccan Journal of Chemistry*, *6*(1), 22–34.

Boumya, W., Khnifira, M., Machrouhi, A., Abdennouri, M., Sadiq, M., Achak, M., & Barka, N. (2021). Adsorption of Eriochrome Black T on the chitin surface: Experimental study, DFT calculations and molecular dynamics simulation. *Journal of Molecular Liquids*, *331*. https://doi.org/10.1016/j.molliq.2021.115706

Caballero, I., Colina, F. G., & Costa, J. (2007). Synthesis of X-type zeolite from dealuminated kaolin by reaction with sulfuric acid at high temperature. *Industrial and Engineering Chemistry Research*, *46*(4), 1029–1038. https://doi.org/10.1021/ie060367y

Cao, J., Sun, Q., Wang, P., Shen, J., & Dai, X. (2020). Synthesize and characterize of Fe_3O_4/ zeolite 4A magnetic nanocomposite. *Journal of Dispersion Science and Technology*, *13*(8), 1–9. https://doi.org/10.1080/01932691.2020.1843480

Carolina, A., Barizão, D. L., Fernandes, M., Andrade, M., Caroline, F., Guttierres, R., & Bergamasco, R. (2020). Green synthesis of iron oxide nanoparticles for tartrazine and

bordeaux red dye removal. *Journal of Environmental Chemical Engineering*, *8*(1), 103618. https://doi.org/10.1016/j.jece.2019.103618

Chai, X., Dong, H., Zhang, Z., Qi, Z., & Chen, J. (2022). Journal of Water Process Engineering A novel Zr-MOF modified by 4 , 6-Diamino-2-mercaptopyrimidine for exceptional Hg (II) removal. *Journal of Water Process Engineering*, *46*, 102606. https://doi.org/10.1016/j.jwpe.2022.102606

Chang, L., Pu, Y., & Jing, P. (2020). Applied Surface Science Magnetic core-shell $MnFe_2O_4$@ TiO_2 nanoparticles decorated on reduced graphene oxide as a novel adsorbent for the removal of ciprofloxacin and Cu (II) from water. *Applied Surface Science*, 53, 148400. https://doi.org/10.1016/j.apsusc.2020.148400

Charcosset, C., Limayem, I., & Fessi, H. (2004). The membrane emulsification process - A review. *Journal of Chemical Technology and Biotechnology*, *79*(3), 209–218. https://doi.org/10.1002/jctb.969

Cheikh, S., Imessaoudene, A., Bollinger, J. C., Hadadi, A., Manseri, A., Bouzaza, A., … Mouni, L. (2023). Complete Elimination of the Ciprofloxacin Antibiotic from Water by the Combination of Adsorption–Photocatalysis Process Using Natural Hydroxyapatite and TiO_2. *Catalysts*, *13*(2). https://doi.org/10.3390/catal13020336

Chohan, Z. H., Supuran, C. T., & Scozzafava, A. (2019). Metal binding and antibacterial activity of ciprofloxacin complexes Metal binding and antibacterial activity of ciprofloxacin complexes. *Journal of Enzyme Inhibition and Medicinal Chemistry*, 20(3): 303–307. https://doi.org/10.1080/14756360310001624948

Christopher, E., Mashifana, T., Kandjou, V., Amani-beni, M., Sadeghifar, H., Fayazi, M., & Thandiwe, N. (2023). Application of zeolite based nanocomposites for wastewater remediation : Evaluating newer and environmentally benign approaches. *Environmental Research*, *231*, 116073. https://doi.org/10.1016/j.envres.2023.116073

Derin, D., Mahamood, A., B, B., M, S. A., & Saton, K. S. (2023). Zeolite Synthesis from Waste materials and its Recent Applications: - A Review. *SSRN Electronic Journal*, *4*(2), 408–423. https://doi.org/10.2139/ssrn.4553520

Desbiolles, F., Howard, E., Blamey, R. C., Barimalala, R., Hart, N. C. G., & Reason, C. J. C. (2020). Role of ocean mesoscale structures in shaping the Angola-Low pressure system and the southern Africa rainfall. *Climate Dynamics*. 54(2), 2345 https://doi:10.1007/s00382-020-05199-1

Damgaard, P.B., Margaryan, A., Schroeder, H., Orlando, L., Willerslev, E., & Allentoft, M.E (2015). Improving access to endogenous DNA in ancient bones and teeth. *Sci Rep*. 17(5), 11184. doi: 10.1038/srep11184.

Das, C., Sen, S., Singh, T., Ghosh, T., Paul, S. S., Kim, T. W., & Biswas, G. (2020). Green synthesis, characterization and application of natural product coated magnetite nanoparticles for wastewater treatment. *Nanomaterials*, *10*(8), 1–19. https://doi.org/10.3390/nano10081615

Daschner De Tercero, M., Röder, C., Fehrenbacher, U., Teipel, U., & Türk, M. (2014). Continuous supercritical hydrothermal synthesis of iron oxide nanoparticle dispersions and their characterization. *Journal of Nanoparticle Research*, *16*(4). https://doi.org/10.1007/s11051-014-2350-1

Deepika, S., Singh M. K., & Nandan M. (2023). Evaluation of Genetic Diversity in Linseed (*Linum usitatissimum L*.). *International Journal of Current Microbiology and Applied Sciences*, 12(9), 2319-7706. https://doi.org/10.20546/ijcmas.2023.1209.011

De Magalhães, L. F., Da Silva, G. R., & Peres, A. E. C. (2022). Zeolite Application in Wastewater Treatment. *Adsorption Science and Technology*, 2022,*2022*. https://doi.org/10.1155/2022/4544104

Demirezen, D. A., & Yilmaz, D. D. (2018). Green synthesis and characterization of iron oxide nanoparticles using *Ficus carica* (common fig) dried fruit extract. *Internal*, 127(2), 25–29. htt:// doi: 10.1016/j.jbiosc.2018.07.024

Deng, Q., Elbeshbishy, E., & Lee, H. S. (2016). Simultaneous regeneration of exhausted zeolite and nitrogen recovery using an air stripping method at alkaline pH. *Water Quality Research Journal of Canada*, *51*(4), 321–330. https://doi.org/10.2166/wqrjc.2016.007

Díaz-Cruz, M. S., García-Galán, M. J., Guerra, P., Jelic, A., Postigo, C., Eljarrat, E.,& Petrovic,

M. (2009). Analysis of selected emerging contaminants in sewage sludge. *TrAC - Trends in Analytical Chemistry*, *28*(11), 1263–1275. https://doi.org/10.1016/j.trac.2009.09.003

Du, T., Long, Y., Liu, L., & Li, G. (2020). Value added utilization of ferronickel slags as raw materials of 4A zeolite for CO_2 reduction. *Adsorption*, *26*(7), 1113–1126. https://doi.org/10.1007/s10450-020-00246-z

Dumitru, M., Neagu, A., Miron, A., In, M., & Dur, L. (2024). Retention of Ciprofloxacin and Carbamazepine from Aqueous Solutions Using Chitosan-Based Cryostructured Composites.*Polymers* 2024, 16, 639. https://doi.org/10.3390/polym16050639

Ebrahiminezhad, A., Zare-hoseinabadi, A., Berenjian, A., & Ghasemi, Y. (2017). Green synthesis and characterization of zero- valent iron nanoparticles using stinging nettle (*Urtica dioica*) leaf extract. https://doi.org/10.1515/gps-2016-0133

Ebrahiminezhad, A., Zare, A., Ajit, H., Saeed, K. S., & Younes, T. (2018). Plant - Mediated Synthesis and Applications of Iron Nanoparticles. *Molecular Biotechnology*, *60*(2), 154–168. https://doi.org/10.1007/s12033-017-0053-4

El-Mansy, M. A. M., El-Bana, M. S., & Fouad, S. S. (2017). On the spectroscopic analyses of 3-Hydroxy-1-Phenyl-Pyridazin-6(2H)one (HPHP): A comparative experimental and computational study. *Spectrochimica Acta - Part A: Molecular and Biomolecular Spectroscopy*, *176*, 99–105. https://doi.org/10.1016/j.saa.2016.12.040

Ertürk, G., & Mattiasson, B. (2017). Molecular imprinting techniques used for the preparation of biosensors. *Sensors (Switzerland)*, *17*(2), 288. https://doi.org/10.3390/s17020288

Fanourakis, S. K., Peña-Bahamonde, J., Bandara, P. C., & Rodrigues, D. F. (2020). Nano-based adsorbent and photocatalyst use for pharmaceutical contaminant removal during indirect potable water reuse. *Npj Clean Water*, *3*(1), 45-60. https://doi.org/10.1038/s41545-019-0048-8

Ferdinand, G., Fregue, R., Tagne, T., Lesly, S., Jiokeng, Z., Fotsop, C. G., &7Tamo, A. K. (2022). Lignocellulosic-Based Materials from Bean and Pistachio Pod Wastes for Dye-Contaminated Water Treatment : Optimization and Modeling of Indigo Carmine Sorption. Polymers 2022, 14(18), 3776; https://doi.org/10.3390/polym14183776

González-González, R. B., Sharma, A., Parra-Saldívar, R., Ramirez-Mendoza, R. A., Bilal, M., & Iqbal, H. M. N. (2022). Decontamination of emerging pharmaceutical pollutants using carbon-dots as robust materials. *Journal of Hazardous Materials*, *423*, 127145 https://doi.org/10.1016/j.jhazmat.2021.127145

Guellati, A., Maachi, R., & Chaabane, T. (2022). Aluminum dispersed bamboo activated carbon production for effective removal of Ciprofloxacin hydrochloride antibiotics : Optimization and mechanism study. *Journal of Environmental Management,* 301, 113765. https://doi.org/10.1016/j.jenvman.2021.113765

Guth, J.-L., Collin, P., & Wey, R. (1970). Préparation et propriétés d'une zéolite du type A enrichie en silicium. *Bulletin de La Société Française de Minéralogie et de Cristallographie*, *93*(1), 59–65. https://doi.org/10.3406/bulmi.1970.6428

Harcel, F., Djioko, K., Ghislain, C., Kamgang, G., Emmanuel, E., & Ada, C. (2024). Efficient removal of pharmaceutical contaminant in wastewater using low-cost zeolite 4A derived from kaolin : Experimental and theoretical studies. *Materials Chemistry and Physics,315,* 128994. https://doi.org/10.1016/j.matchemphys.2024.128994

Hartig, C., Ernst, M., & Jekel, M. (2001). Research note membrane filtration of two sulphonamides in tertiary effluents and subsequent adsorption on activated carbon. *Water Research*, 35(16), 3998–4003. https://doi.org/10.1016/S0043-1354(01)00109-9

Hashemian, S., Hosseini, S. H., Salehifar, H., & Salari, K. (2013). Adsorption of Fe(III) from Aqueous Solution by Linde Type-A Zeolite. *American Journal of Analytical Chemistry*, *04*(07), 123–126. https://doi.org/10.4236/ajac.2013.47a017

Hassan, A. A., Sajid, M., Tanimu, A., Abdulazeez, I., & Alhooshani, K. (2021). Removal of methylene blue and rose bengal dyes from aqueous solutions using 1-naphthylammonium tetrachloroferrate (III). *Journal of Molecular Liquids*, *322*, 114966. https://doi.org/10.1016/j.molliq.2020.114966

Hernández, F., Ibáñez, M., Bade, R., Bijlsma, L., & Sancho, J. V. (2014). Investigation of pharmaceuticals and illicit drugs in waters by liquid chromatography-high-resolution mass spectrometry. *TrAC - Trends in Analytical Chemistry*, *63*, 140–157.

https://doi.org/10.1016/j.trac.2014.08.003

Ho, Y. S., & Mckay, G. (1999). Pseudo-second order model for sorption processes. *Process Biochemistry*. *34*, 451–465. https://doi.org/10.1016/S0032-9592(98)00112-5

Ho, Y. S., & McKay, G. (1998). A Comparison of chemisorption kinetic models applied to pollutant removal on various sorbents. *Process Safety and Environmental Protection*, *76*(4), 332–340. https://doi.org/10.1205/095758298529696

Huang, Z. H., Ji, Z. Y., Zhao, Y. Y., Liu, J., Li, F., Wang, S. Z., & Yuan, J. S. (2020). Efficient degradation of 2-methoxyphenol using heterogeneous-homogeneous synergistic activated persulfate with modified clinoptilolite + heat. *Chemical Engineering Journal*, *400*, 125863. https://doi.org/10.1016/j.cej.2020.125863

Iqbal, A., Sattar, H., Haider, R., & Munir, S. (2019). Synthesis and characterization of pure phase zeolite 4A from coal fly. *Journal of Cleaner Production*, *219*, 258–267. https://doi.org/10.1016/j.jclepro.2019.02.066

Izadiyan, Z., Shameli, K., Miyake, M., Hara, H., Mohamad, S. E. B., Kalantari, K., Taib,S.H.M & Rasouli, E. (2020). Cytotoxicity assay of plant-mediated synthesized iron oxide nanoparticles using *Juglans regia* green husk extract. *Arabian Journal of Chemistry*, *13*(1), 2011–2023. https://doi.org/10.1016/j.arabjc.2018.02.019

Jahangirian, H., Halim, M., Ismail, S., Rafiee-moghaddam, R., Shameli, K., Gharibshahi, E., & Soltaninejad, S. (2013). synthesis and characterization of zeolite / Fe_3O_4 nanocomposite by green quick precipitation method. *Digest Journal of Nanomaterials and Biostructures*, *8*(4), 1405–1413.

Jara-cobos, L., Montero, C., Menendez, M., & Pinos-v, V. (2023). Ciprofloxacin Removal Using Pillared Clays. *Water*, 15(11), 2056; https://doi.org/10.3390/w15112056

Jose, V. R., Zikalala, N., Sakho, E. H. M., & Oluwafemi, O. S. (2020). Green synthesis protocol on metal oxide nanoparticles using plant extracts. In *Colloidal Metal Oxide Nanoparticles*. 2020, 67-82. https://doi.org/10.1016/b978-0-12-813357-6.00006-1

Kanagasubbulakshmi, S., & Kadirvelu, K. (2017). Green synthesis of Iron oxide nanoparticles using *Lagenaria siceraria* and evaluation of its Antimicrobial activity. *Defence Life*

Science Journal, *2*(4), 422. https://doi.org/10.14429/dlsj.2.12277

Khalil, M. I. (2015). Co-precipitation in aqueous solution synthesis of magnetite nanoparticles using iron(III) salts as precursors. *Arabian Journal of Chemistry*, *8*(2), 279–284. https://doi.org/10.1016/j.arabjc.2015.02.008

Khalil, N. (2003). Quantum chemical approach of corrosion inhibition. *Electrochimica Acta*. *48*, 2635–2640. https://doi.org/10.1016/S0013-4686(03)00307-4

Khan, N. A., Shaheen, S., Najam, T., Shoaib, S., Shah, A., Javed, M. S.,& Ashfaq, M. (2020). Efficient removal of norfloxacin by MOF @ GO composite : isothermal , kinetic , statistical , and mechanistic study. *Toxin Reviews*, *103*(16), 915-927. https://doi.org/10.1080/15569543.2020.1801750

Khashei, S. A., Shahidi, A., Taherian, P., & Zeraatkar, Z. (2021). Comparing natural and mineral adsorbents in removing chromium from aquatic environment. *Ain Shams Engineering Journal*, *12*(3), 2593–2601. https://doi.org/10.1016/j.asej.2021.02.019

Khnifira, M., Hamidi, S. El, & Sadiq, M. (2022). Applied Surface Science Adsorption mechanisms investigation of methylene blue on the (001) zeolite 4A surface in aqueous medium by computational approach and molecular dynamics. *Applied Surface Science*, *572*, 151381. https://doi.org/10.1016/j.apsusc.2021.151381

Khnifira, M., Mahsoune, A., Belghiti, M. E., Khamar, L., Sadiq, M., Abdennouri, M., & Barka, N. (2020). Materials Today : Proceedings HF and SiF 4 adsorption on carbon graphite (1 1 1) surface in aqueous medium : A combined DFT and MD simulation approach. *Materials Today: Proceedings*, (2020), 1–7. https://doi.org/10.1016/j.matpr.2020.10.797

Kianfar, E., & Universitesi, I. M. (2020). Zeolites: Properties, Applications, Modification and Selectivity. 2022. 1079-1299 . https://doi.org/10.1080/01614940.2021.2003084

Klosterhaus, S. L., Grace, R., Hamilton, M. C., & Yee, D. (2013). Method validation and reconnaissance of pharmaceuticals , personal care products , and alkylphenols in surface waters , sediments , and mussels in an urban estuary. *Environment International*, *54*, 92–99. https://doi.org/10.1016/j.envint.2013.01.009

Kondori, J., Zendehboudi, S., & James, L. (2019). Molecular dynamic simulations to evaluate

dissociation of hydrate structure II in the presence of inhibitors: A mechanistic study. *Chemical Engineering Research and Design*, *149*, 81–94. https://doi.org/10.1016/j.cherd.2019.05.048

Kora, L., Tiomo, N., Ada, C., Ezema, F. I., Ngoune, J., & Emmanuel, E. (2024). Molecular modelling of energy storage performance on metal organic frameworks / ethane nanoparticles nanofluids mixtures and derivatives. *Materials Today Communications*, *38*, 107756. https://doi.org/10.1016/j.mtcomm.2023.107756

Kovalakova, P., Cizmas, L., McDonald, T. J., Marsalek, B., Feng, M., & Sharma, V. K. (2020). Occurrence and toxicity of antibiotics in the aquatic environment: A review. *Chemosphere*, *251*, 126351. https://doi.org/10.1016/j.chemosphere.2020.126351

Kumfer, B. M., Shinoda, K., Jeyadevan, B., & Kennedy, I. M. (2010). Gas-phase flame synthesis and properties of magnetic iron oxide nanoparticles with reduced oxidation state. *Journal of Aerosol Science*, *41*(3), 257–265. https://doi.org/10.1016/j.jaerosci.2010.01.003

Kummerer, K. (2010) Pharmaceuticals in the Environment: Sources, Fate, Effects and Risks. *Environmental Science and Pollution Research*, 17, 519-521.https://doi.org/10.1146/annurev-environ-052809-161223

Langwaldt, J. (2008). Ammonium removal from water by eight natural zeolites: A comparative study. *Separation Science and Technology*, *43*(8), 2166–2182. https://doi.org/10.1080/01496390802063937

Lata, S., Singh, P. K., & Samadder, S. R. (2015). Regeneration of adsorbents and recovery of heavy metals: a review. *International Journal of Environmental Science and Technology*, *12*(4), 1461–1478. https://doi.org/10.1007/s13762-014-0714-9

Li, K., Li, J., Lu, M., Li, H., & Wang, X. (2016). Preparation and amino modification of mesoporous carbon from bagasse via microwave activation and ethylenediamine polymerization for Pb (II) adsorption. *57*, 19443994. https://doi.org/10.1080/19443994.2016.1138891

Li, S., Huang, T., Du, P., Liu, W., & Hu, J. (2020). Photocatalytic transformation fate and toxicity of ciprofloxacin related to dissociation species: Experimental and theoretical

evidences. *Water Research*, *185*. https://doi.org/10.1016/j.watres.2020.116286

Li, X., Ji, M., Nghiem, L. D., Zhao, Y., Liu, D., Yang, Y.,& Tran, N. H. (2020). A novel red mud adsorbent for phosphorus and diclofenac removal from wastewater. *Journal of Molecular Liquids*, *303*, 112286. https://doi.org/10.1016/j.molliq.2019.112286

Li, Y., Wei, W., Chen, J., Zu, L., Zhou, Y., Wu, J., & Wu, X. (2022). Applied Surface Science Atomic layer deposition precisely modified zeolite 13X : Physicochemical synergistic adsorption of space molecular contaminants. *Applied Surface Science*, *590*, 153084. https://doi.org/10.1016/j.apsusc.2022.153084

Liang, M. K., Deschaume, O., Patwardhan, S. V., & Perry, C. C. (2011). Direct evidence of ZnO morphology modification via the selective adsorption of ZnO-binding peptides. *Journal of Materials Chemistry*, *21*(1), 80–89. https://doi.org/10.1039/c0jm02124e

Ling, W., Wang, M., Xiong, C., Xie, D., Chen, Q., Chu, X.,& Xiao, X. (2019). Synthesis, surface modification, and applications of magnetic iron oxide nanoparticles. *Journal of Materials Research*, *34*(11), 1828–1844. https://doi.org/10.1557/jmr.2019.129

Lingamdinne, L. P., Koduru, J. R., & Karri, R. R. (2019). Green Synthesis of Iron Oxide Nanoparticles for Lead Removal from Aqueous Solutions. *805*(13), 122–127. https://doi.org/10.4028/www.scientific.net/KEM.805.122

Liu, S., Zhang, W., Tan, X., Zhao, F., Huang, W., Du, H.,& Diao, K. (2018). Performance of a zeolite modified with: N, N -dimethyl dehydroabietylamine oxide (DAAO) for adsorption of humic acid assessed in batch and fixed bed columns. *RSC Advances*, *8*(16), 9006–9016. https://doi.org/10.1039/c8ra00166a

Low, S. S., Lim, C. N., Yew, M., Chai, W. S., Low, L. E., Manickam, S., & Show, P. L. (2021). Recent ultrasound advancements for the manipulation of nanobiomaterials and nanoformulations for drug delivery. *Ultrasonics Sonochemistry*, *80*, 105805. https://doi.org/10.1016/j.ultsonch.2021.105805

Low, S. S., Yew, M., Lim, C. N., Chai, W. S., Low, L. E., Manickam, S., & Show, P. L. (2022). Sonoproduction of nanobiomaterials – A critical review. *Ultrasonics Sonochemistry*, *82*, 105887. https://doi.org/10.1016/j.ultsonch.2021.105887

Lucresse, K., Nguena, T., Ghislain, C., Bruno, S., Ngomade, L., Kamdem, A., Madu, C.A & Emmanuel, E. (2023). Mathematical modeling approach for the green synthesis of high-performance nanoporous zeolites Na-X optimized for water vapor sorption. *Materials Today Communications*, *37*, 107406. https://doi.org/10.1016/j.mtcomm.2023.107406

M. Khnifira., W. Boumya., J. Attarki., A. Mahsoune., M. Sadiq., M. Abdennouri., S. K. and N. B. (2022). A combined DFT , Monte Carlo , and MD simulations of adsorption study of heavy metals on the carbon graphite (111) surface A combined DFT , Monte Carlo , and MD simulations of adsorption study of heavy metals on the carbon graphite (111) surface. *Chemical Physics Impact*, *5*, 100121. https://doi.org/10.1016/j.chphi.2022.100121

Ma, Y., Yan, C., Alshameri, A., Qiu, X., Zhou, C., & Li, D. (2014). Synthesis and characterization of 13X zeolite from low-grade natural kaolin. *Advanced Powder Technology*, *25*(2), 495–499. https://doi.org/10.1016/j.apt.2013.08.002

Mahmoud, A. A., Osman, O., Elhaes, H., Ferretti, M., Fakhry, A., & Ibrahim, M. A. (2018). Computational analyses for the interaction between aspartic acid and iron. *Journal of Computational and Theoretical Nanoscience*, *15*(2), 470–473. https://doi.org/10.1166/jctn.2018.7113

Makkar, P., & Ghosh, N. N. (2021). A review on the use of DFT for the prediction of the properties of nanomaterials. *RSC Advances*, *11*(45), 27897–27924. https://doi.org/10.1039/d1ra04876g

Martín-Pozo, L., de Alarcón-Gómez, B., Rodríguez-Gómez, R., García-Córcoles, M. T., Çipa, M., & Zafra-Gómez, A. (2019). Analytical methods for the determination of emerging contaminants in sewage sludge samples. A review. *Talanta*, *192*, 508–533. https://doi.org/10.1016/j.talanta.2018.09.056

Md Ishak, N. A. I., Kamarudin, S. K., & Timmiati, S. N. (2019). Green synthesis of metal and metal oxide nanoparticles via plant extracts: an overview. *Materials Research Express*, *6*(11). https://doi.org/10.1088/2053-1591/ab4458

Meng, F., Wang, L., Pei, M., Guo, W., & Liu, G. (2017). Adsorption of metanil yellow from aqueous solution using polyaniline-bentonite composite. *Colloid and Polymer Science*,

295(7), 1165–1175. https://doi.org/10.1007/s00396-017-4098-5

Mgbemere, Henry E, Ekpe, I. C., & Lawal, G. I. (2017). Zeolite Synthesis , Characterization and Application Areas : A Review. *International Research Journal of Environmental Sciences*. *6*(10), 1–6.

Mgbemere, Henry Ekene, Ekpe, I. C., Lawal, G., Ovri, H., & Chaudhary, A. L. (2019). Preparation and characterization of zeolite type 4a using kaolin from Ajebo, Nigeria. *Pertanika Journal of Science and Technology*, *27*(4), 2427–2438.

Microcalorimetrie, X. P. S. E. T., Fechete, I., Caullet, P., Dumitriu, E., Hulea, V., Guimon, C., & Kessler, H. (2006). zeolithe al-mcm-22 : etude de l ’acidite par. vii(1), 103–120.

Mohammed, A. A., & Kareem, S. L. (2021). Enhancement of ciprofloxacin antibiotic removal from aqueous solution using zno nanoparticles coated on pistachio shell. *Desalination and Water Treatment*, *213*, 229–239. https://doi.org/10.5004/dwt.2021.26674

Mohammed, S. J., M-ridha, M. J., Abed, K. M., & Amal, A. M. (2021). Removal of levofloxacin and ciprofloxacin from aqueous solutions and an economic evaluation using the electrocoagulation process . *International Journal of Environmental Analytical Chemistry*, *103*(16), 1–19. https://doi.org/10.1080/03067319.2021.1913733

Moussa, David, Doubla, A., Kamgang-Youbi, G., & Brisset, J. L. (2007). Postdischarge long life reactive intermediates involved in the plasma chemical degradation of an azoic dye. *IEEE Transactions on Plasma Science*, *35*(2 III), 444–453. https://doi.org/10.1109/TPS.2007.892578

Moussa, Diarra, Narcisse, A., & Meite, L. (2018). Influence de la source lumineuse et de la nature de l ’ eau sur l ’ élimination de la ciprofloxacine . *journal bioresource technology*, 044, 23 - 29

Musa, A. Y., Jalgham, R. T. T., & Mohamad, A. B. (2012). Molecular dynamic and quantum chemical calculations for phthalazine derivatives as corrosion inhibitors of mild steel in 1M HCl. *Corrosion Science*, *56*, 176–183. https://doi.org/10.1016/j.corsci.2011.12.005

Mwendapole, B., & Gang, L. (2022). Investigation of Adsorption Behaviors of Paraffin Waxes on Iron , Iron II Oxide , and Iron III Oxide Surfaces Using the Adsorption Locator Model.

Arabian Journal for Science and Engineering. 47, 11763–11773. https://doi.org/10.1007/s13369-021-06522-6

Nasrollahzadeh, M., Atarod, M., & Sajjadi, M. (2019). Plant-Mediated Green Synthesis of Nanostructures : Mechanisms , Characterization , and Applications. In *An Introduction to Green Nanotechnology*, 28,199-322. https://doi.org/10.1016/B978-0-12-813586-0.00006-7

Natarajan, R., Saikia, K., Kumar, S., Karanam, A., Sri, D., Venkataraman, S., Mohideen,V & Kumar, V. (2022). Chemosphere Understanding the factors affecting adsorption of pharmaceuticals on different adsorbents – A critical literature update. *Chemosphere*, *287*, 131958. https://doi.org/10.1016/j.chemosphere.2021.131958

Nemati, O., Asghar, A., Yazdani, M., & Taghavi, M. (2019). Journal of Water Process Engineering Catalytic ozonation of cipro fl oxacin using γ -Al_2O_3 nanoparticles in synthetic and real wastewaters. *Journal of Water Process Engineering*, *32*, 100894. https://doi.org/10.1016/j.jwpe.2019.100894

Neolaka, Y. A. B., Lawa, Y., Naat, J., & Riwu, A. A. P. (2022). Efficiency of activated natural zeolite-based magnetic composite (ANZ-Fe_3O_4) as a novel adsorbent for removal of Cr (VI) from wastewater. *Journal of Materials Research and Technology*, *18*, 2896–2909. https://doi.org/10.1016/j.jmrt.2022.03.153

Ngeno, E. C., Shikuku, V. O., Orata, F., Baraza, L. D., & Kimosop, S. J. (2019). Caffeine and ciprofloxacin adsorption from water onto clinoptilolite: Linear isotherms, kinetics, thermodynamic and mechanistic studies. *South African Journal of Chemistry*, *72*, 136–142. https://doi.org/10.17159/0379-4350/2019/V72A17

Nisticò, R. (2021). A synthetic guide toward the tailored production of magnetic iron oxide nanoparticles. *Boletin de La Sociedad Espanola de Ceramica y Vidrio*, *60*(1), 29–40. https://doi.org/10.1016/j.bsecv.2020.01.011

Nizam, M. K., Azhari, S., Azan, M., & Tamar, B. (2021). Modified Zeolite as Purification Material in Wastewater Treatment : A Review. *Scientific Research Journal*, 18(2), 177–213. https://doi.org/10.24191/srj.v18i2.12092

Norfazilah Wan Ismail, W., & Umairah Mokhtar, S. (2021). Various Methods for Removal, Treatment, and Detection of Emerging Water Contaminants. *Emerging Contaminants*, 43,2344. https://doi.org/10.5772/intechopen.93375

Nsami, J. N., & Mbadcam, J. K. (2013). The Adsorption Efficiency of Chemically Prepared Activated Carbon from Cola Nut Shells by ZnCl2 on Methylene Blue. *scientific research*. 25,2021. https://doi.org/10.1155/2013/469170

Nwanonenyi, S. C., Obasi, H. C., Obidiegwu, M. U., & Chukwujike, I. C. (2020). Anticorrosion response of polymer mixture on mild steel in hydrochloric acid environment. Emergent Materials, 2020, 663-673. https://doi.org/10.1007/s42247-020-00120-2

Nyankson, E., Adjasoo, J., Efavi, J. K., Amedalor, R., Yaya, A., Manu, G. P., Asare, K., & Amartey, N. A. (2019). Characterization and evaluation of zeolite A/Fe3O4 nanocomposite as a potential adsorbent for removal of organic molecules from wastewater. *Journal of Chemistry*, 2019, 8090756. https://doi.org/10.1155/2019/8090756

Okoli, C., Boutonnet, M., Mariey, L., Järås, S., & Rajarao, G. (2011). Application of magnetic iron oxide nanoparticles prepared from microemulsions for protein purification. *Journal of Chemical Technology and Biotechnology*, *86*(11), 1386–1393. https://doi.org/10.1002/jctb.2704

Oktem, Y. A., Ince, O., Sallis, P., Donnelly, T., & Ince, B. K. (2008). Anaerobic treatment of a chemical synthesis-based pharmaceutical wastewater in a hybrid upflow anaerobic sludge blanket reactor. *Bioresource Technology*, *99*(5), 1089–1096. https://doi.org/10.1016/j.biortech.2007.02.036

Oliveira, L. H., França, D. B., Moraes, A. I. S., Medina-carrasco, S., Fonseca, M. G., Osajima, J. A., Edson,C & Orta, M. (2024). An overview about synthetic high charge micas and their uses. Applied Clay Science, 251, 107325. https://doi.org/10.1016/j.clay.2024.107325

Onal, E. S., Yatkın, T., Aslanov, T., Erg, M., & Ozer, A. (2019). Biosynthesis and Characterization of Iron Nanoparticles for Effective Adsorption of Cr (VI). *International Journal of Chemical Engineering, 2019*(Vi),234,-245.

https://doi.org/10.1155/2019/2716423

Pabalan, R. T., & Bertetti, F. P. (2001). Cation-exchange properties of natural zeolites. *Reviews in Mineralogy and Geochemistry*, *45*(Gottardi 1978), 453–517. https://doi.org/10.2138/rmg.2001.45.14

Pai, S., Kini, S. M., Narasimhan, M. K., Pugazhendhi, A., & Selvaraj, R. (2021). Structural characterization and adsorptive ability of green synthesized Fe_3O_4 nanoparticles to remove Acid blue 113 dye. *Surfaces and Interfaces*, 23, 100947. https://doi.org/10.1016/j.surfin.2021.100947

Panda, S. K., Aggarwal, I., Kumar, H., Prasad, L., Kumar, A., Sharma, A., & Viet, D. (2021). Magnetite nanoparticles as sorbents for dye removal : a review. In *Environmental Chemistry Letters*. Springer International Publishing. https://doi.org/10.1007/s10311-020-01173-9

Parajuli, K., Sah, A. K., & Paudyal, H. (2020). Green Synthesis of Magnetite Nanoparticles Using Aqueous Leaves Extracts of <i>Azadirachta indica</i> and Its Application for the Removal of As(V) from Water. *Green and Sustainable Chemistry*, *10*(04), 117–132. https://doi.org/10.4236/gsc.2020.104009

Patel, M., Kumar, R., Kishor, K., Mlsna, T., Pittman, C. U., & Mohan, D. (2018). Pharmaceuticals of Emerging Concern in Aquatic Systems : Chemistry , Occurrence , E ff ects , and Removal Methods. Chemical Reviews. 2019, 119, 6, 3510–3673. https://doi.org/10.1021/acs.chemrev.8b00299

Petrov, I., & Michalev, T. (2012). Synthesis of Zeolite A : A Review. *Chemistry, Materials Science* 2, 30–35.

Piacentini, E. (2015). Membrane Emulsification. *Encyclopedia of Membranes*, 1–3. https://doi.org/10.1007/978-3-642-40872-4_1947-1

Pico, Y., Belenguer, V., Corcellas, C., Diaz-Cruz, M. S., Eljarrat, E., Farré, M.,& Barcelo, D. (2019). Contaminants of emerging concern in freshwater fish from four Spanish Rivers. *Science of the Total Environment*, *659*, 1186–1198. https://doi.org/10.1016/j.scitotenv.2018.12.366

Popok, V. N., & Kylián, O. (2020). Gas-Phase Synthesis of Functional Nanomaterials. *Applied Nano, 1*(1), 25–58. https://doi.org/10.3390/applnano1010004

Pourazar, M. B., Mohammadi, T., Jafari Nasr, M. R., Javanbakht, M., & Bakhtiari, O. (2020). Preparation of 13X zeolite powder and membrane: Investigation of synthesis parameters impacts using experimental design. *Materials Research Express, 7*(3),16. https://doi.org/10.1088/2053-1591/ab7217

Pradhan, J., Singh, R., & Kumar, B. (2022). Phytosynthesis of iron oxide nanoparticles using juncus inflexus shoot extract. *Biointerface Research in Applied Chemistry, 12*(3), 3790–3799. https://doi.org/10.33263/BRIAC123.37903799

Predoi, D., Iconaru, S. L., Predoi, M. V., Stan, G. E., & Buton, N. (2019). Synthesis, characterization, and antimicrobial activity of magnesium-doped hydroxyapatite suspensions. *Nanomaterials*, *9*(9), 1–20. https://doi.org/10.3390/nano9091295

Quintelas, C., Mesquita, D. P., Ferreira, E. C., & Amaral, A. L. (2019). Quantification of pharmaceutical compounds in wastewater samples by near infrared spectroscopy (NIR). *Talanta*, *194*, 507–513. https://doi.org/10.1016/j.talanta.2018.10.076

Rajiv, P., Mengelizadeh, N., & Mckay, G. (2021). Photocatalytic degradation of ciprofloxacin with Fe_2O_3 nanoparticles loaded on graphitic carbon nitride : mineralisation , degradation mechanism and toxicity assessment. *International Journal of Environmental Analytical Chemistry*, 103(10), 2193-2207. https://doi.org/10.1080/03067319.2021.1890059

Río-gamero, B. Del, Alonso, J. J. S., Kori, N. El, & Meli, N. (2018). Removal of ciprofloxacin from seawater by reverse osmosis. *Environmental Chemistry for a Sustainable World Emerging Contaminants* 217. 1-106. https://doi.org/10.1016/j.jenvman.2018.03.108

Roland, G., Bienvenue, A., Shehla, N., Rahman, A., Thierry, J., & Iqbal, M. (2022). New glycocerebrosides from the trunk of Tabernaemontana contorta Stapf . (Apocynaceae) and their antibacterial activity. *Phytochemistry Letters*. 35 (11), 1757-1765. https://doi.org/10.1016/j.bse.2022.104396

Sabín López, A., Paredes Ramos, M., Herrero, R., & López Vilarinõ, J. M. (2020). Synthesis of magnetic green nanoparticle-Molecular imprinted polymers with emerging contaminants

templates. *Journal of Environmental Chemical Engineering*, *8*(4), 103889. https://doi.org/10.1016/j.jece.2020.103889

Saied, M. El, Shaban, S. A., Mostafa, M. S., & Naga, A. O. A. El. (2022). Efficient adsorption of acetaminophen from the aqueous phase using low-cost and renewable adsorbent derived from orange peels. *Biomass Conversion and Biorefinery*, (0123456789). https://doi.org/10.1007/s13399-022-02541-x

Saleh, T. A., Sari, A., & Tuzen, M. (2017). Optimization of parameters with experimental design for the adsorption of mercury using polyethylenimine modified-activated carbon. *Journal of Environmental Chemical Engineering*, *5*(1), 1079–1088. https://doi.org/10.1016/j.jece.2017.01.032

Samal, K., Mahapatra, S., & Hibzur Ali, M. (2022). Pharmaceutical wastewater as Emerging Contaminants (EC): Treatment technologies, impact on environment and human health. *Energy Nexus*, 6, 100076. https://doi.org/10.1016/j.nexus.2022.100076

Samrot, A. V, Durga, N. S. P., Chamarthy, S., & Sahithya, S. (2018). Utilization of chitosan - coated superparamagnetic iron oxide nanoparticles for chromium removal. *Applied Water Science*, 8, 192. https://doi.org/10.1007/s13201-018-0841-4

Sanderson, H., Brain, R. A., Johnson, D. J., Wilson, C. J., & Solomon, K. R. (2004). Toxicity classification and evaluation of four pharmaceuticals classes: Antibiotics, antineoplastics, cardiovascular, and sex hormones. *Toxicology*, *203*(1–3), 27–40. https://doi.org/10.1016/j.tox.2004.05.015

Sathya, K., Saravanathamizhan, R., & Baskar, G. (2017). Ultrasound assisted Phytosynthesis of Iron Oxide Nanoparticle. *Ultrasonics - Sonochemistry*, 39, 446-451 . https://doi.org/10.1016/j.ultsonch.2017.05.017

Seabra, A. B., Haddad, P., & Duran, N. (2013). Biogenic synthesis of nanostructured iron compounds: Applications and perspectives. *IET Nanobiotechnology*, *7*(3), 90–99. https://doi.org/10.1049/iet-nbt.2012.0047

Sedik, A., Athmani, S., Saoudi, A., Ferkous, H., Ribouh, N., Lerari, D., … Benguerba, Y. (2022). Experimental and theoretical insights into copper corrosion inhibition by

protonated amino-acids. *RSC Advances*, *12*(36), 23718–23735. https://doi.org/10.1039/d2ra03535a

Serna-Galvis, E. A., Berrio-Perlaza, K. E., & Torres-Palma, R. A. (2017). Electrochemical treatment of penicillin, cephalosporin, and fluoroquinolone antibiotics via active chlorine: evaluation of antimicrobial activity, toxicity, matrix, and their correlation with the degradation pathways. *Environmental Science and Pollution Research*, *24*(30), 23771–23782. https://doi.org/10.1007/s11356-017-9985-2

Sert, Ç. S., Koç, F., Len, A., Almásy, L., & Dudás, Z. (2025). Silica aerogels modified with vinyl, epoxide, methacrylate moieties for the removal of ciprofloxacin by adsorption from water. *Separation and Purification Technology*, 354, 129112. https://doi.org/10.1016/j.seppur.2024.129112

Shahid, K., Srivastava, V., & Sillanpää, M. (2021). Protein recovery as a resource from waste specifically via membrane technology — from waste to wonder. *Environmental Science and Pollution Research.* 28, 10262–10282. https://doi.org/10.1007/s11356-020-12290-x

Sharif, M., Zhang, T., Wu, X., Yu, Y., & Zhang, Z. (2020). International Journal of Greenhouse Gas Control Evaluation of CO 2 absorption performance by molecular dynamic simulation for mixed secondary and tertiary amines. *International Journal of Greenhouse Gas Control*, 97, 103059. https://doi.org/10.1016/j.ijggc.2020.103059

Shi, S., Xu, C., Wang, X., Xie, Y., Wang, Y., Dong, Q., … Xu, D. (2020). Electrospinning fabrication of flexible Fe3O4 fibers by sol-gel method with high saturation magnetization for heavy metal adsorption. *Materials and Design*, *186*, 108298. https://doi.org/10.1016/j.matdes.2019.108298

Siipola, V., Pflugmacher, S., Romar, H., Wendling, L., & Koukkari, P. (2020). Low-Cost Biochar Adsorbents for Water Purification Including Microplastics Removal. *Applied Sciences,* 2020, 10(3), 788. https://doi.org/10.3390/app10030788

Simonin, J. P. (2016). On the comparison of pseudo-first order and pseudo-second order rate laws in the modeling of adsorption kinetics. *Chemical Engineering Journal*, *300*, 254–263. https://doi.org/10.1016/j.cej.2016.04.079

Singh, A., Ansari, K. R., Banerjee, P., Murmu, M., Quraishi, M. A., & Lin, Y. (2021). Colloids and Surfaces A : Physicochemical and Engineering Aspects Corrosion inhibition behavior of piperidinium based ionic liquids on Q235 steel in hydrochloric acid solution : Experimental , density functional theory and molecular dynamics study. *Colloids and Surfaces A: Physicochemical and Engineering Aspects*, *623*, 126708. https://doi.org/10.1016/j.colsurfa.2021.126708

Sivalingam, S., & Sen, S. (2018). Optimization of synthesis parameters and characterization of coal fly ash derived microporous zeolite X. *Applied Surface Science*, *455*, 903–910. https://doi.org/10.1016/j.apsusc.2018.05.222

Stan, M., Lung, I., Soran, M. L., Leostean, C., Popa, A., Stefan, M.,& Porav, A. S. (2017). Removal of antibiotics from aqueous solutions by green synthesized magnetite nanoparticles with selected agro-waste extracts. *Process Safety and Environmental Protection*, *107*, 357–372. https://doi.org/10.1016/j.psep.2017.03.003

Sun, Y., Li, H., Li, G., Gao, B., Yue, Q., & Li, X. (2016). Characterization and ciprofloxacin adsorption properties of activated carbons prepared from biomass wastes by H_3PO_4 activation. *bioresource technology*. 217, 239-244. https://doi.org/10.1016/j.biortech.2016.03.047

Surya, M. R., Ismail, A. F., Rahman, M. A., & Sridhar, S. (2014). Mixed matrix membranes of Pebax-1657 loaded with 4A zeolite for gaseous separations. *Separation and Purification Technology*, *129*, 1–8. https://doi.org/10.1016/j.seppur.2014.03.017

Tadic, M., Panjan, M., Tadic, B. V., Lazovic, J., Damnjanovic, V., Kopani, M., & Kopanja, L. (2019). Magnetic properties of hematite (α - Fe_2O_3) nanoparticles synthesized by sol-gel synthesis method: The influence of particle size and particle size distribution. *Journal of Electrical Engineering*, *70*(7), 71–76. https://doi.org/10.2478/jee-2019-0044

Tran, N. B. T., Duong, N. B., & Le, N. L. (2021). Synthesis and Characterization of Magnetic Fe_3O_4/Zeolite NaA Nanocomposite for the Adsorption Removal of Methylene Blue Potential in Wastewater Treatment. *Journal of Chemistry, 539, 35465*. https://doi.org/10.1155/2021/6678588

Tercero, D. M., Röder, C., Fehrenbacher, U., Teipel, U., & Türk, M. (2014). Continuous supercritical hydrothermal synthesis of iron oxide nanoparticle dispersions and their characterization. *Journal of Nanoparticle Research*, 16(4), 2350 doi:10.1007/s11051-014-2350-1

Tu, S., Sena, Ş., Kerkez, Ö., & Abdel, M. (2017). Ef fi cient removal of antibiotics by a novel magnetic adsorbent : Magnetic activated carbon / chitosan (MACC) nanocomposite. 240, 589–596. https://doi.org/10.1016/j.molliq.2017.05.131

Vinayagam, R., Pai, S., Varadavenkatesan, T., Narasimhan, M. K., Narayanasamy, S., & Selvaraj, R. (2020). Structural characterization of green synthesized α-Fe2O3 nanoparticles using the leaf extract of Spondias dulcis. *Surfaces and Interfaces*, *20*, 100618. https://doi.org/10.1016/j.surfin.2020.100618

Vinayagam, R., Zhou, C., Pai, S., & Varadavenkatesan, T. (2021). Structural characterization of green synthesized magnetic mesoporous Fe_3O_4 NPs @ ME. *Materials Chemistry and Physics*, *262*, 124323. https://doi.org/10.1016/j.matchemphys.2021.124323

Vinayagam, V., Murugan, S., Kumaresan, R., Narayanan, M., Sillanpää, M., Viet N Vo, D., … Gadiya, S. (2022). Sustainable adsorbents for the removal of pharmaceuticals from wastewater: A review. *Chemosphere*, 300. 0045-6535. https://doi.org/10.1016/j.chemosphere.2022.134597

Wakejo, W. K., Meshasha, B. T., Kang, J. W., & Chebude, Y. (2022). Enhanced Ciprofloxacin Removal from Aqueous Solution Using a Chemically Modified Biochar Derived from Bamboo Sawdust : Adsorption Process Optimization with Response Surface Methodology. . *Adsorption Science & Technology*, 2022(23):1-23. https:// doi: 10.1155/2022/2699530

Wang, P., Sun, Q., Zhang, Y., & Cao, J. (2019a). One-step hydrothermal synthesis of zeolite KA from kaolin. *Micro and Nano Letters*, *14*(13), 1298–1302. https://doi.org/10.1049/mnl.2019.0190

Wang, P., Sun, Q., Zhang, Y., & Cao, J. (2019b). Synthesis of zeolite 4A from kaolin and its adsorption equilibrium of carbon dioxide. *Materials*, *12*(9), 1–12. https://doi.org/10.3390/ma12091536

Wei, F., Wang, K., Li, W., Ren, Q., Qin, L., Yu, M., Nie.M & Wang, S. (2023). Preparation of Fe/Ni-MOFs for the Adsorption of Ciprofloxacin from Wastewater. *Molecules*, *28*(11), 1–17. https://doi.org/10.3390/molecules28114411

Wei, H., Gui, Y., Kang, J., Wang, W., & Tang, C. (2018). A DFT study on the adsorption of H2S and So2 on Ni doped MoS_2 monolayer. *Nanomaterials*, *8*(9),646. https://doi.org/10.3390/nano8090646

Wu, M., Zhao, S., Jing, R., Shao, Y., Liu, X., Lv, F., & Liu, A. (2019). Competitive adsorption of antibiotic tetracycline and ciprofloxacin on montmorillonite. *Applied Clay Science*, *180*(April). https://doi.org/10.1016/j.clay.2019.105175

Wu, Z., Xie, J., & Liu, H. (2018). and performance of 4A zeolite based on opal waste rock for removal of ammonium ion. *Adsorption Science & Technology*. 36(9-10):1700-1715. https://doi.org/10.1177/0263617418803012

Yang, Y., Zhong, Z., Li, J., Du, H., & Li, Z. (2022). Efficient with low-cost removal and adsorption mechanisms of norfloxacin, ciprofloxacin and ofloxacin on modified thermal kaolin: experimental and theoretical studies. *Journal of Hazardous Materials*, *430*, 128500. https://doi.org/10.1016/j.jhazmat.2022.128500

Yao, G., Lei, J., Zhang, X., Sun, Z., Zheng, S., & Komarneni, S. (2018). Mechanism of zeolite X crystallization from diatomite. *Materials Research Bulletin*, *107*(June), 132–138. https://doi.org/10.1016/j.materresbull.2018.07.021

Zaied, B. K., Rashid, M., Nasrullah, M., Zularisam, A. W., Pant, D., & Singh, L. (2020). A comprehensive review on contaminants removal from pharmaceutical wastewater by electrocoagulation process. *Science of the Total Environment*, *726*, 138095. https://doi.org/10.1016/j.scitotenv.2020.138095

Zavareh, S., Farrokhzad, Z., & Darvishi, F. (2018). Modification of zeolite 4A for use as an adsorbent for glyphosate and as an antibacterial agent for water. *Ecotoxicology and Environmental Safety*, *155*, 1–8. https://doi.org/10.1016/j.ecoenv.2018.02.043

Zhang, Q., Yang, X., & Guan, J. (2019). Applications of Magnetic Nanomaterials in Heterogeneous Catalysis. *ACS Applied Nano Materials*, *2*(8), 4681–4697.

https://doi.org/10.1021/acsanm.9b00976

Zhang, Y., Han, H., Wang, X., Zhang, M., Chen, Y., Zhai, C., & Zhang, C. (2021). Utilization of NaP zeolite synthesized with different silicon species and $NaAlO_2$ from coal fly ash for the adsorption of Rhodamine B. *Journal of Hazardous Materials*, *415*, 125627. https://doi.org/10.1016/j.jhazmat.2021.125627

Zhou, Z., Jin, G., Liu, H., Wu, J., & Mei, J. (2014). Crystallization mechanism of zeolite A from coal kaolin using a two-step method. *Applied Clay Science*, *97–98*, 110–114. https://doi.org/10.1016/j.clay.2014.05.015